

MAGNETIC BEHAVIOR OF BASIC IRON(III) COMPOUNDS

- I. MAGNETIC BEHAVIOR OF THE BASIC IRON
SULFATES AND BASIC IRON CHROMATE
- II. MAGNETIC BEHAVIOR OF DELTA FERRIC
OXIDE HYDROXIDE

Thesis by

Dana Auburn Powers

In Partial Fulfillment of the Requirements
for the Degree of
Doctor of Philosophy

California Institute of Technology
Pasadena, California

1975

(Submitted July 25, 1974)

PREFACE

This thesis describes some studies of iron(III) polymeric compounds in which hydroxide acts as a bridging ligand. The focus of attention has been on the cooperative magnetic behavior of these species. Section I of the thesis deals with basic iron chromates ($M^I Fe_3(CrO_4)_2(OH)_6$ and $Fe(OH)CrO_4$) and basic iron sulfates ($M^I Fe_3(SO_4)(OH)_6$ and $Fe(OH)SO_4$). An appendix to this section is a complimentary investigation of polymeric iron chromates which do not have hydroxide ligands. Section II of the thesis deals with a ferrimagnetic allotrope of ferric oxide hydroxide ("basic iron oxide"). Throughout the thesis, emphasis has been placed on the effect of structure and stoichiometry on the bulk physical properties of chemical species.

The thread of continuity that passes through the thesis is not nearly so important as the differences in philosophy of the two sections. The dissimilarities lie in the way physical behavior of the compounds is treated. In Section I, the structures of the species in question are known. The magnetic behavior of these species is interpreted in terms of these known structures. The impact of small structural alterations on the bulk physical properties is the central theme of this section. Magnetic theory is applied, tested, and perhaps extended in the examination of these compounds. In Section II the structure of the phase, $\delta FeO(OH)$, is unknown. In this section, physical behavior of the phase is used to derive inferences concerning this structure. Variations in the physical

behavior of the phase are assumed to be indicative of structural modification. Heavy reliance is made on the ability of magnetic theory to resolve these modifications.

The thesis involves a great deal of terminology that will be "foreign" to many chemists. Further, there is much confusion of terminology in the literature of magnetism. I have listed below some terms defined as I have used them in the text. The definitions are not lexicographic pearls, and certainly many a solid-state physicist would quibble with them. But I feel they will at least clarify much of the discussion in the text.

Ferromagnetism: In its generic sense this term indicates positive deviations from the Curie-Weiss Law, saturation effects at sufficiently intense magnetic fields, and the possibility of a spontaneous magnetic moment at zero applied field. Hysteresis effects may be implied. In this generic sense, no specific magnetic mechanism is implied. The term is found applied to ferrimagnets, ferromagnets, and weak ferromagnets.

In its specific sense the term denotes a magnetic mechanism in which all the spins of unpaired electrons are aligned. In the case of localized electrons, integral Bohr magneton numbers equal to the number of unpaired electrons on the magnetic ion can be derived from magnetic data.

Ferromagnetic Interaction: This term is used to indicate positive coupling between two magnetic entities. For dimeric,

magnetic compounds, the Heisenberg Hamiltonian, $\mathcal{H} = -J\vec{S}_1 \cdot \vec{S}_2$, has a $J > 0$.

Antiferromagnetism: This is a generic term indicative of negative deviations from the Curie-Weiss Law. Often a maximum in the magnetic susceptibility occurs at some temperature. Unfortunately, the term is often used to imply a spin structure. In simple cases it is used to denote interpenetrating lattices of magnetic ions such that the spins of adjacent ions are equal in magnitude and opposite in orientation. However, the possible mechanisms for spin compensation are so complex that they preclude single-term descriptions.

Antiferromagnetic Interactions: The term is indicative of antiparallel coupling of spins between two magnetic entities. For dimeric, magnetic compounds, the Heisenberg Hamiltonian has a $J < 0$.

Ferrimagnetism: A ferrimagnetic material is analogous to an antiferromagnetic species in which spin compensation is incomplete. Experimentally it is much like a ferromagnet except non-integral Bohr magneton numbers are derived from magnetic data.

Superparamagnetism: This term denotes ferromagnetic (generic sense) species which are in thermodynamic equilibrium. No hysteresis effects are observed. Plots of magnetization versus applied field divided by temperature superimpose for all temperatures above the blocking temperature. This behavior is usually associated with fine-particle species or thin magnetic films. Other equivalent terms

in the literature are "hyperparamagnetism", "apparent paramagnetism", "collective paramagnetism", "quasiparamagnetism", and "sub-domain behavior".

Weak Ferromagnetism. This elusive term denotes positive deviations from Curie-Weiss behavior reminiscent of ferromagnetism. However, Bohr magneton numbers of only 10^{-3} to 10^{-2} of the nominal value can be derived from the magnetic data. The behavior is usually associated with species which are principally antiferromagnetic, but at some temperature display ferromagnetic character. Hysteresis effects often occur due to tremendous anisotropies in such species. Above the transition temperature, these phases obey the Curie-Weiss Law with large, negative Weiss temperatures.

Metamagnetism: Again, this behavior occurs among species which are principally antiferromagnetic, but which at sufficient field strengths become ferromagnetic (generic sense). Magnetic susceptibilities of such species obey the Curie-Weiss Law with positive Weiss temperatures.

In addition to these definitions, appendices follow some of the chapters and are intended to clarify some of the points drawn in the text.

It has been suggested by more than one member of the faculty that a thesis ought to be a description of all of one's graduate work. I estimate that 30% of my graduate tenure was devoted to fixing equipment, 20% to finding equipment necessary to fix other equipment, 10% to

recovering from fixing equipment, and 15% to chatting with secretaries. Though I am certain a description of all of this would make far less dry reading, I have chosen not to include it in the thesis. Several other investigations undertaken during my graduate work have been excluded for the purpose of coherency. These investigations have reached sufficient maturity and have contributed sufficiently to my understanding of the material in the text that they merit enumeration:

- (1) "Characterization of the Thermal Dehydration of Zirconium Oxide Halide Octahydrates," D. A. Powers and H. B. Gray, Inorg. Chem., 12, 2721 (1973).
- (2) "Low Temperature Thermal Decomposition of $\beta\text{FeO}(\text{OH})$," in preparation.
- (3) "Temperature Dependence of Infrared Absorptions Due to Bridging Ligands," P. J. Clendening, D. A. Powers, J. Hare, and H. B. Gray, in preparation.
- (4) "Magnetic Behavior and Structure of Copper Bismethionine," D. A. Powers and H. J. Schugar, in preparation.

The Preface of a thesis is the most auspicious place to acknowledge the assistance one must necessarily receive as a graduate student. Numerous people have assisted me in the acquisition of experimental data, and I have acknowledged them at the appropriate points in the text. The bulk of one's education as a graduate student comes from fellow students. This was certainly true in my case. I

would like to single out Al Schweitzer, Jack Thibeault, and Jeff Hare for their many acts of assistance and explanation.

Long before I came to Caltech, I had read that it was a place where, "...undergraduates are treated like graduate students and graduate students are treated like colleagues." ("The Scientist" Time-Life Modern Living Series, Vol. 2, 1962) It has been my distinct privilege to deal with three faculty members who exemplify this attitude.

Professor Harvey J. Schugar (Visiting Professor from Rutgers University) simply taught me to do chemical research. I cannot express the debt I owe him for this instruction except to wish that he may always have Tootsie Rolls, crystals, and clay.

Professor George R. Rossman (Professor of Minerology and Chemistry) first as a graduate student and then as a faculty member has been a constant source of information, ideas, and encouragement. The cynics who inhabit this or any campus would do well to emulate the cheerful, insatiably curious, and dedicated attitude of this scientist.

It has been a distinct pleasure to be a graduate student working with Professor Harry B. Gray (Professor of Chemistry). It is doubtful that any graduate advisor would have allowed me to pursue research so far afield from his own research interests as did Harry. His contribution to the work as "super consultant" has been significant--probably more so than even he knows. Our association has, for me, been down-right pleasant.

Finally, I am anxious to acknowledge the Fannie and John Hertz Foundation. The Foundation provided more than financial support. The value of their encouragement to pursue my interests in applied physical science cannot be overstated.

Dana A. Powers

Hermosa Beach, Ca.

ABSTRACT OF THESIS

I. The thermomagnetic behavior and infrared spectroscopic features of $\text{KFe}_3(\text{SO}_4)_2(\text{OH})_6$ (jarosite), $(\text{H}_3\text{O})\text{Fe}_3(\text{SO}_4)_2(\text{OH})_6$ (hydronium jarosite), $\text{KFe}_3(\text{CrO}_4)_2(\text{OH})_6$, $\text{Fe}(\text{OH})\text{SO}_4$ (basic iron sulfate), and $\text{Fe}(\text{OH})\text{CrO}_4$ (basic iron chromate) are reported. $\text{Fe}(\text{OH})\text{CrO}_4$ and $\text{KFe}_3(\text{CrO}_4)_2(\text{OH})_6$ are shown to be weak ferromagnets with Curie temperatures of 73 and 71°K, respectively. This unusual magnetic behavior is rationalized in terms of the ionic spin configurations of the phases. Exchange coupling through chromate bridging groups is shown to be weak.

II. The magnetic behavior and the influence of preparative history on the magnetic behavior of $\delta\text{FeO}(\text{OH})$ is reported. $\delta\text{FeO}(\text{OH})$ is shown to be a fine-particulate, uniaxial, magnetic species. Magnetization data for this species are shown to be consistent with the existence of magnetically inactive layers surrounding magnetic particles.

TABLE OF CONTENTS

	PAGE
I. MAGNETIC BEHAVIOR OF THE BASIC IRON SULFATES AND BASIC IRON CHROMATES	1
<u>Chapter 1.</u> Magnetic Behavior and Infrared Spectra of Jarosite, Basic Iron Sulfate, and Their Chromate Analogs.	2
Appendix 1. Structure of Basic Iron Chromate	32
Appendix 2. Factor Group Analysis of Vibrational Modes of Jarosite, Basic Iron Sulfate, and their Chromate Analogs	44
<u>Chapter 2.</u> Weak Ferromagnetism of the Basic Iron Chromates	58
Appendix 1. Magnetic Exchange Interactions through Chromate Bridges: The Magnetic Behavior of $M^I\text{Fe}(\text{CrO}_4)_2 \cdot 2\text{H}_2\text{O}$.	98
II. MAGNETIC BEHAVIOR OF $\delta\text{FeO}(\text{OH})$	130
<u>Chapter 3.</u> Introduction to $\delta\text{FeO}(\text{OH})$ and the Analysis of Short-Range Ordered Species.	131
<u>Chapter 4.</u> Magnetic Behavior of $\delta\text{FeO}(\text{OH})$.	164
<u>Chapter 5.</u> Influence of Cationic Impurities on the Magnetic Behavior of $\delta\text{FeO}(\text{OH})$.	227
Appendix 1. Derivation of the Relationship Between Particle Size and the Coercive Field of a Particle Assemblage.	310

Appendix 2. Derivation of Magnetic Anisotropy from Bulk Magnetic Data.	315
---	-----

PROPOSITIONS	323
--------------	-----

I. MAGNETIC BEHAVIOR OF THE BASIC IRON SULFATES
AND BASIC IRON CHROMATES

CHAPTER 1
MAGNETIC BEHAVIOR AND INFRARED SPECTRA OF
JAROSITE, BASIC IRON SULFATE AND
THEIR CHROMATE ANALOGS*

Abstract

The thermomagnetic behavior and infrared spectroscopic features of $\text{KFe}_3(\text{SO}_4)_2(\text{OH})_6$ (jarosite), $(\text{H}_3\text{O})\text{Fe}_3(\text{SO}_4)_2(\text{OH})_6$ (hydronium jarosite), $\text{KFe}_3(\text{CrO}_4)_2(\text{OH})_6$, $\text{Fe}(\text{OH})\text{SO}_4$ (basic iron sulfate) and $\text{Fe}(\text{OH})\text{CrO}_4$ (basic iron chromate) are reported. Spectroscopic data confirm that $\text{KFe}_3(\text{SO}_4)_2(\text{OH})_6$, $(\text{H}_3\text{O})\text{Fe}_3(\text{SO}_4)_2(\text{OH})_6$, and $\text{KFe}_3(\text{CrO}_4)_2(\text{OH})_6$ are isostructural with $\text{KAl}_3(\text{SO}_4)_2(\text{OH})_6$ (alunite). $\text{Fe}(\text{OH})\text{SO}_4$ and $\text{Fe}(\text{OH})\text{CrO}_4$ are also shown to be of similar structure. All the species are antiferromagnetic over the temperature range 300-76 °K. The compounds $\text{KFe}_3(\text{CrO}_4)_2(\text{OH})_6$ and $\text{Fe}(\text{OH})\text{CrO}_4$ undergo ferrimagnetic transition at 73 and 71 °K, respectively. The other phases remain antiferromagnetic down to 15 °K.

*Parts of this section were submitted for publication in the Journal of Solid State Chemistry by D. Powers, G. R. Rossman, H. J. Schugar, and H. B. Gray.

Magnetic studies of dimeric ferric complexes have shown that the extent of spin-spin interaction through a linear oxobridge is considerably greater than that through dihydroxy or dialkoxy bridges.^{1,2,3} These previous investigations have also identified infrared spectroscopic features which characterize the mode of bridging between ferric ions. These studies are extended in this thesis to examining polymeric, extended-lattice, ferric compounds. Herein are reported the results for $\text{KFe}_3(\text{SO}_4)_2(\text{OH})_6$ (synthetic jarosite), $(\text{H}_3\text{O})\text{Fe}_3(\text{SO}_4)_2(\text{OH})_6$ (hydronium jarosite), $\text{KFe}_3(\text{CrO}_4)_2(\text{OH})_6$, $\text{Fe}(\text{OH})\text{SO}_4$ (basic iron sulfate) and $\text{Fe}(\text{OH})\text{CrO}_4$ (basic iron chromate).

Infrared Results and Absorption Band Assignments

The band positions in the infrared spectra of the compounds examined in this study are presented in Tables 1 and 2. Spectra of $\text{KFe}_3(\text{SO}_4)_2(\text{OH})_6$, $\text{KFe}_3(\text{CrO}_4)_2(\text{OH})_6$, $\text{Fe}(\text{OH})\text{SO}_4$, and $\text{Fe}(\text{OH})\text{CrO}_4$ are shown in Figure 1. Assignment of these bands in these spectra to specific structural motions is complicated by the extended-lattice nature of the species and the considerable overlapping of the absorptions, particularly for the sulfate-containing phases. It must be emphasized, therefore, that the following interpretation represents an attempt to pinpoint only the main vibrational features of the compounds under discussion.

The O—H stretch in $\text{KAl}_3(\text{SO}_4)_2(\text{OH})_6$ produces an intense absorption band at 3482 cm^{-1} and a weaker shoulder at 3502 cm^{-1} .

Table I
Infrared Spectra of Compounds with Alunite Structure

$KFe_3(CrO_4)_2(OH)_6$	$KFe_3(CrO_4)_2(OD)_6$	ν_H/ν_D	$KFe_3(SO_4)_2(OH)_6$	$KFe_3(SO_4)_2(OD)_6$	ν_H/ν_D	$(H_3O^+)Fe_3(SO_4)_2(OH)_6$	$KAl_3(SO_4)_2(OH)_6$	Assignment
3378 s	2502 s	1.35	3385 s 1635 vw	2510 s	1.35	3365 s 1632 s	3502 shld 3482 s	O-H stretch HOH deformation
1002 s 920 s -- 850 s	742 s > 924 s 890† 855 s	1.35 0.99 0.99	1181 1080	1181 1080 1020 w 761 s	1.32	1190 s 1085 s 1002 s	1229 1090 1028 s	ν_3 mode of SO_4^{2-} ν_1 mode of SO_4^{2-} OH deformation
568 w shld 495 s 437 s 412 shld 389 m 348 m	520 w 480 s 438 s 412 shld 390 m 345 m	1.09 1.03 1.00 1.00 1.00 1.01	650 shld 626 s	652 shld 628 s	0.98 1.00	650 shld 616 s	680 m 627 s	ν_3 mode of CrO_4^{2-} ν_4 mode of SO_4^{2-}
321 m 283 s 230 m 199 w 155 w	305 m 269 m 221 m	1.05 1.05 1.04	550 shld 505 s 469 s 441 vw	493 s 472 s 383 vw	1.02 0.99 1.15	505 s 465 s 440 shld	595 w 528 s 486 s 433 w	vibrations of [FeO_6] oct.
	335 w 309 w 245 m 205 m 162 m 95 w	1.00 1.01 0.98 1.00 1.00 1.00					360 m, sh 332 m 291 m 222 m 186 w 90 w	ν_4 mode of CrO_4^{2-} vibrations of [FeO_6] oct and the remainder of the lattice

† Impurity due to $Fe(OH)CrO_4$.

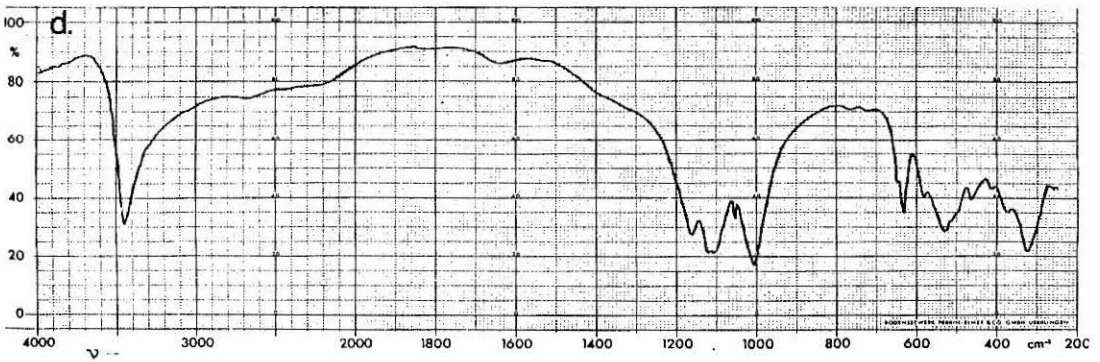
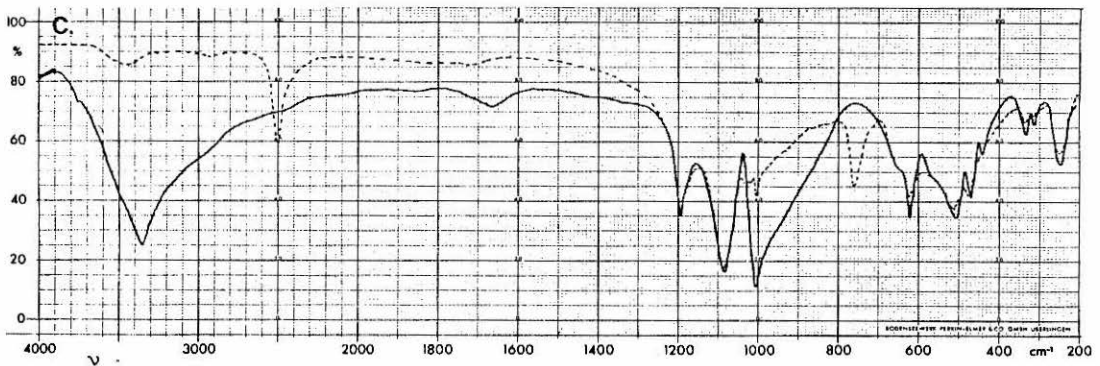
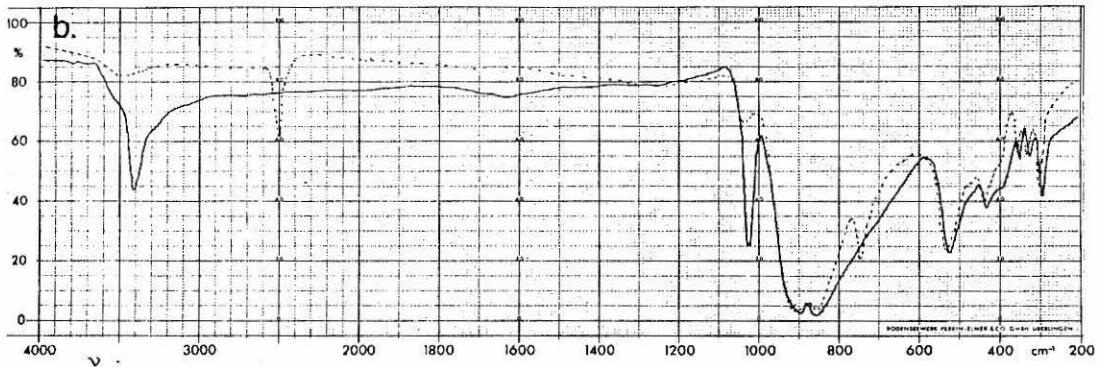
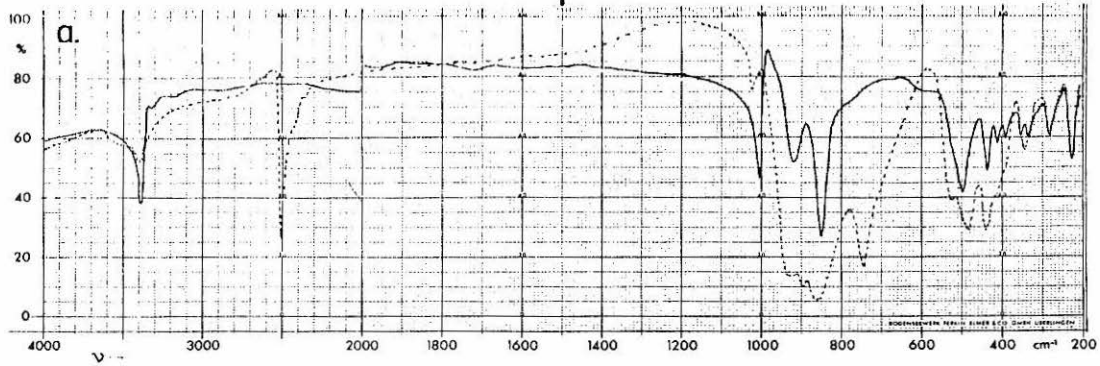
* Not present in all spectra but always weak when present.

Infrared Spectra of Basic Iron Sulfate
and Basic Iron Chromate

s=strong, m=medium, w=weak, vw=very weak

Fe(OH)(CrO ₄)	Fe(OD)CrO ₄	ν_H/ν_D	Fe(OH)SO ₄	Assignment
3418s	2520	1.36	3458s	OH stretch
			1172s	
			1138s	
			1112s	
			1058 m	ν_1 motion of SO ₄ ²⁻
1027s	745s	1.38	1020s	OH deformation
892ss	899 ss	0.99	650w	ν_3 motion of CrO ₄ ²⁻
858 ss	867 ss	0.99		
			638 s	ν_4 motion of SO ₄ ²⁻
527 s	582 s	0.91	585 w	vibrations of (FeO ₆) _{oct}
			538 s	
			505 w	
			468 m	
435 m	437 m	1.00	468 m	vibrations of (FeO ₆) _{oct}
			410vw	
395 w	400 w	0.99		ν_4 motion of CrO ₄ ²⁻
353 m	354 m	1.00		
328 m	330 m	1.00	331 s	vibrations of (FeO ₆) _{oct}
296 s	301 s	0.98	270 w	

Figure 1. Infrared of (a) $\text{KFe}_3(\text{SO}_4)_2(\text{OH})_6$, (b) $\text{KFe}_3(\text{CrO}_4)_2(\text{OH})_6$, (c) $\text{Fe}(\text{OH})\text{CrO}_4$, and (d) $\text{Fe}(\text{OH})\text{SO}_4$. Spectra of the respective deuterated species are indicated by the dotted lines.



The band due to $\nu(\text{OH})$ in the spectrum of $\text{KFe}_3(\text{SO}_4)_2(\text{OH})_6$ is a single intense peak at a somewhat lower energy (3385 cm^{-1}). Upon cooling to 93°K , doublet $\nu(\text{OH})$ structure is resolved, much like that observed in the spectrum of the aluminum phase. Deuteration shifts the main peak in the iron phase to 2510 cm^{-1} ($\nu_{\text{H}}/\nu_{\text{D}} = 1.35$).

The OH deformation in $\text{KFe}_3(\text{SO}_4)_2(\text{OH})_6$ is also at lower energy (1003 cm^{-1}) than its counterpart in the aluminum analog (1028 cm^{-1}). Deuteration shifts the absorption due to this deformation to 761 cm^{-1} . $\nu_{\text{H}}/\nu_{\text{D}} = 1.32$.

The infrared absorptions due to OH motions in the spectrum of $\text{KFe}_3(\text{CrO}_4)_2(\text{OH})_6$ are similar to those in the spectrum of the sulfate analog. The band attributable to OH stretching, which occurs at 3378 cm^{-1} , shifts to 2502 cm^{-1} ($\nu_{\text{H}}/\nu_{\text{D}} = 1.35$) with deuteration and resolves into a doublet when the sample is cooled to 93°K . The OH deformation gives rise to an absorption at 1002 cm^{-1} , which is shifted by deuteration to 742 cm^{-1} ($\nu_{\text{H}}/\nu_{\text{D}} = 1.35$).

The bands at 1181 and 1080 cm^{-1} in the spectrum of $\text{KFe}_3(\text{SO}_4)_2(\text{OH})_6$ are insensitive to deuteration and are assigned to components of the ν_3 mode of coordinated sulfate. The low site symmetry of SO_4^{2-} removes the degeneracy of the ν_3 mode and gives rise to the two absorptions. Similar bands appear at 1229 and 1090 cm^{-1} in the spectrum of $\text{KAl}_3(\text{SO}_4)_2(\text{OH})_6$. The ν_3 mode of CrO_4^{2-} also produces two bands at 920 and 850 cm^{-1} in the spectrum of $\text{KFe}_3(\text{CrO}_4)_2(\text{OH})_6$. The ν_4 mode of sulfate is split by the low site symmetry to give a band

at 626 cm^{-1} and a shoulder at 650 cm^{-1} in the spectrum of $\text{KFe}_3(\text{SO}_4)_2(\text{OH})_6$. Similar bands appear at 626 and 680 cm^{-1} in the spectrum of the aluminum analog. The bands at 389 and 348 cm^{-1} in the spectrum of $\text{KFe}_3(\text{CrO}_4)_2(\text{OH})_6$ are assigned to the ν_4 motion of CrO_4^{2-} .

The low site symmetries of SO_4^{2-} and CrO_4^{2-} ought to make the ν_1 and ν_2 vibrational modes of these groups infrared active. In fully deuterated $\text{KFe}_3(\text{SO}_4)_2(\text{OH})_6$ a sharp, but relatively weak, band at 1020 cm^{-1} can be observed, and is assigned to the ν_1 motion. The assignment is based on the location of ν_1 vibrations of SO_4^{2-} in other compounds.⁹ The infrared spectrum of $\text{KFe}_3(\text{CrO}_4)_2(\text{OH})_6$ does not exhibit any absorption attributable to ν_1 of CrO_4^{2-} . The expected location of ν_1 of chromate, 830 cm^{-1} , may be obscured by absorption bands due to the ν_3 mode. No bands in the spectra of any of the compounds could be assigned to the ν_2 mode of either SO_4^{2-} or CrO_4^{2-} . In the case of CrO_4^{2-} , absorption bands due to ν_2 would be obscured by absorptions attributable to the ν_4 mode. Coupling between the ν_2 mode of SO_4^{2-} and metal ion motion could shift a ν_2 absorption into a region of the spectrum where it could be obscured as well.

The remaining absorption bands are assigned to motions of the FeO_6 or AlO_6 coordination octahedron. Though considerable shifting of these absorptions occurs between iron and aluminum analogs, it was not possible to assign them more specifically.

The spectrum of $(\text{H}_3\text{O})\text{Fe}_3(\text{SO}_4)_2(\text{OH})_6$ is nearly identical to that of its potassium counterpart. Aside from an intensification of the $\nu(\text{OH})$ band, the only new feature in the spectrum is the appearance of a moderately strong band at 1632 cm^{-1} . The spectra of all the other phases show at most only a very weak absorption in this region. All the weak absorptions are readily assignable to absorbed or entrained water. The band in the spectrum of $(\text{H}_3\text{O})\text{Fe}_3(\text{SO}_4)_2(\text{OH})_6$ cannot be so explained, and it could possibly be due to the HOH deformation of the hydronium cation.

The infrared spectra of $\text{Fe}(\text{OH})\text{CrO}_4$ and $\text{Fe}(\text{OH})\text{SO}_4$ are similar to those of $\text{KFe}_3(\text{CrO}_4)_2(\text{OH})_6$ and $\text{KFe}_3(\text{SO}_4)_2(\text{OH})_6$. However, the spectra do allow a clear differentiation among these phases. The absorptions owing to OH vibrational modes are consistently higher in energy in the former compounds. In $\text{Fe}(\text{OH})\text{SO}_4$, the band due to $\nu(\text{OH})$ occurs at 3458 cm^{-1} , and the $\delta(\text{OH})$ band is at 1020 cm^{-1} . In the spectrum of $\text{Fe}(\text{OH})\text{CrO}_4$, these bands are at 3418 and 1027 cm^{-1} , respectively.

The ν_3 mode of SO_4^{2-} in basic iron sulfate is split by the reduced site symmetry into bands at 1172 , 1138 , and 1112 cm^{-1} . Only two broad bands (892 and 858 cm^{-1}) could be resolved for the ν_3 mode of CrO_4^{2-} in the spectrum of basic iron chromate. The ν_4 mode of SO_4^{2-} produces absorption bands at 650 and 638 cm^{-1} , and analogous bands owing to chromate are at 395 and 353 cm^{-1} . The reduced site symmetry of SO_4^{2-} and CrO_4^{2-} would be expected to

render the ν_1 and ν_2 modes infrared active, as well as removing the degeneracies of ν_3 and ν_4 . A weak band at 1058 cm^{-1} in the spectrum of $\text{Fe}(\text{OH})\text{SO}_4$ may be assigned to the ν_1 vibration. Because of the complex nature of the ir spectra, however, no other bands in the basic iron compounds could be assigned unambiguously to ν_1 or ν_2 . Other bands in the spectra are assigned to vibrations of the FeO_6 coordination octahedron.

The ir spectra of samples cooled to 93°K display considerable intensification and resolution of the band attributable to $\nu(\text{OH})$. There is also some shifting of band positions to higher energies. Absorption bands owing to the deformation mode of bridging hydroxide are especially sensitive to temperature. Such acute sensitivity has previously been observed in hydroxy and alkoxy bridged dimers.¹⁻³ The $\delta(\text{OH})$ bands resolve and shift 6 to 10 cm^{-1} higher in energy. Other absorption bands in the ir spectra also show small shifts to higher energy when the samples are cooled.

The far-infrared spectra of $\text{KFe}_3(\text{CrO}_4)_2(\text{OH})_6$ and $\text{Fe}(\text{OH})\text{CrO}_4$ over the region $525\text{-}40\text{ cm}^{-1}$ were examined at several temperatures below 72°K . This region was searched because it should be sensitive to structural perturbations which might be associated with the dramatic change in magnetic behavior of these species at low temperatures (vide infra). However, only a smooth continuation of the band shifts mentioned above was observed.

Magnetic Results

Representative magnetic data obtained in this study are presented in Table 3. All of the samples have magnetic moments per iron of 3.4 to 3.8 Bohr magnetons (B. M.) at room temperature. These moments are considerably lower than the spin-only value of 5.92 B. M. for isolated ferric ion, and are indicative of extensive exchange interaction. All of the samples display a weakly temperature dependent magnetic susceptibility over the temperature range 300 to 76°K (Figure 2). The effective magnetic moments drop substantially over this temperature range.

In the region 300 to 80°K basic iron sulfate and basic iron chromate exhibit the magnetic behavior expected for antiferromagnets. Néel points for these compounds are difficult to determine precisely, because the temperature range over which the magnetic transition occurs is very large. A Néel temperature of 173°K was estimated for $\text{Fe}(\text{OH})\text{SO}_4$. That of $\text{Fe}(\text{OH})\text{CrO}_4$ is more difficult to determine, but appears to be considerably higher at 290°K. Neither compound obeys the Curie-Weiss law over any significant range of the temperatures examined.

The compounds $\text{KFe}_3(\text{CrO}_4)_2(\text{OH})_6$, $\text{KFe}_3(\text{SO}_4)_2(\text{OH})_6$, and $(\text{H}_3\text{O})\text{Fe}_3(\text{SO}_4)_2(\text{OH})_6$ obey the Curie-Weiss law ($\chi = C/(T - \theta_w)$) from 300 to 80°K with Weiss temperatures of about -800°K. The Weiss temperatures indicate extensive antiferromagnetic exchange interactions among the metal ions. Incorporation of these large, negative,

Table III

Magnetic Data for Hydroxobridged Compounds

Temp °K	KFe ₃ (SO ₄) ₂ (OH) ₆		KFe ₃ (CrO ₄) ₂ (OH) ₆		(H ₂ O)Fe ₃ (SO ₄) ₂ (OH) ₆		Fe(OH)SO ₄		Fe(OH)CrO ₄	
	10 ³ χ _M ^(d)	μ _{eff} /Fe	10 ³ χ _M	μ _{eff} /Fe ^(d)	10 ³ χ _M	μ _{eff} /Fe ^(d)	10 ³ χ _M	μ _{eff} /Fe ^(d)	10 ³ χ _M	μ _{eff} /Fe ^(d)
298	15.8	3.54	13.7	3.30	15.1	3.46	6.11	3.84	5.06	3.47
250	16.1	3.28	14.2	3.08	15.7	3.23	6.26	3.54	5.04	3.17
200	16.8	2.99	14.7	2.80	16.3	2.95	6.34	3.18	4.97	2.82
150	17.7	2.66	15.3	2.47	16.9	2.60	6.32	2.75	4.85	2.41
100	18.6	2.22	16.0	2.06	17.8	2.18	6.14	2.22	4.66	1.93
50	19.8	1.62	75.4	b	19.7	1.62	5.89	1.58	13.06	b
15	18.1	0.85	81.8	b	18.0	0.85	6.00	0.84	15.56	b
^θ Weiss	-770 ± 100°K		-770 ± 100°K		-840 ± 100°K		(a)		(a)	
^θ Neél	45 ± 10°K		(b)		50 ± 10°K		173 ± 10°K		290 ± 40°K	
^ω μ _{298°K} ^(c)	6.69		6.80		6.78		(a)		(a)	

diamag. corr.^e = -195 × 10⁻⁶ cgs -200 × 10⁻⁶ cgs -195 × 10⁻⁶ cgs -62.0 × 10⁻⁶ cgs -64 × 10⁻⁶ cgs

a) does not obey Curie-Weiss Law.

b) not a simple antiferromagnet--see text.

c) From $\mu_{\text{eff}}^{\omega} = 2.828 \sqrt{\chi_M^{\omega} (T - \theta)}$.d) From $\mu_{\text{eff}} = 2.828 \sqrt{\chi_M T}$.

e) From reference (8).

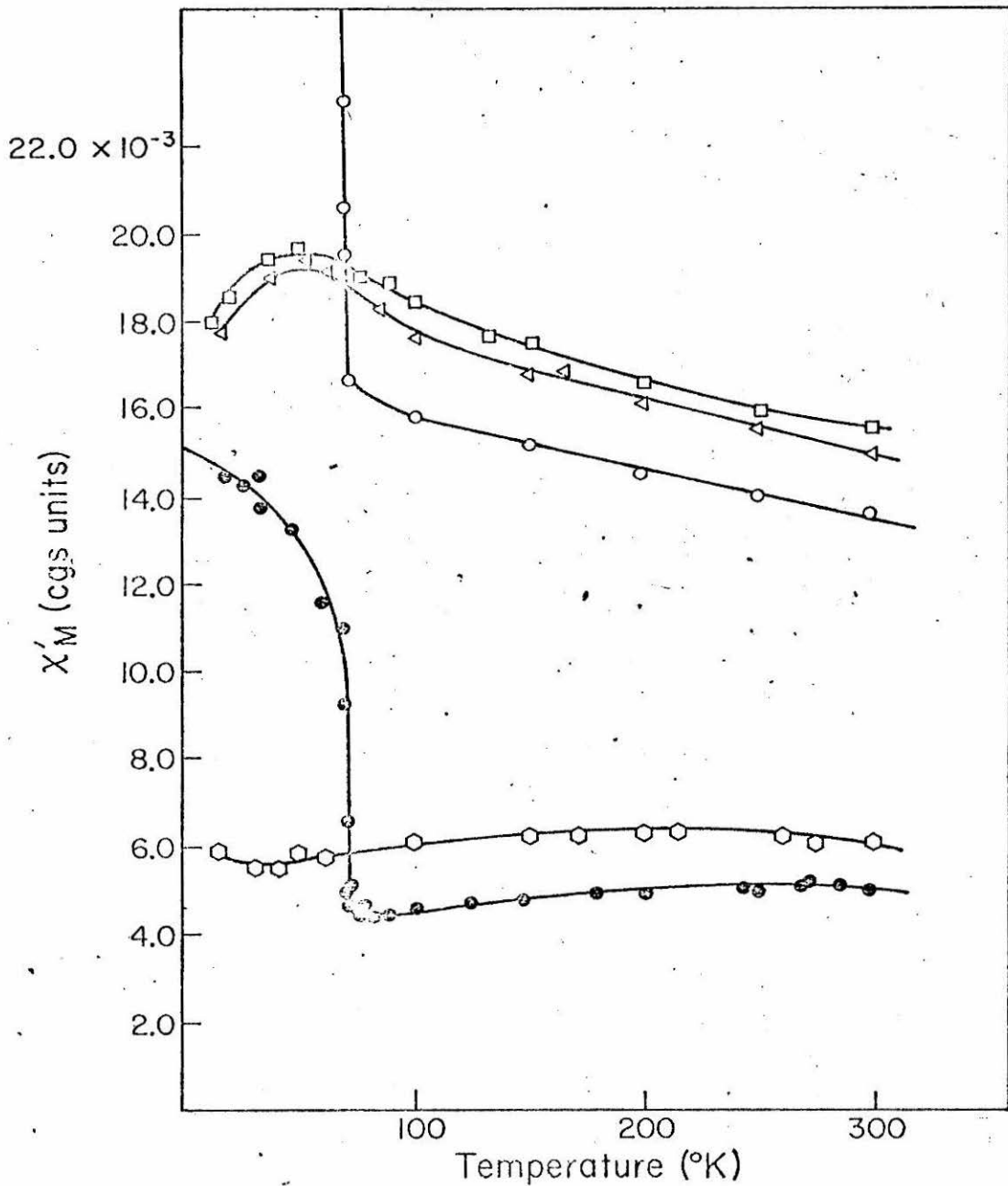


Figure 2. Molar susceptibility versus temperature for \bullet $\text{KFe}_3\text{-(CrO}_4\text{)}_2\text{(OH)}_6$, Δ $\text{H}_3^+\text{OFe}_3\text{(SO}_4\text{)}_2\text{(OH)}_6$, \square $\text{KFe}_3\text{(SO}_4\text{)}_2\text{(OH)}_6$, \circ Fe(OH)SO_4 and \circ Fe(OH)CrO_4 .

Weiss temperatures in the computation of effective magnetic moments yields values of about 6.8 B.M. These large values suggest that the iron ions are in the $S = 5/2$ state, but that simple Weiss theory fails to compensate properly for the exchange interactions among the metal ions. The compounds behave magnetically over the temperature region 300 to 80°K as antiferromagnets above their Néel points. The field dependences of their magnetizations are typical of such antiferromagnets. The magnetizations vary linearly with applied field up to 11,000 oe, and pass through zero at zero applied field.

Below 76°K the sulfate-containing phases all retain their antiferromagnetic character. The compounds $\text{KFe}_3(\text{SO}_4)_2(\text{OH})_6$ and $(\text{H}_3\text{O})\text{Fe}_3(\text{SO}_4)_2(\text{OH})_6$ have sharp Néel points at 45 and 50°K, respectively. Small increases in the magnetic susceptibilities of these species at the lowest temperature are probably due to paramagnetic impurities. On the other hand, the chromate phases undergo abrupt changes in magnetic behavior in the lower temperature region. At 71 and 73°K, respectively, the magnetic susceptibilities of $\text{Fe}(\text{OH})\text{CrO}_4$ and $\text{KFe}_3(\text{CrO}_4)_2(\text{OH})_6$ rise sharply (Figure 3). These transitions occur over a temperature range of less than 2°K. Once the transition occurs, the magnetization of each of these species displays saturation effects. $\text{KFe}_3(\text{CrO}_4)_2(\text{OH})_6$ is magnetically soft and its magnetization loop has no hysteresis losses ($H_c < 10$ oe) (Figure 4). Reversal of the magnetization once the applied field is reversed, however, is quite slow, requiring three hours to accomplish at -80 oe and 63°K.

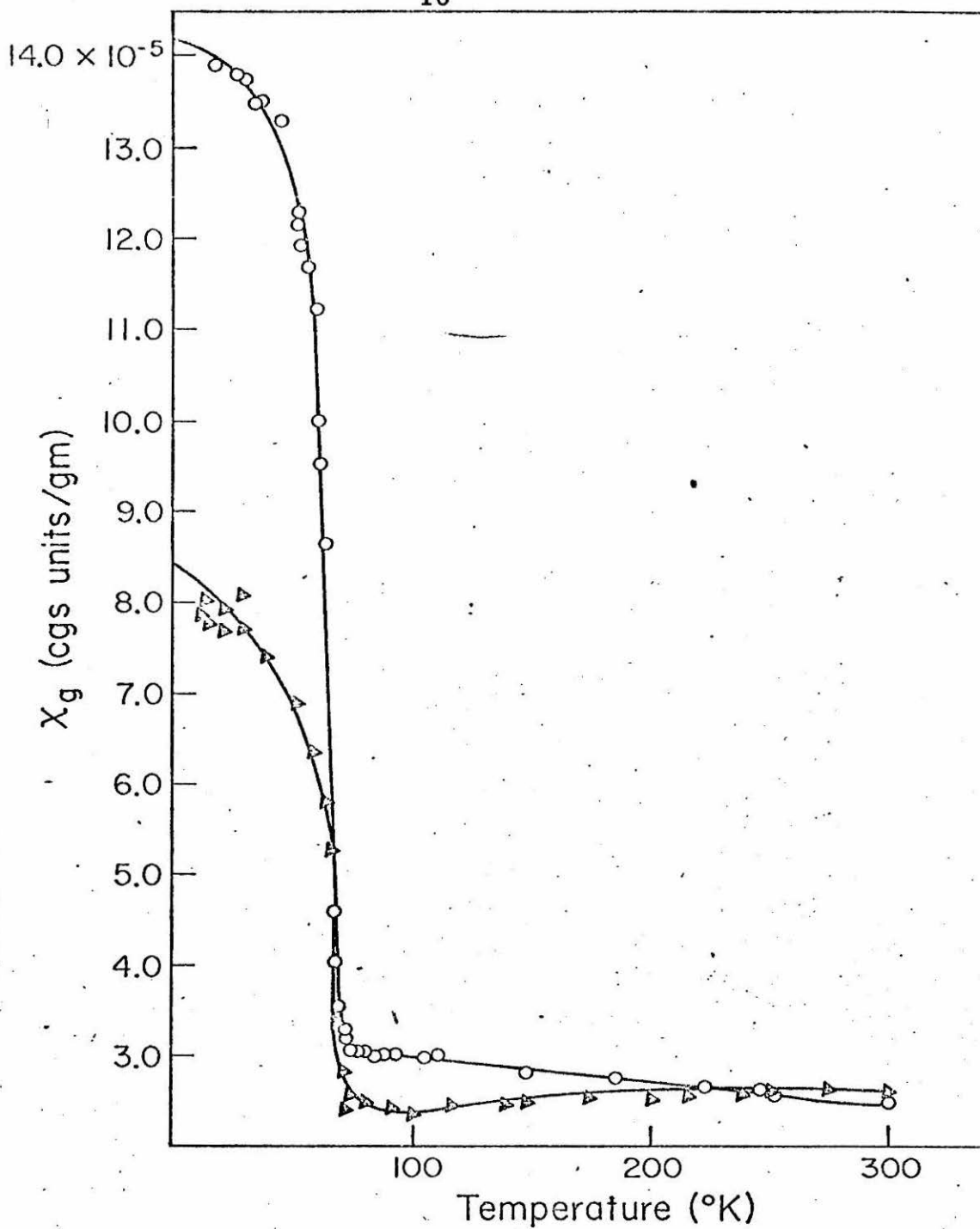


Figure 3. Gram susceptibility versus temperature for

○ $\text{KFe}_3(\text{CrO}_4)_2(\text{OH})_6$ and $\Delta \text{Fe}(\text{OH})\text{CrO}_4$.

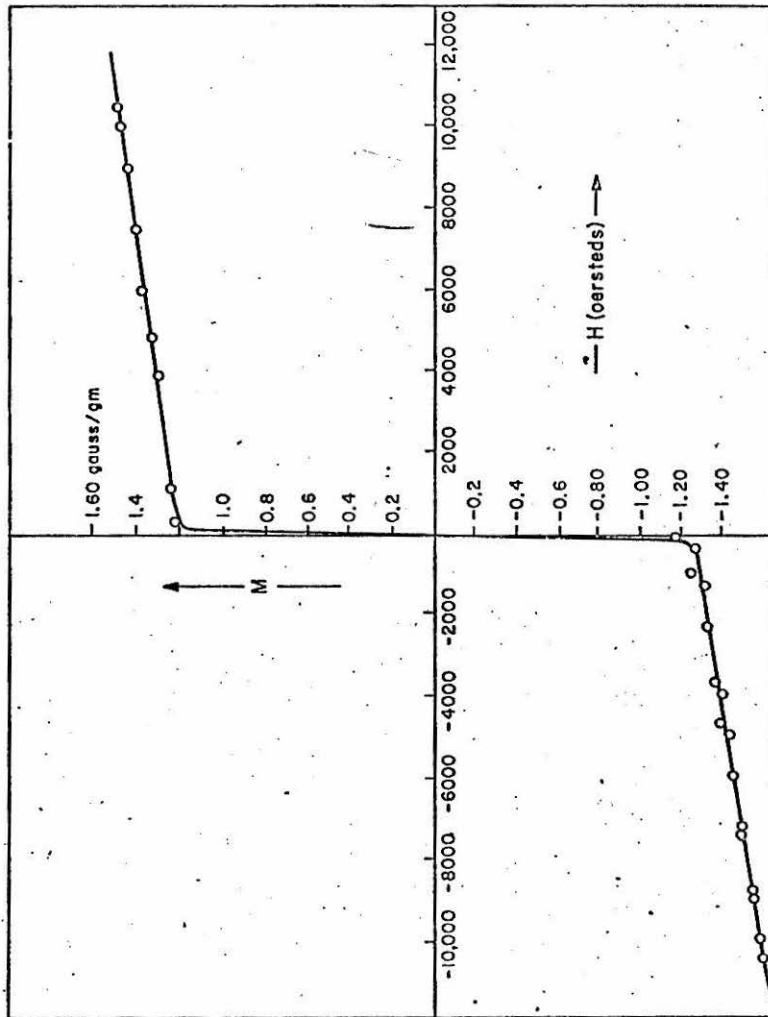


Figure 4. Gram magnetization versus applied field for $KFe_3(CrO_4)_2(OH)_6$ at 28°K.

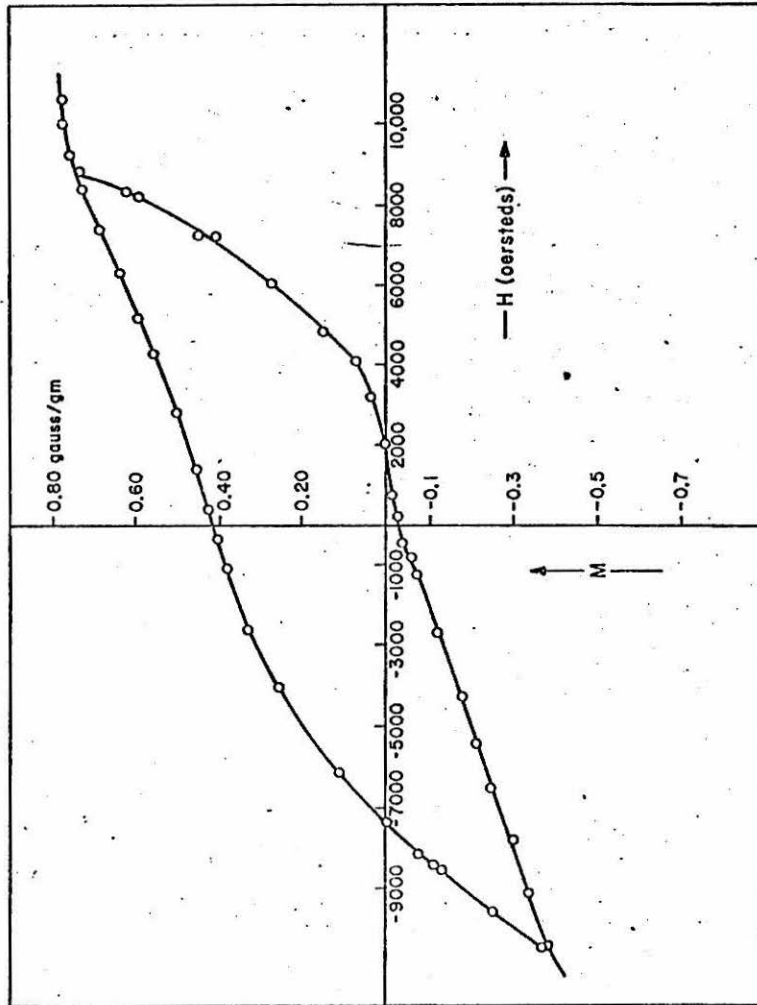


Figure 5. Gram magnetization versus applied field at 33°K for Fe(OH)CrO₄.

On a shorter time scale, hysteresis losses appear and the magnetization loop is considerably distorted from the centrosymmetric form. $\text{Fe}(\text{OH})\text{CrO}_4$ is extremely hard magnetically. Its magnetization loop shows huge hysteresis losses (Figure 5). The coercive field is 7000 oe at 55°K and greater than 11,000 oe at 29°K. The magnetization loop of $\text{Fe}(\text{OH})\text{CrO}_4$ is severely distorted along the magnetization (M) axis as well as along the applied field (H) axis. Even at the highest field used in this study (11,000 oe), $\text{Fe}(\text{OH})\text{CrO}_4$ did not saturate. It is possible that the hysteresis loop of basic iron chromate is a minor loop, which would account for its distorted, wasp-waisted form.¹⁰

When samples of $\text{KFe}_3(\text{CrO}_4)_2(\text{OH})_6$ are contaminated with small amounts of $\text{Fe}(\text{OH})\text{CrO}_4$, they also have magnetization loops distorted along the M and H axes. It may be noted that Watanabe¹¹ observed similar behavior in LaFeO_3 contaminated with a magnetically hard impurity.

Saturation magnetizations for both chromate phases indicate a magnetic moment ($n = \sigma_0, \infty \text{ MW} / \beta N_A$) of only 0.005 B.M., which is some 1000 times smaller than the nominally expected value for ferromagnetic ferric ($S = 5/2$) ions.

Discussion

The infrared spectra are consistent with the X-ray powder diffraction data showing that $\text{KFe}_3(\text{CrO}_4)_2(\text{OH})_6$, $(\text{H}_3\text{O})\text{Fe}_3(\text{SO}_4)_2(\text{OH})_6$, $\text{KFe}_3\text{-CrO}_4)_2(\text{OH})_6$, and $\text{KAl}_3(\text{SO}_4)_2(\text{OH})_6$ are isostructural. This structure (Figure 6) consists of metal ions located in slightly distorted octahedral

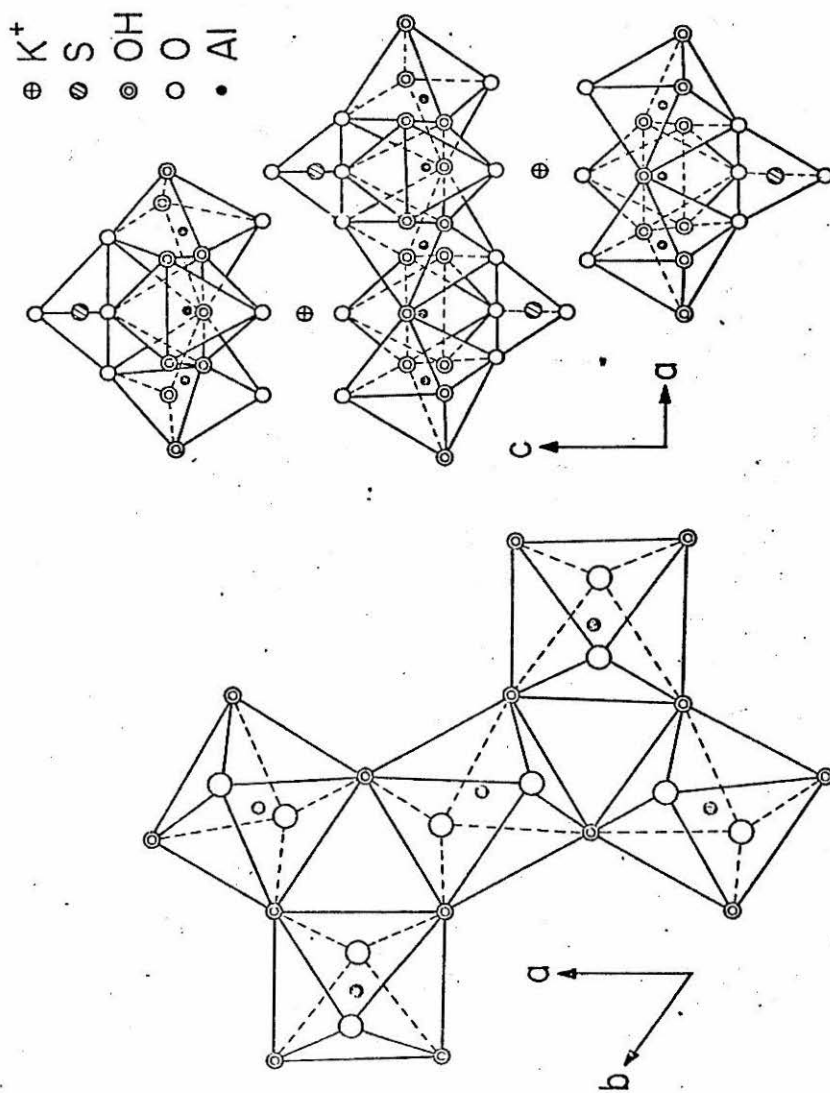


Figure 6. Structure of $KAl_3(SO_4)_2(OH)_6$ viewed along the c and the b axes.
 (After Wang (12)).

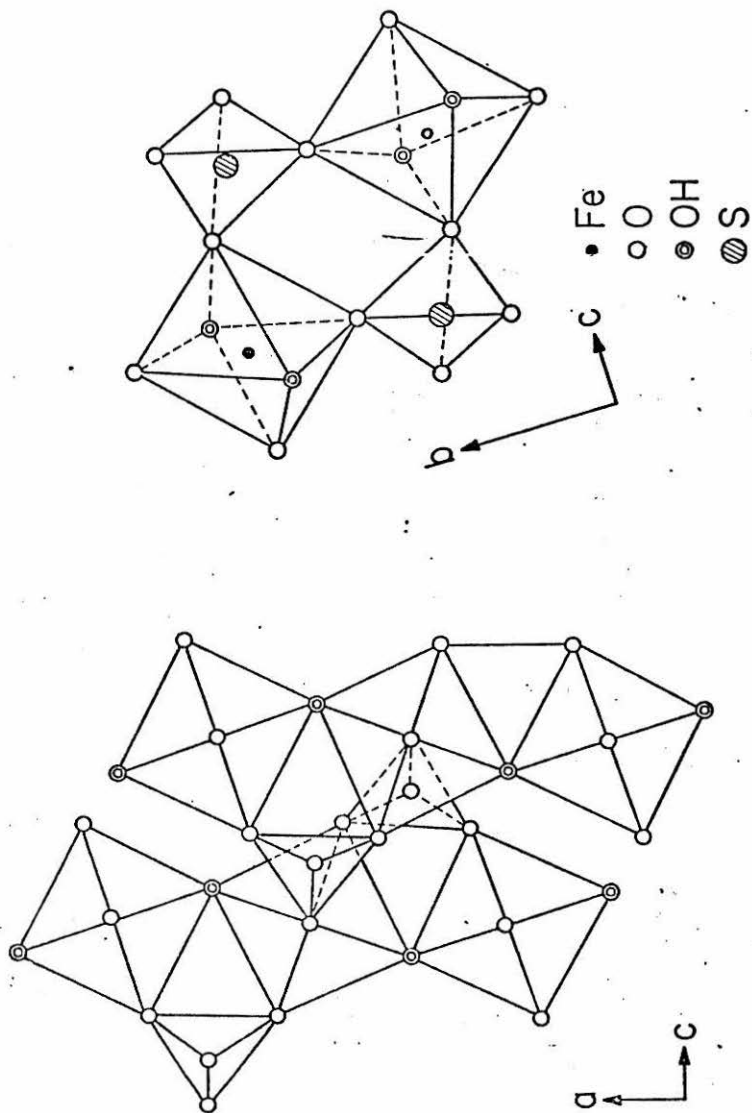


Figure 7. Structure of $\text{Fe}(\text{OH})\text{SO}_4$, viewed along the b and a axes. (After Johansen (4).)

coordination polyhedra; each polyhedron has four bridging hydroxides in a plane and sulfate or chromate oxygens at the apices.¹² Three of the sulfate or chromate oxygens are coordinated to metal ions and the symmetry of the SO_4^{2-} or CrO_4^{2-} groups is reduced to C_s . The metal ions are joined together by the sulfate or chromate groups and the network of dihydroxy bridges to form sheets separated by the uncoordinated sulfate or chromate oxygens and the cations, K^+ or H_3O^+ .

The ir spectra also show that $\text{Fe}(\text{OH})\text{CrO}_4$ has the basic iron sulfate structure, consistent with the X-ray powder diffraction results of Bounin and Lecerf.⁵ In this structure (Figure 7) ferric ions in distorted octahedral coordination polyhedra form polymeric chains. The metal ions are linked by two, trans hydroxy bridges and coordinated sulfate or chromate oxygens. All sulfate and chromate oxygens are coordinated and the symmetries of the SO_4^{2-} and CrO_4^{2-} groups are, again, reduced to C_s . The chains are linked together by coordinated sulfate or chromate groups.⁴

The reduction in symmetry of the ideally tetrahedral chromate and sulfate is reflected in the infrared spectra. Vibrations due to the ν_3 and ν_4 modes, which are infrared active in T_d symmetry, are no longer degenerate and produce several absorption bands in the ir spectra of all of the phases. In the spectra of the sulfate-containing phases, an absorption band may be assigned to $\nu_1(\text{SO}_4)^{2-}$, which is inactive in T_d symmetry.

The band assigned to HOH deformation in the ir spectrum of $(\text{H}_3\text{O})\text{Fe}_3(\text{SO}_4)_2(\text{OH})_6$ provides some evidence for (H_3O^+) as a valid structural entity in this compound. However, the differences in the spectral results obtained for this species and those expected for coordinated or lattice water are not great enough to allow a firm conclusion on this question.

The infrared spectra allow some improvement in the structural characterization of OH in these phases. The ir band position of the O—H stretch is sensitive to hydrogen bonding interaction and may be used as a spectral ruler for hydrogen bond lengths.¹³ All hydrogen bonds were assumed to be linear, in keeping with the known structures of $\text{Fe}(\text{OH})\text{SO}_4$ and $\text{KAl}_3(\text{SO}_4)_2(\text{OH})_6$. The hydrogen bond length calculated for $\text{KAl}_3(\text{SO}_4)_2(\text{OH})_6$ is $3.00 \pm 0.02 \text{ \AA}$. The only available structural information concerning basic iron sulfate reports that there is no hydrogen bonding.⁴ However, we calculate that the hydrogen bond lengths for basic iron sulfate and basic iron chromate are 2.87 and 2.84 \AA , respectively.

The $\text{KFe}_3(\text{SO}_4)_2(\text{OH})_6$ structure has been treated theoretically as consisting of magnetically isolated sheets with ferric ions in a kagome array.^{15,16} The basic iron sulfate structure has been treated as a collection of magnetically isolated infinite chains.¹⁷ Since the chromate and sulfate phases are isostructural, and above their respective transition temperatures the magnetic behavior is quite similar, $\text{Fe}(\text{OH})\text{CrO}_4$ and $\text{KFe}_3(\text{CrO}_4)_2(\text{OH})_6$ can be treated in ways

analogous to those used for their sulfate counterparts. These theoretical results require that magnetic exchange occur only between nearest neighbor metal ions within the chain or sheet. The reduction in the effective magnetic moment from the value expected for isolated ferric ($S = 5/2$) ion is then a good indication of the strength of the antiferromagnetic coupling between the metal ions.

An interesting comparison between the temperature behavior of the effective magnetic moments of these polymeric species and that of moments for octahedrally coordinated ferric ions in various states of aggregation is shown in Figure 8. Magnetically isolated ferric ions have temperature independent magnetic moments of 6.0 B.M. Ferric dimers which are antiferromagnetically coupled through dihydroxy bridges have "reduced" 300°K moments of 5.1 B.M. per iron. This moment drops to 1.0 B.M. at 17°K. Oxobridged iron(III) dimers at 300°K have even lower moments of about 2.0 B.M., indicative of the stronger antiferromagnetic coupling between the two metal ions. The effective moments for these oxobridged species drop to near zero at 30°K. The moments for the polymeric species in this study lie between those for the hydroxy bridged dimers and the oxobridged ones. The availability of interaction with more than one nearest neighbor metal ions makes exchange through the hydroxy bridges of the polymeric species more extensive than in the simple dimeric compounds, but not so effective as exchange through a linear oxobridge. Closer examination of the data shows that the moment for

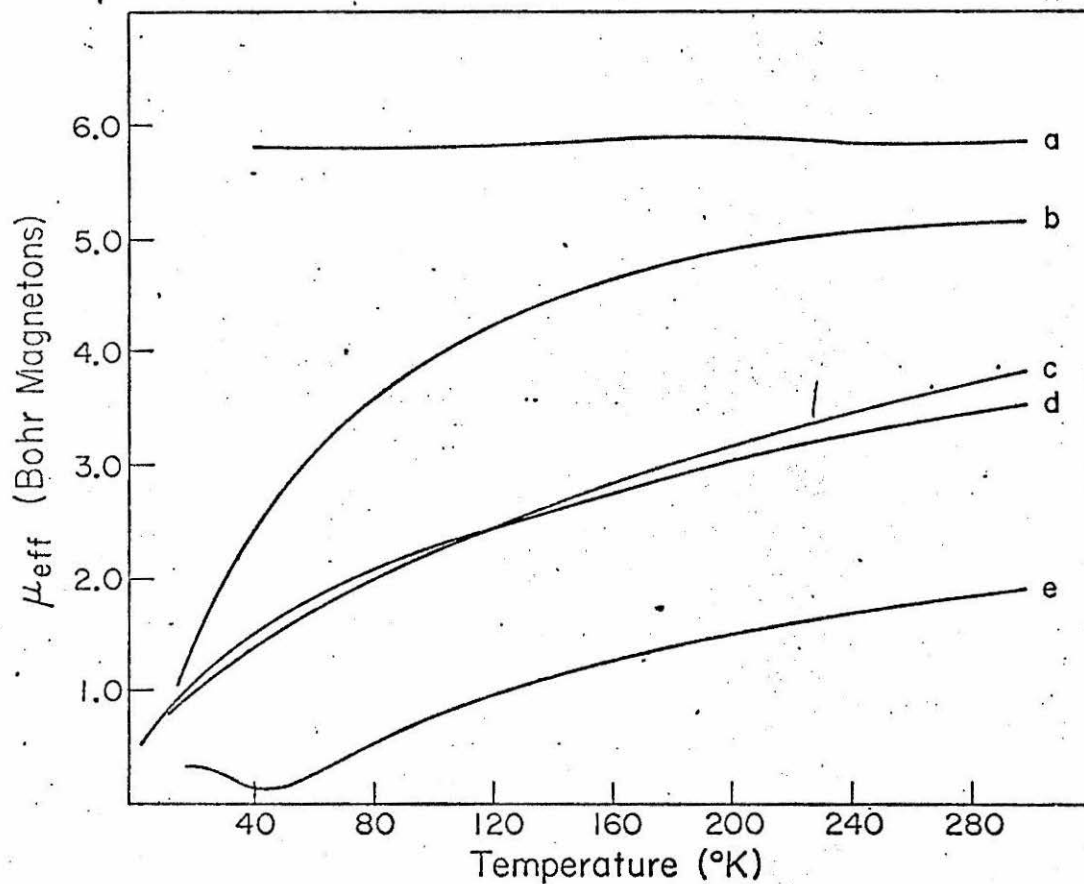


Figure 8. μ_{eff} versus temperature for (a) $\text{Fe}(\text{picolinate})_2(\text{H}_2\text{O})\text{Cl}$, (b) $[\text{Fe}(\text{picolinate})_2(\text{OH})]_2$, (c) $\text{Fe}(\text{OH})\text{SO}_4$, (d) $\text{KFe}_3(\text{SO}_4)_2(\text{OH})_6$, (e) $\text{enH}_2[\text{FeHEDTA}]_2\text{O} \cdot 6\text{H}_2\text{O}$.

$\text{Fe}(\text{OH})\text{SO}_4$ is somewhat higher than the moment for $\text{KFe}_3(\text{SO}_4)_2(\text{OH})_6$. Similarly, $\text{Fe}(\text{OH})\text{CrO}_4$ has a higher moment than $\text{KFe}_3(\text{CrO}_4)_2(\text{OH})_6$. In the basic iron sulfate structure each metal ion can interact magnetically with only two nearest neighbor metal ions, whereas in the alunite structure a metal ion can interact with either three or four nearest neighbors. Consequently, exchange is less effective in the basic iron sulfate structure and the magnetic moment should be, as is observed, higher than for compounds with the alunite structure. Chromate-containing species also have enhanced exchange interactions in the 300 to 80°K temperature range relative to species containing sulfate. Chromate ion possibly introduces small changes in the bond lengths and angles in the coordination polyhedra surrounding the metal ions. The differences between chromate and sulfate manifest themselves most clearly in the magnetic behavior below 76°K, where the chromate-containing species exhibit ferrimagnetic behavior, whereas those with sulfate remain antiferromagnetic. The magnetic transition made by $\text{Fe}(\text{OH})\text{CrO}_4$ and $\text{KFe}_3(\text{CrO}_4)_2(\text{OH})_6$ does not mark a phase change. The infrared spectra of these compounds are virtually identical at temperatures above and below their transition points. The transition points are correctly the Curie points of these phases.

The saturation magnetizations of $\text{Fe}(\text{OH})\text{CrO}_4$ and $\text{KFe}_3(\text{CrO}_4)_2(\text{OH})_6$ are quite low, reminiscent of so-called weak ferromagnetism. Weak ferromagnetism is a poorly understood phenomenon which has

been reviewed by Moriya.¹⁸ Compounds that are weakly ferromagnetic typically have very sharp transition points, and above the transition point follow Curie-Weiss behavior with large, negative Weiss temperatures. A variety of mechanisms, such as defects in stoichiometry,¹⁹ antiferromagnetic domains with magnetized walls, grain boundary interactions,²⁰ or the intrinsic nature of the material^{18,21,22} have been invoked to explain the occurrence of weak ferromagnetism. It is difficult to choose among these possible mechanisms. Rationalizing the onset of weak ferromagnetism based on spin configurations is attractive, as both the chromate phases develop well-formed, though small, crystals and their magnetic properties vary little from sample to sample. It is well known that a linear chain of spins cannot develop stable ferromagnetism.²³ The approximation that treats basic iron chromate as linear, independent, chains of ferric ions must fail below 73°K. Takano *et al.*¹⁵ proposed that metal ions in a kagome array, such as in $\text{KFe}_3(\text{SO}_4)_2(\text{OH})_6$ and $\text{KFe}_3(\text{CrO}_4)_2(\text{OH})_6$, could adopt a stable antiferromagnetic structure only with a triangular spin arrangement. In a collinear spin arrangement, the metal ions in a kagome array could develop stable ferromagnetism. Thus, a possible interpretation of the results is that the onset of weak ferromagnetism in $\text{KFe}_3(\text{CrO}_4)_2(\text{OH})_6$ marks the change from a triangular to a collinear spin arrangement.

Experimental

The following compounds were prepared by published procedures and characterized by elemental analyses and X-ray powder-diffraction patterns: $\text{Fe}(\text{OH})\text{SO}_4$,⁴ Calcd (%): Fe, 33.06; S, 56.87. Found: Fe, 32.85, 33.04; S, 57.03, 57.01. $\text{Fe}(\text{OH})\text{CrO}_4$ ⁵ Calcd (%): Fe, 29.54; Cr, 27.54. Found: Fe, 29.15; Cr, 27.11. $\text{KFe}_3(\text{CrO}_4)_2(\text{OH})_6$ ⁵ Calcd (%): Fe, 30.99; Cr, 19.24; K, 7.23. Found: Fe, 30.77, 30.87; Cr, 18.95, 18.95; K, 6.99. $\text{KFe}_3(\text{SO}_4)_2(\text{OH})_6$ ⁶ Calcd (%): Fe, 33.45; S, 12.80; K, 7.81. Found: Fe, 33.41; S, 13.01; K, 7.68.

Two additional samples were used in this study: $(\text{H}_3\text{O})\text{Fe}_3(\text{SO}_4)_2(\text{OH})_6$, prepared by the method of Brauer.⁷ Calcd (%): Fe, 34.85; S, 13.40; K, 0.00. Found: Fe, 34.81; S, 13.55; K < 0.03; and a natural sample of $\text{KAl}_3(\text{SO}_4)_2(\text{OH})_6$ of Japanese origin, whose identity and purity were confirmed by X-ray powder diffraction.

Partially deuterated analogs of the above species were obtained by using D_2O in place of H_2O as solvent in the preparative methods. Nearly completely deuterated samples of $\text{KFe}_3(\text{SO}_4)_2(\text{OH})_6$ and $\text{KFe}_3(\text{CrO}_4)_2(\text{OH})_6$ were prepared either from anhydrous reagents or from starting materials which had been recrystallized from D_2O . The deuterated species were characterized by X-ray powder diffraction, infrared spectroscopy, and optical microscopy.

Infrared spectra were taken on Perkin-Elmer Model 225 and Model 180 spectrophotometers using KBr and TlBr discs (4000 - 200 cm^{-1}) and paraffin wax films on polyethylene (400 - 40 cm^{-1}).

Magnetic data were collected on a PAR Model FM-1 vibrating sample magnetometer calibrated with $\text{HgCo}(\text{SCN})_4$. Field strengths were measured with a Bell Model 600 A gaussmeter and Hall probe. Temperatures were measured with a Lakeshore Cryotronics GaAs diode or thermocouples calibrated against the diode. Diamagnetic corrections were taken from published data.⁸ X-ray powder diffraction patterns were obtained with a Debye Scherrer camera with film mounted in the Stramanis arrangement. Samples were mounted in 0.3 Glaskapillern tubes and subjected to rotation and reciprocation during exposure to iron-filtered cobalt $K\alpha$ radiation.

References

1. H. J. Schugar, G. R. Rossman, and H. B. Gray, J. Amer. Chem. Soc., 91, 4564-66 (1969).
2. H. J. Schugar, G. R. Rossman, C. G. Barraclough, and H. B. Gray, J. Amer. Chem. Soc., 94, 2683-90 (1972).
3. C.-H. S. Wu, G. R. Rossman, H. B. Gray, G. S. Hammond, and H. J. Schugar, Inorg. Chem., 11, 990-4 (1972).
4. G. Johansson, Acta Chem. Scand., 16, 1234 (1962).
5. A. Bounin and A. Lecerf, Comp. Rend. Ser. C., 262, 1782 (1966).
6. J. G. Fairchild, Amer. Min., 18, 543 (1933).
7. G. Brauer, ed. Handbook of Preparative Inorganic Chemistry, 2nd ed., 1507 (1965).
8. P. W. Selwood, Magnetochemistry, 2nd ed., Interscience Publishers, New York (1956).
9. K. Nakamoto, Infrared Spectra of Inorganic and Coordination Compounds, 2nd ed., Wiley Interscience, New York (1970).
10. I. S. Jacobs and C. P. Bean, in Magnetism, Vol. III, G. T. Rado and Harry Suhl, eds., Chap. 6, Academic Press, New York, 1963.
11. Hiroshi Watanabe, J. Phys. Soc. Japan, 14, 511 (1959).
12. R. Wang, W. F. Bradley, and H. Steinfink, Acta Cryst., 18, 249 (1965).
13. K. Nakamoto, M. Margoshes, and R. E. Rundle, J. Amer. Chem. Soc., 77, 6480 (1959).

14. S. B. Hendricks, Amer. Min., 22, 773 (1937).
15. M. Takano, T. Shinjo, and T. Takada, J. Phys. Soc. Japan, 30, 1949-53 (1971).
16. I. Soyuzi, Prog. Theor. Phys., 6, 306 (1951).
17. R. W. Cattrall, K. S. Murray, and K. I. Peverill, Inorg. Chem., 10, 1301 (1971).
18. T. Moriya in Magnetism, Vol. I, G. T. Rado and Harry Suhl, eds., Academic Press, New York, 1963, Chap. 3.
19. L. Néel, Ann. Phys. Ser., 4, 249 (1949).
20. Y. Y. Li, Phys. Rev., 101, 1450 (1956).
21. I. Dzyaloshinsky, J. Phys. Chem. Solids, 4, 241 (1958).
22. I. S. Jacobs and C. P. Bean, J. Applied Phys., 29, 537 (1958).
23. J. H. Van Vleck, Revs. Mod. Phys., 17, 34 (1945).
24. C. M. Warshaw, Am. Mineralogist, 41, 291 (1956).

APPENDIX 1
STRUCTURE OF BASIC IRON CHROMATE

The structural chemistries of sulfate and chromate groups are, in many instances, quite similar. One might predict, therefore, that two species as similar as basic iron sulfate ($\text{Fe}(\text{OH})\text{SO}_4$) and basic iron chromate ($\text{Fe}(\text{OH})\text{CrO}_4$) would crystallize in similar space groups.

Johansson¹ found the single-crystal X-ray data from $\text{Fe}(\text{OH})\text{SO}_4$ could be refined based on the orthorhombic space group $\text{P}_{nma}-\text{D}_{2h}^{16}$ ($a = 7.33 \pm 0.005$, $b = 6.41 \pm 0.005$, $c = 7.14 \pm 0.005 \text{ \AA}$, $z = 4$). He allowed that the data were also consistent with the space group $\text{Pn}2_1a$. Basic indium sulfate was found, in the same study, to be isomorphous, though weak reflections not allowed by the limiting conditions of the space group were detected.

Bounin and Lecerf,² on the other hand, reported that X-ray powder diffraction data taken from $\text{Fe}(\text{OH})\text{CrO}_4$ indicated that this phase crystallized in the monoclinic space group $\text{P}2_1/c - \text{C}_{2h}^5$ ($a = 13.32 \pm 0.04$, $b = 7.32 \pm 0.02$, $c = 13.13 \pm 0.04 \text{ \AA}$, $\beta = 121.5^\circ \pm 0.2^\circ$; $z = 12$). The authors did not, however, so index their powder diffraction data, nor did they show how calculated data compared to observed data. They chose the monoclinic space group in preference to an orthorhombic group because of some very weak reflections they felt an orthorhombic group could not account for. The above cell description by these authors was later corrected to $\text{P}2_1/a$ ($a = 13.13$, $b = 7.32$, $c = 12.93$, $\beta = 118^\circ 31'$, $z = 12$).³ In the course of the study described in the

previous chapter, basic iron chromate was characterized, again from powder diffraction data, as crystallizing in an orthorhombic system.

The description of the unit cell will have some impact on the interpretation of physical data from the phase. Consequently, the X-ray data merit the closer examination provided by this appendix.

X-ray powder diffraction data are not easily acquired from basic iron chromate. There is an intense scattering edge in the diffraction pattern which obscures all of the back-reflection region and adds greatly to the background radiation of the forward-reflection region. The phase is produced by a hydrothermal precipitation from a concentrated ferric iron-chromate solution. The product is subject to contamination by other precipitants which might produce weak X-ray reflections. The fine crystalline product grows on vessel walls during preparation which may also give rise to spurious X-ray diffraction behavior.

Table 1 reproduces the diffraction data reported by Bounin and Lecerf, as well as that collected in the course of this study and that by an independent investigator.⁴ The former authors did not describe their experimental procedure adequately to permit evaluation of their data. As reported, it is quite precise and of high resolution. During this study and the independent study, hand-selected microcrystals were exposed to iron-filtered cobalt $K\alpha$ radiation. No

Table 1

Observed "d-Spacings" and Intensities in
the X-ray Powder Diffraction Pattern of Basic Iron Chromate

Investigators					
Bounin and Lecerf ²		This Study		Independent Study ⁴	
d(Å)	Intensity	d(Å)	Intensity	d(Å)	Intensity
4.89	23	4.89	2	4.89	w, b
3.646	20	3.642	2	3.62	m
3.334	100	3.334	10	3.33	s
3.177	15	3.180	2	3.16	m
2.652	12	2.649	1	2.64	w
2.391	9	2.390	1	2.39	w
2.375					
2.340	6	2.340	1	2.33	w
2.287	9	2.280	1	2.29	w
2.132	7	2.127	1	2.12	w
2.067	7	2.070	1	2.07	w
2.041	9	2.049	1	2.04	w
1.899	<1				
1.867	11	1.868	3	1.867	w
1.859					
1.828	1				
1.789	<1				
1.756	<1				
1.727	<1				

Table 1 (Continued)

Investigators					
Bounin and Lecerf ²		This Study		Independent Study ⁴	
<u>d(Å)</u>	<u>Intensity</u>	<u>d(Å)</u>	<u>Intensity</u>	<u>d(Å)</u>	<u>Intensity</u>
1.706	2				
1.6881	<1				
1.6746	20	1.669	3	1.668	m
1.6646					
1.6435	11	1.647	1	1.642	w
1.6297	3				
1.6210	3				
1.5948	18	1.596	2	1.595	m
1.5898					
1.5197	1				
1.5025	7				
		1.4840	1	1.483	w

differences were noted in the patterns of products prepared from static solutions or stirred solutions where wall growth was not possible. Many of the very weak reflections reported previously were not located. D-spacing for the more intense lines were in some disagreement with those of Bounin and Lecerf. The background radiation or limits of the instrumentation might account for these difficulties. However, the possibility that some of the previously reported lines are due to impurities does exist.

Ultimately, the choice of the space group of $\text{Fe}(\text{OH})\text{CrO}_4$ will rest on the ability of the space group to predict the observed diffraction data. An orthorhombic unit cell will fit the observed data at least as well as the proposed monoclinic unit cells in contradiction of the claim by Bounin and Lecerf. Table 2 lists calculated d-spacings and reflection assignments for the two proposed monoclinic space groups. The assignments were made by finding the best fit calculated d-spacing subject to the limiting conditions of the space group.⁵ These fits to a monoclinic systems are not particularly good. Especially disturbing is the poor fit to the high-order reflections, which ought to be the most accurate d-spacings of the pattern.

Table 3 lists a similar calculation for an orthorhombic unit cell ($a = 7.72$, $b = 6.66$, $c = 7.30\text{\AA}$). The cell parameters for this calculation were obtained from the experimental data by the trial and error method of Lipson, and do not represent an optimal parameter set.

Table 2
 Calculated d-Spacings and Assignments Derived
 from Proposed Monoclinic Space Groups Fitting
 X-ray Powder Diffraction Data from Fe(OH)CrO₄

P2 ₁ /c				P2 ₁ /a (ref. 3)		
<u>d_{obs} (Å)</u>	<u>d_{calc} (Å)</u>	<u>h k l</u>	<u> \Delta d /d_{obs}</u>	<u>d_{calc} (Å)</u>	<u>h k l</u>	<u> \Delta d /d_{obs}</u>
4.89	4.84	111	0.0102	4.93	111	0.0082
3.646	3.657	112	0.0030	3.660	020	0.0038
3.334	3.362	310	0.0084	3.330	202	0.0012
3.177	3.185	121	0.0025	3.208	121	0.0096
2.652	2.647	410	0.0015	2.651	302, 320	0.0004
2.391	2.385	130	0.0025	2.387	130	0.0017
2.375	2.376	321	0.0004	2.361	114	0.0059
2.340	2.340	411	0.0000	2.307	500	0.0141
2.287	2.285	131	0.0009	2.291	131	0.0017
2.133	2.124	402	0.0038	2.130	231	0.0005
2.067	2.066	313	0.0005	2.062	124	0.0024
2.041	2.041	033	0.0000	2.051	033	0.0048
1.899	1.900	400	0.0005	1.898	323	0.0005
1.867	1.866	006	0.0005	1.867	224	0.0000
1.859	1.856	323	0.0016	1.860	610	0.0005
1.828	1.839	034	0.0060	1.830	040	0.0011
1.789	1.787	413	0.0011	1.790	125	0.0005
1.756	1.760	125	0.0023	1.754	431	0.0011

Table 2 (Continued)

$P2_1/c$				$P2_1/a$		
$d_{\text{obs}}(\text{\AA})$	$d_{\text{calc}}(\text{\AA})$	$h k \ell$	$ \Delta d /d_{\text{obs}}$	$d_{\text{calc}}(\text{\AA})$	$h k \ell$	$ \Delta /d_{\text{obs}}$
1.727	1.724	134	0.0017	1.714	611	0.0041
1.706	1.704	106	0.0012	1.702	620	0.0023
1.6881	1.6813	620	0.0046	1.6863	142	0.0010
1.6746	1.6782	611	0.0021	1.6765	530	0.0011
1.6646	1.6625	530	0.0013	1.6650	404	0.0002
1.6435	1.6431	043	0.0002	1.6421	333	0.0008
1.6297	1.6224	700	0.0048	1.6280	432	0.0010
1.6210	1.6167	522	0.0026	1.6220	234	0.0006
1.5948	1.5923	242	0.0016	1.6030	315	0.0051
1.5898	1.5840	710	0.0036	1.5895	341	0.0002
1.5197	1.5150	216	0.0031	1.5156	424	0.0030
1.5025	1.4956	630	0.0046	1.5028	720	0.0002

Tables 2 and 3 also list a difference parameter $|\Delta d|/d_{\text{obs}}$ where Δd is the difference between the observed (d_{obs}) and calculated (d_{calc}) d-spacings. Summation of these difference parameters for all lines yields a parameter, r , reflecting the "goodness-of-fit" of the model space group.

$$r = \sum_{\text{all lines}} \frac{|\Delta d|}{d_{\text{obs}}}$$

The r -values for the three calculations are cited in Table 4. It has been assumed that the data of Bounin and Lecerf are accurate in spite of the objections mentioned earlier. The r -values indicate that an orthorhombic cell can be used to describe these data, and may in fact be a better description.

Prediction of the observed density of basic iron chromate is an additional criterion for a proposed space group to satisfy. The observed density reported in this study was determined by picnometry over water and is in agreement with that reported previously.² Table 4 lists the observed and calculated densities. The orthorhombic space group provides a superior calculated value of the density.

Interpretation of magnetic or spectroscopic data is facilitated by a unit cell of low Z . Final selection of the proper space group for basic iron chromate will have to await single-crystal structure determination. In the meantime, approximating this structure as orthorhombic of probable space group $Pnma$ ($a = 7.72 \pm 0.01$, $b = 6.66 \pm 0.01$,

Table 3

Calculated d-Spacings and Assignments

Derived From an Orthorhombic Unit Cell

(a = 7.72, b = 6.66, c = 7.30Å) Fitting X-ray Powder

Diffraction Data for Fe(OH)CrO₄

$d_{\text{obs}}(\text{Å})$	$d_{\text{calc}}(\text{Å})$	h k l	$ \Delta /d_{\text{obs}}$
4.89	4.92	011	0.0061
3.646	3.650	002	0.0010
3.334	3.334	210	0.0000
3.177	3.200	012	0.0072
2.652	2.652	202	0.0000
2.391	2.400	310	0.0038
2.375	2.383	221	0.0033
2.340	2.344	122	0.0017
2.287	2.286	013	0.0004
2.133	2.124	031	0.0042
2.067	2.074	222	0.0034
2.041	2.048	131	0.0034
1.899	1.904	123	0.0026
1.867	1.866	401	0.0005
1.859	1.861	231	0.0010
1.828	1.825	004	0.0016
1.789	1.797	411	0.0045
1.756	1.751	223	0.0028

Table 3 (Continued)

$d_{\text{obs}}(\text{\AA})$	$d_{\text{calc}}(\text{\AA})$	h k ℓ	$ \Delta d /d_{\text{obs}}$
1.727	1.716	114	0.0063
1.706	1.706	402	0.0000
1.6881	1.6809	330	0.0043
1.6746	1.6700	420	0.0027
1.6646	1.6650	040	0.0002
1.6435	1.6400	033	0.0021
1.6297	1.6278	421	0.0011
1.6210	1.6223	041	0.0008
1.5948	1.6004	024	0.0035
1.5898	1.5885	141	0.0008
1.5197	1.5185	422	0.0008
1.5025	1.5041	510	0.0010

Table 4

Goodness-of-fit and Density from
Model Space Groups for FeOHCrO_4

	Monoclinic <u>$P2_1/c$</u>	Monoclinic <u>$P2_1/a$</u>	<u>Orthorhombic</u>
Goodness of Fit	0.0771	0.0776	0.0737
Density	3.45	3.45	3.34

(Observed density is 3.38 ± 0.02 .)

$c = 7.30 \pm 0.01 \text{ \AA}$, $z = 4$) with iron ions on 4(c) sites is not seriously at odds with the X-ray data.

References

1. G. Johansson, Acta Chem. Scand., 16, 1234 (1962).
2. A. Bounin and A. Lecerf, Compt. Rend., 262C, 1782 (1966).
3. "Crystal Data Determination Tables," 3rd ed., Vol. 2, J. D. H. Donnay and H. M. Ondik, eds., National Bureau of Standards, 1973.
4. I am indebted to E. Bingham of the Division of Geology for these data.
5. "International Tables of X-ray Crystallography," N. F. M. Henry and K. Lonsdale, eds., Vol. 1, Kynoch Press, Birmingham, England, 1952.

APPENDIX 2
 FACTOR GROUP ANALYSIS OF VIBRATIONAL MODES

Correlation diagrams and the spectral activity of the external and internal modes for some pertinent chromate and sulfate structures are shown in the tables below. The factor group analysis was done by the correlation method.¹ The spectral activity is denoted by R for Raman activity, IR for infrared activity, and O for modes inactive in either Raman or infrared spectra.

(A) $\text{Fe}(\text{OH})\text{XO}_4$ (X = S in basic iron sulfate; X = Cr in basic iron chromate)

Basic iron sulfate has been shown to crystallize in the space group $\text{Pnma} - \text{D}_{2h}^{16}$ No. 62 with 4 formula units per unit cell.² Basic iron chromate can be treated in the same symmetry.³ The allowed site symmetries in this unit cell are 2C_i (4), C_s (4), C_i (8). The locations of the ions are:

<u>Ion</u>	<u>Site Symmetry</u>
4 Fe	C_s
4 OH	C_s
4 XO_4	C_s

The cell must be treated as a primitive cell with only one Bravais lattice point. The correlation diagram is presented in Table 1. The spectral activity of the vibrational modes is tabulated below.

Table 1

Correlation Diagram and Spectral Activity of External and Internal Modes

of $\text{Fe}(\text{OH})\text{XO}_4$. Acoustic Modes are B_{1u} , B_{2u} , and B_{3u}

Ions	Modes	Point Group	Site Group	Factor Group
External	Internal	Symmetry	Symmetry	Symmetry D_{2h}
		T_d	C_s	
	ν_1	$A(\text{R})$	$A'(\text{IR}, \text{R})$	$A_g(\text{R}) + B_{1g}(\text{IR}) + B_{2u}(\text{IR}) + B_{3u}(\text{IR})$
	ν_2	$E(\text{R})$	$A'(\text{IR}, \text{R})$ + $A''(\text{IR}, \text{R})$	$A_g(\text{R}) + B_{1g}(\text{R}) + B_{2u}(\text{IR}) + B_{3u}(\text{IR})$ + $B_{2g}(\text{R}) + B_{3g}(4) + A_u(\text{O}) + B_{1u}(\text{IR})$
	ν_3, ν_4	$T_2(\text{IR}, \text{R})$	$2A'(\text{IR}, \text{R})$ + $A''(\text{IR}, \text{R})$	$2A_g(\text{R}) + 2B_{1g}(\text{R}) + 2B_{2u}(\text{IR}) + 2B_{3u}(\text{IR})$ + $B_{2g}(\text{R}) + B_{3g}(\text{R}) + A_u(\text{O}) + B_{1u}(\text{IR})$
	trans	$T_2(\text{IR}, \text{R})$	$2A''(\text{IR}, \text{R})$ + $A''(\text{IR}, \text{R})$	$2A_g(\text{R}) + 2B_{1g}(\text{R}) + 2B_{2u}(\text{IR}) + 2B_{3u}(\text{IR})$ + $B_{2g}(\text{R}) + B_{3g}(\text{R}) + A_u(\text{O}) + B_{1u}(\text{IR})$
	libration	$T_1(\text{O})$	$A'(\text{IR}, \text{R})$ + $2A''(\text{IR}, \text{R})$	$2B_{2g}(\text{R}) + 2B_{3g}(\text{R}) + 2A_u(\text{O}) + 2B_{1u}(\text{IR})$ + $A_g(\text{R}) + B_{1g}(\text{R}) + B_{2u}(\text{IR}) + B_{3u}(\text{IR})$

 $4\text{XO}_4 =$

Table 1 (Continued)

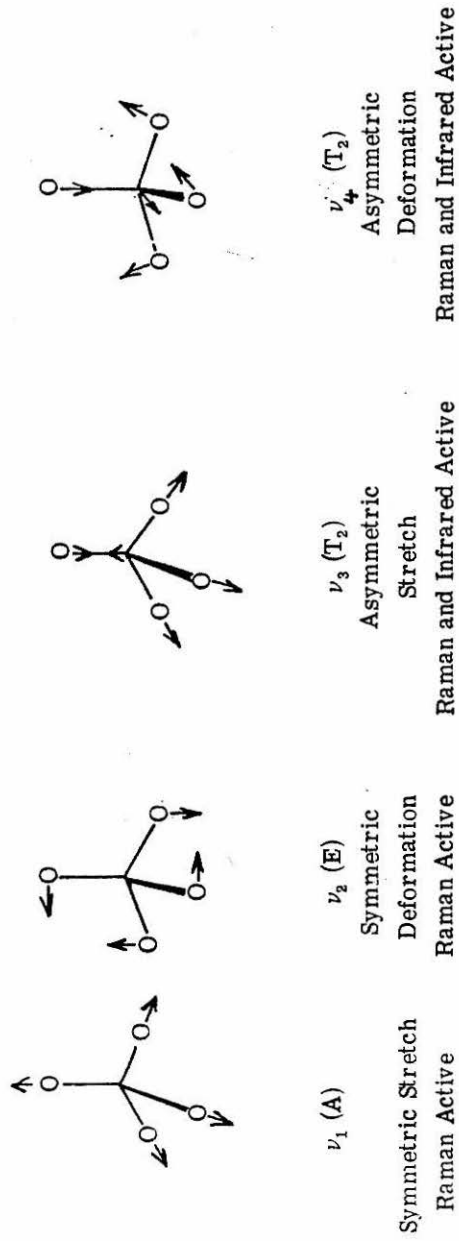
Ions	Modes		Point Group Symmetry	Site Group Symmetry	Factor Group Symmetry
	External	Internal			
4Fe(III)				C_s	
				$A'(\text{IR})$ — $A_g(\text{R}) + B_{1g}(\text{R}) + B_{2u}(\text{IR}) + B_{3u}(\text{IR})$ $A''(\text{IR})$ — $B_{2g}(\text{R}) + B_{3g}(\text{R}) + A_u(\text{O}) + B_{1u}(\text{IR})$	
4OH ⁻				$C_{\infty, v}$	
	stretch		$\Sigma^+(\text{IR}, \text{R})$	$A'(\text{IR}, \text{R})$	$A_g(\text{R}) + B_{1g}(\text{R}) + B_{2u}(\text{IR}) + B_{3u}(\text{IR})$ ⁴⁶
	trans			$A'(\text{IR}, \text{R})$	$A_g(\text{R}) + B_{1g}(\text{R}) + B_{2u}(\text{IR}) + B_{3u}(\text{IR})$
	lib, trans			$A''(\text{IR}, \text{R})$	$B_{2g}(\text{R}) + B_{3g}(\text{R}) + A_u(\text{O}) + B_{1u}(\text{IR})$

Factor Group Species (D_{2h})	Lattice Vibrations	Acoustic Vibrations	Librations	XO_4 Internal Modes	OH Internal Modes
A_g (R)	6		1	6	1
B_{1g} (R)	4		3	6	
B_{2g} (R)	5		2	3	1
B_{3g} (R)	3		4	3	
A_u (O)	3		4	3	
B_{1u} (IR)	4	1	2	3	1
B_{2u} (IR)	3	1	3	6	
B_{3u} (IR)	<u>5</u>	<u>1</u>	<u>1</u>	<u>6</u>	<u>1</u>
Total	33	3	20	36	4

$$3N = 3(4 \times 8) = 96 = 33 + 3 + 20 + 36 + 4$$

There are 35 infrared allowed vibrations and 46 Raman allowed modes exclusive of the acoustic modes. As would be expected from the centrosymmetric factor group there are no coincident bands active in both the Raman and infrared spectra. These modes will give rise to 35 absorptions in the infrared spectrum and 46 absorptions in the Raman spectrum.

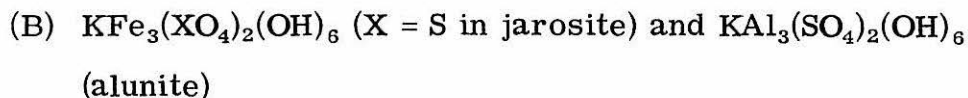
The modes arising from the XO_4 and OH internal vibrations are of principal interest. Under point group symmetry, T_d , the XO_4 group has only two infrared allowed modes and four Raman allowed modes (see Figure 1). Reduction of the point symmetry and factor group coupling yield many more infrared and Raman active modes. The ν_1

Figure 1. Vibrational modes of XO_4^- group under T_d symmetry

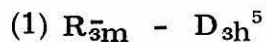
The degeneracy of these modes can be lifted by site symmetry.

Coupling due to the factor group can multiply the number of modes in which these primary modes contribute

symmetric stretch yields two infrared active modes and two Raman active modes. The symmetric deformation yields three infrared modes and four Raman active modes. The asymmetric modes each produce five infrared modes and six Raman modes. Factor group coupling splits the OH stretch into two infrared and two Raman modes.



Single crystal X-ray structure determination has been carried out only on alunite,^{4,5} Jarosite⁴ and its chromate³ analog have been shown to have the same structure. The structure of alunite has been refined in the space groups R_{3m} (4) and R_{3m}^- (5). Choice between these space groups was made empirically in both cases. Fundamental differences in the vibrational modes allowed under these two symmetries can provide the basis for a more informed choice of space group. The centrosymmetric group R_{3m} ought to yield no coincident modes that are both infrared and Raman allowed whereas such coincident modes would occur in the acentric space group R_{3m}^- . The factor group analysis is carried out below in both space groups.



There is one formula unit per unit cell. Consequently, the cell must be treated as primitive with one Bravais lattice point. Possible site symmetries in R_{3m}^- are: $2D_3$ (1), C_{3v} (2), $2C_{2n}$ (3), $2C_2$ (6), C_s (6), C_i (6). The ion locations are:

<u>Ion</u>	<u>Site Symmetry</u>
K	D _{3d}
3Fe ^{III}	C _{2h}
2XO ₄ ⁼	C _{3v}
6OH ⁻	C _s (6)

The correlation diagram is presented in Table 2. The spectral activity of the vibrational modes is catalogued below:

<u>Factor Group Species (D_{3d})</u>	<u>Lattice Vibrations</u>	<u>Acoustic Modes</u>	<u>Librations</u>	<u>XO₄ Internal Modes</u>	<u>OH Internal Modes</u>
A _{1g} (O)	3			3	1
A _{2g} (R)	1		3		
E _g (R)	4		3	3	1
A _{1u} (O)	2		3		
A _{2u} (IR)	5	1		3	1
E _u (IR)	<u>7</u>	<u>1</u>	<u>3</u>	<u>3</u>	<u>1</u>
Total	33	3	18	18	6

$$3N = 3(26) = 78 = 33 + 3 + 18 + 18 + 6$$

There are 26 allowed Raman modes and 37 infrared modes with no coincident modes allowed by both the infrared and Raman selection rules. These vibrational modes will give rise to 15 absorptions in the Raman spectrum and 23 absorptions in the infrared spectrum. The symmetric stretch and symmetric deformations of the XO₄ group each give rise to one infrared-allowed mode under the action of the site and

Table 2

Correlation Diagram and Spectral Activity of External and Internal Modes of

$\text{KFe}_3(\text{XO}_4)_2(\text{OH})_6$ or Alunite Assuming $R\bar{3}m$ Space Group. Acoustic Modes are A_{2u} and E_u

Ions	Modes		Point Group	Site Group	Factor Group Symmetry
	External	Internal	Symmetry	Symmetry	C_{3v}
2XO_4^-	ν_1		T_d	C_{3v}	
			$A(\text{R})$	$A_1(\text{IR}, \text{R})$	$A_{1g}(\text{R}) + A_{1u}(\text{IR})$
	ν_2		$E(\text{R})$	$E(\text{IR}, \text{R})$	$E_g(\text{R}) + E_u(\text{IR})$
	ν_3, ν_4		$T_2(\text{IR}, \text{R})$	$A_1(\text{IR}, \text{R}) + E(\text{IR}, \text{R})$	$2A_{1g}(\text{O}) + 2A_{2u}(\text{IR}) + 2E_g(\text{R}) + 2E_u(\text{IR})$
	trans		$T_2(\text{IR}, \text{R})$	$A_1(\text{IR}, \text{R}) + E(\text{IR}, \text{R})$	$A_{1g}(\text{R}) + A_{2u}(\text{IR}) + E_g(\text{R}) + E_u(\text{IR})$
	lib		$T_1(\text{O})$	$A_2(\text{O}) + E(\text{IR}, \text{R})$	$A_{2g}(\text{R}) + A_{1u}(\text{O}) + E_g(\text{R}) + E_u(\text{IR})$
K^+			D_{3d}		
	trans			$A_{2u}(\text{IR})$	$A_{2u}(\text{IR})$
				$E_u(\text{IR})$	$E_u(\text{IR})$

2XO_4^-

K^+

51

Table 2 (Continued)

Ions	Mode		Point Group Symmetry	Site Group Symmetry	Factor Group Symmetry
	External	Internal			
3Fe(III) or 3Al ³⁺	trans	A _{2u} (IR)	C _{∞v}	A _{2u} (IR)	A _{1u} (O) + E _u (IR)
		B _u (IR)		B _u (IR)	2A _{2u} (IR) + 2E _u (IR)
6OH ⁻	stretch	Σ ⁺ (IR, R)	C _s	A'(IR, R)	2A _{1g} + 2E _g (R) + 5Σ
		Σ ⁺ (IR, R)		A'(IR, R)	2A _{2u} (IR) + 2E _u (IR)
		Σ ⁺ (IR, R)		A'(IR, R)	A _{1g} (R) + E _g (R) + A _{2u} (IR) + E _u (IR)
lib, trans	lib, trans	Π(IR, R)	C _s	A''(IR, R)	A _{2g} (R) + E _g (R) + A _{1u} (O) + E _u (IR)
		Π(IR, R)		A''(IR, R)	A _{1u} (O) + E _u (IR)

factor groups. The ν_3 and ν_4 modes are each split into two infrared-active modes. The OH stretch is split under the action of the factor group into four infrared active modes.

$$(2) R_{3m} - C_{3v}^5$$

Again the unit cell is primitive and there is just one Bravais lattice point. The allowed site symmetries are $C_{3v}(1)$, $C_s(3)$, $C_1(6)$. The ion locations are:

<u>Ion</u>	<u>Site Symmetry</u>
K^+	C_{3v}
$3 Fe^{III}$ or $3 Al^{3+}$	C_s
$2 XO_4^-$	C_{3v}
$6 OH$	C_{3v}

The correlation diagram is presented in Table 3. The spectral activity of the modes is catalogued below.

Factor Group Species C_{3v}	Lattice Vibrations	Acoustic Modes	Librations	XO_4 Internal Modes	OH Internal Mode
A_1 (IR, R)	10	1		6	6
A_2 (O)	1		2		
E (IR, R)	<u>11</u>	<u>1</u>	<u>8</u>	<u>6</u>	<u>—</u>
Total	33	3	18	18	6

$$3N = 3(26) = 78 = 33 + 3 + 18 + 18 + 6$$

There are 72 allowed modes exclusive of the acoustic modes. They will give rise to 47 absorptions. All of the modes are coincident and

Table 3

Correlation Diagram and Spectral Activity of External and Internal Modes of

 $\text{KFe}_3(\text{XO}_4)_2(\text{OH})_6$ and Alunite Assuming R_{3m} Space Group. Acoustic Modes are A_1 and E.

Ions	Modes		Point Group Symmetry	Site Group Symmetry	Factor Group Symmetry
	External	Internal			
2XO_4	ν_1		T_d A(R)	C_{3v} A ₁ (IR, R)	2A ₁ (IR, R)
	ν_2		E(R)	E(IR, R)	2E(IR, R)
	ν_3, ν_4		T ₂ (IR, R)	2A ₁ (IR, R) + 2E(IR, R)	4A ₁ (IR, R) + 4E(IR, R)
	trans		T ₂ (IR, R)	A ₁ (IR, R) + E(IR, R)	2A ₁ (IR, R) + 2E(IR, R)
	libration		T ₂ (O)	A ₂ (O) + E(IR, R)	2A ₂ (O) + 2E(IR, R)
K^+				C_{3v}	
	trans		A ₁ (IR, R)	A ₁ (IR, R)	A ₁ (IR, R)
3Fe(III) OR 3Al^{3+}				C_s	
			A'(IR, R)	A'(IR, R)	2A ₁ (IR, R) + 2E(IR, R)
			A''(IR, R)	A''(IR, R)	A ₂ (O) + E(IR, R)

Table 3 (Continued)

Ions	Modes		Point Group Symmetry	Site Group Symmetry	Factor Group Symmetry
	External	Internal			
6OH ⁻			$C_{\infty v}$	C_{3v}	
	stretch		$\Sigma^+(\text{IR}, \text{R})$	$A_1(\text{IR}, \text{R})$	$6A_1(\text{IR}, \text{R})$
	trans		$\Sigma^+(\text{IR}, \text{R})$	$A_1(\text{IR}, \text{R})$	$6A_1(\text{IR}, \text{R})$
	trans, lib		$\Pi(\text{IR}, \text{R})$	$E(\text{IR}, \text{R})$	$6E(\text{IR}, \text{R})$

Table 4
 Effects of Factor Group Coupling on the Internal Modes of
 XO_4 in $\text{KFe}_3(\text{XO}_4)_2(\text{OH})_6$ Under Space Groups R_{3m}^- and R_{3m}

Point Symmetry Modes	Allowed Modes in R_{3m}^-	Allowed Modes in R_{3m}
ν_1	$\text{A}_{1g}(\text{R}) + \text{A}_{2u}(\text{IR})$	$2\text{A}_1(\text{IR}, \text{R})$
ν_2	$\text{E}_g(\text{R}) + \text{E}_u(\text{IR})$	$2\text{A}_1(\text{IR}, \text{R})$
ν_3	$\text{A}_{1g}(\text{R}) + \text{A}_{2u}(\text{IR})$ + $\text{E}_g(\text{R}) + \text{E}_u(\text{IR})$	$2\text{A}_1(\text{IR}, \text{R}) + 2\text{E}(\text{IR}, \text{R})$
ν_4	$\text{A}_{1g}(\text{R}) + \text{A}_{2u}(\text{IR})$ + $\text{E}_g(\text{R}) + \text{E}_u(\text{IR})$	$2\text{A}_1(\text{IR}, \text{R}) + 2\text{E}(\text{IR}, \text{R})$

should be observable in both the infrared and Raman spectra of species of this structure. Comparing this result with that found for the space group R_{3m}^- one sees that a clear choice between the two space groups is possible. Table 4 displays the expected vibrational activity of the internal modes of the XO_4 group for the R_{3m} and R_{3m}^- structures. The differences in these vibrations could also be used to choose between the space groups. However, for practical reasons, this differentiation would best be used to confirm a choice based on the coincidence of absorption bands in Raman and infrared spectra.

(3) For completeness sake it should be noted that factor group analysis of the species $M^I Fe(CrO_4)_2 \cdot 2H_2O$ ($M^I = Na^+, K^+, Tl^+, NH_4^+$) has recently been published.⁶

References

1. W. G. Fateley, N. T. McDevitt, and F. F. Bentley, Applied Spectroscopy, 25, 155 (1971).
2. G. Johanssen, Acta Chem. Scand., 16, 1235 (1962).
3. A. Bounin and A. Lecerf, Compt. Rend. Ser. C., 262, 1782 (1966).
4. S. B. Hendricks, Amer. Min., 22, 773 (1937).
5. R. Wang, W. F. Bradley, and H. Steinfink, Acta Cryst., 18, 249 (1965).
6. A. Millier and P. Graveriau, Spectrochim. Acta, 29, 2043 (1973).

CHAPTER 2

WEAK FERROMAGNETISM IN THE BASIC IRON CHROMATES

Abstract: $\text{NH}_4\text{Fe}_3(\text{CrO}_4)_2(\text{OH})_6$ is shown to be isomorphous with $\text{KFe}_3(\text{CrO}_4)_2(\text{OH})_6$. Its magnetic susceptibility deviates from the Curie-Weiss law below 67°K in a manner analogous to that of the potassium analog. Mossbauer, esr, and magnetization data are presented for the basic iron chromates. These data indicate that the positive deviations of the magnetic susceptibility from Curie-Weiss law are due to ferromagnetic spin ordering. Weak ferromagnetism is discussed in terms of ionic spin configurations.

The magnetic behavior of the basic iron chromates is indeed striking. This is especially so in light of the unobtrusive behavior of the basic iron sulfates. Complete clarification of the origin of this unusual behavior will, of course, have to await detailed X-ray and neutron diffraction studies. While these results are unavailable, the next-best procedure is the acquisition of extensive data on the species in the hope that a consistent rationalization can be developed. To this end, the esr, Mossbauer, and magnetization data for $\text{Fe}(\text{OH})\text{CrO}_4$ and $\text{KFe}_3(\text{CrO}_4)_2(\text{OH})_6$ are reported in this chapter.

An especially useful technique for rationalization of spectroscopic data is the comparison of data for species of varying stoichiometry but of similar structure. Preparation of such altered basic iron chromates proved extraordinarily difficult despite the diversity of known isostructural basic iron sulfates. One such altered species, $\text{NH}_4\text{Fe}_3(\text{CrO}_4)_2(\text{OH})_6$, was prepared. Characterization of this phase is also reported in this chapter.

Rationalization of the magnetic behavior of basic iron chromate seems to directly confront the rather difficult problem of exchange interactions between a metal ion having d electrons and one whose d-orbitals are vacant. The results of the investigation reported in the appendix, however, indicate that the electronic structure of bridging chromate groups can be discounted as a major contributor to the magnetic behavior of the phases. Instead, in this chapter, the behavior is discussed in terms of the localized ionic spin configurations.

Experimental

(A) Preparation of Compounds. The samples of $\text{Fe}(\text{OH})(\text{CrO}_4)$ and $\text{KFe}_3(\text{CrO}_4)_2(\text{OH})_6$ used in this study were the same as those described in Chapter 1. It was found that $\text{KFe}_3(\text{CrO}_4)_2(\text{OH})_6$ could be formed only in a very narrow range of experimental conditions. Attempts to prepare the Li^+ , Na^+ , and Cs^+ salts failed. The ammonium salt was prepared by the following procedure. A solution of 0.5F $\text{Fe}(\text{NO}_3)_3 \cdot 9\text{H}_2\text{O}$, 0.5F $(\text{NH}_4)_2\text{Cr}_2\text{O}_7$, and 1.0F NH_4NO_3 was sealed in a Pyrex tube and heated for 2 hours at 110°C . A fine particulate product began to precipitate after 15 minutes of heating. Infrared spectra and X-ray diffraction data showed this species to be the desired ammonium salt (see Tables 1 and 2). Analysis: Calcd (%): for $\text{NH}_4\text{Fe}_3(\text{CrO}_4)_2(\text{OH})_6$: Fe, 32.23; Cr, 20.01; N, 2.69. Found (%): Fe, 32.25; Cr, 19.89; N, 2.11; K < 0.05%; Na < 0.005%. Prolonged heating of the reaction mixture (~ 24 hours) or heating for shorter times at 140°C yielded a red, crystalline and as yet unidentified product. Analysis: Found(%): Fe, 18.87; Cr, 25.11. X-ray powder diffraction data for this phase are reported in Table 2.

(B) Instrumental Analysis.

Infrared, X-ray, and magnetic data were collected as described in Chapter 1. ESR data were obtained with a Varian X-band esr spectrometer Model V4500-10A. The spectrometer was equipped with a dewar capable of maintaining the temperature of the sample constant ($\pm 1^\circ$) over the range 9-300 °K. Calibration of the spectrometer was checked

Table 1

Infrared Absorption Band Positions of $\text{NH}_4\text{Fe}_3(\text{CrO}_4)_2(\text{OH})_6$

<u>Position (cm^{-1})</u>	<u>Remarks</u>	<u>Assignment</u>
3460	w, shld	ν_{OH}
3390	s	ν_{OH}
3150	m, broad	ν_{NH}
2940	w, broad	ν_{NH}
1400	s	δ_{NH}
995	s	δ_{OH}
915	shld	ν_3 mode of CrO_4^{2-}
845	s	
585	shld	vibrations of FeO_6 octahedron
495	s	
430	s	ν_4 mode of CrO_4^{2-}
388	m	
350	w, sh	
325	w, sh	vibrations of FeO_6 and remainder of the lattice
275	w	
240	w	
225	vw	
194	s	
148	m	

Table 2
X-ray Powder Diffraction Patterns

$\text{NH}_4\text{Fe}_3(\text{CrO}_4)_2(\text{OH})_6$				Unknown	
d (Å)	I	Index	d_{calc}	d	I
5.95	3	003	5.93	7.39	8
5.19	7	012	5.21	5.16	2
3.70	4	110	3.72	4.38	7
3.15	10	113	3.15	4.20	4
3.07	1	202	3.03	3.88	8
2.961	4	006	2.965	3.70	1
2.603	3	024	2.607	3.61	4
2.359	5	107	2.364	3.33	8
2.105	1	018	2.102	3.22	1
2.017	5	033	2.017	3.15	1
1.989	1	027	1.995	3.07	10
1.977	2	009	1.977	3.02	1
1.858	5	220	1.858	2.837	3
1.750	3	312	1.750	2.729	6
1.653	1	134	1.657	2.551	1
1.641	3	128	1.641	2.513	2
1.604	2	401	1.603	2.411	1
1.576	3	042	1.583	2.342	2
1.558	4	0 2 10	1.557	2.205	1
1.515	2	404	1.513	2.145	5
1.459	3	137	1.460	2.114	1

Table 2 (Continued)

$\text{NH}_4\text{Fe}_3(\text{CrO}_4)_2(\text{OH})_6$				Unknown	
$d(\text{\AA})$	I	Index	d_{calc}	d	I
1.446	1	039	1.454	1.975	5
1.406	1	410	1.405	1.890	1
1.392	1	318	1.392	1.858	2
1.368	4	143	1.367	1.836	3
				1.809	1
				1.771	3
				1.757	1
				1.697	2
				1.688	1
				1.653	2
				1.638	3
				1.600	4
				1.538	3
				1.436	4
				1.391	1
				1.374	1

with the spectrum of DPPH. I gratefully acknowledge Paula Clendening for her assistance in the acquisition of some of these data. Mossbauer data were kindly supplied by Professor Rolf Herber of Rutgers University. The source for the spectra was cobalt in palladium.

Results

(A) Structure and Magnetic Behavior of $\text{NH}_4\text{Fe}_3(\text{CrO}_4)_2(\text{OH})_6$.

X-ray powder diffraction data from $\text{NH}_4\text{Fe}(\text{CrO}_4)_2(\text{OH})_6$ could be indexed in terms of a hexagonal unit cell of dimensions $a = 7.432 \pm 0.015$, $c = 17.793 \pm 0.005 \text{ \AA}$. Intensities and absences in the powder diffraction pattern show it isomorphous with $\text{KFe}_3(\text{CrO}_4)_2(\text{OH})_6$. Replacement of the potassium ion with ammonium ion results only in increased separation of the sheets of iron ions. The intraplanar geometry is little affected, and the intraplanar separation of Fe(III) ions for both species is 3.72 \AA .

The temperature dependence of the molar magnetic susceptibility of $\text{NH}_4\text{Fe}_3(\text{CrO}_4)_2(\text{OH})_6$ is shown in Figure 1. Representative magnetic data are tabulated in Table 3. The susceptibility obeys the Curie-Weiss law over the temperature region 80-300°K with a Curie constant of $11.86 \text{ cgs-deg-mol}^{-1}$ and a Weiss temperature of -562°K . At 67°K the molar susceptibility abruptly deviates from the Curie-Weiss law in a manner analogous to that of the potassium salt. A detail of the transition region is shown in Figure 2. In all respects the magnetic behavior of $\text{NH}_4\text{Fe}_3(\text{CrO}_4)_2(\text{OH})_6$ is analogous to $\text{KFe}_3(\text{CrO}_4)_2(\text{OH})_6$ though the Curie and Weiss temperatures are lower.

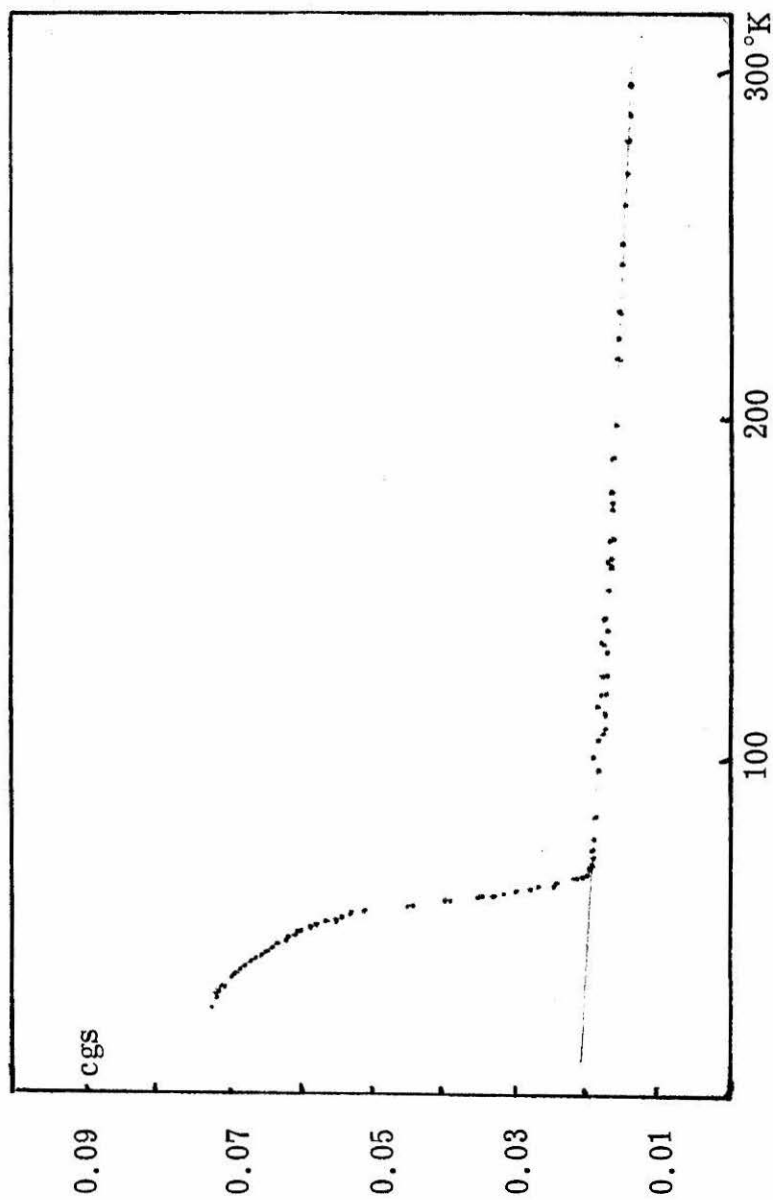


Figure 1. Molar susceptibility of $\text{NH}_4\text{Fe}_3(\text{CrO}_4)_2(\text{OH})_6$ versus temperature. Solid line is calculated from Curie Weiss law with $C = 11.85$, $\theta = -562^\circ\text{K}$.

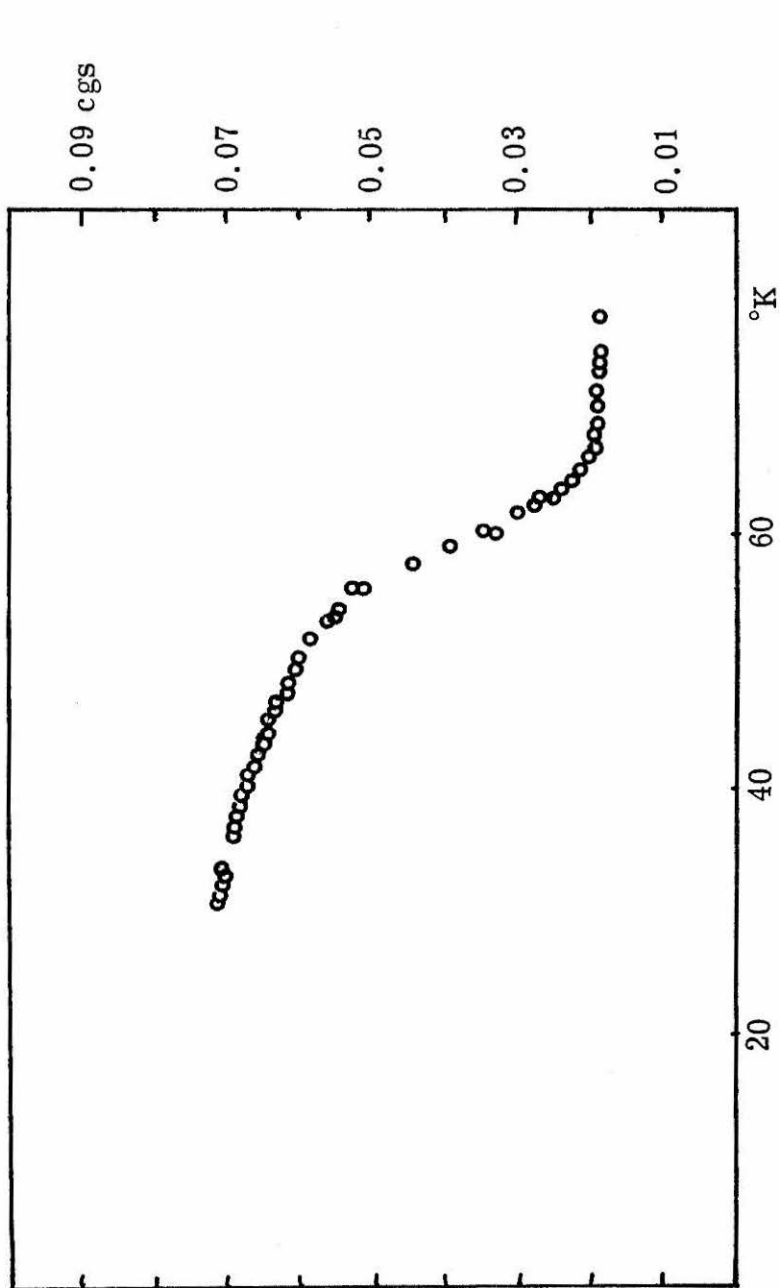


Figure 2. Detail of transition region of molar susceptibility of $\text{NH}_4\text{Fe}_3(\text{CrO}_4)_2(\text{OH})_6$ versus temperature.

Table 3

Representative Magnetic Data for $\text{NH}_4\text{Fe}_3(\text{CrO}_4)_2(\text{OH})_6$

Diamagnetic Correction = -200×10^{-6} cgs

<u>T</u>	<u>$\chi_{M'} \times 10^3$</u>	<u>$\mu_{\text{eff}}/\text{Fe}$</u>
299	13.74	3.31
273	14.21	3.22
252	14.66	3.14
232	15.01	3.05
199	15.51	2.87
165	16.32	2.68
150	16.79	2.59
125	17.68	2.43
101	18.65	2.24
770	18.74	1.96
74.2	18.74	1.92
71.2	18.88	1.89
67.5	19.06	1.85
65.8	19.93	1.87
65.5	20.04	1.87
63.0	24.15	2.01
62.8	26.46	2.10
60.0	34.53	2.35
57.50	44.21	2.60
50.0	60.02	2.83
45.2	64.14	2.78

Table 3 (Continued)

<u>T</u>	<u>$\chi_{M'} \times 10^3$</u>	<u>$\mu_{\text{eff}}/\text{Fe}$</u>
40.8	66.92	2.70
36.5	69.30	2.60
31.0	71.60	2.43

(B) Mossbauer and ESR Data.

Mossbauer data for Fe(OH)CrO_4 and $\text{KFe}_3(\text{CrO}_4)_2(\text{OH})_6$ are listed in Table 4. The room temperature spectrum of both species is a doublet absorption as would be expected for iron in an environment distorted from perfect octahedral symmetry. The temperature dependence of the quadrupole splitting ($\sim +0.007$ mm/sec/100°K) further indicates that the electric field gradient at the iron nucleus is principally due to the ligand field. Both spectra are consistent with that expected for high-spin iron(III).

Down to temperatures near the transition temperature (~ 71 °K), the spectrum of $\text{KFe}_3(\text{CrO}_4)_2(\text{OH})_6$ remains a simple doublet absorption. Below the transition temperature the spectrum splits into the six line spectrum indicative of an internal field. At 5°K, this internal field is 465 Koe. The empirical relation, $H_1 = 220 \langle S \rangle$ Koe, would predict a field of 550 Koe.¹

The spectrum of Fe(OH)CrO_4 develops a six-line character at 83.5°K, some 10°K above its transition temperature. The internal field at 83.5°K is 320 Koe. At 5°K, the field increases to 440 Koe. The internal field detected above the ferromagnetic transition temperature is consistent with the antiferromagnetic behavior of Fe(OH)CrO_4 indicated by its magnetic susceptibility. No such internal field is detected in $\text{KFe}_3(\text{CrO}_4)_2(\text{OH})_6$ above its transition temperature since this species is a paramagnet in this temperature region.

Table 4

Mossbauer Data for the Basic Iron Chromates

	<u>T</u> <u>(°K)</u>	δ^a <u>(mm/sec)</u>	Δ^b <u>(mm/sec)</u>	<u>I^c</u>
Fe(OH)CrO ₄	297	0.377	0.932	1.073
	83.5	H _i = 320 KOe		--
	~ 5	H _i = 440 KOe		--
KFe ₃ (CrO ₄) ₂ (OH) ₆	297	0.383	0.868	0.930
	83.5	0.482	0.884	0.958
	78	0.488	0.884	0.962
	5	H _i = 465 KOe		

^a Isomer shift versus Pd(Co⁵⁷).

^b Quadrupole splitting.

^c Intensity ratio of doublet peaks.

Data from Table 4 can be compared to that reported for $\text{KFe}_3(\text{SO}_4)_2(\text{OH})_6$.^{2, 3} Room temperature isomer shift for this species is 0.22 mm/sec with a quadrupole splitting of 1.15 mm/sec. At 42°K the internal field is 490 Koe.

Esr spectra of $\text{Fe}(\text{OH})\text{CrO}_4$ and $\text{KFe}_3(\text{CrO}_4)_2(\text{OH})_6$ are shown in Figures 3 and 4, respectively. Parametric values are tabulated below.

Table 5

Esr Data for Basic Iron Chromates

$\text{KFe}_3(\text{CrO}_4)_2(\text{OH})_6$	$g_1 = 2.0019$	$A^a = 525 \text{ oe}$
	$g_2 = 4.313$	$A = 75 \text{ oe}$
$\text{Fe}(\text{OH})\text{CrO}_4$	$g = 2.0043$	$A = 512 \text{ oe}$
$\text{Fe}(\text{OH})\text{SO}_4$	$g = 2.0034$	$A = 451 \text{ oe}$

^a Width of absorption band at half height.

The spectrum of $\text{Fe}(\text{OH})\text{CrO}_4$ consists of a single very intense absorption very similar to the spectrum of $\text{Fe}(\text{OH})\text{SO}_4$ also shown in Figure 3. The g-value is quite close to the free-electron value expected for high-spin Fe(III). The bandwidth exhibits a shallow temperature dependence down to 85°K as shown in Figure 5. Below 85°K the bandwidth increases rapidly. Below 79°K no intelligible spectrum could be resolved. Such behavior is characteristic of a species whose spins order at low temperature.

The spectrum of $\text{KFe}_3(\text{CrO}_4)_2(\text{OH})_6$ is less intense and far more difficult to obtain. It apparently consists of two clear absorptions at

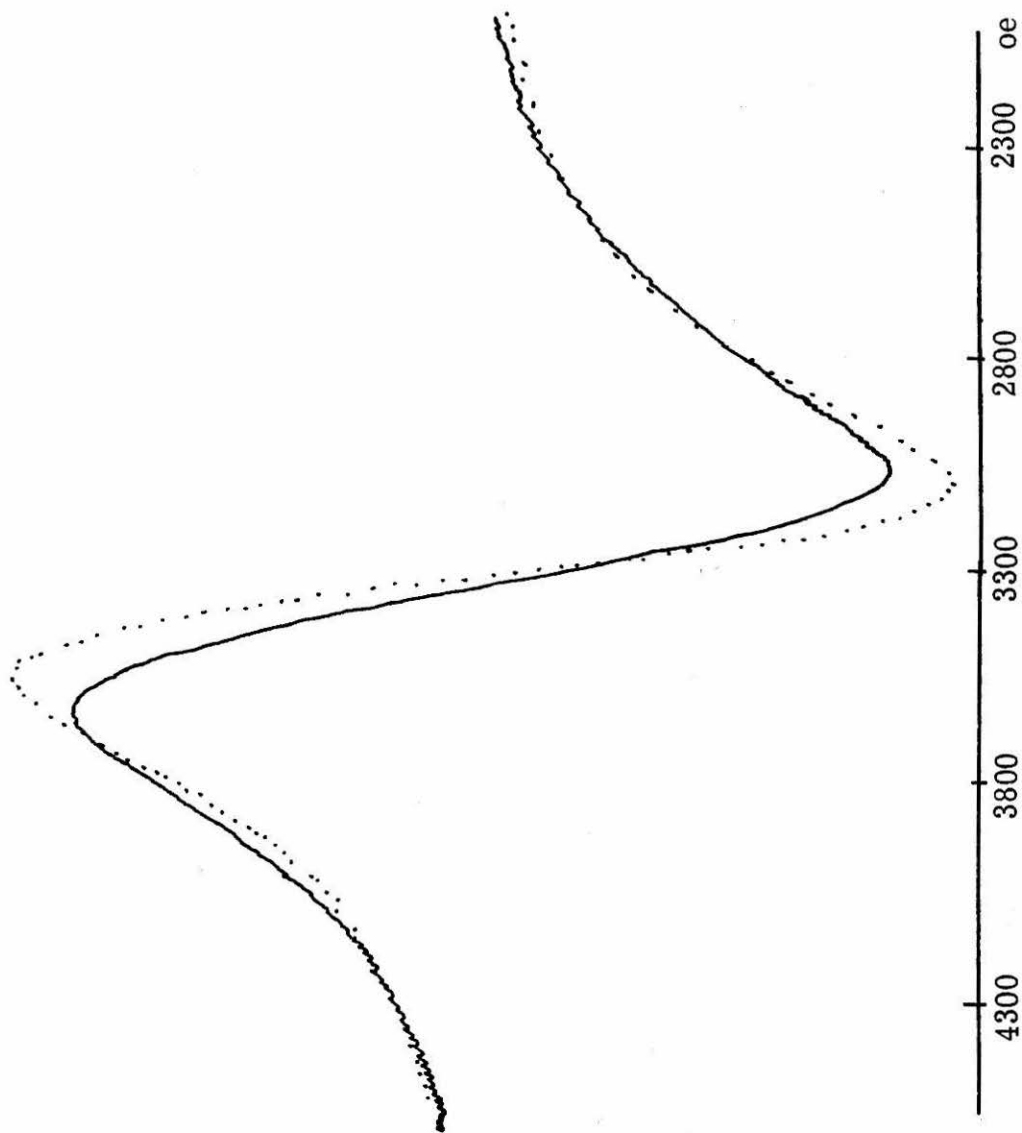


Figure 3. Esr spectrum of Fe(OH)CrO_4 (solid line) and Fe(OH)SO_4 (dotted line) at ambient temperature.

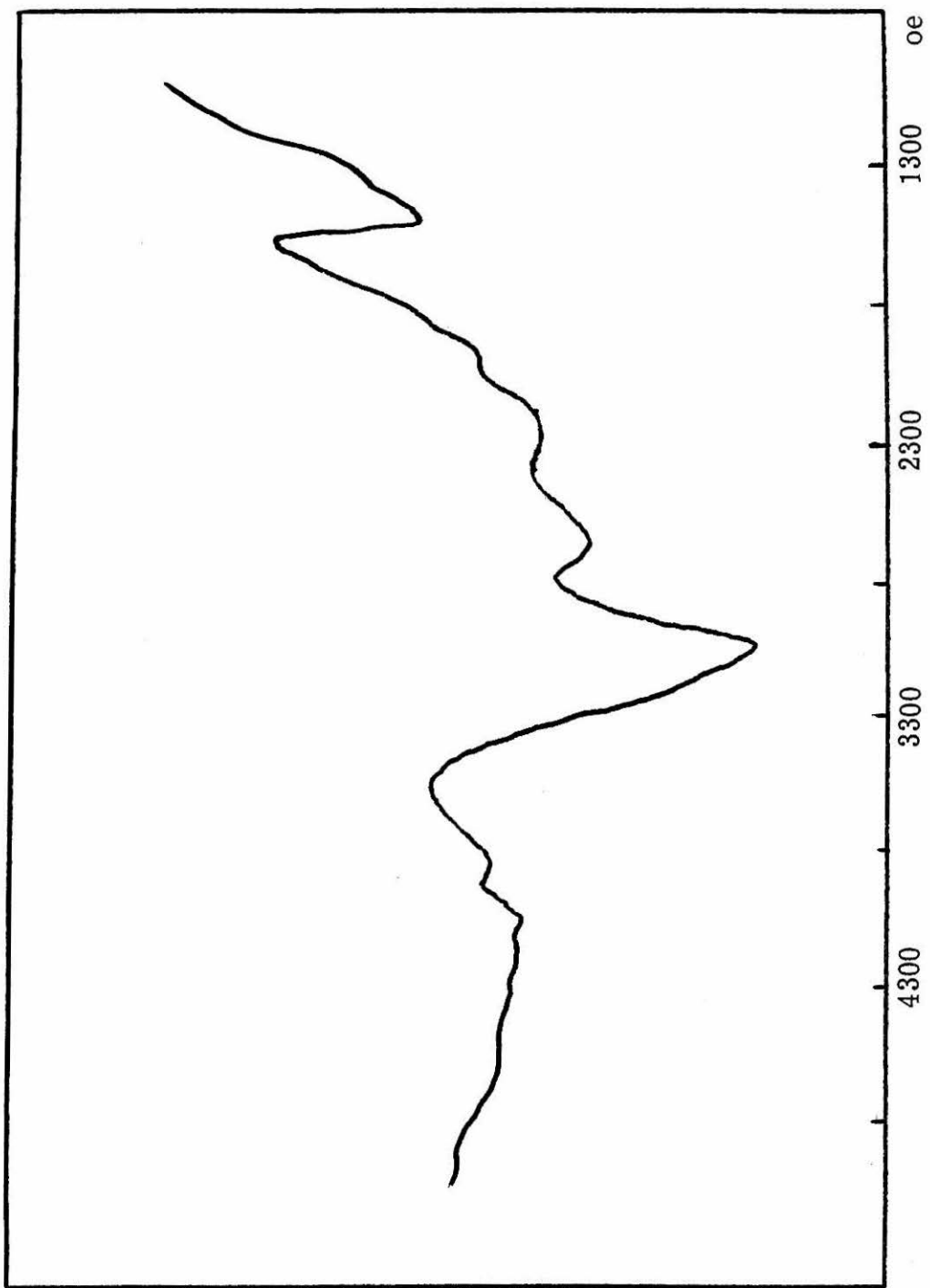


Figure 4. Esr spectrum of $\text{KFe}_3(\text{CrO}_4)_2(\text{OH})$ at ambient temperature.

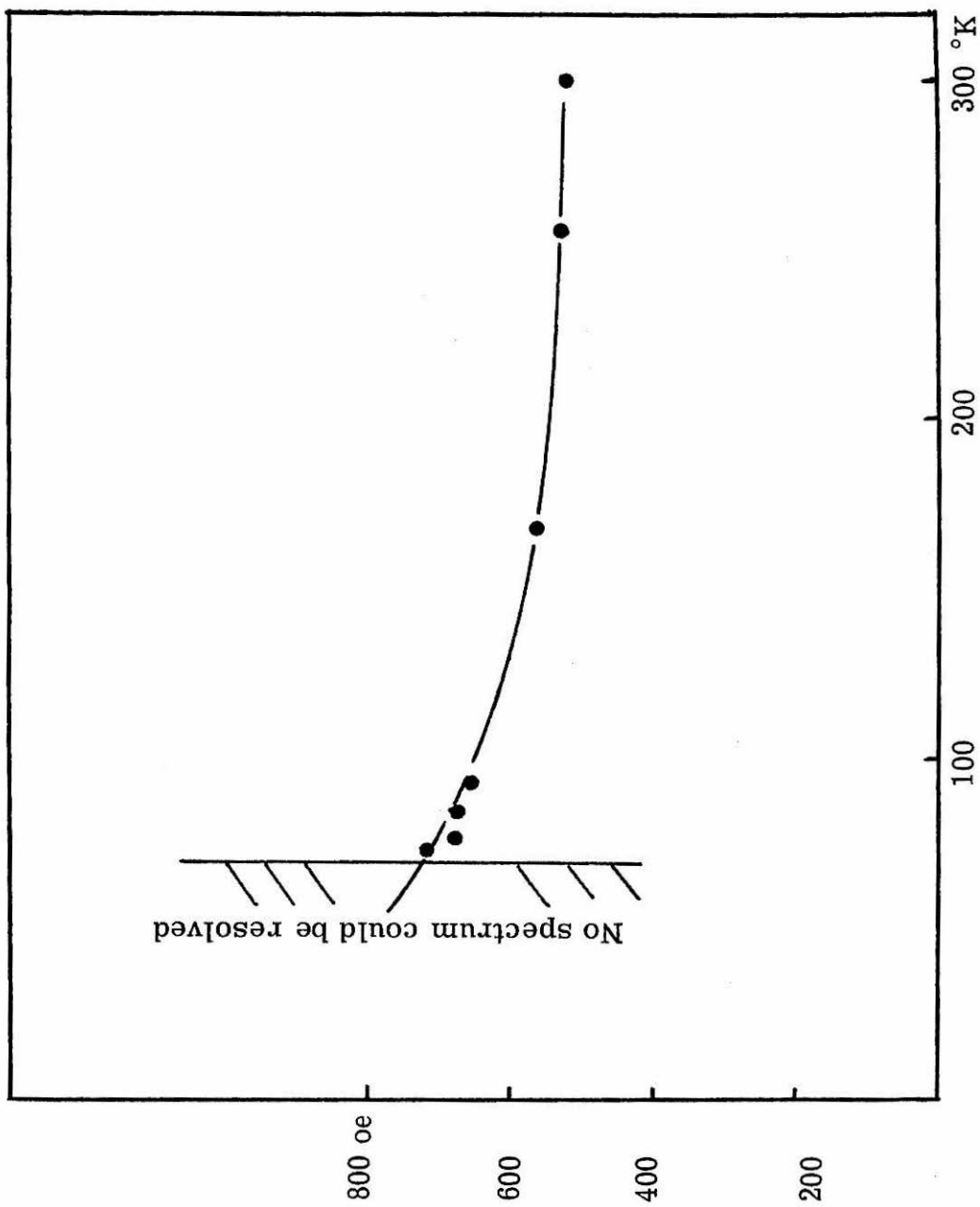


Figure 5. Temperature dependence of bandwidth of esr signal from Fe(OH)CrO_4 . Below 79°K no intelligible spectrum could be resolved.

$g_1 = 2.0019$ and at $g_2 = 4.313$ as well as several minor inflections between the major absorptions.

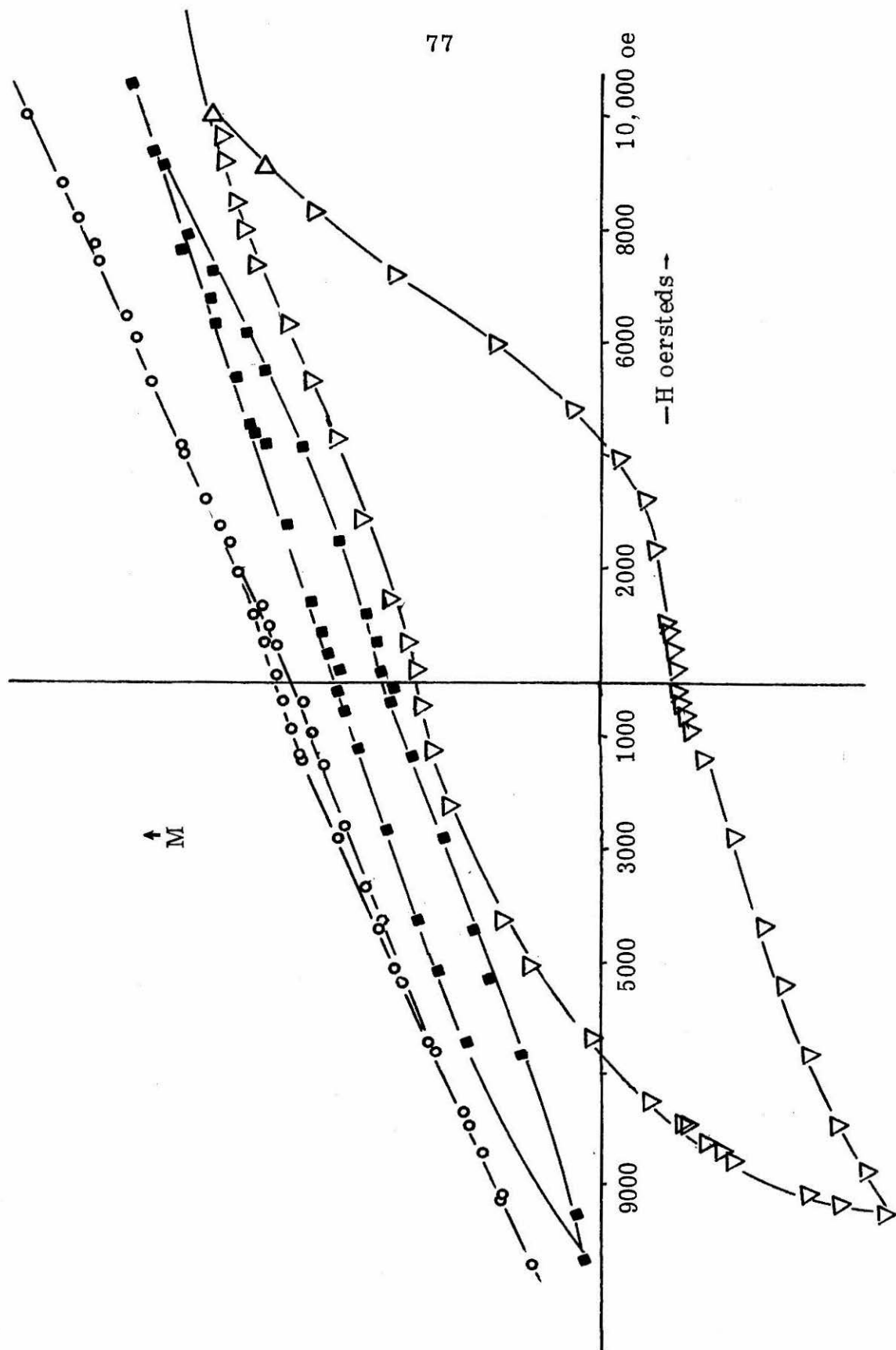
The structure of $\text{KFe}_3(\text{CrO}_4)_2(\text{OH})_6$ is sufficiently anisotropic that esr absorptions polarized in the plane and perpendicular to the plane might be resolved in powder spectra. The absorption at $g_1 = 4.313$ is at far too low a field to be easily rationalized as the perpendicular absorption. A shoulder on the g_1 absorption is more readily assigned to this absorption. No assignment can be offered for the g_2 band at this time.

(C) Magnetization.

Magnetization curves for both $\text{KFe}_3(\text{CrO}_4)_2(\text{OH})_6$ and $\text{Fe}(\text{OH})\text{CrO}_4$ above their respective transition temperatures are devoid of either saturation or hysteresis effects for applied fields up to 11,000 oe. When $\text{Fe}(\text{OH})\text{CrO}_4$ is cooled below its transition temperature, its magnetization curves are badly distorted from the familiar centrosymmetric form. Figure 6 shows magnetization loops for samples cooled to 45.5, 23.0, and 18.0 °K. The loops are wasp-waisted and shifted along the magnetization axis (vertical axis in Figure 6). The apparent shift along the applied field axis is probably due to the vertical shift of the loop. The general appearance of the loops is that of minor loops and suggest that the applied field is insufficient to allow the moment to approach saturation.

Watanabe⁴ observed similar distortions in the magnetization curves of LaFeO_3 . He found that when the samples were cooled in very

Figure 6. Magnetization loops for Fe(OH)CrO_4 at 45.5 (Δ), 23.0 (\blacksquare), and 18°K (\circ). Vertical axis is magnetization in arbitrary units.



weak (< 30 oe) magnetic fields and then brought to saturation much of the distortion along the magnetization axis was lost. This phenomenon and other evidence drawn from the magnetization data led Watanabe to conclude that the distortion was due to a magnetically, very hard, impurity.

When $\text{Fe}(\text{OH})\text{CrO}_4$ was cooled to 23°K in the residual magnetic field of the spectrometer used in this study and then magnetized in an applied field of $10,500$ oe, no loss of distortion was observed in the subsequent magnetization curve. The residual field of the magnetometer was estimated to be ~ 80 oe, somewhat higher than that used by Watanabe. But, since no loss of distortion was observed, and since the magnetization of $\text{Fe}(\text{OH})\text{CrO}_4$ does not vary with preparation significantly, it is likely that the hysteresis loops are intrinsic to the phase and not due to impurities.

An alternative hypothesis that will account for the distortion of the loops is that the magnetization in $\text{Fe}(\text{OH})\text{CrO}_4$ is very anisotropic. The magnetocrystalline anisotropy constant (K) is approximately related to the magnetization by the Stoner-Wohlfarth expression,⁵

$$K = 1/2 M_s H_a$$

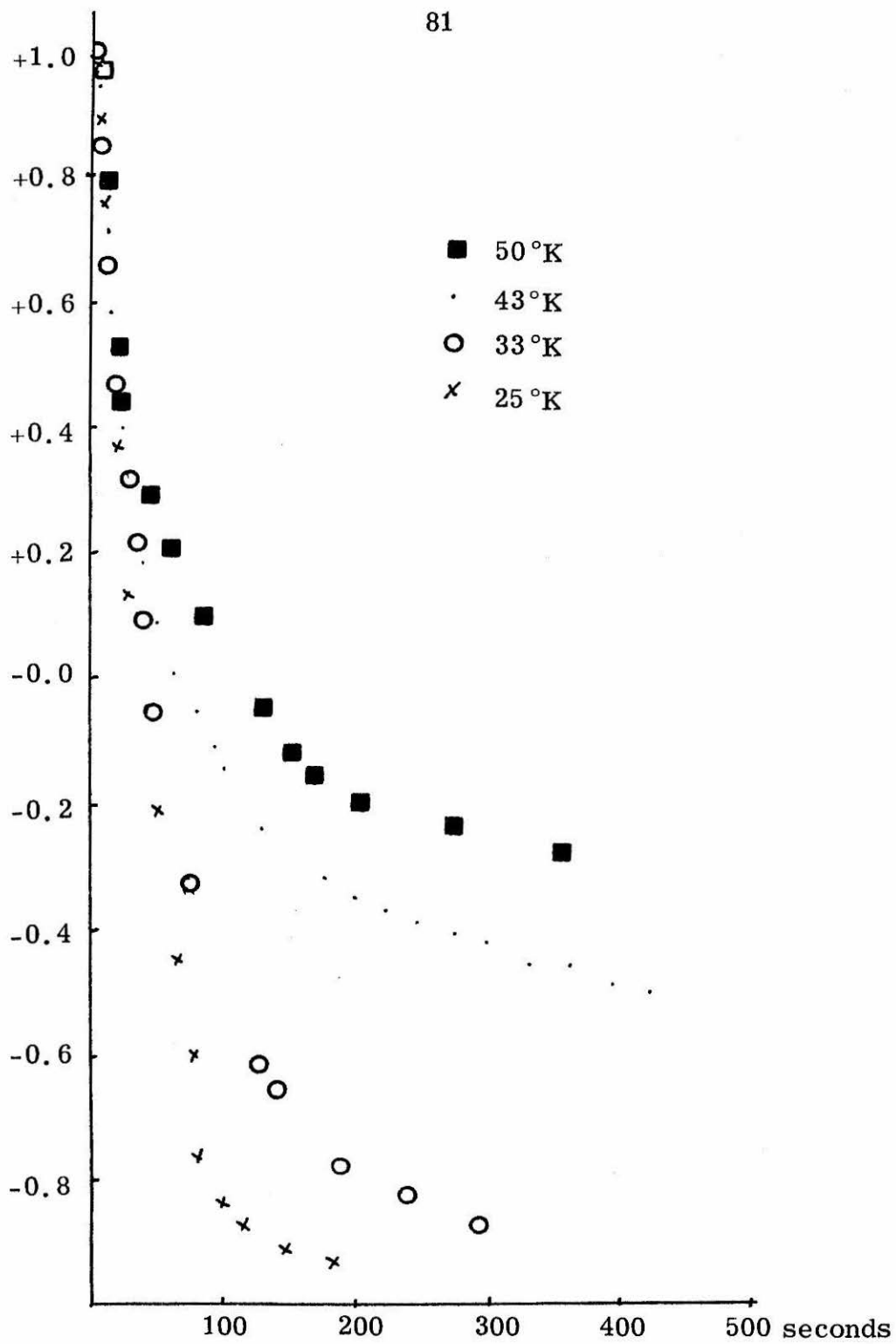
Where M_s is the saturation magnetization per unit volume and H_a is the anisotropy field. At 0°K the anisotropy field is equal to the coercive field. At higher temperatures the relationship is only approximate. The magnetization curves of $\text{Fe}(\text{OH})\text{CrO}_4$ defy precise extrapolation to infinite field. However, by using the magnetization at $10,500$ oe and

the coercive field as approximations of the desired quantities, an estimate of K can be made. The estimate of K at 45.5°K is ~ 7600 ergs/cm³ and increases to $\sim 13,000$ ergs/cm³ at 33°K . At lower temperatures no estimate can be made from the data presented here. Obviously, the fields due to the magnetocrystalline anisotropy are sufficient to prevent saturation with the applied fields available to the instrument used in this study. Consequently, the magnetization loops are highly distorted minor loops.

The proposition of magnetocrystalline anisotropy will also account for the slow reversal of the magnetic moment in $\text{KFe}_3(\text{CrO}_4)_2(\text{OH})_6$. Figure 7 shows the results of an experiment done as follows: A sample of $\text{KFe}_3(\text{CrO}_4)_2(\text{OH})_6$ was cooled to a temperature below the Curie temperature and magnetized in a field of 11,000 oe. The field was then slowly reduced to 144 oe. The field was then reversed to -151 oe. Reversal of the field required at most 30 seconds. In Figure 7 the relative magnetization of the sample is plotted as a function of time. At 62°K complete reversal of the moment requires at least 3 hours. The rate of reversal increases with decreasing temperature.

The temperature dependence of the rate of reversal is surprising. In zero field, the rate would decrease with decreasing temperature. However, in a magnetic field the barrier to reversal is reduced by the magnetization energy which is itself very temperature dependent. The structure of $\text{KFe}_3(\text{CrO}_4)_2(\text{OH})_6$ is well disposed to give rise to uniaxial magnetoanisotropy. If so, the magnetic energy of the phase is given by

Figure 7. Relative magnetization of samples cooled to the indicated temperature versus time after reversal of applied field from +144 to -151 oe.



$$E_M = K \sin^2 \theta - MH \cos \theta$$

where θ is the angle between the easy axis of magnetization and the applied field. The energy barrier (E_b) to rotation of the magnetic moment is then

$$E_b = K + \frac{M^2 H^2}{4K} - MH$$

(see Appendix 1 to Chapter 5).

Discussion

(A) Modelling the Magnetic Behavior of Fe(OH)CrO₄ and Fe(OH)SO₄.

Any consideration of the magnetic behavior of basic iron chromate, particularly above the ferromagnetic transition temperature, must be accompanied by consideration of the magnetic behavior of basic iron sulfate. The most striking feature of the structure of these species is the linear chains of hydroxo-bridged ferric ions. It is tempting to describe the magnetic behavior of these phases in terms of a linearly coupled array of paramagnetic ions. Such a linear model will fail to predict the ferromagnetic transition of basic iron chromate as mentioned in Chapter 1. The magnetic data for temperatures above the Curie temperature is too small for any meaningful calculation. But, the magnetic susceptibility of basic iron sulfate above 75°K is quite similar to that of the chromate analog. A fit of its magnetic behavior to a linear model would allow some estimation of the exchange forces in basic iron chromate.

The magnetic susceptibility of $\text{Fe}(\text{OH})\text{SO}_4$ was fit to Fisher's solution to the Heisenberg linear chain⁶ scaled to finite spin as described in Appendix 1. Models neglecting and allowing interchain magnetic interaction were obtained. Excellent statistical fits, apparently far better than those found in previous attempts,⁷ were obtained. However, parametric values associated with the fits were completely unrealistic. When no interchain interaction was allowed, the calculated g was 1.902 and the intrachain interaction was -14.8 cm^{-1} . When interchain interactions were allowed, the calculated g was 1.944, the intrachain interaction -15.7 cm^{-1} , and the interchain interaction was $+0.02 \text{ cm}^{-1}$. Both calculations failed to reproduce the experimental g -value of 2.0034 and cannot be given much significance.

(B) Ionic Spin Configurations in $\text{Fe}(\text{OH})\text{CrO}_4$.

Magnetic behavior of $\text{Fe}(\text{OH})\text{CrO}_4$ defies approximation in terms of a linear array of coupled paramagnetic ions. Description of the magnetic behavior must then be based on models of higher dimension. Unfortunately, closed solutions to such models are not yet available for $S = 5/2$ systems, and a more qualitative treatment of $\text{Fe}(\text{OH})\text{CrO}_4$ must be made. Such a treatment lacks the pleasing quantitative features of a model such as Fisher's, but in a search for the origins of weak ferromagnetism it will serve.

The Hamiltonian describing the spin structure of basic iron chromate must be invariant under spin reversal and the symmetry operations of the crystallographic group. The form of this Hamiltonian

can be found by considering the irreducible representations of the spin symmetry following the method of Bertaut.⁸

The spins of the ferric ions in this model are treated as classical, axial vectors located at the Fe(III) sites within the unit cell, these sites are $\pm (x, 1/4, z)$; $\pm (1/2x, 1/4, 1/2-z)$ where $x = 0.125$, $z = 0.250$ (see Figure 7). The symmetry operations of the crystallographic group which will transform any Fe(III) ion site into any other are chosen to be

- (1) two-fold screw axis at $(0, y, 0)$ labelled $\tilde{2}_y$
- (2) two-fold screw axis at $(x, 1/4, 1/4)$ labelled $\tilde{2}_x$
- (3) the inversion center (T) at $0, 0, 0$

These symmetry operations rather than the mirror plane operations of the Hermann-Mauguin definition of the crystallographic group were chosen for computational simplicity. The effect of the symmetry operations is shown in Table 6.

Table 6
Effect of Symmetry Operations on the
Fe(III) Sites in $\text{Fe}(\text{OH})\text{CrO}_4$

Metal Ion Originally on Site	Under the Action of the Symmetry Operations This Becomes Site		
	$\tilde{2}_x$	$\tilde{2}_y$	(T)
1	4	3	3
2	3	4	4
3	2	1	1
4	1	2	2

The spins located at the ferric sites are vectors of components S_i^α $i = 1(1)4$, $\alpha = x, y, z$. The effects of symmetry operations on these vectors will be quite complex. It is far easier to find linear combinations of the spin vectors whose transformation properties are more obvious. Fortunately, a set of such linear combinations is easily found and readily interpretable. The combinations are

$$F = S_1 + S_2 + S_3 + S_4$$

$$G = S_1 + S_2 - S_3 - S_4$$

$$A = S_1 - S_2 + S_3 - S_4$$

$$C = S_1 - S_2 - S_3 + S_4$$

The source of the spin combinations and their labels becomes much more obvious if one examines the $\text{Fe}(\text{OH})\text{CrO}_4$ structure perpendicular to the (011) plane. The Fe(III) sites then form a rectangle with the 1-4 and 2-3 sides corresponding to the hydroxide bridge between the ions. The spin configurations are shown diagrammatically in Figure 8 where a darkened circle corresponds to spin up and open circle to spin down.

The F combination corresponds to a ferromagnetically coupled system. From the magnetic data, this is clearly not the ground state of either basic iron sulfate or basic iron chromate. The C combination corresponds to ferromagnetically coupled chains of ferric ions with anti-ferromagnetic interchain coupling. Such ferromagnetic coupling between hydroxide bridges is certainly at odds with past experience with hydroxide or oxobridged dimers. The G and A combinations correspond to antiferromagnetic coupling through the hydroxide bridges.

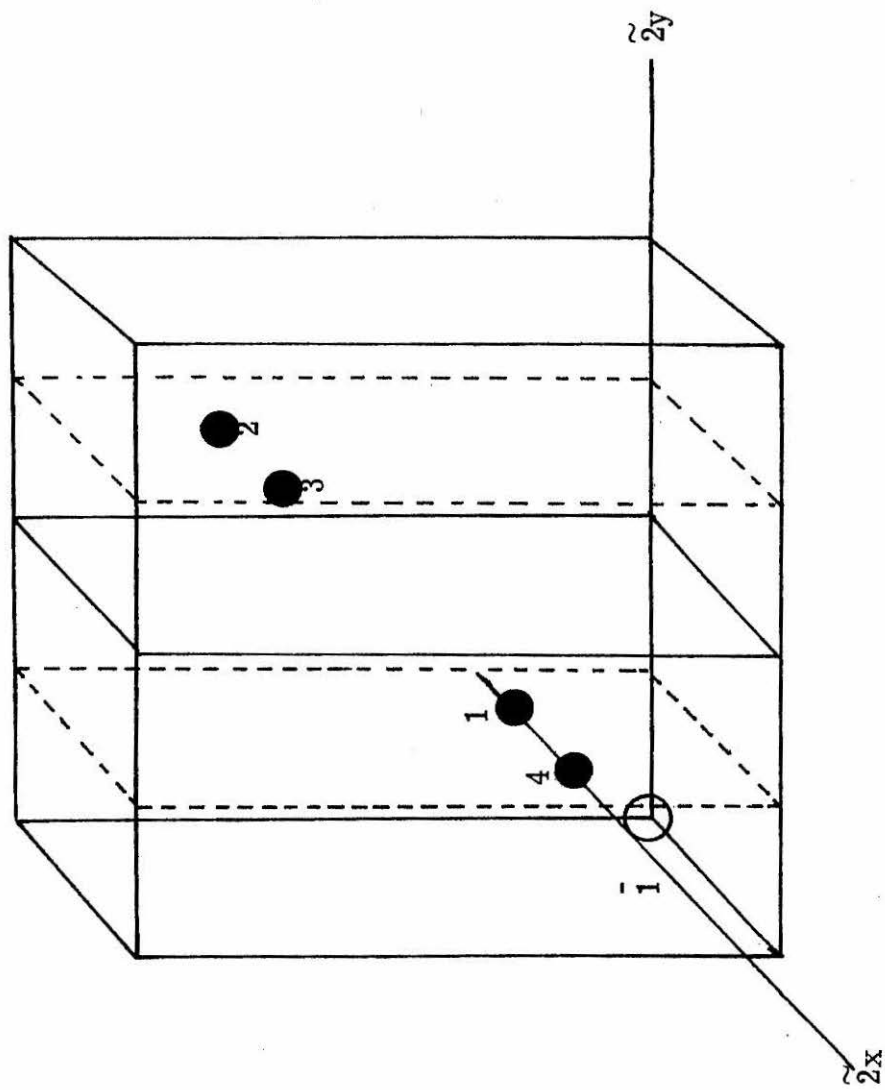


Figure 8. Magnetic ion sites in Fe(OH)CrO_4 . Symmetry operations are $\tilde{2}x$ at $(x, 1/4, 1/4)$, $\tilde{2}y$ at $(0, 0, 0)$ and $\bar{1}$ at $(0, 0, 0)$.

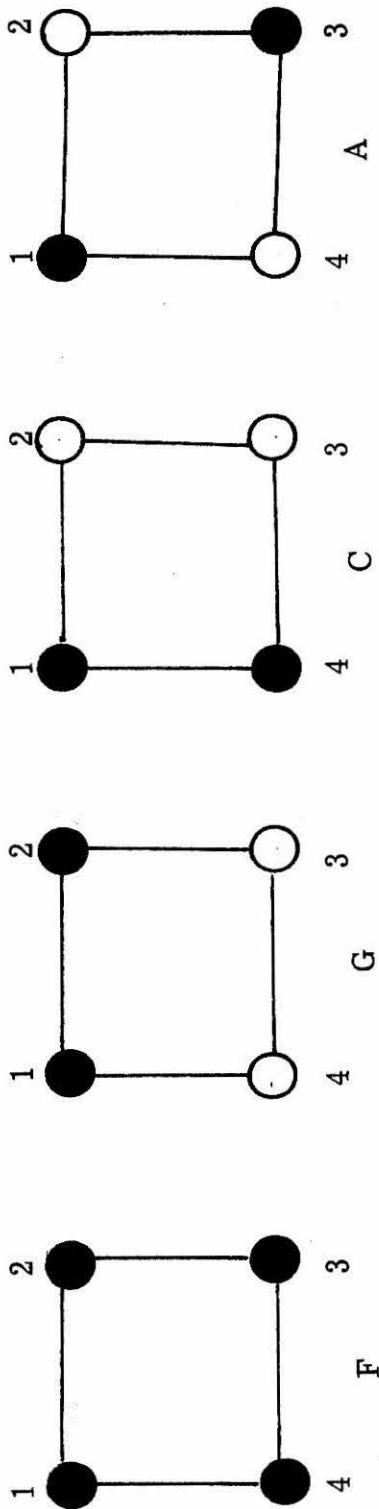


Figure 9. Diagrammatic representations of spin combinations in Fe(OH)CrO_4 . Darkened

circles correspond to spin up. Open circles correspond to spin down.

One of these combinations was implicitly assumed in magnetic studies of $\text{Fe}(\text{OH})\text{SO}_4$ ⁷ and in the above attempts to model the behavior of basic iron sulfate and chromate in terms of linear chains.

Since F, C, A, and G are but combinations of axial spins, they too will have components in the x, y, and z directions. The transformation properties of these components under the action of the symmetry operations are shown in Table 7.

Table 7

Transformation Properties of Components of the Spin Combinations

E	$\tilde{2}_x$	$\tilde{2}_y$	$\bar{1}$
Fx	Fx	-Fx	Fx
Fy	-Fy	Fy	Fy
Fz	-Fz	-Fz	Fz
Gx	-Gx	Gx	-Gx
Gy	Gy	-Gy	-Gy
Gz	Gz	Gz	-Gz
Cx	Cx	Cx	-Cx
Cy	-Cy	-Cy	-Cy
Cz	-Cz	Cz	-Cz
Ax	-Ax	-Ax	Ax
Ay	Ay	Ay	Ay
Az	Az	-Az	Az

The transformation properties give rise to eight irreducible representations of the group defined by the symmetry operations. These representations correspond to magnetic space groups such as those enunciated by Opechowski and Guccione.⁹

Table 9

Representations and Magnetic Groups of $\text{Fe}(\text{OH})\text{CrO}_4$

<u>Class</u>	<u>Components</u>		<u>Magnetic Space Group</u>
Γ_1	Fx	Az	Pnm' a'
Γ_2	Fy		Pn' ma'
Γ_3	Fz	Ax	Pn' m' a
Γ_4	Gx	Cz	Pnm' a
Γ_5	Gy		Pn' ma
Γ_6	Gz	Cx	Pn' m' a'
Γ_7	Cy		Pnma
Γ_8	Ay		Pnm' a

The Hamiltonian describing the ionic spin arrangement in a system is invariant under symmetry operations. Consequently, only terms of even order in the spin components may appear in the Hamiltonian. Further, only spin components from the same symmetry classification can interact. If exchange forces within the system are isotropic, only pure spin modes (A, C, G, F) will appear in the Hamiltonian. But, when exchange forces in the system are anisotropic, as they surely must be in basic iron chromate, mixed modes may appear.

Mixing of modes must occur, of course, only among spin components of the same symmetry class and be of even order. For most systems of identical magnetic ions, Hamiltonian terms of order two suffice to describe the spin configuration. Table 9 lists the invariant terms of the Hamiltonian of order 2 in terms of their symmetry class. From this

Table 9

Invariants

<u>Symmetry</u> <u>Class of Components</u>	<u>Isotropic</u> <u>Terms</u>	<u>Anisotropic</u> <u>Terms</u>
Γ_1	$Fx^2 ; Az^2$	$FxAz$
Γ_2	Fy^2	
Γ_3	$Fz^2 ; Ax^2$	$FzAx$
Γ_4	$Gx^2 ; Cz^2$	$GxCz$
Γ_5	Gy^2	
Γ_6	$Gz^2 ; Cx^2$	$GxCx$
Γ_7	Cy^2	
Γ_8	Ay^2	

table it is apparent that weak ferromagnetism is possible for two symmetry classes-- Γ_1 and Γ_3 . From the magnetic data it is clear that the ground state spin configuration of $Fe(OH)CrO_4$ is not well described by a pure ferromagnetic mode. From Table 9, then, the ground state spin configuration must be either Az or Ax .

The Hamiltonian which describes the ionic spin configuration of $Fe(OH)CrO_4$ is then either

$$\mathcal{H} = aAz^2 + bFxAz$$

and weak ferromagnetism appears along the [100] direction, or

$$\mathcal{H} = a'Ax^2 + b'FzAx$$

and weak ferromagnetism appears along the [001] direction.

Weak ferromagnetism due to either of these Hamiltonians will be very anisotropic. The magnetic moment cannot exist along any but the symmetry allowed direction. Consequently, large coercive fields will be necessary to reverse the magnetism. When such fields are not supplied, magnetization curves will be minor loops and have the distorted appearance of those loops found for $\text{Fe}(\text{OH})\text{CrO}_4$ in this study.

The coupling of the ferromagnetic mode to the ground state antiferromagnetic spin mode is brought about by the anisotropic exchange terms. The most important of these terms will be Dzialoshinski-Moriya coupling, $(\vec{D} \cdot \vec{S} \times \vec{S})$, pseudodipolar coupling and crystalline field anisotropy. No emphatic choice among these mechanisms can be made based on the data herein. Dzialoshinski-Moriya coupling and pseudodipolar coupling (ϕ_{RR}) are dependent on the isotropic exchange⁸ as shown below

$$D \sim \frac{\Delta g}{g} J_{\text{RR}} \quad \phi \sim \left(\frac{\Delta g}{g}\right)^2 J_{\text{RR}}$$

where $\Delta g = g - 2.0024$ and J_{RR} is the isotropic exchange constant. Crystalline field anisotropy is independent of J_{RR} . ESR data for $\text{Fe}(\text{OH})\text{CrO}_4$ and the obviously large J_{RR} indicated from the magnetic susceptibility suggest that D-M coupling may predominate.

No decision can be made from the above arguments about the spin configuration of Fe(OH)SO_4 except that its configuration is not Γ_2 .

(C) Spin Configuration of $\text{KFe}_3(\text{CrO}_4)_2(\text{OH})_6$.

Magnetic susceptibility of $\text{KFe}_3(\text{CrO}_4)_2(\text{OH})_6$ is not consistent with a model of antiferromagnetically coupled sheets of ferromagnetically coupled ferric ions. Such a structure would give rise to metamagnetism, which was not observed in the magnetic behavior of the phase.

Above the transition temperature the magnetic behavior of $\text{KFe}_3(\text{CrO}_4)_2(\text{OH})_6$ is analogous to the behavior of $\text{KFe}_3(\text{SO}_4)_2(\text{OH})_6$. In treating this latter compound, Tokano et al.² proposed a non-collinear spin structure shown in Figure 10 to account for the antiferromagnetic behavior. This analysis was based on consideration of isotropic exchange terms in the energy expression for the in-plane components of the spins. Clearly, the arrangement of spins shown in Figure 10 is invariant under the symmetry operations of the crystallographic space group. A spin arrangement of the z-components of the spins oriented "up" is also invariant under the symmetry operations and consequently belongs to the same symmetry class as the arrangement shown in Figure 10. (That is, both arrangements transform as magnetic space group $R\bar{3}m'$.) Coupling between these spin modes will, of course, give rise to weak ferromagnetism. Again, the coupling is due to the anisotropic exchange terms. Symmetry conditions have shown that in hexagonal space groups anisotropic exchange is due to D-M coupling.

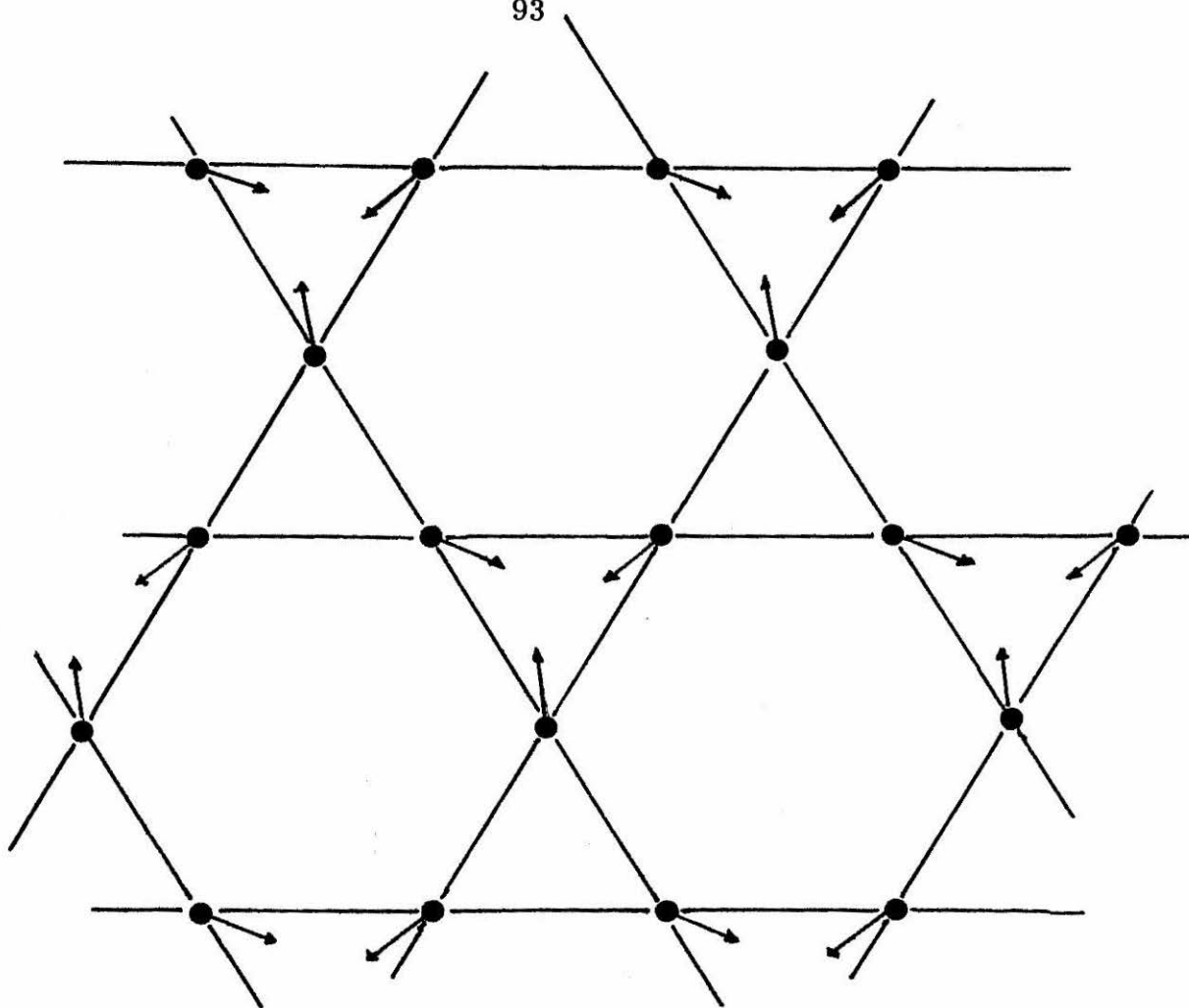


Figure 10. Spin configuration proposed for an antiferromagnetic Kagomé array of $S = 5/2$ ions. After reference 2.

(D) Modeling the Magnetic Behavior of $M^I\text{Fe}_3(\text{CrO}_4)_2(\text{OH})_6$ in Terms of Sheets of Canted Spins.

The above argument proposed that the magnetic behavior of $M^I\text{Fe}_3(\text{CrO}_4)_2(\text{OH})_6$ is that of sheets of canted spins. The magnetic susceptibility of such an assemblage ought to deviate from Curie-Weiss law behavior according to the expression¹⁰⁻¹²

$$\Delta\chi \sim |T - T_c|^\gamma \quad \text{equation 1}$$

The parameter T_c is ostensibly the Curie temperature, but is best thought of as a parameter determined by the isotropic exchange interactions and the structure of the sheet. For instance, for a Heisenberg infinite square lattice¹¹

$$T_c = \frac{J}{5K} (z - 1) [2S(S + 1) - 1]$$

where z is the number of nearest neighbors.

Typically, comparison between experimental and theoretical behavior in terms of equation 1 is made by plotting $\ln\chi$ versus $\ln|T - T_c|$. The slope of such a plot yields γ . However, log-log plots are notoriously insensitive. A superior procedure is to fit the deviation of the magnetic susceptibility from Curie-Weiss behavior to equation 1 by least-squares estimation of the nonlinear parameters. The results of such a fit for $M^I\text{Fe}_3(\text{CrO}_4)_2(\text{OH})_6$ near the transition temperature are shown in Figure 11. Errors in the parametric values represent the upper and lower support planes of the nonlinear confidence levels.

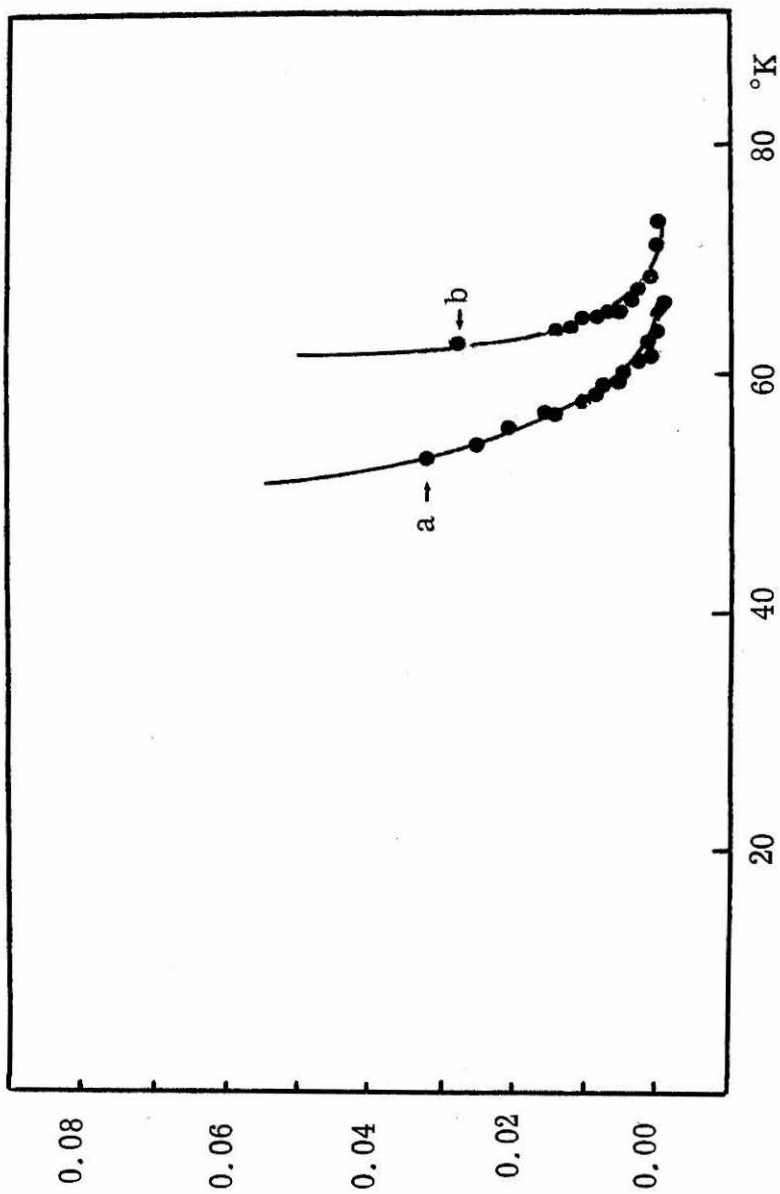


Figure 11. Fit of deviation of molar susceptibility of (a) $\text{NH}_4\text{Fe}_3(\text{CrO}_4)_2(\text{OH})_6$

($T_c = 71.2 \pm 0.5^\circ\text{K}$; $\gamma = 2.95 \pm 0.11$) and (b) $\text{KFe}_3(\text{CrO}_4)_2(\text{OH})_6$

($T_c = 82.0 \pm 1.0^\circ\text{K}$; $\gamma = 3.25 \pm 0.15$) from Curie-Weiss law in terms of equation 1 in text.

Little is known theoretically about the kagomé array $S = 5/2$ ions found in the species $M^I\text{Fe}_3(\text{CrO}_4)_2(\text{OH})_6$ so the T_c values cannot be related to the isotropic exchange interactions. The γ values, however, compare well with the predicted values for a Heisenberg square lattice¹¹ ($\gamma = 2.82$) and the value found for $(\text{CH}_3\text{NH}_3)_2\text{MnCl}_4$ ¹² ($\gamma = 2.59$). They are at odds with values predicted from the Ising model ($\gamma = 1.75$)¹⁰ and those found for three dimensional structures ($\gamma = 1.2 - 1.4$).¹²

References

1. G. K. Wertheim and J. P. Remeika, Phys. Letters, 10, 14 (1964).
2. M. Tokano, T. Shinjo, and T. Takada, J. Phys. Soc. Japan, 30, 1049 (1971).
3. A. Z. Hryniewicz, J. Kubisz, and D. S. Kuigawczuk, J. Inorg. Nucl. Chem., 27, 2513 (1965).
4. H. Watanabe, J. Phys. Soc. Japan, 14, 511 (1959).
5. E. C. Stoner and E. P. Wohlfarth, Philos. Trans. Roy. Soc., A240, 74 (1948).
6. M. E. Fisher, Am. J. Phys., 32, 343 (1964).
7. R. W. Cattrall, K. S. Murray, and K. I. Perverill, Inorg. Chem., 10, 1301 (1971).
8. E. F. Bertaut, "Spin Configurations of Ionic Structures," in Magnetism, Vol. III, G. T. Rado and H. Suhl, eds., Academic Press, 1963, New York.
9. W. Opechowski and R. Guccione, Magnetism, Vol. IIA, G. T. Rado and H. Suhl, eds., Academic Press, 1965, New York.
10. J. W. Essam and M. E. Fischer, J. Chem. Phys., 38, 802 (1963).
11. H. E. Stanley and T. A. Kaplan, Phys. Rev. Letters, 17, 913 (1966).
12. B. G. Gerstein, private communication.

APPENDIX 1
MAGNETIC EXCHANGE INTERACTIONS
THROUGH CHROMATE BRIDGES:
THE MAGNETIC BEHAVIOR OF $M^{(I)}Fe(CrO_4)_2 \cdot 2H_2O$

The results cited in Chapter 1 suggest that bridging chromate ions may sponsor unusual exchange interactions between magnetic ions. The magnetic behavior of $M^I Fe(CrO_4)_2 \cdot 2H_2O$ ($M^I = Na^+, K^+, NH_4^+, Tl^+, Cs^+$) tests this hypothesis. In these species all bridging ligation is provided by chromate ions, and there are no bridging hydroxide groups such as those in the basic iron chromates. The wealth of experimental experience with hydroxide bridged dimers suggests that these ligands ought to be principal exchange pathways. Exchange through the hydroxide bridges may be modified by other bridging ligation. This appendix yields some estimate of the modification that might be provided by bridging chromate ligands.

EXPERIMENTAL

(A) Preparation of Compounds.

The species $M^I\text{Fe}(\text{CrO}_4)_2 \cdot 2\text{H}_2\text{O}$ ($M^I = \text{Na}^+, \text{K}^+, \text{NH}_4^+, \text{Tl}^+$) were prepared by the methods of Bonnin, et al.¹ The cesium salt was prepared by allowing a solution of 0.5 F $\text{Fe}(\text{NO}_3)_3 \cdot 9\text{H}_2\text{O}$ and 0.5 F $\text{Cs}_2\text{Cr}_2\text{O}_7 \cdot 2\text{H}_2\text{O}$ to slowly evaporate.

All products were free-flowing powders which, upon microscopic examination, proved to consist of fine prismatic crystals. Analytic data are cited in Table 1. Water analyses were by thermogravimetric analysis.

(B) Instrumental Analysis.

The identity of the species was confirmed by X-ray powder diffraction using iron filtered $\text{CoK}\alpha$ radiation. D-spacings and tentative assignments for the sodium salt are cited in Table 2. The data for $\text{CsFe}(\text{CrO}_4)_2 \cdot 2\text{H}_2\text{O}$ were interpreted in terms of the unit-cell parameters

$$a = 14.79 \quad b = 5.57 \quad c = 11.02 \quad \beta = 109^\circ$$

Thermal analyses were done with a DuPont 900 differential thermal analyzer and a DuPont 950 thermogravimetric analyzer.

Infrared, magnetic, and esr data were collected as described in Chapters 1 and 2. Mossbauer spectra of $\text{KFe}(\text{CrO}_4)_2 \cdot 2\text{H}_2\text{O}$ were obtained by Dr. Rolf Herber of Rutgers University.

Table 1
 Elemental Analysis of $M^I\text{Fe}(\text{CrO}_4)_2 \cdot 2\text{H}_2\text{O}$

<u>Cation</u>		<u>M^I</u>	<u>Fe</u>	<u>Cr</u>	<u>H₂O</u>
Na	Found	6.35	16.15	29.89	10.54
	Calc	6.63	16.10	29.98	10.38
K	Found	10.72	15.43	28.55	10.00
	Calc	10.77	15.39	28.65	9.92
NH ₄	Found ^a	4.26	16.50	30.82	b
	Calc ^a	4.10	16.33	30.42	10.53
Tl	Found	38.80	10.49	19.30	6.90
	Calcd	38.69	10.57	19.69	6.82
Cs	Found	29.00	12.43	23.00	7.96
	Calc	29.10	12.23	22.77	7.88

^a Percent nitrogen.

^b Other thermal decomposition reactions interfere with determination of water content by thermal means.

101
Table 2

D-spacings and Assignments for X-ray Powder Diffraction

Pattern of $\text{NaFe}(\text{CrO}_4)_2 \cdot 2\text{H}_2\text{O}$

<u>d</u> (Observed) (Å)	<u>Relative</u> <u>Intensity</u>	<u>d</u> (Calculated) (Å)	<u>Assignment</u> h k l		
5.05	9	5.03	1	1	0
4.89	3	4.78	0	1	1
3.55	10	3.51	2	0	2
3.35	4	3.356	400, 112		
3.04	10	3.03	3	1	1
2.961	4	2.945	2	1	2
2.786	5	2.856	0	1	3
2.716	7	2.712	0	2	0
2.663	5	2.645	1	1	3
2.515	1	2.515	2	2	0
2.441	2	2.443	4	0	2
2.390	2	2.388	0	2	2
2.236	2	2.238	6	0	0
2.195	2	2.197	5	1	1
2.146	3	2.156	2	2	2
2.105	3	2.110	023, 502, 420		
1.888	3	1.889	0	1	5
1.836	5	1.831	6	0	2
1.798	1	1.795	1	1	5
1.778	4	1.779	0	3	1
1.728	3	1.727	513, 620		
1.688	3	1.690	7	1	1

Table 2 (Continued)

<u>d</u> <u>(Observed)</u> <u>(Å)</u>	<u>Relative</u> <u>Intensity</u>	<u>d</u> <u>(Calculated)</u> <u>(Å)</u>	<u>Assignment</u>		
			<u>h</u>	<u>k</u>	<u>l</u>
1.624	3	1.622	7	0	2
1.580	2	1.573	3	1	5
1.522	2	1.527	5	1	4
1.486	3	1.484	2	2	5
1.430	2	1.428	0	2	6

(C) Computer-fitting of Magnetic Data

Nonlinear least-squares estimation of parameters was used to fit the magnetic data to theoretical expressions described in the text.

The fitting procedure was as follows:

- (1) all parameters were allowed to vary until convergence was obtained.
- (2) input parameters were then varied to search for absolute minima in the parameters space.
- (3) parameters were allowed to vary in groups of two to insure no pseudominima were observed.

In all cases the optimal parameters found under the above procedures differed by less than 0.05%. Statistical tests used for convergence were variance ratio statistics, student's t, epsilon test, gamma-lambda test, and the gamma epsilon test.

STRUCTURE OF $M^I\text{Fe}(\text{CrO}_4)_2 \cdot 2\text{H}_2\text{O}$

Single-crystal X-ray structure determination of $\text{NaFe}(\text{CrO}_4)_2 \cdot 2\text{H}_2\text{O}$ has shown that this species crystallizes in the monoclinic space group $C_{2h}^6-C_{21c}$, $a = 14.25$, $b = 5.43$, $c = 10.69\text{\AA}$, $\beta = 109.3^\circ$, and $z = 4$. The structure consists of linear chains of ferric ions running parallel to the b axis of the unit cell. Adjacent ferric ions along the chains are bridged by two cis chromate groups (see figure 1). Two equivalents of trans coordinated water complete the coordination polyhedron of the ferric ion. The chains are separated by the monovalent ions and there are no interchain bonding units.

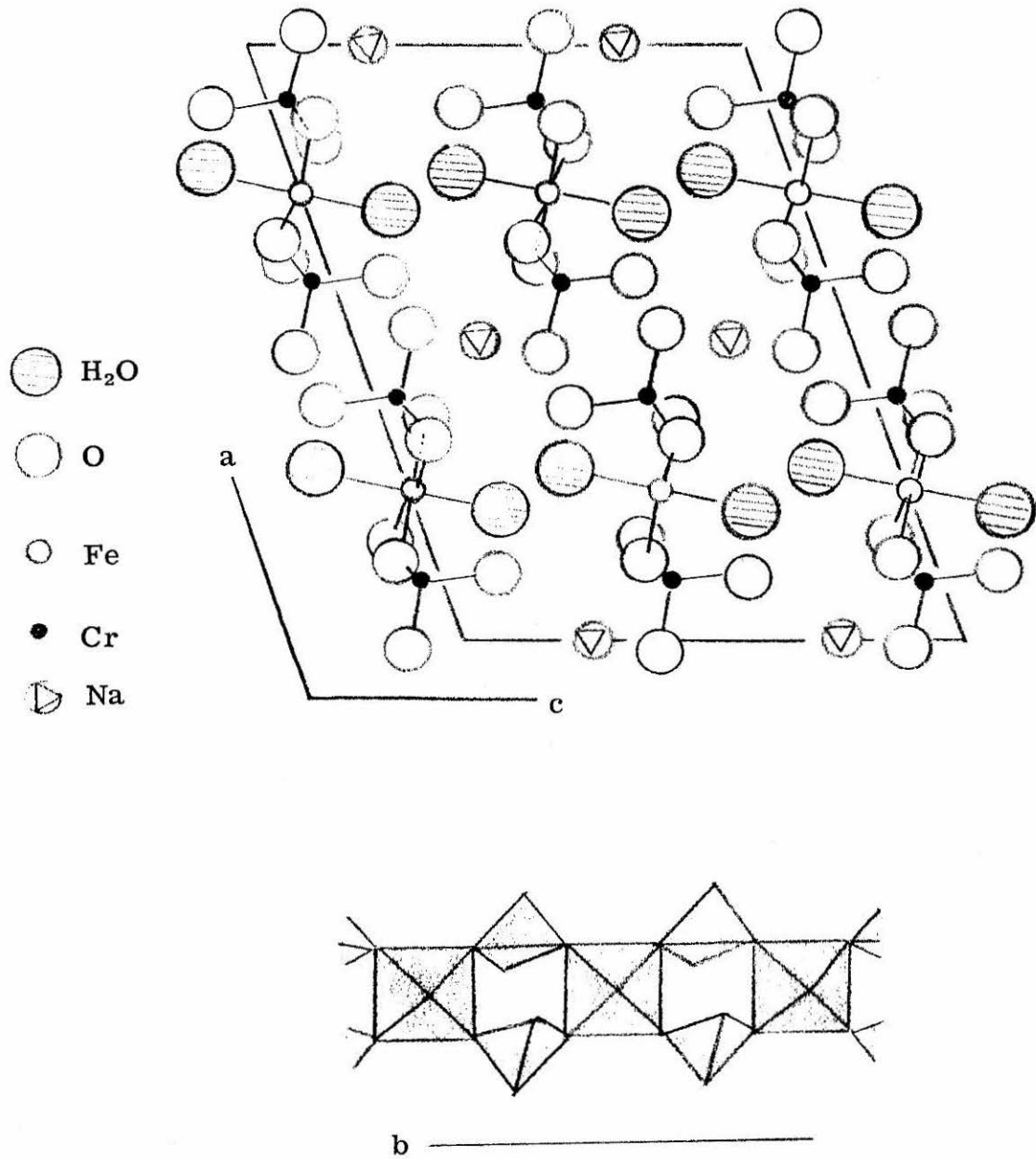


Figure 1. Structure of $\text{NaFe}(\text{CrO}_4)_2 \cdot 2\text{H}_2\text{O}$ (after reference 2).

Table 3

X-ray Powder Diffraction Patterns of $M^I\text{Fe}(\text{CrO}_4)_2 \cdot 2\text{H}_2\text{O}$

M^I	K		NH_4		Tl		Cs	
	d Å	I	d Å	I	d Å	I	d Å	I
	5.13	5	7.55	4	7.21	1	4.39	3
	4.89	4	6.99	2	6.90	5	4.10	2
	3.62	6	5.20	10	4.99	1	3.99	1
	3.39	4	4.96	4	4.87	8	3.64	5
	3.13	10	4.36	4	4.80	6	3.45	10
	3.00	6	3.94	1	4.36	7	3.22	7
	2.890	1	3.63	9	3.65	4	3.05	7
	2.815	4	3.41	3	3.54	1	2.950	3
	2.754	6	3.37	4	3.49	1	2.761	7
	2.696	3	3.16	10	3.39	6		
	2.578	3	3.04	4	3.14	10	2.605	1
	2.554	1	2.841	3	3.00	7	2.530	1
	2.448	1	2.754	9	2.815	6	2.435	6
	2.277	2	2.599	2	2.754	7	2.354	4
	2.199	4	2.443	1	2.720	5	2.301	4
	2.138	4	2.303	2	2.587	6	2.232	1
	1.938	3	2.236	1	2.556	3	2.203	3
	1.908	2	2.218	1	2.454	2	2.184	4
	1.881	1	2.150	2	2.414	2	2.064	6
	1.851	3	2.083	1	2.334	3	2.027	1

Table 3 (Continued)

M^I	K		NH_4		Tl		Cs	
	d Å	I	d Å	I	d Å	I	d Å	I
	1.815	1	1.954	2	2.205	6		
	1.794	1	1.872	3	2.161	3	1.867	3
	1.742	2	1.825	3	2.146	6	1.710	6
	1.719	1	1.789	1	1.994	3	1.662	7
	1.657	3	1.763	1	1.948	5	1.619	2
	1.568	2	1.725	2	1.922	3	1.580	3
	1.506	2	1.665	1	1.890	3	1.528	3
	1.450	2	1.535	4	1.855	3	1.482	3
	1.378	2			1.809	4	1.433	2
					1.755	3	1.390	3
					1.661	4		
					1.636	4		
					1.609	1		
					1.580	3		
					1.561	1		
					1.549	1		
					1.511	2		
					1.480	3		
					1.456	3		
					1.423	1		
					1.419	2		
					1.402	1		
					1.381	3		

Table 4

Infrared Spectra of $M^I\text{Fe}(\text{CrO}_4)_2 \cdot 2\text{H}_2\text{O}$

$M^I =$	Na	NH_4	K	Cs	Tl	Assignments ^a
	3400 s	3450 m	3420 s	3405 m	3350 s, b	ν_{OH}
		3200 s				ν_{NH}
	1590 m	1590 m	1588 m	1617 m	1582 s	δ_{OH}
		1410 s				δ_{NH}
	960 s	980 w	955 s	982 s		
		951 s	920 s	951 s	940 s	
	928 s	938 s		937 s	909 s	
		920 sh				$\nu_3(\text{CrO}_4)$
	840 s					
		870 w		870 s		
		830 s	825 sh			
	810 w					
	785 s	790 s	790 s	800 s	814 s	$\nu_{\text{Fe-O}}$
		755 s		760 s	770 s	$\nu_1(\text{CrO}_4)$
	720 s		710 sh		700 sh	
			500 w			
	430 s	430 s	420 s	432 s		$\nu_2(\text{CrO}_4)$
	415 w			420 w	412 s	
	352 m	378 w		379 w	362 w	
		392 w				
	330 m	332 s	330 m	332 m	323 w	$\nu_4(\text{CrO}_4)$
				285 s	250 w	

^aAfter reference 3.

X-ray powder diffraction has shown that the K^+ , NH_4^+ , Tl^+ salts are isomorphous¹ though the cell parameters cited in this reference are in error. Herein, it is shown that the Cs^+ salt is also of similar structure. Recent infrared data have suggested that the NH_4^+ salt may have a slightly modified space group.³

The linear chain structure of $M^I Fe(CrO_4)_2 \cdot 2H_2O$ is chemically quite apparent. However, the species will behave magnetically like linear chains of magnetic ions only if exchange along the chains is significantly greater than any interchain magnetic exchange interaction. Table 5 shows that the separation between ions within the chains is not greatly different from the interchain separation of magnetic ions. Consequently, the magnetic behavior of $M^I Fe(CrO_4)_2 \cdot 2H_2O$ can be described in terms of linear chains only if the bridging chromate groups sponsor the principal exchange interactions.

Since interchain interactions will most likely be direct exchange, they will be most sensitive to variations in the chain spacing. From Table 5 it is apparent that the interchain separations are far more sensitive to cation size than is the intrachain separation of ions which is largely controlled by the bridging chromate groups. Consequently, any interchain interactions should be quite "cation" dependent whereas interchain coupling should be insensitive to the cation.

The thermal dehydration of the $M^I Fe(CrO_4)_2 \cdot 2H_2O$ species shows that a physically meaningful range of cation sizes has been used in this study. Loss of water from this structure is accelerated by hydrogen

Table 5

Ferric Ion Separations in $M^I\text{Fe}(\text{CrO}_4)_2 \cdot 2\text{H}_2\text{O}$

M^I	r_{cation} (Å)	Fe-Fe (intrachain)	Fe-Fe along "c" axis	Fe-Fe (along "a" axis)
Na	0.95	5.425	7.62	5.975
K	1.33	5.51	7.76	6.089
NH_4	1.48	5.54	7.81	6.127
Tl	1.40	5.55	7.79	6.098
Cs	1.69	5.57	7.90	6.175

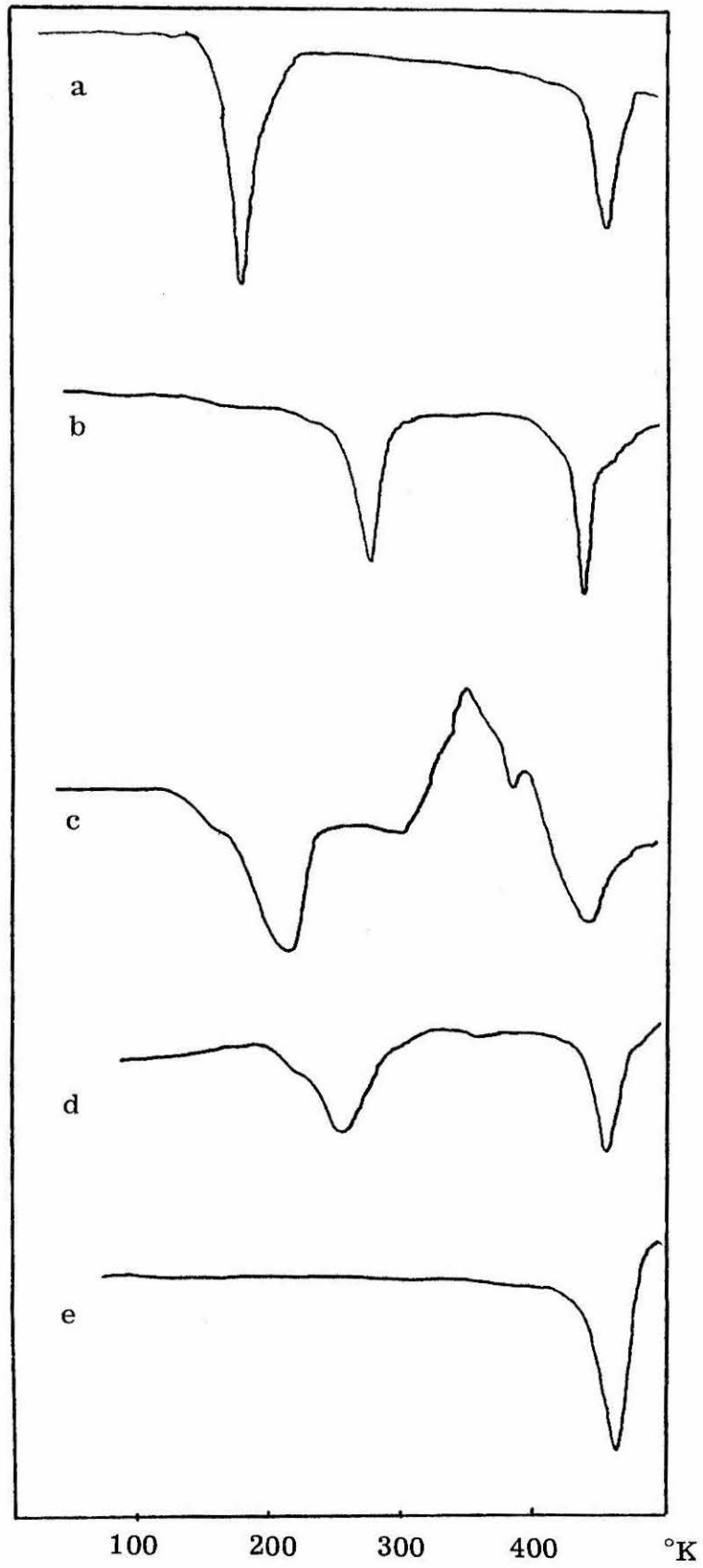
Table 6
 Thermal Decomposition of $M^I\text{Fe}(\text{CrO}_4)_2 \cdot 2\text{H}_2\text{O}$

<u>Cation</u>	<u>Temperature of Dehydration^a (°C)</u>	<u>Temperature of Decomposition^a (°C)</u>	<u>$r_M^{(I)}$ (Å)</u>
Na	171	451	0.95
K	240	432	1.33
NH ₄	(207) ^b	(450) ^b	1.48
Tl	247	452	1.40
Cs	462	< 550	1.69

^a Temperatures were determined from the dta thermograms as the point at which the thermal event begins and not dta peak positions.

^b Other thermal events make estimation of these temperatures very difficult.

Figure 2. Differential thermograms for (a) $\text{NaFe}(\text{CrO}_4)_2 \cdot 2\text{H}_2\text{O}$,
(b) $\text{KFe}(\text{CrO}_4)_2 \cdot 2\text{H}_2\text{O}$, (c) $\text{NH}_4\text{Fe}(\text{CrO}_4)_2 \cdot 2\text{H}_2\text{O}$,
(d) $\text{TlFe}(\text{CrO}_4)_2 \cdot 2\text{H}_2\text{O}$, (e) $\text{CsFe}(\text{CrO}_4)_2 \cdot 2\text{H}_2\text{O}$. The
first peak in each thermogram corresponds to the loss
of two equivalents of water.



bonding of the water between chains. This bonding, in turn, is dependent on the chain separation. Figure 2 and Table 6 show that the dehydration endotherm of $M^I\text{Fe}(\text{CrO}_4)_2 \cdot 2\text{H}_2\text{O}$ varies significantly among the species investigated. This variation is roughly in accord with the cation size. Thermal decomposition of the chromate group is much less sensitive to the cation as would be expected.

RESULTS

(A) Mössbauer and Electron Spin Resonance.

Mössbauer spectra of $\text{KFe}(\text{CrO}_4)_2 \cdot 2\text{H}_2\text{O}$ are shown in Figure 3. The spectrum consists of a well-formed doublet as would be expected for iron(III) in a coordination polyhedron significantly distorted from cubic form. Little variation in the spectrum occurs over the temperature range of 297-20°K.

Table 7

Mössbauer Data for $\text{KFe}(\text{CrO}_4)_2 \cdot 2\text{H}_2\text{O}$

T (°K)	δ^a (mm/sec)	Δ^b (mm/sec)	$\frac{d\delta}{dT}$ (mm/sec/ 100°)	$\frac{d\Delta}{dT}$ (mm/sec/ 100°)	I_1/I_2^c
297	-0.358	0.947	--	--	1.023
78	-0.508	0.896	--	--	1.082
20	-0.548	0.885	--	--	1.094
			-0.069	0.024	

^a Isomer shift versus $\text{Pd}(\text{Co}^{57})$. ^b Quadrupole splitting. ^c Intensity ratio of two members of the doublet.

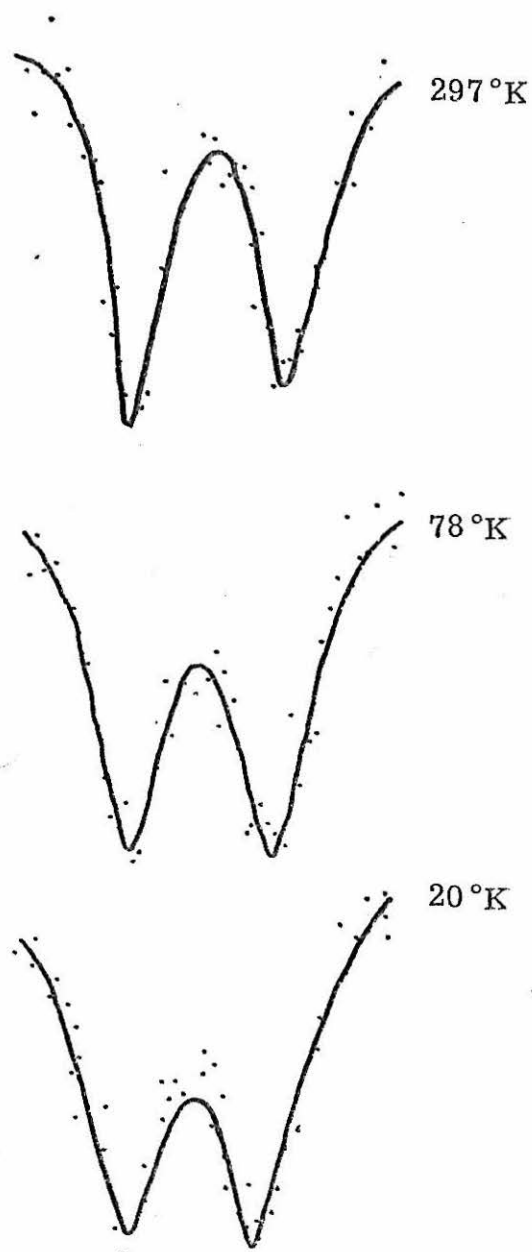


Figure 3. Mössbauer spectrum of $\text{KFe}(\text{CrO}_4)_2 \cdot 2\text{H}_2\text{O}$ at 297, 78, and 20°K . Experimental points denoted by dots. Solid line is the product of Lorentzian line shape analysis.

The isomer shift in $\text{KFe}(\text{CrO}_4)_2 \cdot 2\text{H}_2\text{O}$ is quite negative compared to that found for other ferric iron species. Shifts of 1.115 and 0.320 mm/sec at -130°C have been reported for $\text{Fe}_3(\text{PO}_4)_2 \cdot 8\text{H}_2\text{O}$ and $\text{FePO}_4 \cdot 4\text{H}_2\text{O}$, respectively.⁴ Shifts for $\text{Fe}_2(\text{SO}_4)_3$ and $\text{KFe}_3(\text{SO}_4)_2(\text{OH})_6$ at 78°K have been reported as -0.121 and 0.265 mm/sec, respectively.⁵ The shift is also at odds with those of other iron chromates (see above). A large negative isomer shift of this type is indicative of unusual electron density at the ferric nucleus.

The quadrupole splittling is fairly temperature independent. The electric field gradient must be predominantly due to the coordination environment of the ferric ion and relatively insensitive to temperature.

Esr spectra of the species consisted of a single, very intense absorption. The breadths of adsorptions increased smoothly with temperature (see figure 4) and did not show any behavior which might be indicative of spin ordering to 9°K . Room temperature g-values and line widths for the compounds are recorded in Table 8. The most striking feature of these data is the very atypical behavior of the thallium salt. Whereas g-values for all other species are greater than the value for a free electron, the g-value for $\text{TlFe}(\text{CrO}_4)_2 \cdot 2\text{H}_2\text{O}$ is 1.979. Further, the bandwidth of the thalium salt signal is 2.5 to 10 times as great as that of the other salts.

(B) Magnetic Data

Magnetic data of all the compounds were found to fit the Curie-Weiss Law ($\chi_M = C/(T - \theta)$) to 20°K . Weiss and Curie constants found

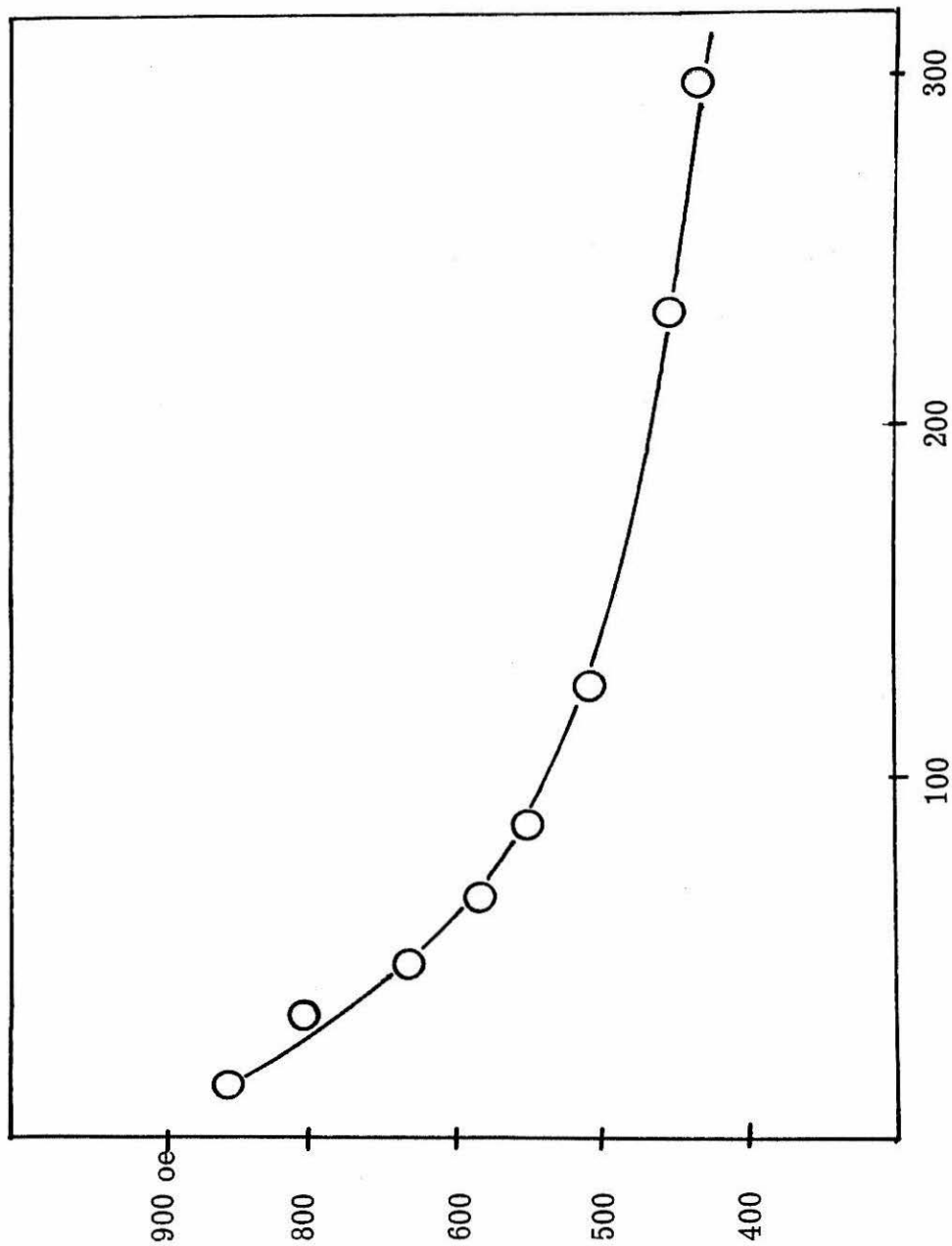


Figure 4. Temperature dependence of esr bandwidth of $\text{NaFe}(\text{CrO}_4)_2 \cdot 2\text{H}_2\text{O}$.

Table 8

G-Values and Band Widths from ESR Data for $M^I\text{Fe}(\text{CrO}_4)_2 \cdot 2\text{H}_2\text{O}$

<u>M^I</u>	<u>g-value</u>	<u>Band width (oersteds)</u>
Na	2.0245	465
K	2.035	555
NH ₄	2.017	159
Tl	1.979	1360
Cs	2.0165	240

by least-squares fitting of the data are cited in Table 9. The temperature dependence of the magnetic susceptibility and effective magnetic moment of $\text{NaFe}(\text{CrO}_4)_2 \cdot 2\text{H}_2\text{O}$ are displayed in Figures 5 and 6. In general, the magnetic behavior of the species was typical of $S = 5/2$ paramagnetic ions. Effective magnetic moments were little reduced from the spin-only value at room temperature. No field dependence could be detected in the magnetic susceptibility. Again, the data from the thallium salt were unusual.

Table 9

Fit of Magnetic Data to the Curie-Weiss Law

$\underline{M^I}$	\underline{C}	$\underline{\theta}$ $(^\circ\text{K})$	$\underline{\mu_{\text{eff}}(298^\circ\text{K})}$
Na^+	4.478	-11.84	5.87
K^+	4.468	-10.02	5.88
NH_4^+	4.200	- 6.465	5.73
Tl^+	3.789	- 0.5503	5.50
Cs^+	4.441	- 9.321	5.87

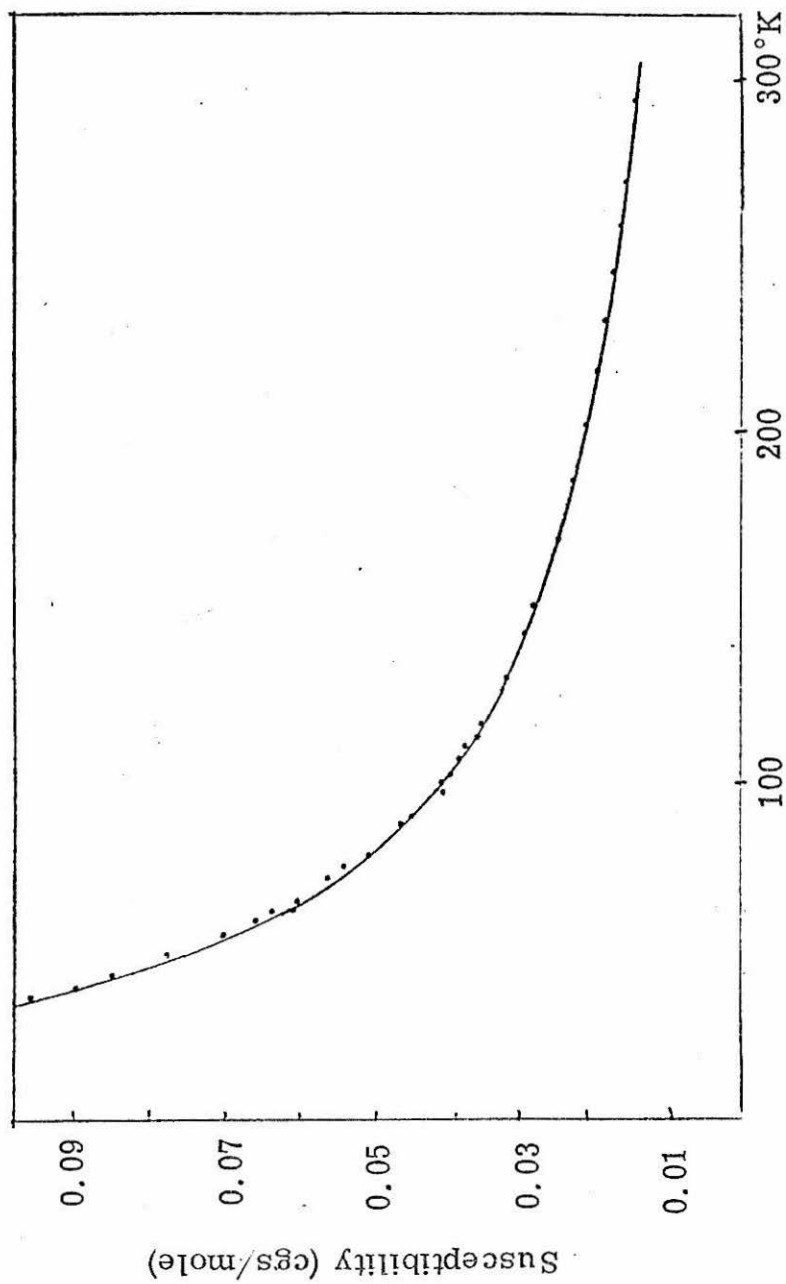


Figure 5. Fit of molar susceptibility of $\text{NaFe}(\text{CrO}_4)_2 \cdot 2\text{H}_2\text{O}$ corrected for ligand diamagnetization to the Curie-Weiss expression $\chi = 4.478/T + 11.84$. Experimental points indicated by dots. Solid line is the least-squares best estimate.

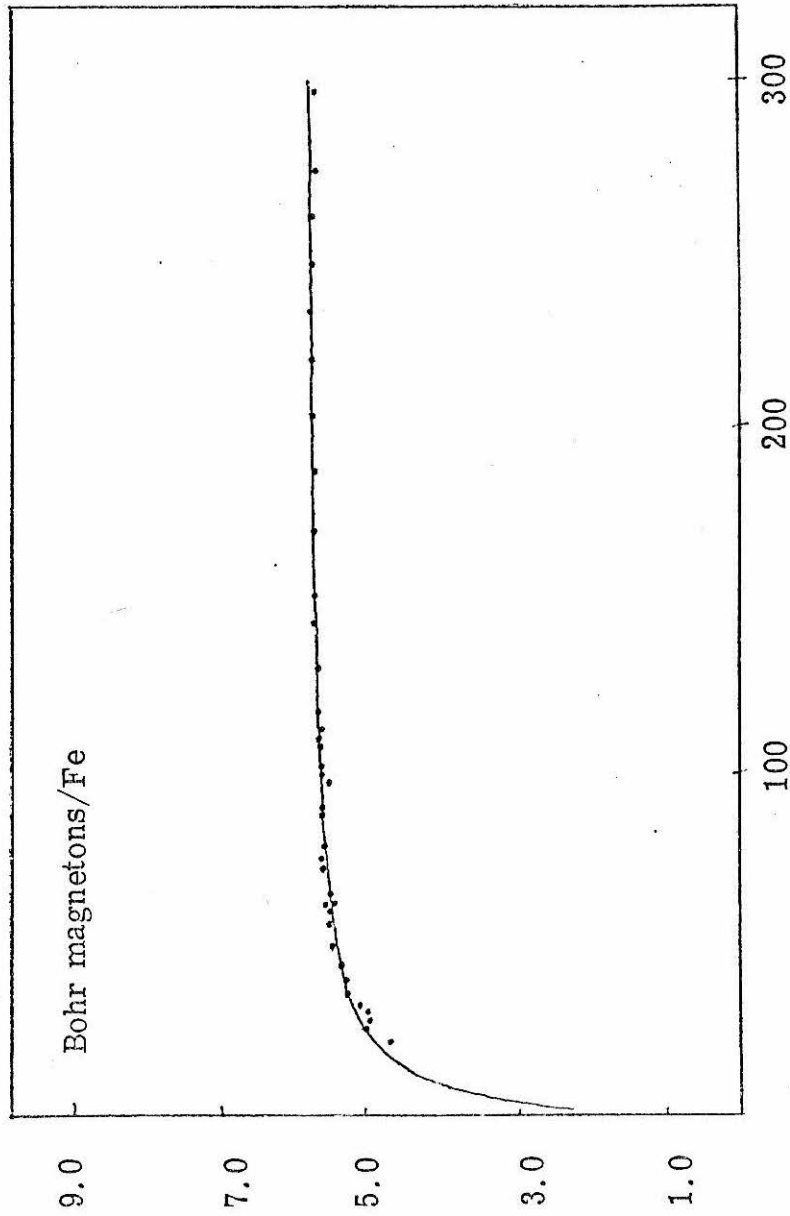


Figure 6. Temperature dependence of the effective magnetic moment ($\mu_{\text{eff}} = 2.828 \sqrt{\chi T}$) of $\text{NaFe}(\text{CrO}_4)_2 \cdot 2\text{H}_2\text{O}$. Experimental points are indicated by dots. Solid line derived from the least-squares best estimate of the Curie Weiss behavior shown in

Figure 5.

(C) Analysis of the Magnetic Data

Theoretical and experimental treatment of $S = 1/2$ paramagnetic ions coupled in linear chains has indeed been extensive. Analysis of $S = 5/2$ ions similarly located in linear chains is a more complicated problem and has not been pursued with the fervor of the $S = 1/2$ case.⁶ A method of analysis that is promising though fraught with numerous approximations draws from Fisher's analytic solution to the Heisenberg coupling in the limit of $S \rightarrow \infty$.⁷ The Hamiltonian for a linear system of $N + 1$ spins is

$$\mathcal{H} = -2J S(S+1) \sum S_i \cdot S_{i-1} - g\mu_\beta [S(S+1)]^{\frac{1}{2}} \sum_{i=0}^N H \cdot S_i$$

Fisher's solution treats spin as a classical vector. However, a solution is also possible if quantized spin is assumed. The powder susceptibility derived from this solution scaled to finite quantized spin is

$$\chi_{\text{powder}} = \frac{N g^2 S(S+1)}{3kT} \mu_\beta^2 \left[\frac{1+c}{1-c} \right] \quad \text{eqn 1}$$

$$c = \coth[2JS(S+1)/kT] - kT/[2JS(S+1)]$$

This susceptibility will adequately account for the magnetic behavior of the system, provided interchain interactions are negligible.

When they are not, but are small relative to the intrachain interactions, an empirical correction to equation 1 can be made yielding

$$\chi_{\text{powder}} = \frac{Ng^2 \mu_{\beta}^2 S(S+1)}{3K(T-\theta)} \left[\frac{1+c}{1-c} \right] \quad \text{eqn 2}$$

where c has the same meaning as before. The parameter θ represents the molecular field correction, and as such is related to the interchain interaction constant by

$$\theta = \frac{2zJ_i}{3S(S+1)k}$$

where z is the number of nearest neighbors, J_i the interchain interaction constant and k the Boltzmann constant.

Magnetic data for the compounds in question were fit to equations 1 and 2 allowing g , J/k and g , J/k , θ to be free parameters respectively. The values of the parameters so derived are cited in Tables 10 and 11. Figures 7 and 8 show the fit of the data for $\text{NaFe}(\text{CrO}_4)_2 \cdot 2\text{H}_2\text{O}$. The calculated g value, which can be independently determined, was taken as an indicator of the significance of the theoretical expression in describing the magnetic behavior of the specimen. From the parametric values in the above tables, it is apparent that only when specific account of interchain interactions are made does the theoretical expression account well for the magnetic behavior. The interactions along the chains are all antiferromagnetic. Interactions between chains are antiferromagnetic

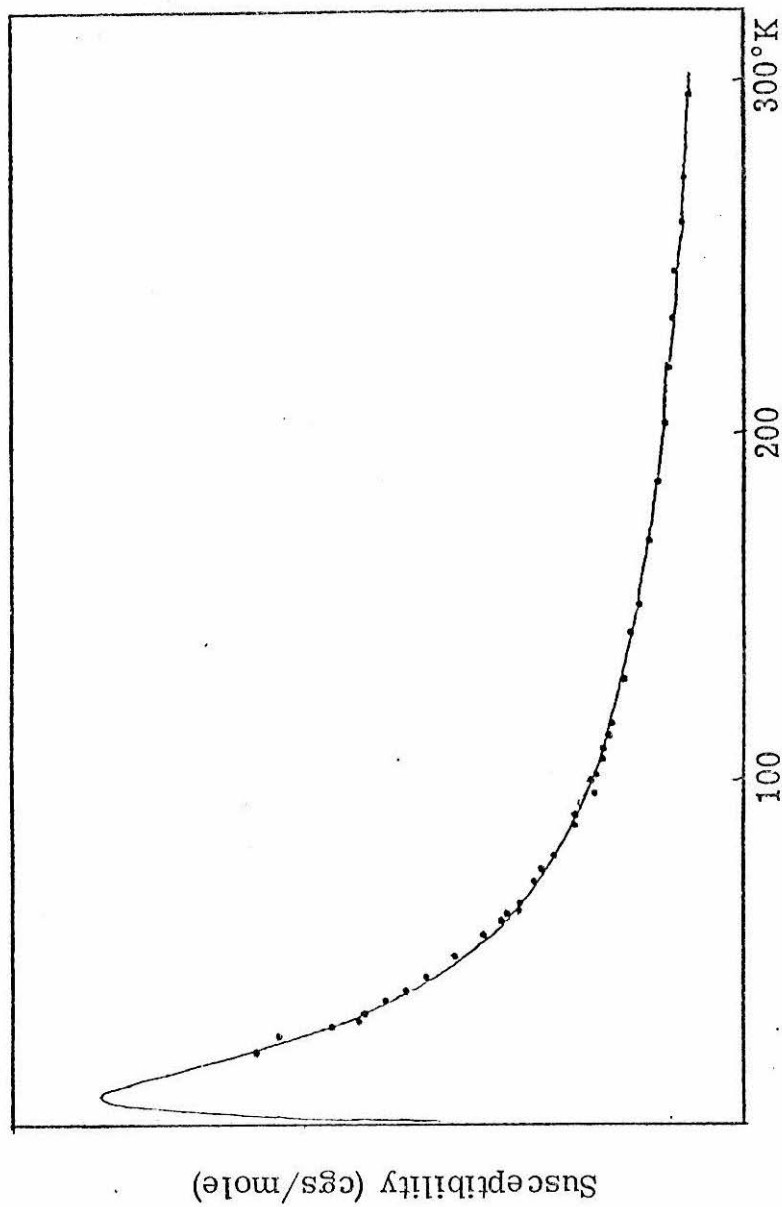


Figure 10. Fit of molar susceptibility of $\text{NaFe}(\text{CrO}_4)_2 \cdot 2\text{H}_2\text{O}$ corrected for ligand diamagnetism to equation 1. Parametric values are $g = 2.0081$

$$J/K = -0.962.$$

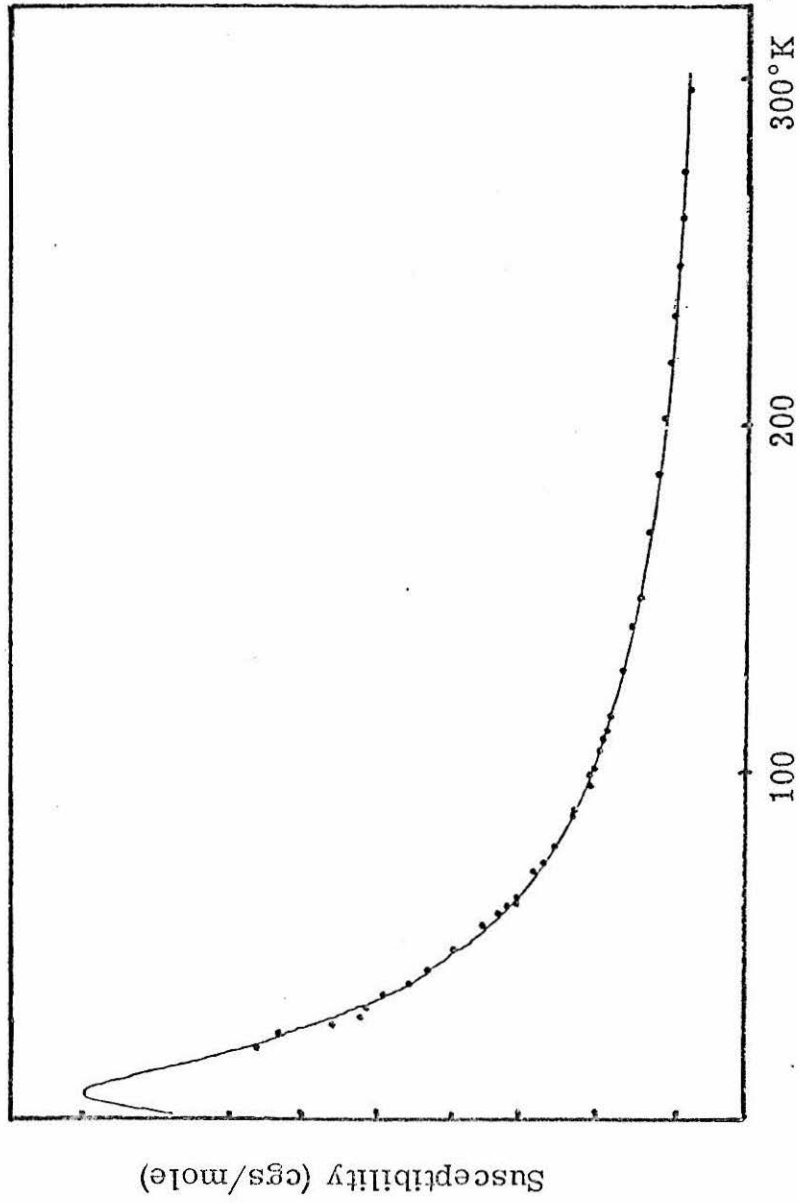


Figure 11. Fit of molar susceptibility of $\text{NaFe}(\text{CrO}_4)_2 \cdot 2\text{H}_2\text{O}$ corrected for $g = 2.0232$,

$$J/K = -0.822, \theta = -2.11.$$

Table 9

Fit of Data to Fisher's Equation without
Attending to Interchain Interactions ($\theta = 0.0$; fixed)

<u>M^I</u>	<u>g calc</u>	<u>J (cm⁻¹)</u>	<u>r(Å)</u>
Na	2.0081	-0.962	0.95
K	2.0043	-0.873	1.33
NH ₄	1.9712	-0.657	1.48
Tl	1.837	+0.523	1.40
Cs	1.985	-0.1721	1.69

Table 10

Fit of Magnetic Data to Fischer's Equation

Allowing Interchain Interactions (θ Free and Allowed to Vary)

M^I	g_{cal}	J/k	$\theta(^{\circ}K)$	J_i/k
Na	2.0232	-0.822	-2.11	-0.045
K	2.043	-0.765	-1.24	-0.026
NH ₄	2.017	-2.29	+13.57	+0.290
Tl	1.979	-2.03	+19.17	+0.410
Cs	2.016	-0.732	-0.93	-0.020

for the Na^+ , K^+ , and Cs^+ salts, but ferromagnetic and much stronger for the ammonium and thallium salts. The very weak interchain interaction in the Na^+ , K^+ , and Cs^+ salts must occur by a direct exchange pathway. The much greater intrachain interaction is therefore probably sponsored by the chromate bridges. In an ideal situation this exchange ought to be independent of cation size. The weak dependence in J on cation size among the Na^+ , K^+ , and Cs^+ salts reflects the slight dependence of the intrachain separation of magnetic ions and the consequent variations in the structure of the coordination spheres surrounding the magnetic ions.

DISCUSSION

The magnetic behavior of $\text{M}^{\text{I}}\text{Fe}(\text{CrO}_4)_2 \cdot 2\text{H}_2\text{O}$ can be described in terms of linear chains provided account is made of the significant interchain interactions. Intrachain interactions are sponsored by the chromate bridges, but are weak. Such unspectacular interactions are unlikely to give rise to the unusual magnetic behavior found in the basic iron chromates.

The interchain interactions divide the salts of $\text{M}^{\text{I}}\text{Fe}(\text{CrO}_4)_2 \cdot 2\text{H}_2\text{O}$ into two categories--(1) those that are salts of relatively hard, unpolarizable, alkali metal cations and (2) salts of the polarizable ammonium and thallium ions. In the first category interchain interactions are antiferromagnetic and decrease significantly with cation size. Intrachain interactions are far less sensitive to the cation. The magnetic behavior of salts of the second category must be influenced

by factors other than those considered in the structural discussion above. Interchain interactions are ferromagnetic, and intrachain interactions are greatly enhanced relative to those occurring in the alkali metal salts. Simple direct exchange is not likely to be the source of the interchain interactions in these species. The polarizable nature of the cations allows them to form weak bonding interactions between the chains. These bonding effects can in turn provide interchain exchange pathways. In cases of spin $1/2$ systems hydrogen bonding analogous to this behavior of the cations has been speculated to be a source of ferromagnetic coupling between magnetic entities.⁸ Involvement of the ammonium and thallium cations in some sort of exchange interactions is definitely implied by the esr band width of the compounds.

References

1. A. Bonnin, A. Hardy, and A. Lecerf, Compt. Rend., 266, 1227 (1968).
2. A. Hardy and P. Gravereau, Compt. Rend., 271, 1304 (1970).
3. A. Millier and P. Gravereau, Spectrochim. Acta, 29, 2043 (1973).
4. Corrected for Pd(Co⁵⁷) source from data by E. Fluck, Adv. Inorg. and Radiochemistry, H. J. Emelius and A. G. Sharple, eds., 6, 433 (1964).
5. Corrected for Pd(Co⁵⁷) source from data by P. R. Brady, P. P. F. Wigley, and J. F. Duncan, Rev. Pure Appl. Chem., 12, 165 (1962); and M. Takano, T. Shinjo and T. Takada, J. Phys. Soc. Japan, 30, 1049 (1971).
6. T. Smith and S. A. Friedberg, Phys. Rev., 176, 660 (1968).
7. M. E. Fisher, Am. J. Phys., 32, 343 (1964).
8. D. N. Hendrickson, private communication.

SECTION II. THE MAGNETIC BEHAVIOR OF DELTA FERRIC
OXIDE HYDROXIDE

CHAPTER 3
INTRODUCTION TO
DELTA FERRIC OXIDE HYDROXIDE

Abstract

The difficulties involved in the structural analysis of short-range ordered species are described. Conditions necessary for the analysis of structure by bulk phenomena are derived. A review of the previous work with delta ferric oxide hydroxide is presented.

(A) An Approach to the Investigation of Short-Range Ordered

Materials. Structural characterization of molecular species is the show-piece of modern chemistry. X-ray structure determination of solid phases with long-range order has become a matter of routine. Instrumental techniques are capable of elucidating structural nuances of such phases to ridiculous levels of subtlety. Structural characterization of fine-particulate matter, which possess at most short-range order is not similarly advanced. Structural investigations of this type of species are characterized by inconsistent results obtained with great difficulty. The short-range order considerably reduces the effectiveness of instrumental analysis. These inherently "integral" techniques can only produce inferences, which are inherently ambiguous, concerning an "average" structure. The fine particulate nature of these species precludes detailed X-ray crystallographic determinations. Low level impurity concentrations will

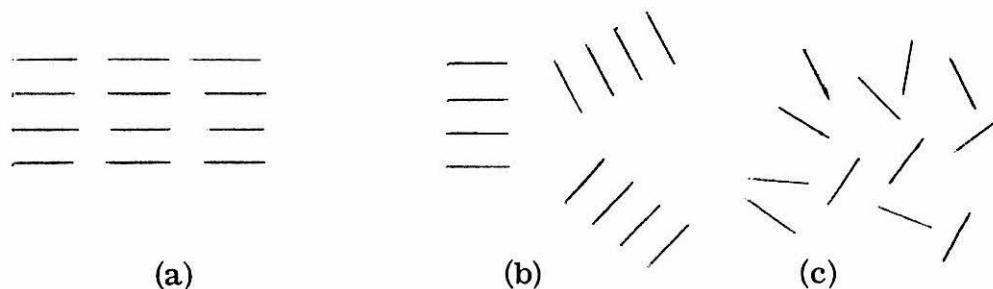


Figure 1. Schematic diagram illustrating (a) long-range order, (b) short-range order, and (c) disorder.

drastically affect the properties and stability of fine particulate-phases. An excellent example is provided by the beta ferric oxide hydroxide phase which is stabilized by as little as one part in four thousand of chloride ion.¹ Chemical techniques are often insufficient, or at least subject to sufficiently erroneous interpretation, to provide even chemical composition! For instance the stoichiometry of β -Al₂O₃ was not correctly described for 17 years after the phase was first reported.²

The structural features important in the investigation of short range order species include all those topics typically reported in structural determinations of long-range ordered species--unit cell size and composition, bonding between atomic constituents, unit cell packing, and so forth. In addition, there are also many features, neglected in well-ordered structures, which are of fundamental importance. These include:

- (a) particle size, shape, and size distribution
- (b) interparticle interactions
- (c) surface structure and composition
- (d) impurity locations and effect of impurities on structure and physical properties
- (e) intraparticle structure including pore and cavity structure.

Surface effects are particularly important in fine particulate species since the surface species represent such a large fraction of particulate composition. (A spherical particle of 100Å radius made up of 10Å cubic

unit cells would have 30% of its chemical constituents present as surface species.) Impurities often aggregate at the particle surface and can dramatically affect the behavior of the bulk species.

All of the structure features, and particularly impurity concentration, particle size, and structure disorder, are altered by minor variations in the preparative history of a given sample. Without proper attention to this phenomenon, reproducible physical and structural results are often unobtainable. A recent study of Prussian blue is illustrative.³

Metastability is yet another difficulty presented by fine particulate systems. The tendency of disordered phases to alter with time is responsible, more than any other feature of such species, for many erroneous reports.

The tremendous array of difficulties associated with the study of fine particulate matter has not made these species particularly attractive research topics. In fact, one can go so far as to say that the academic community has avoided them like lepers. The tremendous commercial importance of fine particulate matter has led to many empirical studies of specific properties of such materials. However, no general method of structural characterization has appeared.

As ought to be abundantly clear now, a single experimental technique applied to a single sample of short-range ordered fine-particulate matter is unlikely to yield conclusive or reliable structural information. The following chapters illustrate an approach far more

likely to yield structural characterizations which can be viewed with some confidence. It cannot be supposed that the structural detail routinely achieved with long-range ordered species is possible, and certainly the approach will not generally yield such a refined structural description. It will provide microscopic information not readily available from the "single experiment" results.

The procedure uses structure-sensitive bulk properties of the species in question as the primary source of data. At first glance this may seem inconsistent with the goal of obtaining a microscopic description of the phase. On reflection it is obvious that macroscopic properties are but summations of microscopic events. Deconvolution of the summation will yield microscopic structural information. Herein lies the fundamental limit to the detail the approach can provide. The microscopic events involved in the summation must occur over some physical range. Deconvolution can be carried to the dimension of this range and no further. If the macroscopic data involve the summation of subnuclear events, the structural refinement possible is very great indeed. If the microscopic events involve interactions among many unit cells within the phase the resolution will be quite low relative to the familiar results of structural determinations of long range ordered material. The latter is the case in the example below. Such low resolution may seem inconsequential to the reader involved in more refined studies. But, observe this. The most obvious choice for the macroscopic property that provides the structure-sensitive "handle"

will be that property which makes the phase of interest. The structural information provided by this property will deal with those features of the structure which most directly affect the property. The worth of the information is apparent by tautology.

The dimension constraint described above is but one of the constraints that apply to the approach. Other constraints are best seen by examining the logic of the approach.

Let P be the bulk physical property to be examined. It will be dependent on a set of structural features $\{\eta_i | i = 1(1)m\}$ and a set of intensive physical variables $\{q_j | j = 1(1)s\}$. Then P can be expressed as:

$$P = F(\{\eta_i\}; \{q_j\}) \quad \text{equation 1}$$

The goal of the approach is to describe the initially unknown set of structural features $\{\eta_i\}$ to the limit of the resolution prescribed by the dimension constraint. To do this, a constraint hereafter known as the Weak Constraint must be considered. Let the set Q consist of elements P_{kj} such that P_{kj} is the k^{th} order derivative of P with respect to the intensive variable q_j . That is,

$$Q = \{P_{kj} | P_{kj} = \frac{\partial P_k}{\partial q_j} |_{q_i \neq q_j}\} \quad k = 0, 1, 2, \dots$$

Let T be the number of nonzero elements of Q . Then the number of nonzero elements of the set $\{\eta_i\}$ that are to be uniquely described must be no greater than T

$$m \leq T$$

This is a weak constraint because most systems can be made to satisfy this requirement. The value of m can be reduced by examining data from other types of experiments. The ambiguity of the results of single experiments is greatly reduced when comparison to other data is possible. This interplay will allow some reduction in the size of the set $\{\eta_i\}$.

The structure features $\{\eta_i\}$ will manifest themselves in a set of effects $\{\epsilon_\ell; \ell = 1(1)u\}$

$$\{\epsilon_\ell\} = C\{\eta_i\} \text{ where } C = \{C_{i\ell}\} \quad \text{equation 2}$$

The elements of the set $\{\epsilon_\ell\}$ are aspects of P and equation 2 is simply a restatement of equation 1. Usually P is described experimentally in terms of the set $\{\epsilon_\ell\}$. Obeying the Weak Constraint lifts any condition for resolution on the dimensions of C . Each of the elements of $\{\epsilon_\ell\}$ will be dependent on the set of intensive variables $\{q_i\}$ and a set of parameters $\{a_{j,\ell}^v \mid v = 1(1)b\}$. Thus

$$\epsilon_\ell = g_\ell(\{q_i\}; \{a_{j,\ell}^v\})$$

Typically the structure features $\{\eta_i\}$ will be described by the sXu sets of parameters $\{a_{j,\ell}^v\}$. To completely define these parameters it is necessary that an additional constraint be satisfied.

Let the set $\{d_{j,\ell}^k\}$ be the set of k^{th} order derivatives of ϵ_ℓ with respect to the intensive variable q_j . The number of nonzero elements in this set is $D_{j,\ell}$. Let the number of nonzero elements in the set $\{a_{j,\ell}^v\}$ be $A_{j,\ell}$. For there to be a complete description of the

sets $\{a_{j,\ell}^V\}$ it is necessary that $A_{j,\ell}$ be no greater than $D_{j,\ell}$ for all j and ℓ . That is

$$A_{j,\ell} \leq D_{j,\ell} \quad j = 1(1)s, \ell = 1(1)u$$

This constraint will hereafter be known as the Strong Constraint. Quite obviously a system satisfying the Strong Constraint will also satisfy the Weak Constraint. The Strong Constraint also has ramifications in the experimental aspects of the approach. In general it requires that several samples varying in some effect ϵ_ℓ or equivalently in the structure feature $\eta_i = \sum b_{\ell i} \epsilon_\ell$ be examined in terms of P. Specifically, the Strong Constraint requires that the number of samples varying in ϵ_ℓ be at least equal to the $\sum A_{j,\ell}$.

This latter aspect of the Strong Constraint points out a second feature of the approach. As is often the case in science, the approach is ill-suited for the determination of absolutes, but serves well for the detection of differences. Clearly, analysis of data from a single sample will fail to take proper advantage of this asset of the approach. In fact, the Strong Constraint indicates that any attempt to use data from a single sample will necessarily lead to ambiguous results. Since the differences in the effects will be used to describe the structure, it is necessary that the sample set be sufficiently large to allow the evaluation of all of the differences.

The dimension, Weak, and Strong Constraints are necessary conditions for the deconvolution of the bulk physical data, but not sufficient. The success of the approach will largely be dictated by the

ability to produce sample set varying in the set of effects $\{\epsilon_{\rho}\}$. How this is to be done will be completely unknown at the outset of any investigation. Often common sense, chemical intuition, and trial and error will be the only tools available for determining the variables which can be used. Further, it will be nearly impossible to produce samples varying in just one effect or one structural feature. The use of statistics, multiple correlations, and large sample sets cannot be avoided.

The approach has generality beyond that of the example which follows this introduction. The central requirement is only that for any phase under investigation there be a structure-sensitive physical property that can be used as a "handle" for evaluating the structure. The approach is indeed laborious and not one to be undertaken lightly. But, in those cases where the need to know outweighs the need to publish, it is probably the only technique available.

B. An Introduction to Delta Ferric Oxide Hydroxide. The investigations reported in the chapters following this introduction are in the broadest sense attempts to describe the structure of the delta modification of ferric oxide hydroxide (delta basic iron oxide, $\delta\text{FeO}(\text{OH})$, or $\delta\text{Fe}_2\text{O}_3 \cdot \text{H}_2\text{O}$). This species is ferromagnetic, which is surely the only redeeming feature of an otherwise ugly, extremely fine-particulate, red-brown mass. It is one of the four ferric oxide hydroxide phases. The structural relationships among the phases are described in Table 1.

Table 1. The Phases of Ferric Oxide Hydroxide

α -FeO(OH)	goethite
diaspore structure	(Pbnm) a = 4.59 b = 9.94 c = 3.02
β -FeO(OH)	akaganeite
hollandite structure	(I4/m) a = 10.48 c = 3.06
γ -FeO(OH)	lepidocrocite
boehmite structure	(Cmcm) a = 3.87 b = 12.51 c = 3.06
δ -FeO(OH)	" δ rust"
hexagonal	a = 2.95 c = 4.53

Of the various phases, the alpha and gamma are the most familiar and appear as the common minerals goethite and lepidocrocite. Lepidocrocite is also found as freshly formed rust. The beta phase is also a mineral -akaganite. Known natural sources of this phase are in Japan,⁴ on surfaces of fallen Russian satellites,⁵ and in moon dust.⁶ The delta phase is a completely synthetic allotrope.

The previous work on the delta phase is marked by inconsistent, incomplete, and often erroneous results characteristic of studies of short-range order material. The X-ray powder diffraction pattern consists of only five broad lines. Spectroscopic data are diffuse and poorly resolved. Physical data concerning the phase often vary by powers of ten from author to author.

The original identification of the phase is generally accredited to Glemser and Gwinner.⁷ These authors reported a ferromagnetic oxide

they described as $\delta\text{Fe}_2\text{O}_3$, which resulted from the treatment of ferrous hydroxide with hydrogen peroxide in a strongly alkaline medium. The structure was described as hexagonal with $a = 5.09 \text{ \AA}$, $c = 4.41 \text{ \AA}$. However, earlier Chevalier⁸ described a ferromagnetic oxide he too felt had the stoichiometry Fe_2O_3 which was prepared in a very similar manner. Both of these phases were in all probability $\delta\text{FeO}(\text{OH})$. Recently, Conley⁹ has reported a phase of the stoichiometry $\delta\text{Fe}_2\text{O}_3 \cdot \text{H}_2\text{O}$. Okamoto¹⁰ has severely criticized this report and claimed that Conley's phase is really $\gamma\text{Fe}_2\text{O}_3$.

In 1959 Francombe and Rooksby¹¹ showed that stoichiometry of the product of the Glemser and Gwinner reaction was that of a ferric oxide hydroxide. They also corrected the description of the unit cell to hexagonal, $a = 2.95 \text{ \AA}$, $c = 4.53 \text{ \AA}$.

The problem of impurities is not negligible in dealing with $\delta\text{FeO}(\text{OH})$. As has already been mentioned it is just one of four very similar phases of ferric oxide hydroxide which, in turn, is but one of the oxide stoichiometries formed by iron(III).

If one inspects the oxide chemistry of trivalent, first-row, transition metal ions and other trivalent metal ions one can see a certain symmetry in the stability of the oxide stoichiometries (Table 2). Nearly all stable trivalent ions form sesquioxides. Hydroxide phases are far less stable. True hydroxides, rather than hydrated oxides, appear first with manganese(III). Oxide hydroxides are a somewhat intermediate phase. Their stability increases among the

Table 2

Representative Oxide Chemistry of Trivalent,
First-Row, Transition Metal Ions, and Other Trivalent Ions

Ion	Ionic Radius (Å)	Sesquioxides	Oxide Hydroxides	Hydroxides
Ti(III)	0.79	Ti ₂ O ₃	none	none
V(III)	0.74	Karelianite (α-V ₂ O ₃) V ₂ O ₃ ^a	Montroseite VO(OH)	none
Cr(III)	0.69	α-Cr ₂ O ₃	CrO(OH)	none
Mn(III)	0.67	α-Mn ₂ O ₃ βMn ₂ O ₃ γMn ₂ O ₃	αMnO(OH) βMnO(OH) γMnO(OH)	4Mn(OH) ₂ · Mn(OH) ₃
Fe(III)	0.64	Hematite (αFe ₂ O ₃) Maghemite (γFe ₂ O ₃) βFe ₂ O ₃ δFe ₂ O ₃ (?)	Goethite (αFeO(OH)) lepidocrocite (γFeO(OH)) Akaganeite (βFeO(OH)) δFeO(OH)	Fe(OH) ₃ (cubic) Fe(OH) ₃ (monoclinic)
Co(III)	0.63	Co ₂ O ₃	I-CoO(OH) II-CoO(OH) α-CoO(OH)	4Co(OH) ₂ · Co(OH) ₃
Ni(III)	0.62	Ni ₂ O ₃	αNiO(OH) βNiO(OH)	doubtful

Table 2 (Continued)

Ion	Ionic Radius (Å)	Sesquioxides	Oxide Hydroxides	Hydroxides
Al(III)	0.50		γ NiO(OH)	
		Corrundum	diaspore	gibbsite
		(α Al ₂ O ₃)	(α AlO(OH))	(α -Al(OH) ₃)
		$\gamma, \delta, \delta', f, \theta$	boehmite	bayerite
		i, K, X-Al ₂ O ₃	(γ AlO(OH))	(β -Al(OH) ₃)
			hydro- argillite	
			(γ -Al(OH) ₃)	
Sc (III) ^b	0.81	α -Sc ₂ O ₃	α ScO(OH)	
		γ -Sc ₂ O ₃	γ ScO(OH)	Sc(OH) ₃
In(III)	0.81	α -In ₂ O ₃	InO(OH)	In(OH) ₃
		β -In ₂ O ₃		Dzhalindile
		C-In ₂ O ₃		(In(OH ₃) ₃)
Ga(III)	0.62	α -Ga ₂ O ₃	GaO(OH)	Ga(OH) ₃
		β -Ga ₂ O ₃		

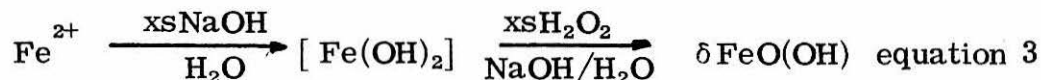
^a Low temperature form.

^b One should note that the oxide chemistry of scandium(III) is yet another demonstration of the dissimilarities between scandium and the transition metals.

transition metal ions starting with vanadium(III). The three stoichiometries and the trivalent oxidation state of the metal ion are sufficiently stable in iron(III) to foster full development of the chemistry. Further, the ionic radius of Fe(III) is such that multiple phases form within each stoichiometry.

Not only is the oxide chemistry of iron(III) rich, but the phases are closely related. Figure 2 shows common pathways often involving mild conditions, for the conversion between phases.

Delta ferric oxide hydroxide is prepared by treating a ferrous salt with excess alkali metal hydroxide solution and then oxidizing with excess hydrogen peroxide as shown in equation 3.



This particular pathway is fraught with potential side reactions which would yield undesired iron oxides. Figure 3 shows that the speed of the oxidation step will dictate the phase produced. Particularly noxious to any study of the ferromagnetic $\delta\text{FeO}(\text{OH})$ are impurities due to $\gamma\text{Fe}_2\text{O}_3$ or Fe_3O_4 which are themselves ferromagnetic. Incomplete oxidation can generally be avoided by the use of huge excesses of hydrogen peroxide. However, it was found when the excess alkali metal hydroxide concentration exceeded 11F that preparations using even tremendous excesses of peroxide at nearly boiling temperatures would often yield only magnetite. Slow oxidation can be avoided by careful use of inert atmosphere techniques in the preparation and

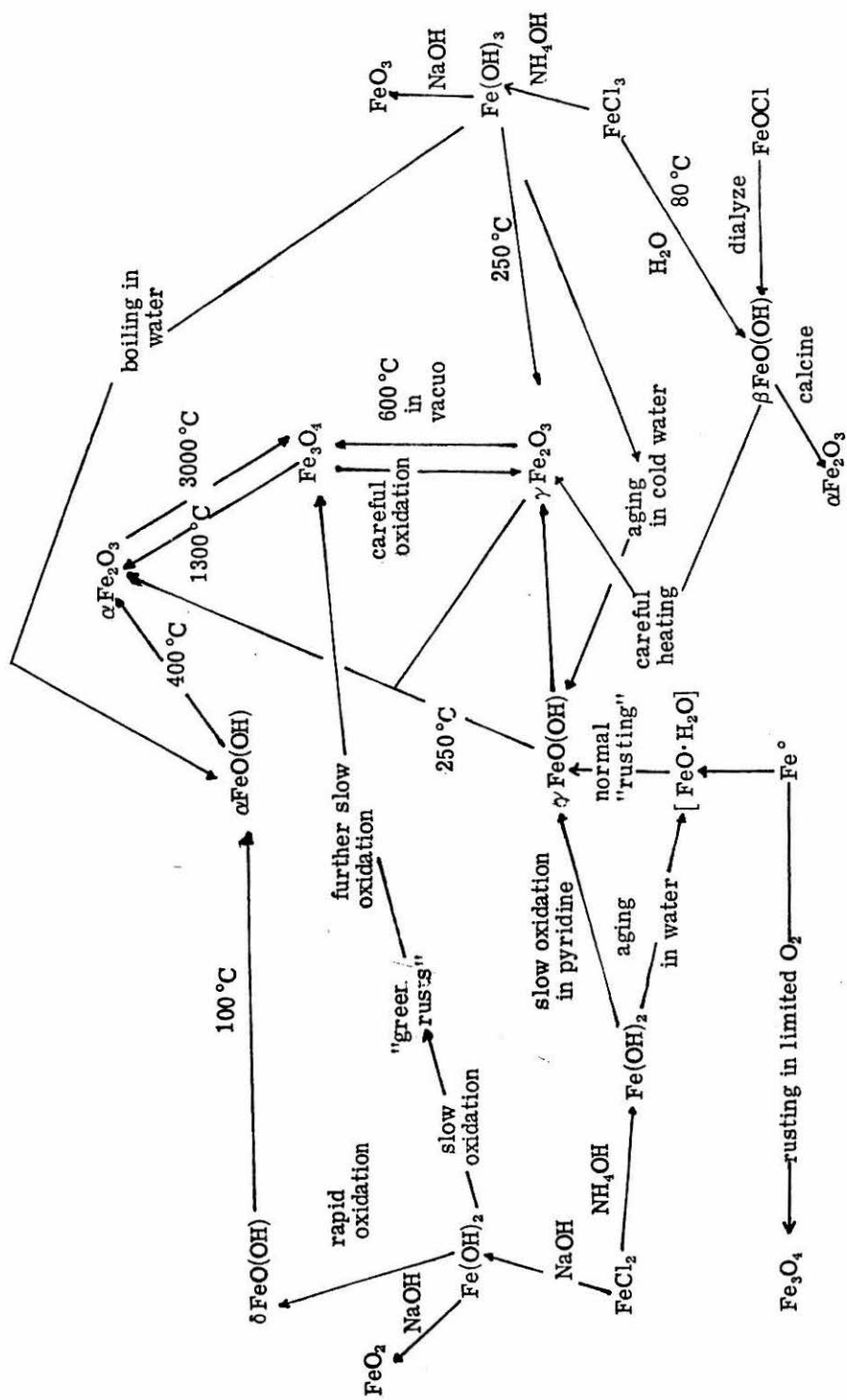


Figure 2. Common pathways for the preparation of various iron oxide phases.

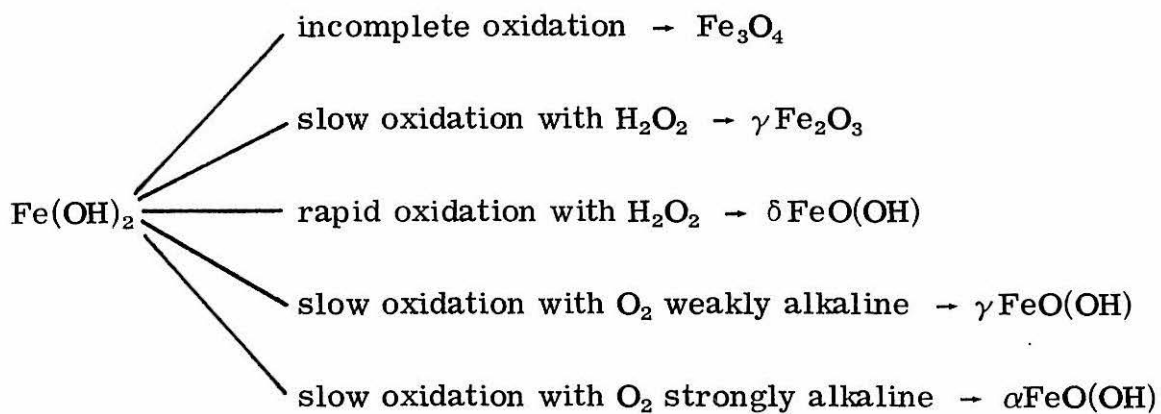


Figure 3. Competing reactions in the oxidation of ferrous hydroxide.

handling of the intermediate ferrous hydroxide.

Francombe and Rooksby called attention to the similarity of the structure of $\delta\text{FeO}(\text{OH})$ to that of $\alpha\text{FeO}(\text{OH})$ and $\text{Fe}(\text{OH})_2$. These authors formulated a model of the structure as ferric ions equally distributed between the oxide and hydroxide sheets of the hexagonal-close-pack oxygen lattice. Twenty percent of the ferric ions were located in tetrahedral sites and eighty percent in octahedral sites. They rationalized the easy transformation of the delta phase into the alpha phase as relocation of the tetrahedral ferric ions into octahedral sites. The Francombe and Rooksby model has been widely adopted and hereafter will be referred to as the "80/20 model". Bernal *et al.*¹² confirmed much of the experimental work of Francombe and Rooksby. They showed that the transformation of the delta to the alpha phase was accompanied by a smooth variation in the cell parameters. They also described the formation of the delta phase in terms of a topotactic transformation of ferrous hydroxide.

The structures of ferrous hydroxide and $\alpha\text{FeO}(\text{OH})$ are shown in Figure 4. X-ray powder diffraction data for these phases and $\delta\text{FeO}(\text{OH})$ are listed in Table 3.

The similarities among the phases of ferric oxide hydroxide can also be seen in their infrared spectra (Figure 5). Those portions of the infrared spectra which can be assigned to the vibrations of protonated groups are the best resolved features of the spectra. They are also the portions most sensitive to structure variations. It is well known that the OH stretching vibration can be related to hydrogen bond lengths.¹³

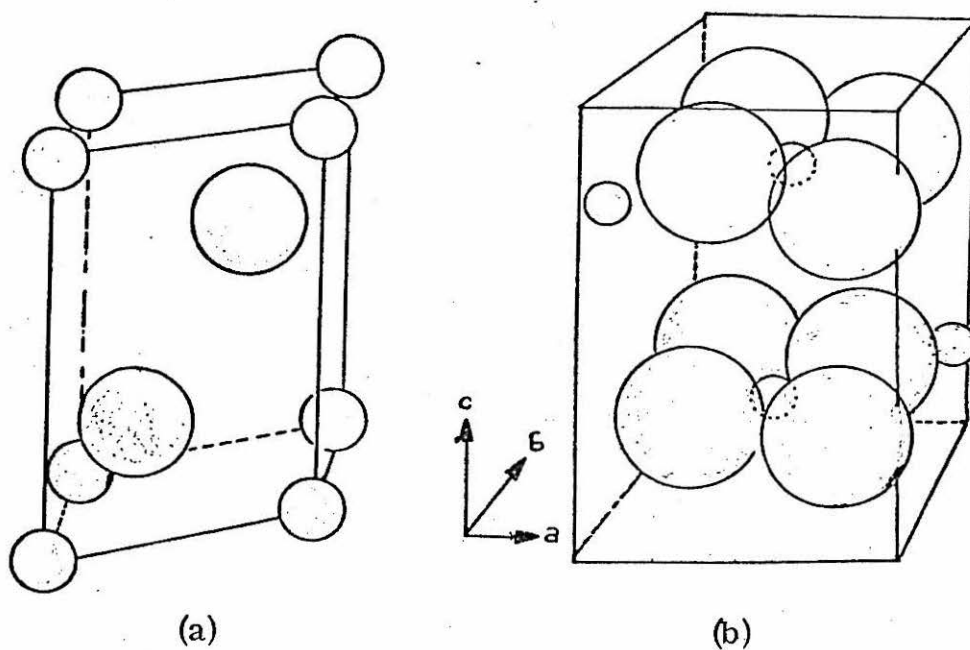


Figure 4. Oxygen (large circles) and iron (small circles) positions in (a) $\text{Fe}(\text{OH})_2$ (D_{3d}^3 , C_{3m} ; hexagonal $a = 3.26$, $c = 4.605$, $z = 1$) and (b) $\alpha\text{-FeO}(\text{OH})$ (D_{2h}^{16} , P_{bnm} ; orthorhombic, $a = 4.64$, $b = 10.0$, $c = 3.03$, $z = 4$). In (b) the "c" axis has been exaggerated and the "b" axis diminished for clarity.

Table 3. X-ray Powder Diffraction d Spacings

$\alpha\text{FeO(OH)}$			$\delta\text{FeO(OH)}$			Fe(OH)_2 (ref. 2)		
index	d	intensity	index	d	intensity	index	d	intensity
020	4.99	10						
110	4.18	100	001	4.20	3(broad)	001	4.60	vs
120	3.38	10						
130	2.69	30				100	2.82	s
021	2.58	8	100	2.54	10			
111	2.45	25				101	2.40	vs
140	2.25	20	101	2.22	5(broad)			
221	1.72	20	102	1.70	5(broad)	102	1.78	s
151,160	1.56	15				110	1.63	s
250,002	1.50	10				111,003	1.54	m
061	1.45	10	110	1.48	2	200	1.41	vw
						103,201	1.35	m

Hartert and Glemser¹⁴ have shown that the OH deformation frequency can be related to the effective OH radius. From these relations a metal oxygen bond distance can be derived. The results of such calculations for the phases of ferric oxide hydroxide are shown in Table 4. From this table one can see that a certain similarity exists between the delta and alpha phase. The delta phase, however, has longer hydrogen bond distances and less interaction among the unit cells.

The thermal behavior of $\delta\text{FeO(OH)}$ has been a source of an amazing amount of confusion. It is now fairly well established that the

Figure 5. Infrared spectra of (a) α -FeO(OH), (b) β -FeO(OH), (c) γ -FeO(OH), and (d) δ -FeO(OH). Samples were prepared in TlBr discs.

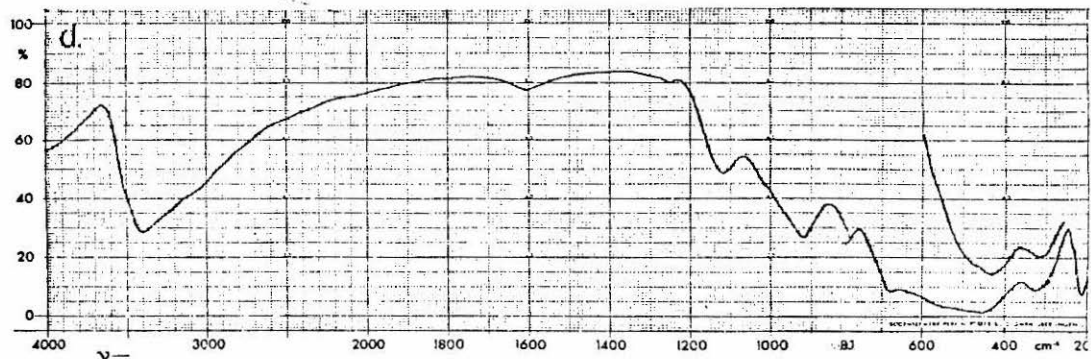
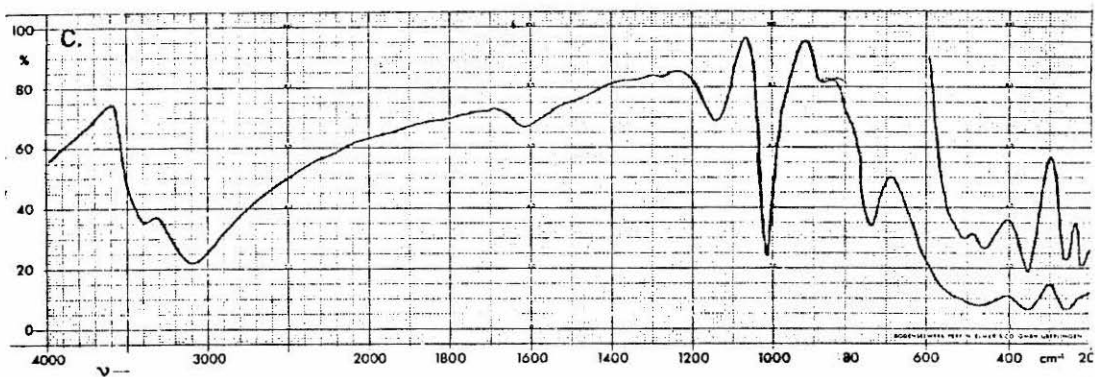
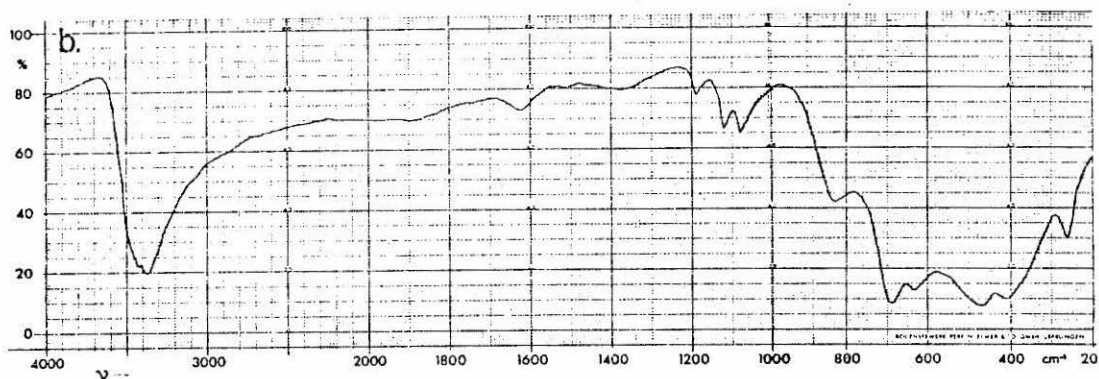
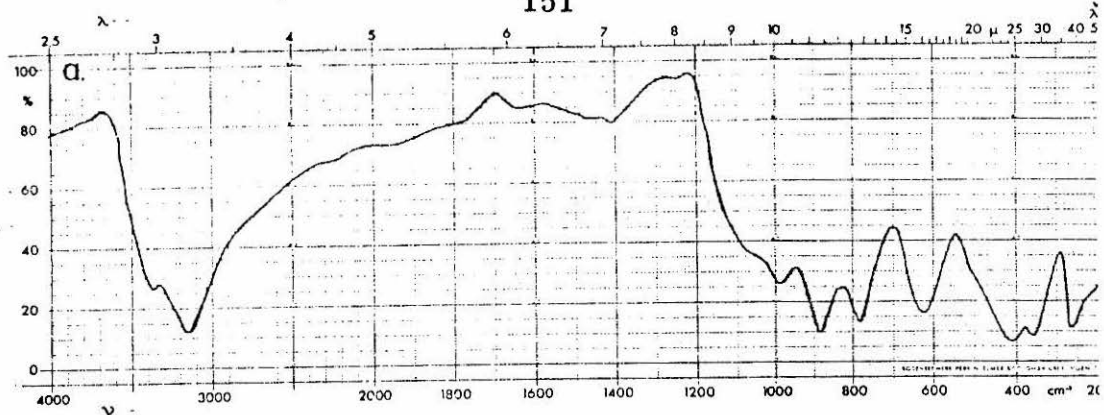


Table 4

Hydrogen Bond Lengths and Metal-Oxygen Bond Lengths
in Allotrope of FeO(OH) Calculated from their Infrared Spectra

Phase	Hydrogen	Bond Length	Metal-Oxygen	Bond Length
	Calculated ^a	Literature	Calculated ^b	Literature
	(Å)	(Å)	(Å)	(Å)
α FeO(OH)	2.75 ± 0.03	2.72^c	$2.08, 2.16 \pm 0.05$	$2.06, 2.13^c$
β FeO(OH)	2.92 ± 0.03	--	1.72 ± 0.05	--
γ FeO(OH)	2.74 ± 0.03	2.74^d	$1.97, 1.88 \pm 0.05$	$2.02, 2.05^d$
δ FeO(OH)	2.85 ± 0.03	--	$1.90-1.99 \pm 0.05$	--

^a Following ref. 13.

^b Following ref. 14.

^c From refs. 29 and 30.

^d From ref. 31.

phase transforms into $\alpha\text{FeO}(\text{OH})$ and subsequently into $\alpha\text{Fe}_2\text{O}_3$.^{7,8} The temperatures at which these transformations occur have been variously reported, and seem to depend critically on the preparative history of a given sample. A listing of the temperatures at which conversion of the delta phase into the alpha phase occurs as reported by several authors is displayed in Table 5. This table illustrates the inconsistent data that will often be drawn from poorly ordered materials. A differential thermogram of a well crystallized sample and a poorly crystallized sample of $\delta\text{FeO}(\text{OH})$ is shown and assigned in Figure 6. The thermograms differ in the temperature at which transformation is initiated and the sharpness of the transformation. Throughout the work reported in succeeding chapters of this thesis, no sample of $\delta\text{FeO}(\text{OH})$ was found to survive prolonged heating above 80°C . One must conclude that many of the temperatures listed in Table 4 are simply wrong. Unwarranted faith in the stability of the delta phase has led to a number of erroneous reports concerning its magnetic behavior.

The magnetic properties have also been variously reported. Most authors recognized that the intensity of magnetization varied from sample to sample. Many recognized that this dependence was due to variations in the preparations of the samples. Chevalier⁸ reported magnetic moments in the range of 0.6 to ~ 7.0 emu/gm. Bernal *et al.*¹² reported only that the moment was as high as 19 emu/gm. Creer¹⁵ noted that the moment varied between ~ 0 and 21 emu/gm. Mackay¹⁶ found that the magnetic behavior was sample preparation

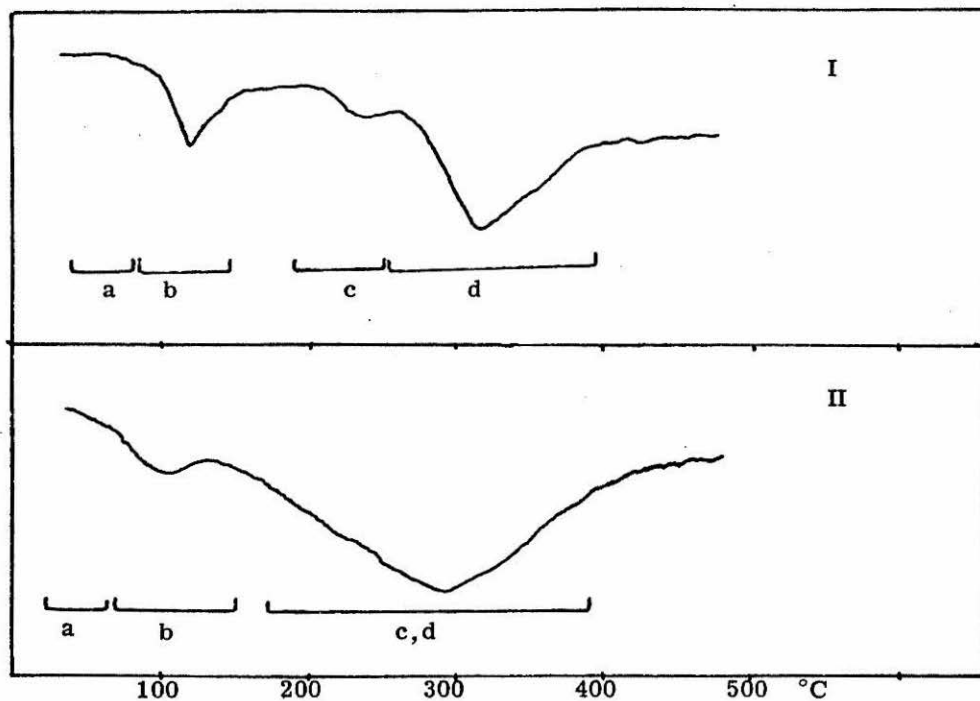


Figure 6. Differential thermograms of well-crystallized (I) and poorly crystallized (II) $\delta\text{FeO}(\text{OH})$. Brackets enclose separate regions of thermal alteration.

"a" loss of adsorbed water; "b" conversion to amorphous $\alpha\text{-FeO}(\text{OH})$. Some hematite is also formed especially with poorly crystalline species; "c" sintering of $\alpha\text{-FeO}(\text{OH})$. This alteration is less visible in poorly crystalline species because of the early onset of hematite formation; "d" conversion of $\alpha\text{FeO}(\text{OH})$ to hematite.

Table 5

Reported Temperatures of the δ FeO(OH) to
 α FeO(OH) Phase Transformation

<u>Temperature ($^{\circ}$C)</u>	<u>Reference</u>
150-200	7
~ 100	8
~ 80	11
96-120	12
variable 40 to 80	18
150-200	15
145-177	19
265	17
195	2
~ 96	16

dependent and ran as high as 10 emu/gm. Sara¹⁷ found that the moment increased with the alkalinity of the medium in which oxidation of the ferrous hydroxide occurred. He reported a maximum moment of ~ 73 emu/gm. Some of Sara's measurements may have been done on Fe₃O₄ (see below). Most authors do not report any hysteresis losses, and δ FeO(OH) has been acknowledged, until recently, to be devoid of such losses.^{15,16} Simpson¹⁸ examined a series of samples of δ FeO(OH) and found them superparamagnetic. Hysteresis did not appear above blocking temperatures of about 230°K. Moments for these samples were between 6 and 24 emu/gm. Earlier, authors

have noted anisotropy^{11, 12} in the behavior of $\delta\text{FeO}(\text{OH})$ which ought to have given rise to hysteresis. However, many previous authors have either ignored the hysteresis properties or simply cited low hysteresis losses. Okamoto¹⁹ reported samples with moments between 10 and 38 emu/gm which had coercive fields of up to 200 gauss at room temperature. Recently a patent has been issued for the preparation of $\delta\text{FeO}(\text{OH})$ with a moment of 25 emu/gm at saturation and a coercive field of ~ 500 gauss.²⁰

In a series of three reports, Okamoto²¹⁻²³ discussed a black iron oxide he identified as $\delta\text{FeO}(\text{OH})$. The black color is very difficult to rationalize. Many attempts were made by this author to repeat Okamoto's preparation. Each resulted in the formation of Lafort's magnetite, badly contaminated with hematite. Much of the data Okamoto reported is consistent with this product.

Rossiter and Hodgson²⁴ found that Mossbauer data could be collected from $\delta\text{FeO}(\text{OH})$ only when the sample was cooled to liquid nitrogen temperatures. Their data for the various phases of ferric oxide hydroxide are shown in Table 6.

Rossiter and Hodgson cited the "80/20 model," proposed by Francombe and Rooksby, as the structure of $\delta\text{FeO}(\text{OH})$. However, they were able to resolve only a single six-line spectrum typical of magnetically coupled ferric ions in octahedral sites. In fact, not one scrap of evidence to confirm the "80/20 model" has yet appeared. The model is exactly that--a model developed from the limited X-ray

Table 6
Mossbauer Data for the Phases of
Ferric Oxide Hydroxide

		Isomer Shift		Internal Field
		(mm/sec)	Splitting(mm/sec)	(Koe)
α FeO(OH)	295 °K	0.53	0 ± 0.1	364 ± 37
	77 °K	0.78		515 ± 43
β FeO(OH)	295 °K	0.43	0.62 ± 0.06	0
	77 °K	--	--	466 ± 49
γ FeO(OH)	295 °K	0.48	0.54 ± 0.06	0
	77 °K	0.62	0.62 ± 0.06	0
δ FeO(OH)	77 °K	0.45	0 ± 0.1	533 ± 51

The internal field of δ FeO(OH) is completely consistent with the empirical value for high spin Fe(III), $H_{\text{internal}} = 220 \langle S_z \rangle = 550$ Koe.²⁵ The similarities of the spectrum of δ FeO(OH) to that of α FeO(OH) are obvious.

data available on δ FeO(OH) and tutored by some prejudice. The prejudice for locating iron ions in tetrahedral sites seems totally based on the existence of such tetrahedral iron ions in other ferromagnetic iron oxides such as γ Fe₂O₃ and Fe₃O₄. Ions in tetrahedral sites are, of course, not all required for the development of ferromagnetism. Recently, Okamoto¹⁹ has proposed an alternative model for the structure of δ FeO(OH) with all ferric ions located in octahedral sites. A schematic comparison of the 80/20 model and Okamoto's new model is shown in Figure 7. Quantitative aspects of both models are in some disagreement with infrared results. X-ray diffraction must be expected to be a poor basis for structural modelling of δ FeO(OH). Not only is the X-ray data from the phase of poor quality but it is so limited that the scattering effects of the phase fail to satisfy the Strong Constraint mentioned above. Any model formed from the prediction of X-ray scattering by δ FeO(OH) will be ambiguous in some of its structural features. A much stronger criterion for a model to fulfill is the prediction of the magnetic behavior of the phase.

Both the 80/20 model and Okamoto's new model of the δ FeO(OH) structure require hexagonal-close-packing of the oxygen lattice. The stronger criterion of prediction of magnetic behavior runs immediately counter to this requirement. Gisolf²⁶ has shown that iron oxides with magnetic ions located in hexagonal-close-pack non-magnetic arrays will not develop ferromagnetism. Obviously, a packing arrangement of the oxide lattice much looser than hexagonal-

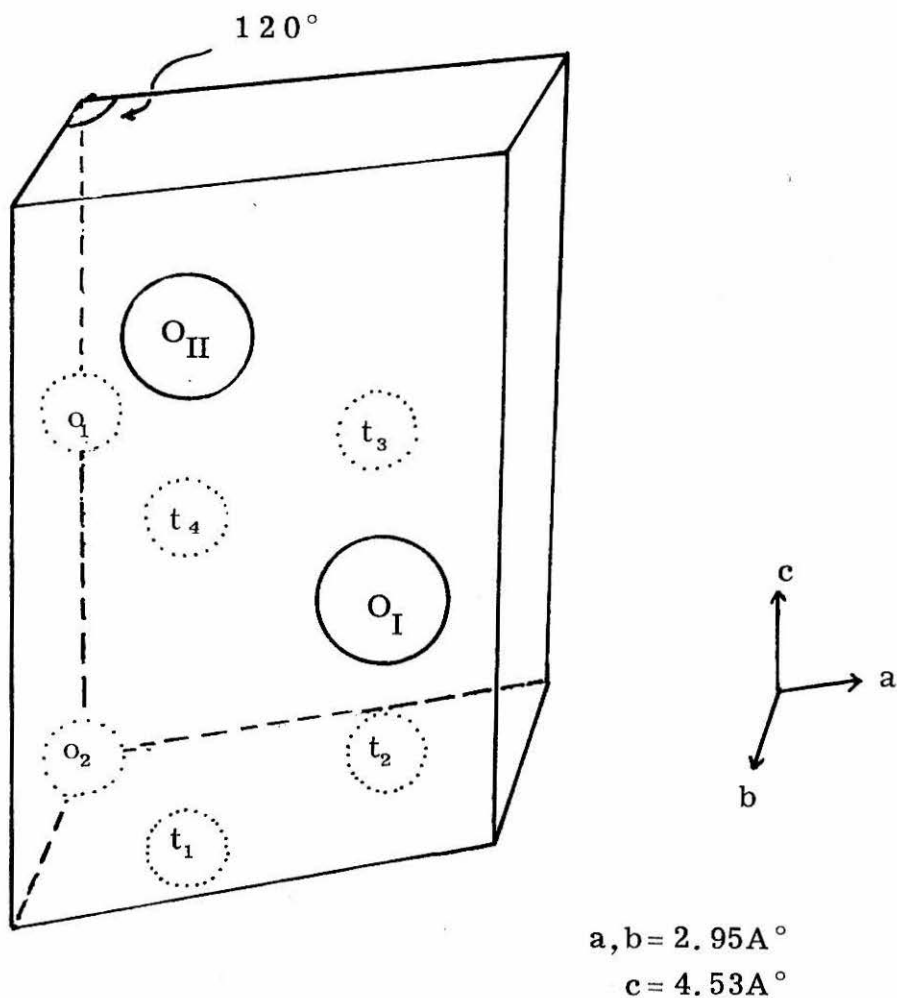


Figure 7. Proposed unit cell of $\delta\text{FeO}(\text{OH})$ oxygen ions, O_I and O_{II} , located at $(1/3, 2/3, 1/4)$ and $(2/3, 1/3, 3/4)$ respectively. Francombe and Rooksby¹¹ locate 80% of the ferric ions randomly in octahedral sites O_1 and O_2 at $(001/2)$ and (000) respectively. The remaining ferric ions are randomly distributed in the tetrahedral sites T_1, T_2, T_3, T_4 at $(2/3, 1/3, 0)$, $(1/2, 2/3, 0)$, $(1/3, 2/3, 1/2)$ and $(2/3, 1/3, 1/2)$ respectively. Okamoto's model¹⁹ locates all ferric ions randomly distributed in the octahedral sites.

close-pack exists in $\delta\text{FeO}(\text{OH})$, and the structure of the phase must be far more complex than the two models derived from X-ray results suggest. Certainly a structure as simple as that in figure 7 would fail to predict the observed magnetic behavior.

The inconsistent and sample-dependent physical properties of $\delta\text{FeO}(\text{OH})$ initially sparked the investigations reported in the chapters following this introduction. The magnetic properties were of especial interest. Magnetic properties do satisfy the Strong Constraint mentioned earlier, and can be expected to yield insights concerning the structure of $\delta\text{FeO}(\text{OH})$ to limits of the dimension constraint. Structure, interpreted in the broad sense to include particle morphology, spin arrangement, and the like, would be expected to affect these magnetic properties:

- (1) saturation magnetization
- (2) anisotropy
- (3) coercive field
- (4) remanent magnetization
- (5) initial susceptibility

Besides structure, these properties will be affected by:

- (1) chemical composition
- (2) impurities
- (3) strain
- (4) particle orientation and packing
- (5) particle size and size distribution

Intensive variables to which magnetic properties are most sensitive are:

- (1) temperature
- (2) applied magnetic field
- (3) pressure

References

1. C. Epperson, A. Gremillion, and J. Fergeson, Inorg. Chem., 4, 1495 (1965).
2. R. R. Ridgway, A. A. Klein, Wm. J. O'Leavy, Trans. Electrochem. Soc., 70, 71 (1936).
3. R. E. Wilde, S. N. Ghosh, and B. J. Marshall, Inorg. Chem., 9, 2512 (1970).
4. M. Nambu, Ganseki Kobutsu Kosho Gakkaishi, 59, 143 (1968).
5. U. B. Marvin, J. Geophys. Res., 68, 5059 (1963).
6. G. Rossman, private communication of results by Peter Bell and David Hk. Mao.
7. O. Glemser and E. Gwinner, Z. anorg. Chem., 163, 240 (1939); Naturwissenschaften, 26, 739 (1939).
8. R. Chevalier, Compt. Rendus, 184, 674 (1927).
9. R. F. Conley, J. Amer. Ceram. Soc., 60, 124 (1967).
10. S. Okamoto, J. Amer. Ceram. Soc., 51, 54 (1968).
11. M. H. Francombe and H. P. Rooksby, Clay Minerals Bulletin, 4, 1 (1959).
12. J. D. Bernal, D. R. Dasgupta, and A. L. Mackay, Clay Minerals Bulletin, 4, 15 (1959).
13. K. Nakamoto, M. Margoshes, and R. E. Rundle, J. Amer. Chem. Soc., 77, 6480 (1955).
14. E. Hartert and O. Glemser, Zeitschrift Electrochemie, 7, 746 (1956).

15. K. M. Creer, J. Geomag. Geoelect., 13, 86 (1962).
16. A. L. Mackay, Croat. Chemica Acta, 31, 67 (1959); CA:54:116302.
17. J. Sara, Chem. Listy, 63, 112 (1969); CA:70:92805n.
18. A. W. Simpson, J. Applied Phys., 33, 1203S (1962).
19. S. Okamoto, J. Amer. Ceram. Soc., 51, 594 (1968).
20. S. Okamoto, Japanese Patent 69, 09730; CA:71:P65496b.
21. S. Okamoto, Kogyo Kagaku Zasshi, 67, 1845 (1964); CA:62:8635d.
22. S. Okamoto, Kogyo Kagaku Zasshi, 67, 1850 (1964); CA:62:8635e.
23. S. Okamoto, Kogyo Kagaku Zasshi, 67, 1855 (1964); CA:62:8636d.
24. M. J. Rossiter and A. E. M. Hodgson, J. Inorg. Nucl. Chem., 27, 63 (1965).
25. G. K. Wertheim and J. P. Remeika, Phys. Letters, 10, 14 (1964).
26. J. Gisolf, Physica, 25, 677 (1949).
27. D. S. Kulgawczuk, A. Obuszko, and A. Szytula, Phys. Status Solid, 26, K83 (1968).
28. G. V. Loseva and N. V. Murashko, Izv. Akad. Nauk. SSR Neorg. Mater., 7, 1467 (1961); CA:75:133922x.
29. W. Hoppe, Z. Kristallographia, 103, 73 (1940).
30. L. S. D. Glasser and L. Ingam, Acta Cryst., B24, 1233 (1968).
31. R. W. G. Wyckoff, "Crystal Structure," Vol. 1, 2nd ed., Interscience, New York, 1963.

CHAPTER 4

MAGNETIC BEHAVIOR OF $\delta\text{FeO}(\text{OH})$

Abstract: It is shown that $\delta\text{FeO}(\text{OH})$ may be described as a fine particulate ferrimagnet. Hysteresis properties are ascribed to uniaxial magnetocrystalline anisotropy. The variations in magnetic behavior with particle size are described. It is proposed that these variations can be attributed to a magnetically dead region surrounding each particle.

This chapter presents a physical description of δ FeO(OH), traces the alterations of this description with the preparative history of individual samples of the phase, and describes the impact of these alterations on the magnetic behavior of the samples. The previous chapter dwelt at some length on the wide range of reported magnetic behavior of delta ferric oxide hydroxide. It will be readily apparent that the source of the discrepancies lies in the variations in the preparative procedures used by earlier authors.

Experimental

(A) Preparation. The oxidation of ferrous hydroxide precipitated from ferrous sulfate described in the previous chapter was used to prepare the samples of δ FeO(OH). All operations were done under an atmosphere of high purity nitrogen or argon scrubbed free of residual oxygen by bubbling through columns of acidic chromous chloride solution, and using standard inert-atmosphere techniques.

Stock ferrous solutions were prepared by allowing a solution of 0.187F FeSO₄·7H₂O (Allied) in deoxygenated water stand for one week over clean iron wire (99.999% Fe). The stock solutions were ferric-iron-free when tested with potassium ferrocyanide solution.

Ferrous hydroxide was precipitated from strongly alkaline media prepared as follows. A charge of the appropriate amount of

NaOH and NaCl was dissolved in the minimum amount of water. This solution was filtered to remove any sodium carbonate. The solution was then diluted to the chosen concentration and boiled under an inert atmosphere in the reaction vessel. This vessel was a round-bottom triple-neck flask equipped with a mechanical or magnetic stirrer, a thermometer, and a side-arm port sealed with a rubber septum, as well as a capillary to admit inert gas. Solution concentrations were 1 to 10F NaOH and 0 to 9F NaCl. Solution volumes of 400, 800, 1200, and 1500 ml were used. The reaction vessel and its contents were then thermostated at temperatures in the range of $0 \pm 1^\circ$ to $95 \pm 3^\circ\text{C}$ in a 40 liter water bath. Final Cl^- and OH^- concentrations were determined by silver chloride precipitation and titration with 1.002N HCl to a phenolphthalein end-point, respectively.

Twenty-two ml of ferrous stock solution was syringed into the precipitation medium with rapid stirring. The voluminous precipitate was snow-white in color. The procedure was discontinued if any discoloration indicative of partial oxidation was observed. The precipitate was aged for times varying from a few seconds to several hours. Thirty-five ml of fresh 30% hydrogen peroxide (Mallinkrodt) was then syringed into the slurry with vigorous stirring, and the side-arm port removed from the reaction vessel.

Caution: $\delta\text{FeO}(\text{OH})$ is a very efficient catalyst for the decomposition of hydrogen peroxide. The decomposition is at least

10,000 times as rapid over $\delta\text{FeO}(\text{OH})$ as it is over other iron oxide phases. The oxidation of ferrous hydroxide is sometimes accompanied by violent frothing and spewing of the caustic oxidation medium. Protective clothing and shields should be used during this operation.

Eighty to one-hundred-fold excesses of hydrogen peroxide were used in the oxidation. Twenty-five fold excesses yielded poorly crystalline samples as noted previously.¹ Ten-fold excesses produce Lafort's magnetite² badly contaminated with other oxides of iron.

When the formal concentration of hydroxide exceeds 11F, only Lafort's magnetite can be prepared by the above procedure (Figure 1). It has long been known that intensely alkaline media interfere with the oxidation of ferrous ion.² When the formal concentration of hydroxide is less than 1F, poorly crystalline, often contaminated, $\delta\text{FeO}(\text{OH})$ is produced (Figure 2). This may be the result of the solubility of ferrous hydroxide in such media.

The slurry of product in caustic solution was repeatedly washed by decantation with large volumes of distilled water until uncontrollable peptidization occurred. Centrifugation was usually necessary to concentrate the final product. Dilute ammonia solution did not prove particularly useful for controlling peptidization. Some acceleration of the washing process occurred when dilute acetic acid was added to later washes. This was not done for the samples used in this study for fear of injury to the final product. The product was collected by freeze drying.



Figure 1. Lafort's magnetite prepared by incomplete oxidation of ferrous sulfate in strongly alkaline media. Magnification = 121360 \times .

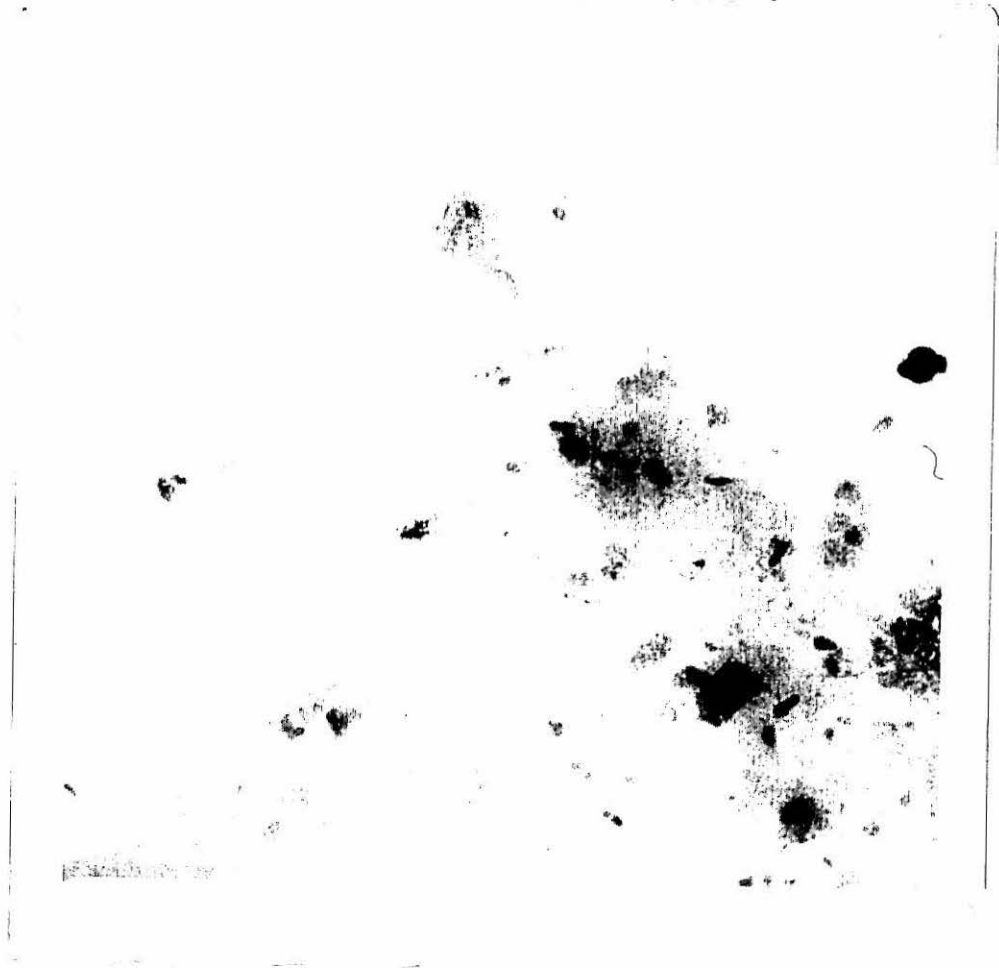


Figure 2. Contaminated $\delta\text{FeO}(\text{OH})$ prepared when a hydroxide concentration of precipitation medium is $< 0.8F$.
Magnification = $190240\times$.

The samples were reddish-brown, though the exact hue varied from sample to sample. Products of smallest particle size were quite dark and badly agglomerated. Care was taken to avoid subjecting the samples to temperatures greater than 30°C.

(B) Analysis and Characterization. Analytic and preparative details of the samples used in this study are presented in Tables 1, 2, 3, and 4. Water analyses were done by heating about 20 mg of sample to constant weight in a DuPont model 950 thermogravimetric attachment to a DuPont model 900 differential thermal analyzer. Trace sodium analyses were by atomic adsorption or sodium bismuthate gravimetric analysis. Iron analyses were by chromate titration³ or commercial EDTA titration.⁴ Tests for chloride or sulfate ions with silver nitrate or barium chloride, respectively, were negative. No siliceous material nor material insoluble in 3N HCl solution was detected.

Samples were authenticated by their X-ray powder diffraction patterns. Samples were mounted in 0.2 mm Glaskapilliern tubes and subjected to rotation and reciprocation during irradiation by an iron-filtered cobalt $K\alpha$ source. Data were collected on film mounted in the Stramannis arrangement in a Debye-Scherrer camera. D-spacings of the five observed reflections were in agreement with previous reports.^{1,5} No variations in the d-spacings were observed in the patterns of the various samples. Considerable variation in line-breadth especially in the (101) and (102) reflections was noted. No lines due to other oxides of iron were detected.

Electron micrographs of the samples were taken with a Phillips model 300 electron microscope. Samples were dispersed on 300 mesh Parlodion coated grids. Maximum resolution was about 25 Å. The Feret's statistical diameter⁶ of at least 100 particles were measured from photographic data. These measurements were fitted to normal and log-normal distributions by plotting cumulative percent number density versus diameter or log-diameter, respectively. Geometric-mean-particle size (GMPS) and geometric standard deviation (σ_g) were obtained by common procedures from these plots.⁶

Volumetric-mean-particle-size (VMPS) has far more significance to the phenomena discussed in this chapter than does the geometric parameter. VMPS can be readily calculated from the electron micrographic data by the formula:

$$\log \left(\frac{\text{GMPS}}{\text{VMPS}} \right) = -6.908 \log^2 \sigma_g$$

Magnetic data were collected with instruments and techniques described in Chapter 1. The magnetometer was calibrated with $\text{HgCo}(\text{SCN})_4$. This calibration was checked against an annealed nickel cylinder and a sample of $\text{Ni}(\text{en})_3\text{S}_2\text{O}_3$. All measurements were taken with a maximum relative error of 1%. Samples of 0.2-0.3 grams of $\delta\text{FeO}(\text{OH})$ which had been lightly ground and evacuated to remove surface water were used. Immobilizing the samples in Ducoa cement or dilution of the samples with NaCl or alumina did not significantly affect the magnetic data.

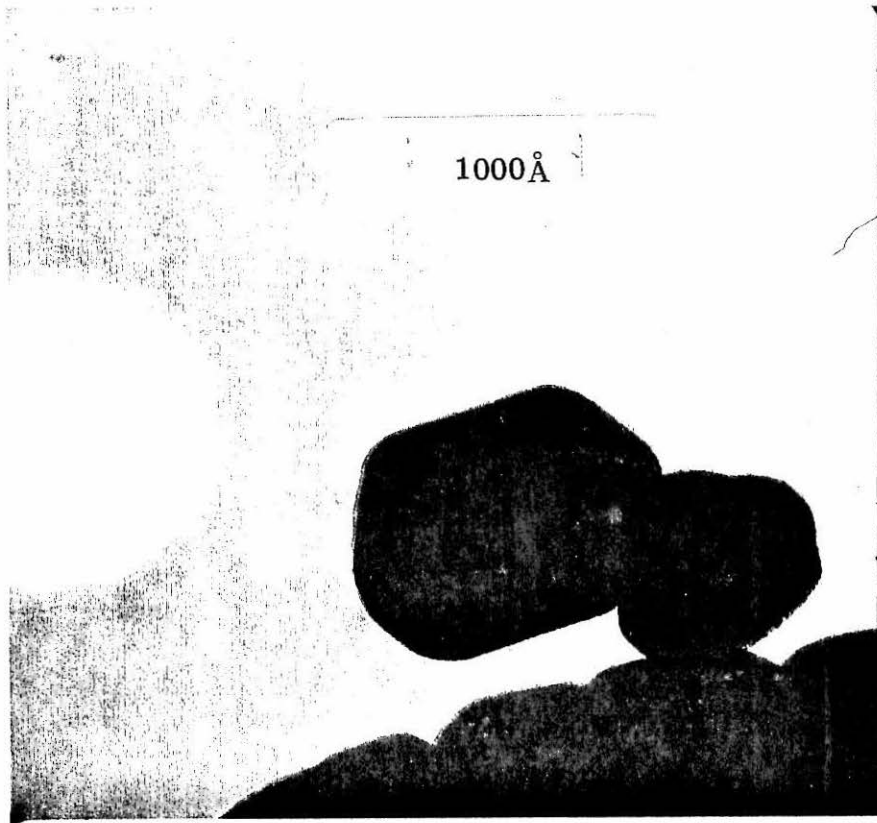


Figure 3 . δ FeO(OH) particle. Magnification 230,000X.



Figure 4 . $\delta\text{FeO}(\text{OH})$ particles agglomerating in chains.

Magnification = 68500X.

Table 1

Analytic and Descriptive Data for Samples of $\delta\text{FeO}(\text{OH})$ Prepared
in Salt Solutions of Varying Composition

Sample No.	Conditions of Preparative Medium ^a		[Na ⁺] ^b		[OH] ^c		[Cl] ^c		n ^d		Descriptive Data		Analytical Data for Product- $\delta\text{FeO}(\text{OH})$	
	F	F	F	F	F	F	F	F	GMPs (Å)	σ g	VMPs (Å)	H ₂ O ^e (%)	Na ⁺ (%)	f
1	1.05	1.05	0.00	1.074	306	1.44	456	4.3	0.005					
2	5.03	0.95	4.08	1.414	342	1.43	502	3.6	0.083					
3	6.07	1.23	4.84	1.864	346	1.52	585	2.5	0.12					
4	6.75	6.75	0.00	2.092	449	1.43	660	1.9	0.16					
5	4.85	4.85	0.00	1.490	398	1.51	662	2.6	0.22					
6	7.50	5.01	2.49	2.406	501	1.44	746	1.5	0.17					
7	10.02	10.02	0.00	3.241	666	1.45	1007	1.6	0.22					
8	9.03	9.03	0.00	2.744	759	1.52	1284	1.6	0.26					
9	10.45	6.05	4.40	3.156	918	1.49	1501	0.90	0.25					
10	12.50	6.43	6.07	4.101	1017	1.47	1750	1.10	0.31					
11	13.90	9.11	4.79	4.628	1150	1.42	2030	0.92	0.29					
12	13.07	10.22	2.86	4.386	1406	1.45	2502	0.78	0.35					

Table 1 (Continued)

-
- a Samples were prepared with $0.0034F Fe^{2+}$ and aged ten minutes at $55^{\circ}C$ prior to oxidation.
- b By summation of $[OH^{-}]$ and $[Cl^{-}]$. Error = $\pm 1.5\%$.
- c Error = $\pm 1.0\%$.
- d Viscosity of medium relative to water at $55^{\circ}C$. Error = $\pm 5\%$.
- e Water in excess of that expected from the stoichiometry $FeO(OH)$ or $Fe_2O_3 \cdot H_2O$. Error = $\pm 0.2\%$.
- f Error = $\pm 0.005\%$.

Table 2

Analytic and Descriptive Data for Samples of $\delta\text{FeO(OH)}$ Prepared from
 Ferrous Hydroxide Aged for Varying Lengths of Time Prior to Oxidation
 Conditions of Preparative Medium^a Descriptive Data Analytic Data for Product- $\delta\text{FeO(OH)}$

Sample No.	Time of Aging ^b (min)	GMPS		VMPS	H ₂ O ^c		Na ⁺ d (%)
		(Å)	σ g		(Å)	(%)	
13	0.27	(115) ^f	1.55	202	4.9	0.22	
14	1.0	245	1.42	356	4.9	0.052	
15	2.0	200	1.44	300	5.1	0.033	
16	5.0	250	1.46	418	4.8	0.034	
17	5.0	350	1.42	502	3.6	0.098	
18	5.0	477	1.43	700	2.1	0.18	
19	8.0	615	1.41	880	1.4	0.21	
20	10.0	410	1.43	601	3.1	0.12	
21	10.0	543	1.46	835	1.2	0.26	
22	15.0	720	1.44	1070	1.0	0.22	
23	15.0	1030	1.40	1450	0.70	0.26	
24	120.0	1455	1.45	2200	0.10	0.28	

Table 2 (Continued)

- a Sample prepared in a medium of 7.50F NaOH at 50 °C with 0.0034F Fe²⁺.
- b Error = ± 0.17 minutes.
- c Water in excess of that expected for the stoichiometry FeO(OH) or Fe₂O₃·H₂O. Error = ± 0.2%.
- d Error = ± 0.005%.
- e Particle size based on the measurement of only 35 particles.

Table 3

Analytic and Descriptive Data for Samples of $\delta\text{FeO}(\text{OH})$ Prepared at Different Temperatures

Sample No.	Conditions of Preparative Medium ^a		Descriptive Data			Analytic Data for Product- $\delta\text{FeO}(\text{OH})$	
	Temperature ($^{\circ}\text{C}$)		GMPS (\AA)	σ g	VMPS (\AA)	H_2O^b (%)	$\text{Na}^+ e$ (%)
25	0 ± 1		175	1.47	276	5.1	0.025
26	23 ± 1		175	1.42	397	4.4	0.092
27	23 ± 1		250	1.43	368	3.4	0.071
28	37 ± 2		280	1.41	400	3.9	0.088
29	47 ± 2		290	1.44	432	4.1	0.112
30	55 ± 2		470	1.41	650	1.85	0.212
31	55 ± 3		384	1.41	548	3.0	0.132
32	60 ± 3		410	1.43	612	3.3	0.152
33	72 ± 2		422	1.43	638	2.5	0.155
34	81 ± 2		470	1.44	702	2.22	0.150
35	92 ± 2		505	1.41	722	1.90	0.165
36	95 ± 2		520	1.46	801	1.50	0.211

178

Table 3 (Continued)

- ^a Samples were prepared in a medium 7.50F in NaOH with 0.034F Fe²⁺ and aged 5.0 minutes prior to oxidation.
- ^b Water in excess of that expected from the stoichiometry FeO(OH) or Fe₂O₃·H₂O. Error = ± 0.2%.
- ^c Error = ± 0.005%.

Table 4

Analytic and Descriptive Data for Samples of $\delta\text{FeO(OH)}$ Prepared with Varying Supersaturations of Ferrous Ion

Sample No.	Conditions of Preparative Medium ^a		Descriptive Data		Analytic Data for Product $-\delta\text{FeO(OH)}$		
	$[\text{Fe}^{2+}]^b$		VMPS	σ_g	GMPS	H_2O^c (%)	$\text{Na}^+ d$ (%)
37	0.0103		507	1.42	350	3.5	0.15
38	0.0051		352	1.44	235	4.2	0.055
39	0.0034		350	1.43	240	4.8	0.043
40	0.0027		330	1.48	210	4.85	0.035

180

^a Samples prepared in a medium of 7.42F NaOH, aged for 2.0 minutes at 50°C prior to oxidation.

^b Error = $\pm 0.1\%$.

^c Water in excess of that expected for the stoichiometry FeO(OH) or $\text{Fe}_2\text{O}_3 \cdot \text{H}_2\text{O}$. Error = $\pm 0.2\%$.

^d Error = $\pm 0.005\%$.

Viscosity data were collected with a Fenske viscometer mounted in a 25 liter water bath. The viscometer was calibrated with triple distilled water. Measurements of relative viscosity had maximum relative errors of 5%.

Density was determined by picnometry. Quantities of material were allowed to stand several days in the picnometer under triple distilled water prior to actual measurements. Densities for all samples were 3.7-3.9 grams/cm³.

Results

(A) Physical Description of δ FeO(OH) and the Effect of Preparative History on this Description. Electron micrographs show the particles of δ FeO(OH) to be hexagonal plates of nearly equal 'a' and 'b' axes with the plate face perpendicular to the 'c' axis. Figure 3 shows a fairly large ($\sim 2000\text{\AA}$) δ FeO(OH) particle. Some particles were less perfectly formed as though they had been fractured or were the product of cementation of two or more hexagonal particles. When the particles were dispersed in distilled water, they agglomerated in chains with no face-to-face or face-to-edge aggregation of the platelets (Figure 4). When the particles were dispersed in an aqueous solution containing a surfactant such as 0.5% sodium stearate or 0.1% sperm oil, more severe agglomeration of the particles occurred (Figure 5). In photographs of these agglomerates, it was occasionally possible to observe particles edge-on. Though insufficient data could be collected for detailed statistical analysis of particle thickness,

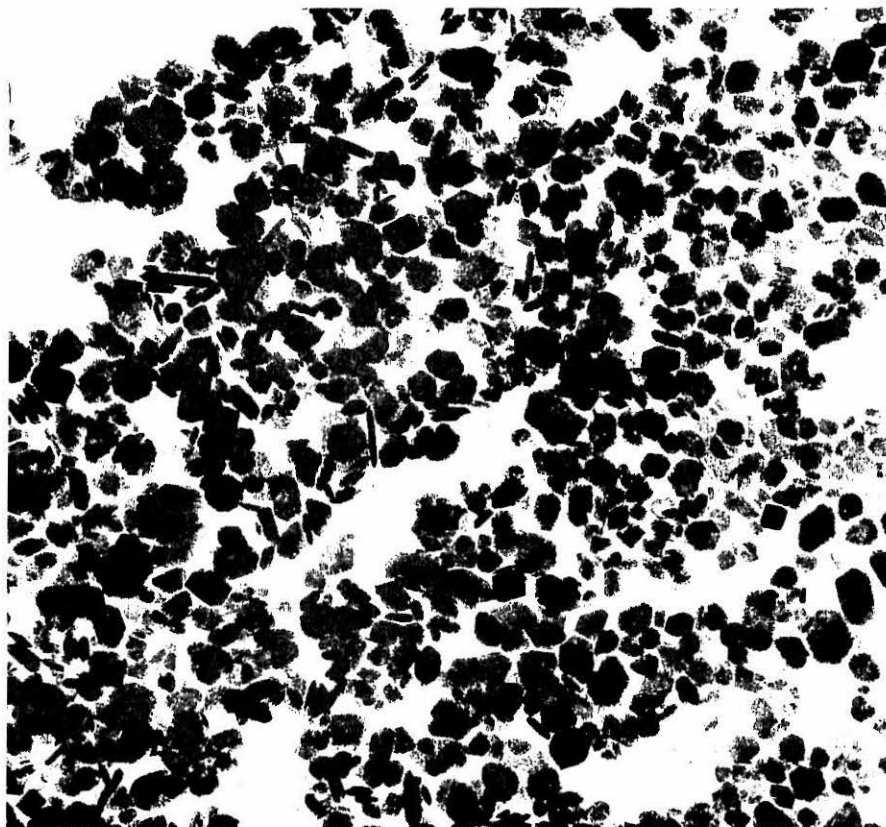


Figure 5. $\delta\text{FeO}(\text{OH})$ dispersed from a solution of 0.5% sperm oil in water. Magnification = 92650 \times .

it appears that the platelets are about one-sixth as thick as they are long. The narrow dimension along the c-axis would account for the breadth of X-ray powder diffraction reflections indexed in this axis.

The geometric size distribution of each of the samples is sharp, monodisperse, and can be fitted to log-normal distribution function with a minimum confidence of 87% measured by the chi-squared test. As shown in Figure 6, the fit to the log-normal function is quite good even for the largest and smallest particle sizes where data are more difficult to collect. Figure 7 presents the distribution determined in Figure 6 in terms of particle diameter and frequency. Final parameters of the distributions of the various samples are cited in Tables 1, 2, 3, and 4.

Though the means of the size distributions vary by a factor of more than ten among the samples, the standard deviations of the means are quite constant and vary by only a few percent. This fortuitous happen-stance greatly facilitates intersample-comparisons. The two-parameter distribution functions can be treated as single-parameter functions determined solely by their means (GMPS or VMPS). This simplification and the sharpness of the distribution functions allow correlations between the behavior of a bulk sample and its entire particle-size distribution to be made by regressing the behavior against only the mean of the distribution. The spread of particle sizes about the mean is not negligible, but its effects can be treated as perturbations on the general trend of a regression.

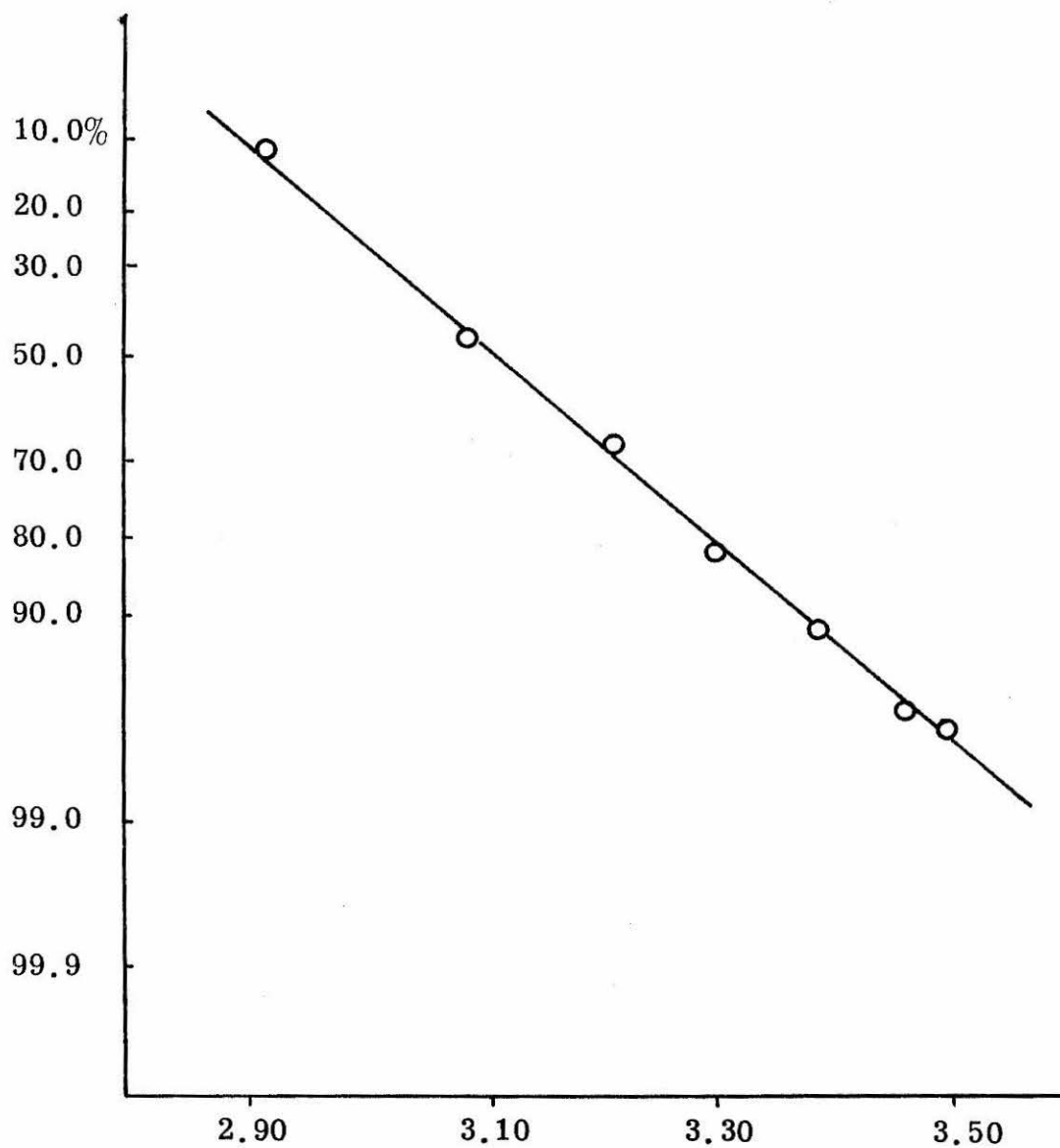


Figure 6. Fit of particle-size distribution determined from electron micrographic data to log-normal distribution. VMPS = 1284\AA , $\sigma = 1.43$. Confidence level of fit is 93%.

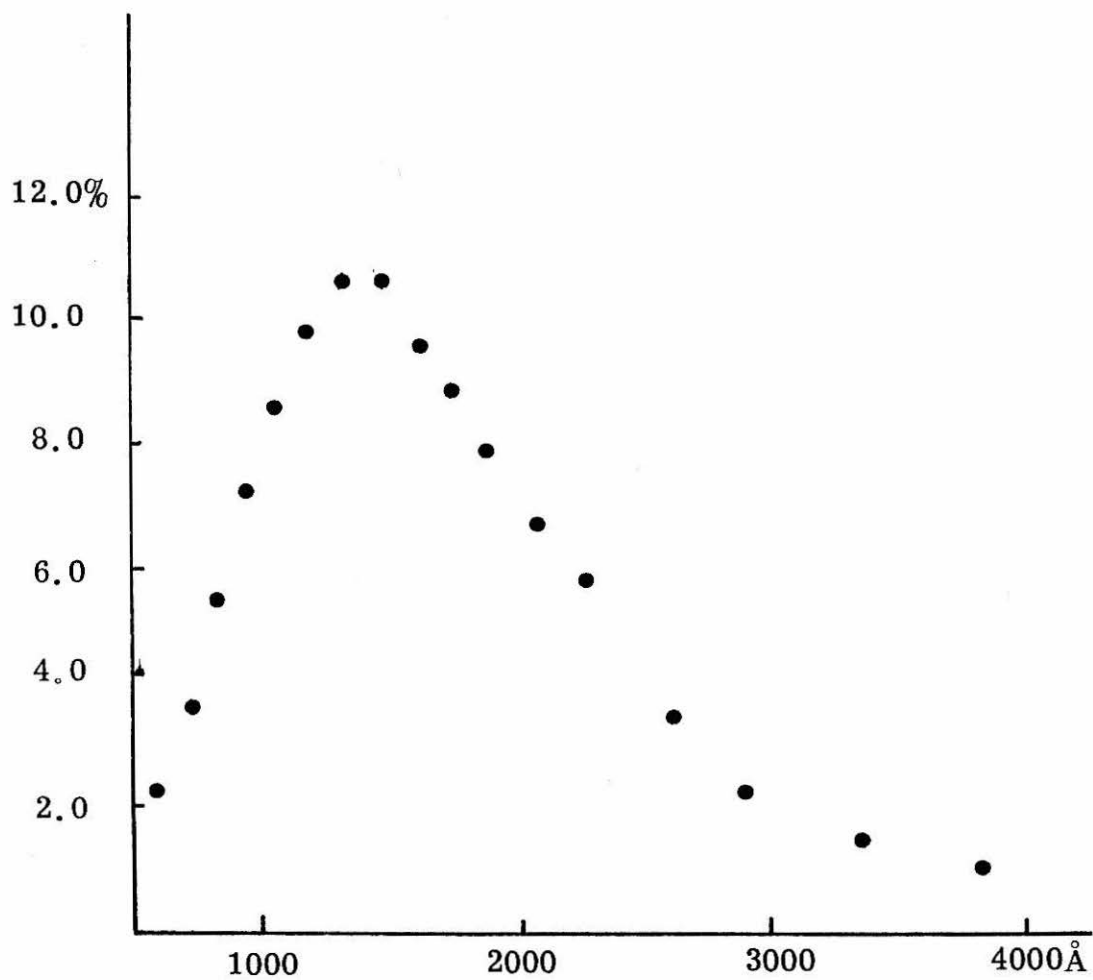


Figure 7. Volumetric particle size distribution for sample of VMPS = 1284Å, $\sigma = 1.43$.

The physical descriptions of the $\delta\text{FeO}(\text{OH})$ samples were controlled primarily by the procedures of formation and treatment of the intermediate ferrous hydroxide prior to oxidation. The precipitation medium had an especially direct effect. The VMPS of the samples increased with increasing concentration of solutes in the medium. A linear regression between VMPS and the formal sodium ion concentration of the precipitation medium accounted for 90% of the variation in particle size among samples 1-13 (Figure 8). For dilute (1.0 F) and very concentrated ($\sim 14.0\text{F}$) sodium ion solutions the observed VMPS deviates from the regression in keeping with the observations noted in the Experimental section.

Particle size also gives the appearance of being dependent on the hydroxide concentration of the medium. However, correlations of no better than 43% confidence could be developed for this behavior. Covariance between sodium ion and hydroxide ion concentrations account for all the observed dependence. No improvement in the hydroxide correlation could be developed when formal concentrations were converted to activity using published data.⁷⁻⁹

Viscosity of the precipitation medium is also strongly covariant with solute concentration. Regressions between viscosity and VMPS were somewhat poorer than the regression against formal sodium ion concentration. The limited precision of viscosity data made statistical correlations infeasible.

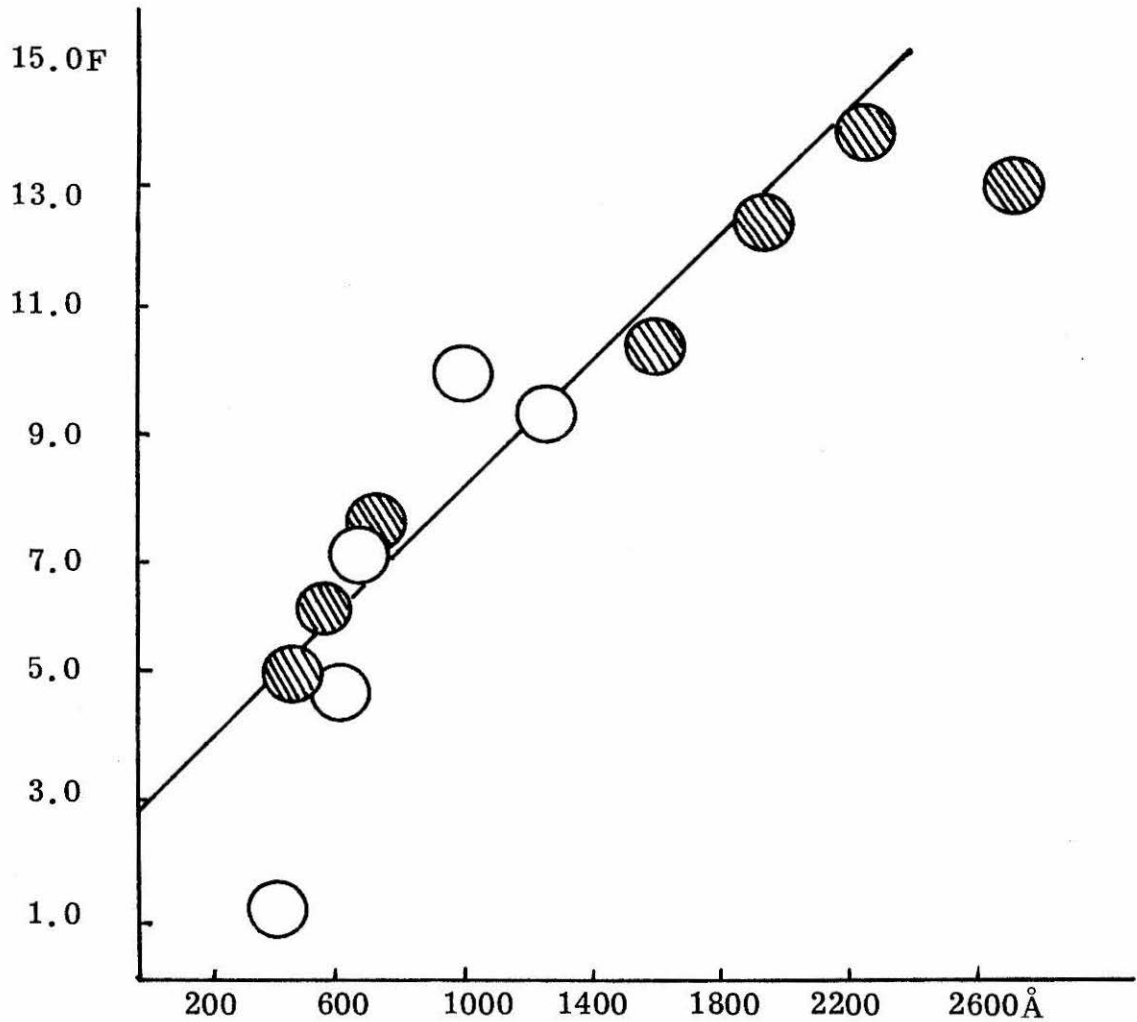


Figure 8. VMPS versus Na^+ concentration. Samples were prepared in 0.0034F ferrous ion solution at 55°C and were aged 10 minutes prior to oxidation. Shaded circles correspond to samples prepared in a mixed medium of NaOH and NaCl . Open circles represent compounds prepared in NaOH solution. Linear, least squares regression line is $\text{VMPS} = -585 + 193(\text{Na}^+)\text{\AA}$. Confidence level of regression is 90%.

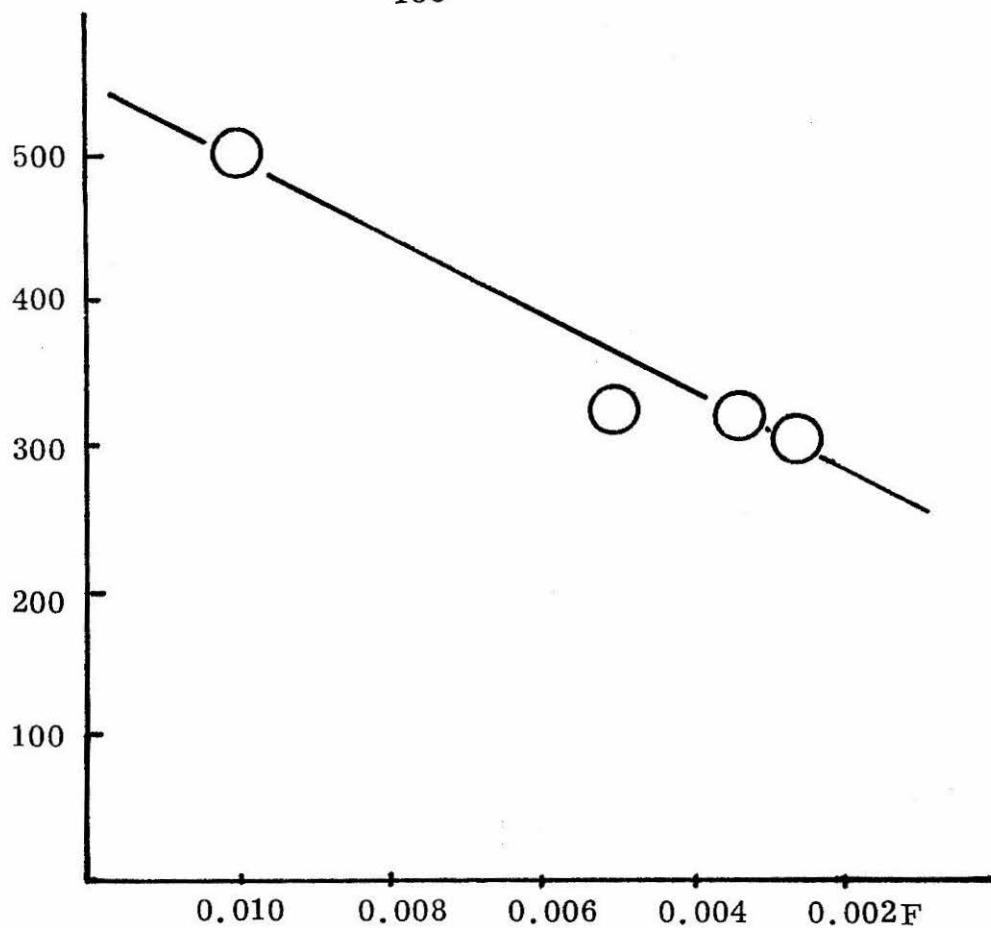


Figure 9. VMPS as a function of ferrous ion concentration used in preparing samples. Samples were prepared in 7.42F Na⁺ ion solution at 50°C and aged 2 minutes prior to oxidation. Linear, least-squares regression line is $VMPS = 259 + 23.3 ([Fe^{2+}] \times 10^3) \text{Å}$.

VMPS was also observed to increase with the concentration of ferrous ion in the precipitation medium (Figure 9). Too little data could be collected for meaningful inferences to be drawn from the observations. The linear regression line in Figure 9 is therefore intended merely for reference.

The temperature at which the intermediate ferrous hydroxide was produced (T_p), and the length of time it was aged prior to oxidation also influenced the particle size of the oxidation product. Figure 10 shows the variation of VMPS among samples 25-36 with T_p . The linear regression in this figure accounts for 92% of the variation.

Figure 11 shows the increase in $\delta\text{FeO}(\text{OH})$ particle with the length of time the intermediate ferrous hydroxide was aged at 50°C . For aging times up to 15 minutes, the growth of particles is linear in time. For longer aging times, particle size falls well away from the linear regression in the figure. Particles of $\delta\text{FeO}(\text{OH})$ produced from ferrous hydroxide which had been aged for less than 30 seconds were badly formed and possibly dendritic or flocculent (Figure 12).

The oxidation process and subsequent treatment of the oxidation product had little effect on the physical description when hydrogen peroxide was used as the oxidant. The presence of chloride ion in the precipitation medium for some of the samples had no discernible impact on the product, though it is known that chloride ion accelerates the oxidation of ferrous ion at lower pH.¹⁰ When solute concentration was above one molar, the oxidation medium did not affect the product.

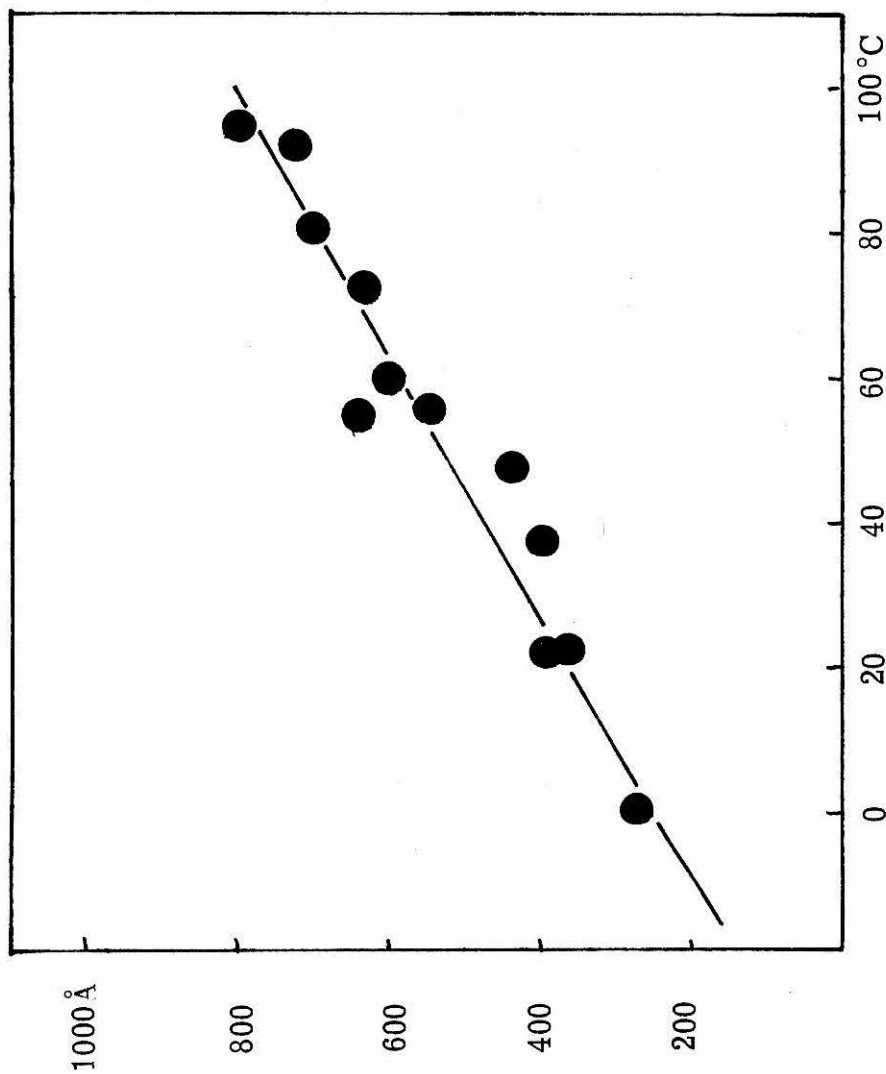


Figure 10. VMPS versus the temperature of preparations. Samples were prepared with 0.0034F ferrous ion, 7.50F Na⁺ ion and aged 5 minutes prior to oxidation.

Linear, least-squares regression line is $VMPS = [252 + 5.48T(^{\circ}C)] \text{ \AA}$.

Figure 11. VMPS as a function of the time intermediate ferrous hydroxide was aged at 50°C prior to oxidation. Samples were prepared in 0.0034F ferrous ion and 7.50F Na⁺ ion solution. Shaded point was not included in linear regression. Linear least squares regression line is VMPS = [184 + 67.3t(minutes)] Å.

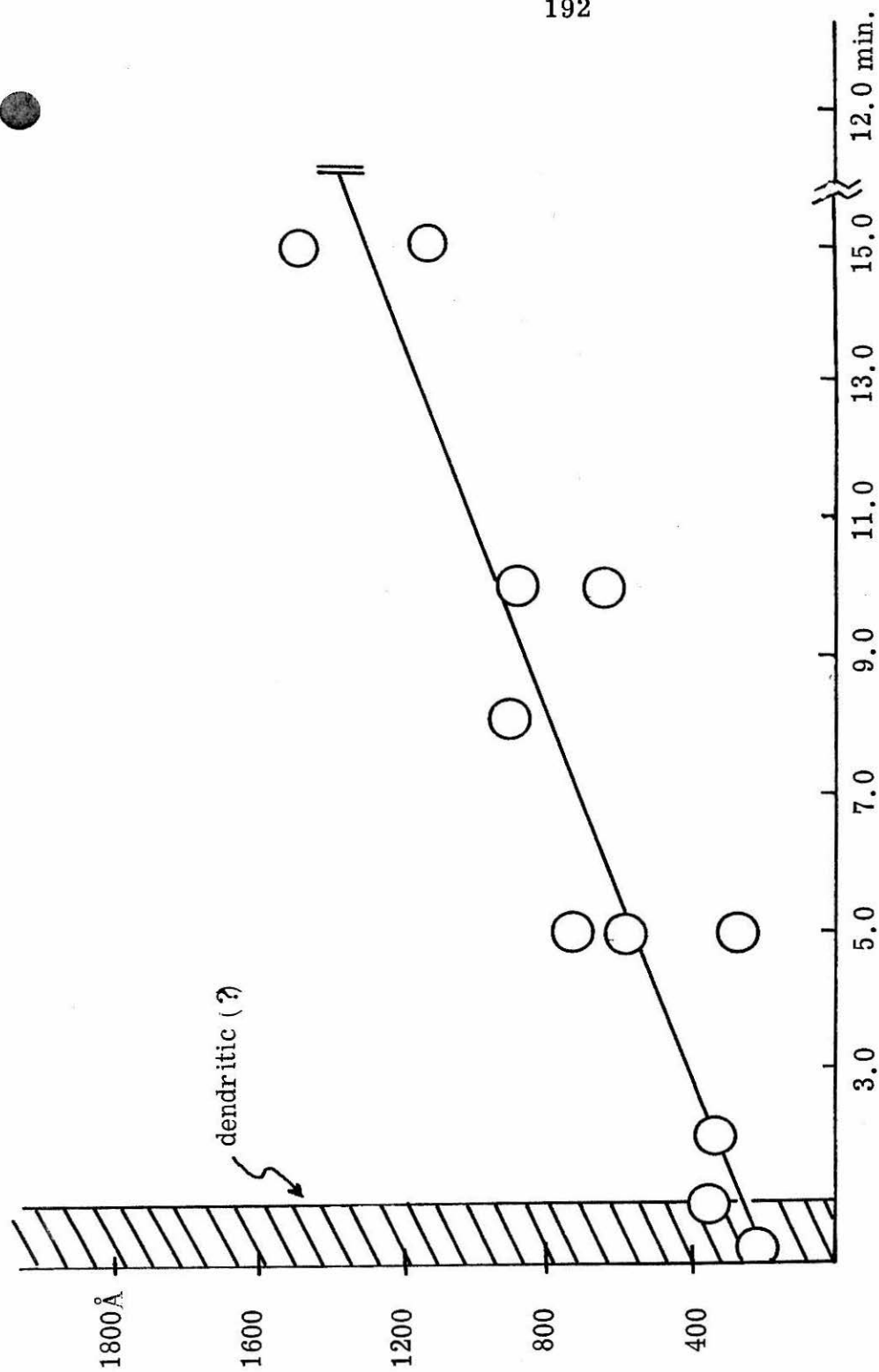




Figure 12. Flocculates prepared by very rapid quenching of δ FeO(OH).
Magnification $\sim 220,000\times$.

Identical samples of ferrous hydroxide precipitated in 10F NaOH and oxidized in 1.0F and 10F NaOH yielded δ FeO(OH) samples of nearly identical VMPS (1030 and 1007Å, respectively). When solute concentration fell well below 1F, the oxidation product was badly contaminated with other oxides of iron.

When peroxide was generated in vitro by hydrothermal decomposition of ammonium persulfate, a very undesirable product was obtained (Figure 13). This product gave X-ray powder diffraction reflections of δ FeO(OH), though the lines were quite broad. The particles are badly distorted from the hexagonal shape described above.

Air oxidation was quite slow and yielded an unidentifiable mix of iron oxides. The X-ray powder diffraction pattern of this product consisted of just two broad reflections which could not be assigned to δ FeO(OH).

(B) Magnetic Behavior of δ FeO(OH) and the Effects of Sample Description on this Behavior. Detailed magnetic data were collected on samples 1-12 and 25-36 at applied fields of up to 11,000 oersteds and over the temperature range 35-300°K. Room temperature magnetization curves were measured for samples 13-24. Magnetic parameters determined for the samples are tabulated in Tables 5, 6, and 7.

All samples were intensely magnetic. Their susceptibilities exhibited saturation effects in applied fields (H) greater than 1600

Table 5

VMPS (Å)	$\sigma_{O,\infty}$ (gauss/gm)	n (BM)	$H_c(O)$ oersteds	$\frac{\sigma_R(0)}{\sigma_{O,\infty}}$	T_b (°K)	$\sigma_s(298)$ (gauss/gm)	$H_c(298)$ oersteds	$\frac{\sigma_R(298)}{\sigma_s(298)}$	$K(O)^e$
456	20.19	0.32	1000	0.48	190	16.62	0	0	3.8×10^4
502	18.01	0.29	980	0.48	220	14.90	0	0	3.4×10^4
585	20.34	0.32	1100	0.50	260	16.82	0	0	4.2×10^4
660	21.28	0.34	1170	0.50	340	17.61	55	0.08	4.7×10^4
662	19.08	0.30	1040	0.49	315	15.79	35	0.04	3.8×10^4
746	24.55	0.39	1260	0.50	(320) ^f	20.32	62	0.11	5.9×10^4
1007	24.77	0.39	900	0.50	(310)	20.49	20	0.31	4.2×10^4
1284	25.82	0.41	1320	0.51	(325)	21.37	95	0.34	6.5×10^4
1501	23.99	0.38	1280	0.49	(325)	19.83	105	0.36	5.8×10^4
1750	26.36	0.42	1450	0.50	(350)	21.78	175	0.35	7.3×10^4
2030	24.40	0.39	1350	0.50	(> 330)	20.18	145	0.41	6.3×10^4
2502	25.18	0.40	1430	0.50	(> 340)	20.83	160	0.38	6.8×10^4

^a Error ± 0.20 gauss/gm. ^b Error ± 100 oe. ^c Error $\pm 2\%$. ^d Error $\pm 20^\circ$. ^e $K(O) = 1/2 \sigma_{O,\infty} H_c(O)/\rho$.

^f From extrapolation.

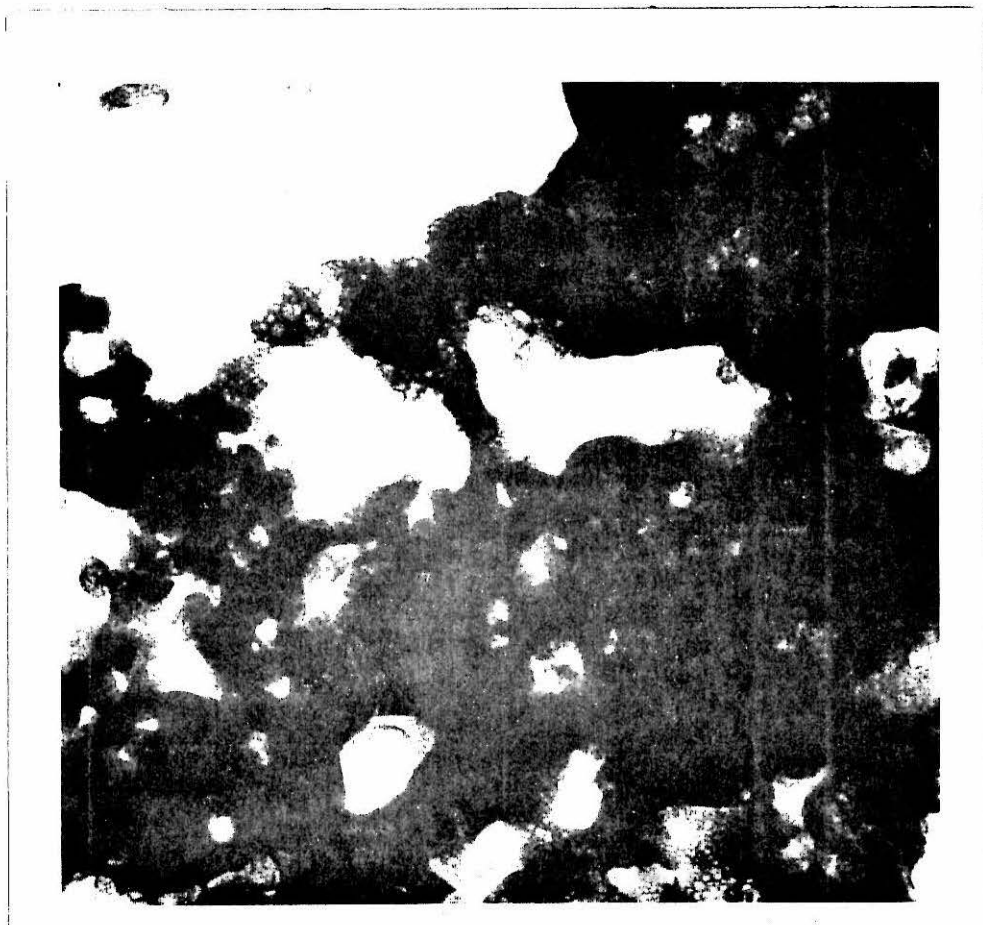


Figure 13. δ FeO(OH) prepared by oxidation of δ FeO(OH) in strongly alkaline (10F NaOH) medium with ammonium persulfate. Magnification = 190,240 \times .

oersteds. Magnetization curves for the samples were centrosymmetric and devoid of any distortion that might be attributed to exchange anisotropy.^{11,12} No sudden alterations in the magnetic behavior at low temperatures which might be indicative of structure modification were observed.

Saturation magnetizations ($\sigma_{\infty}(T)$) were determined by extrapolation of plots of magnetization ($\sigma(T)$) versus the reciprocal of the applied field ($1/H$) to infinite field. Similar extrapolation of plots of $\sigma(T)$ versus $1/H^2$ yielded infinite field magnetizations that were within 5% of the $\sigma_{\infty}(T)$ values. Saturation magnetizations at various temperatures were fitted to equation 1.

$$\sigma_{\infty}(T) = \sigma_{\infty}(0) (1.0 - aT^n) \quad \text{eqn. 1}$$

The fit between experimental data and this expression was not especially sensitive to the value of the exponential parameter 'n'. (Figure 14). Table 8 cites parametric values for the "best-fit" of experimental data from samples 1-12 to equation 1 with $n = 3/2, 2, 5/2$. Also in Table 8 are parametric values found from least-squares estimation of all parameters in equation 1. These latter parameters account for the experimental data with 99% confidence and were used in all succeeding computations.

$\delta\text{FeO}(\text{OH})$ is seriously decomposed at elevated temperatures. In this study no sample was observed to survive prolonged heat treatment at 80°C. For this reason, it was not possible to experimentally determine the Curie temperature (T_c). Extrapolation of equation 1

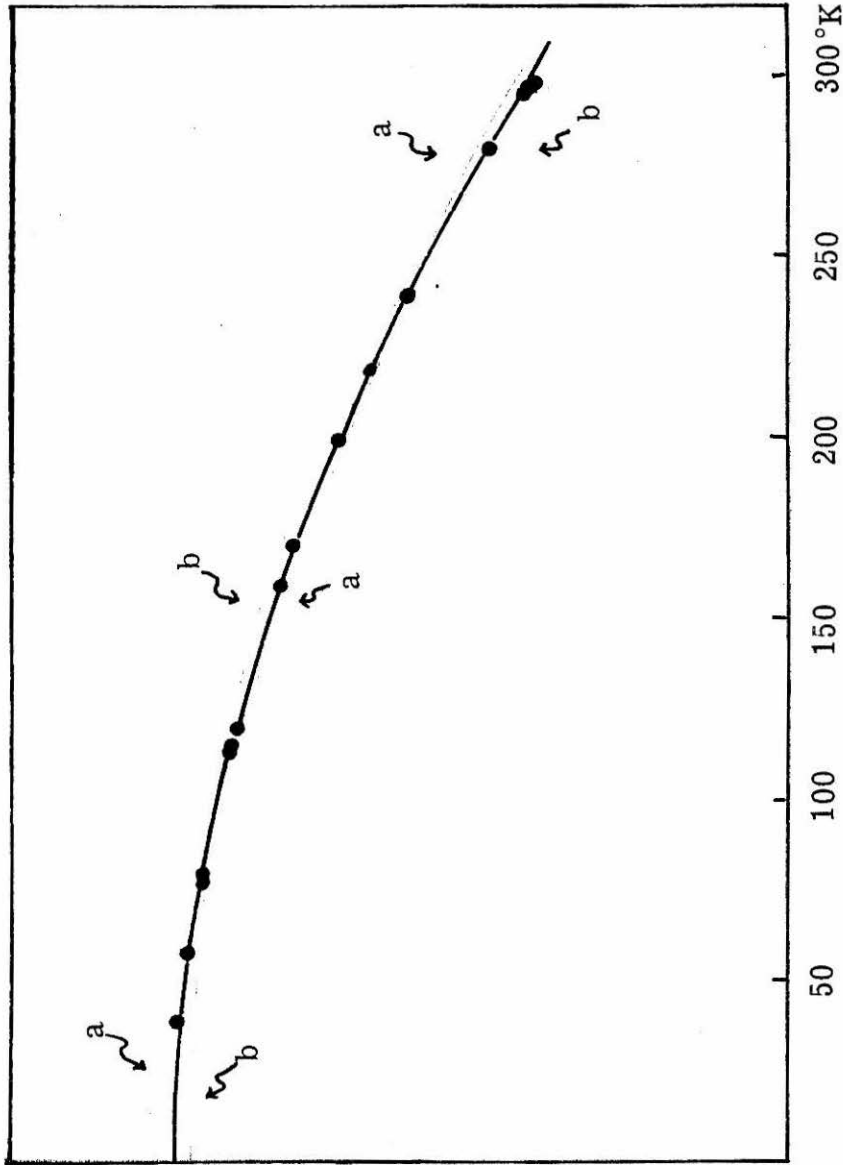


Figure 14. Fit of $\sigma_{\infty}(T)$ to $\sigma_{\infty}(O) = \sigma_{\infty}(O) (1.0 - aT^n)$ for samples of VMPS = 1284Å. Line 'a' corresponds to $n = 2.5$ and line b to $n = 1.5$. Heavy dark line is the best-fit line with parameters $\sigma_{\infty}(O) = 25.82$ gauss/gm, $a = 2.70 \times 10^{-6}$, $n = 1.94$.

using the parameters cited in Table 8 to zero magnetization does provide an estimate of T_c . Curie temperatures so derived are quite dependent on the value of the parameter n . Best-fit values of n yield temperatures of $740 \pm 20^\circ\text{K}$. The estimated Curie temperatures found for various n cited in Table 8 show that all magnetic measurements in this study were made at temperature well below T_c .

Saturation magnetization at 0°K , $\sigma_\infty(0)$, is not sensitive to the other parameters in equation 1. Bohr magneton numbers (μ) for the samples were computed from $\sigma_\infty(0)$ using equation 2.

$$\mu = \frac{\sigma_\infty(0) \cdot \text{MW}}{\beta \cdot N_A} \quad \text{eqn. 2}$$

MW = formula weight of $\delta\text{FeO}(\text{OH})$

N_A = Avogadro's number

β = Bohr magneton

For all the samples, μ was less than one, and much less than the nominal value expected for high-spin Fe(III).

The magnetic behavior of $\delta\text{FeO}(\text{OH})$ was quite sensitive to the physical description of the samples, and consequently sensitive to the preparative history of the samples. Figure 15 shows the dependence of $\sigma_\infty(0)$ on particle size. For VMPS between 456 and 700\AA , $\sigma_\infty(0)$ increases sharply. The increase in $\sigma_\infty(0)$ for VMPS $> 700\text{\AA}$ is slower and apparently asymptotic.

Thermal treatment of the intermediate ferrous hydroxide prior to oxidation caused more complicated variations in $\sigma_\infty(0)$. As the

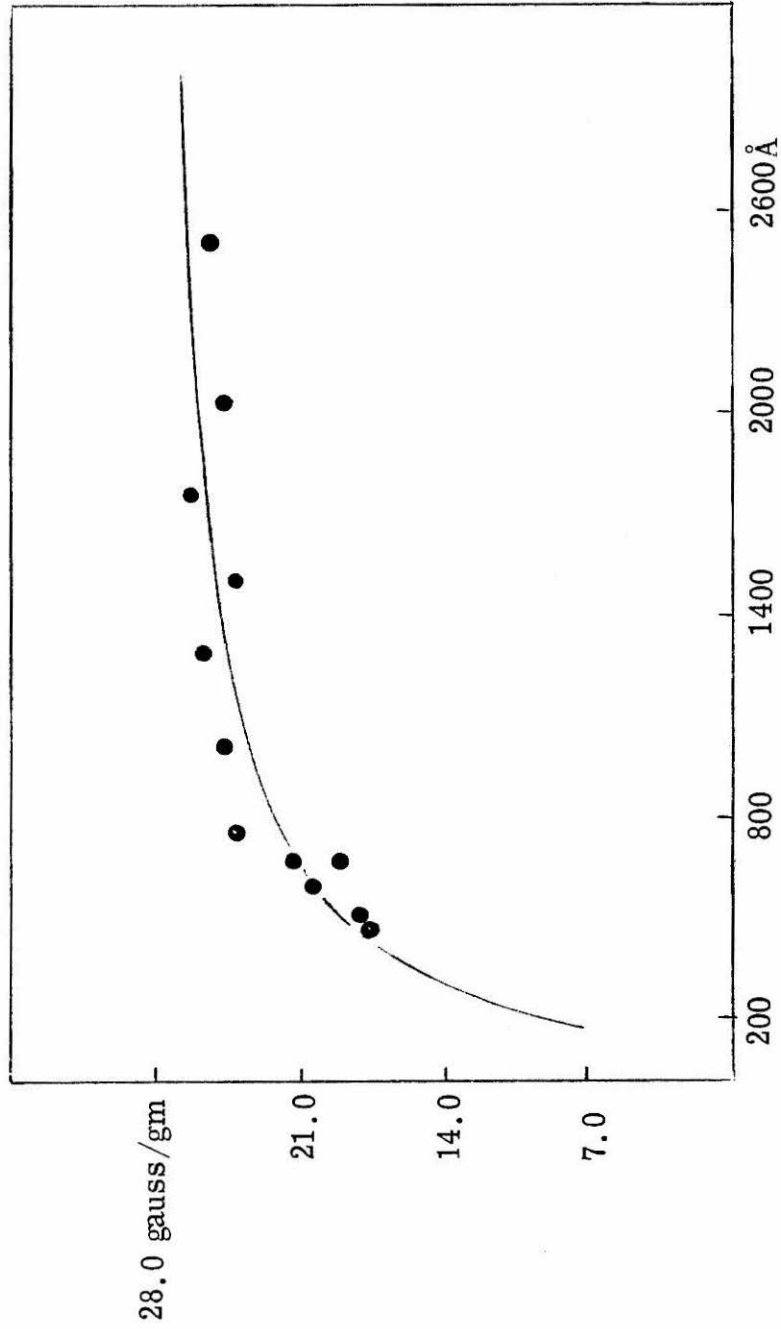


Figure 15. Dependence of $\sigma_{\infty}(O)$ on particle size (VMPS). Solid line is magnetization calculated from the model discussed in the text.

temperature of sample preparation increased, $\sigma_{\infty}(0)$ increased to a broad maximum at $T_p = 40-60^{\circ}\text{C}$ (Figure 16). For $T_p > 60^{\circ}$ there is a systematic decline in $\sigma_{\infty}(0)$. A similar maximum occurs in the dependence of $\sigma_{\infty}(298)$ on the time the intermediate ferrous hydroxide is aged (Figure 17).

Unlike sample description, magnetization behavior of $\delta\text{FeO}(\text{OH})$ was affected by hydrothermal treatment. Figure 18 shows the systematic fall in magnetic moment with hydrothermal aging at 50, 80, and 100°C . The rate at which the moment falls is strongly temperature dependent. At 50°C there is little change in the moment after 3 days of aging. As shown in Table 9, the particle size distributions of the samples was relatively unchanged by the hydrothermal treatment. After five days of aging at 100°C , two additional, weak, broad lines at d-spacings of $4.29 \pm 0.20\text{\AA}$ and $2.73 \pm 0.10\text{\AA}$ appear in the X-ray powder diffraction pattern of the aged material. The breadth of the lines prevents accurate determination of their positions. The well-known thermal decomposition of $\delta\text{FeO}(\text{OH})$ to $\alpha\text{FeO}(\text{OH})$ suggests that these additional lines may be due to the 110 and 130 reflections of the α phase. No additional lines were observed in the diffraction patterns of the material aged at 50 and 80°C . The tremendous background scattering in the patterns may have prevented such lines from being detected. Electron micrographs of the aged material were little altered from those of the starting material (Figure 24).

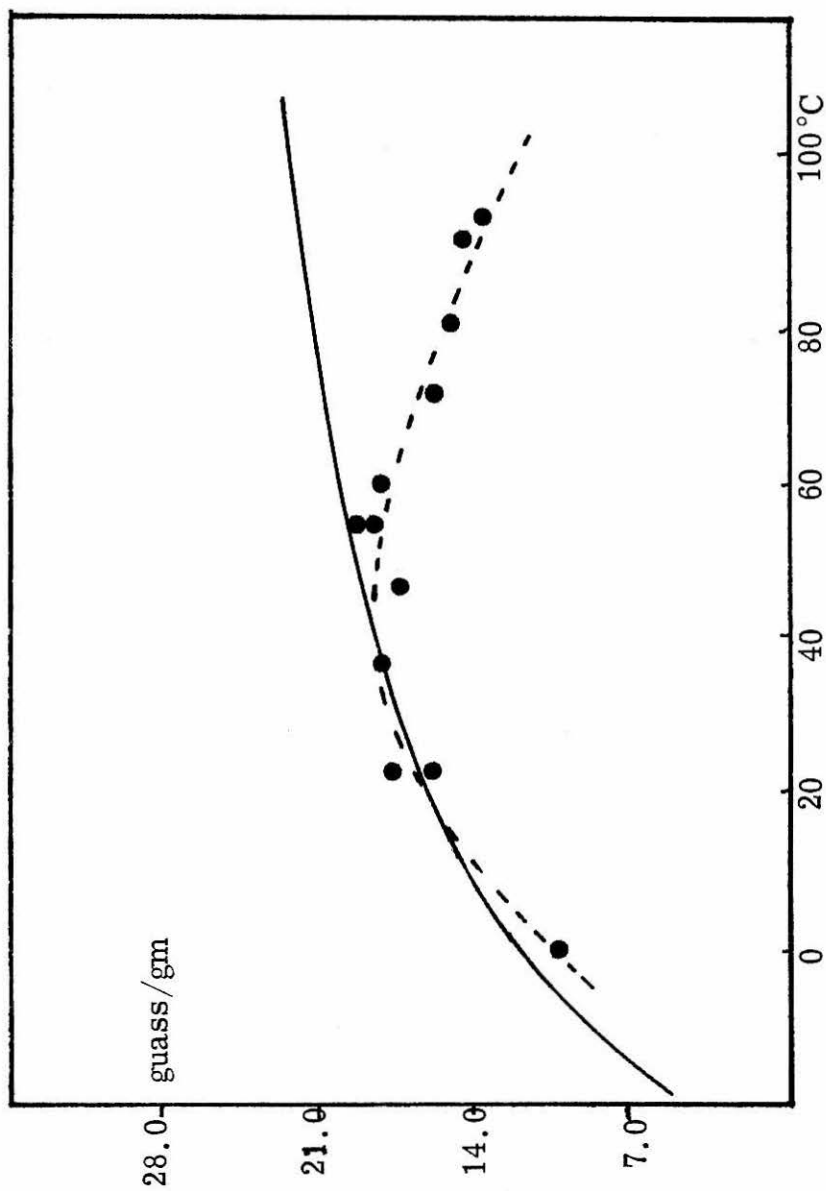


Figure 16. Dependence of $\sigma_{\infty}(O)$ on the temperature of sample preparation. Dashed line is best-fit polynomial $VMPS = 10.15 + 0.426T - 0.0065T^2$. Confidence of fit is 95%. Solid line is magnetization calculated from model discussed in the text.

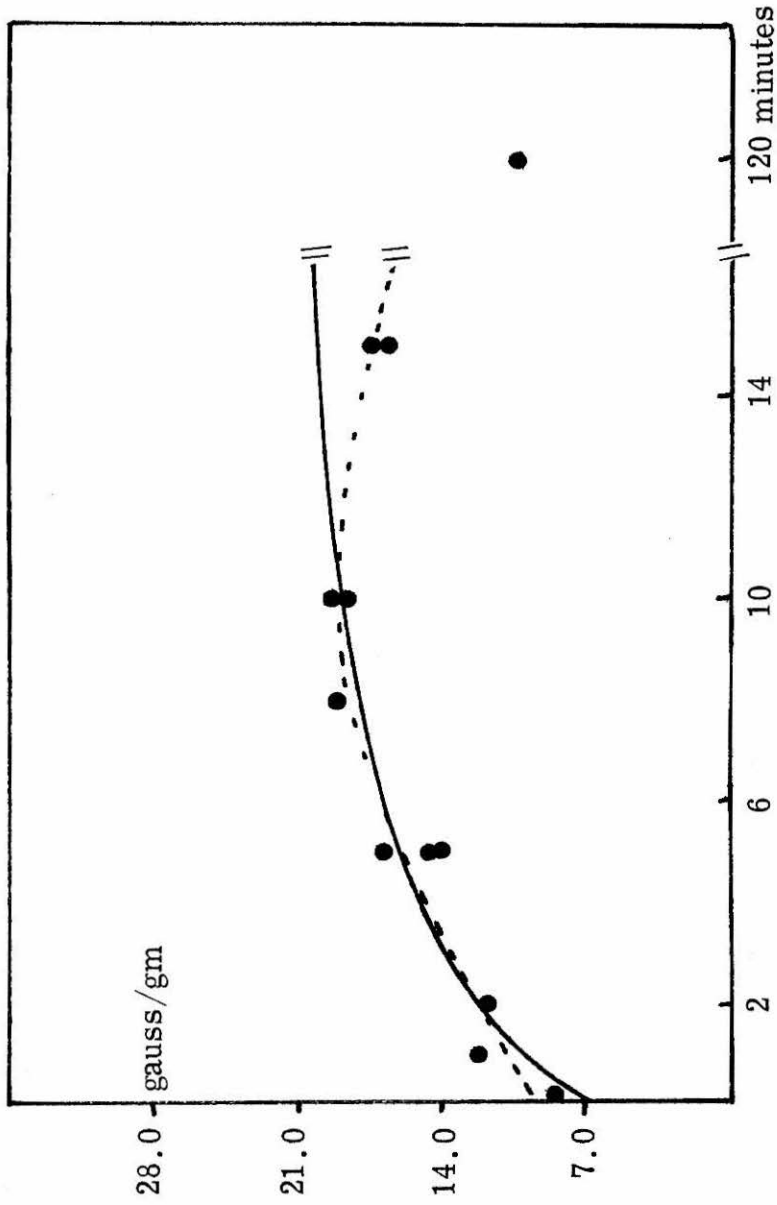


Figure 17. Variation in $\sigma_{\infty}(298)$ with the time the intermediate ferrous hydroxide was aged. Dashed line is the best-fit polynomial expression $\text{VMPS} = 8.74 + 1.94t - 0.10t^2$. Confidence of fit is 95%. Solid line is magnetization calculated from the model in the text.

Table 6

 $\sigma_{\infty}(298)$ for Samples 13-24

Sample No.	$\sigma_{\infty}(298)$	$\sigma_{\infty}(298)$	VMPS (Å)
	(observed) gauss/gm	(calculated) ^a gauss/gm	
13	8.46	7.50	202
14	12.31	13.07	356
15	11.87	11.43	300
16	14.05	14.40	418
17	14.73	15.80	507
18	17.00	17.68	700
19	19.22	18.73	880
20	18.76	16.85	601
21	19.48	18.55	835
22	17.65	19.57	1070
23	16.83	20.52	1450
24	10.46	21.51	2200

^a Calculated moment for a particle of the indicated size assuming the particle is surrounded by a magnetically dead layer 31 Å thick and that $\sigma_{\infty}(T) = \sigma_{\infty}(O) (1 - 2aT^2)$.

Table 7

 $\sigma_{\infty}(\text{O})$ for Samples 25-35

Sample No.	$\sigma_{\infty}(\text{O})$		VMPS (\AA)
	Observed	Calculated ^a	
25	10.2	9.80	212
26	17.73	16.80	397
27	15.88	16.26	368
28	18.13	17.00	402
29	17.40	17.77	432
30	19.20	20.85	650
31	18.41	19.67	548
32	18.18	20.40	600
33	15.82	20.80	638
34	15.00	21.40	702
35	14.50	21.62	722
36	13.62	22.23	801

^a Calculated for a particle of the observed VMPS assuming that a magnetically dead region 31 \AA thick surrounds the particle and the bulk magnetization is 28.63 gauss/gm.

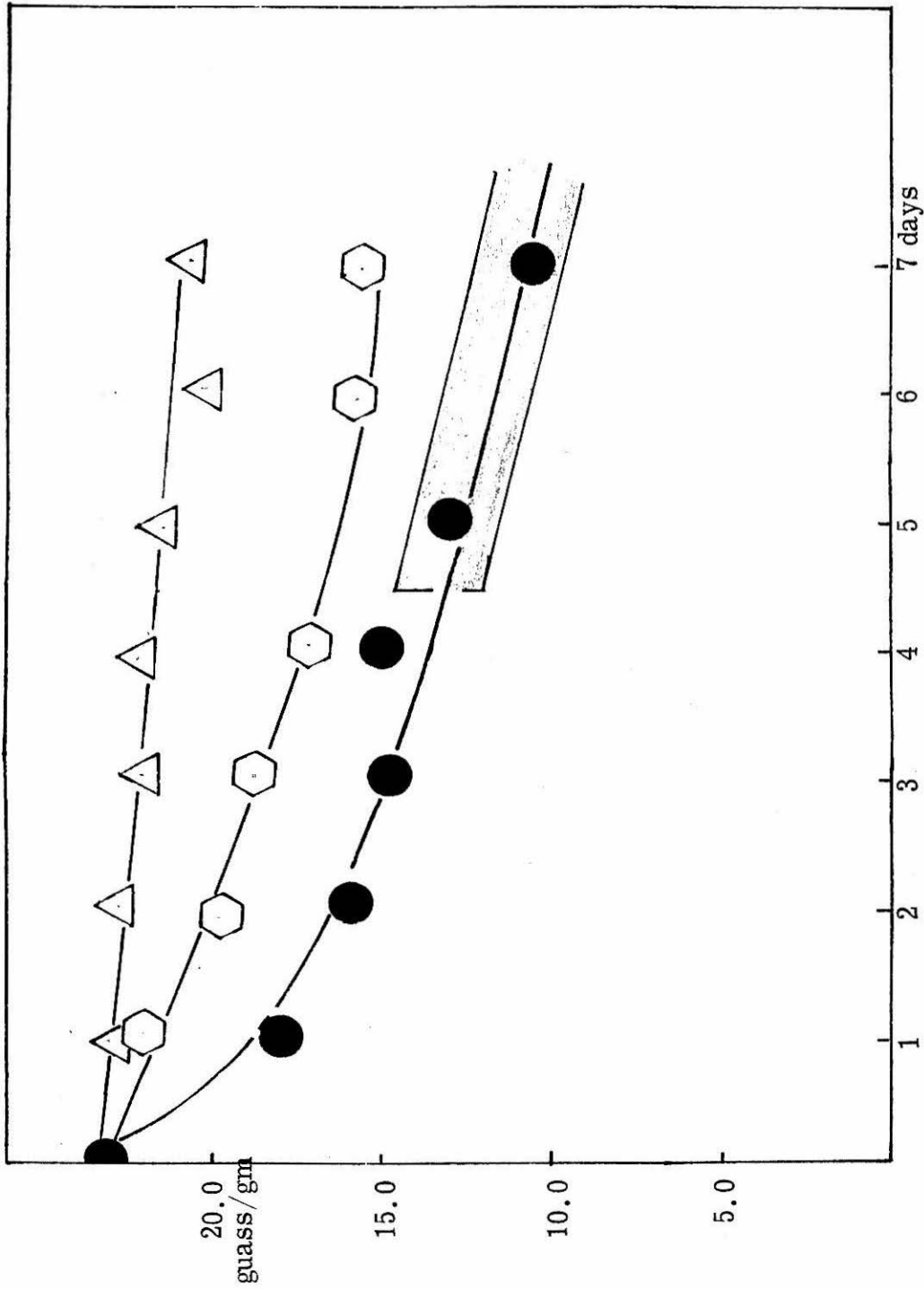


Figure 18. Decay of $\sigma_{\infty}(298)$ during hydrothermal treatment at 100°C (○), 80°C (◻), and 500°C (△). In shaded portion of figure, the sample no longer has the X-ray powder diffraction pattern of pure $\delta\text{FeO}(\text{OH})$.

The rate of ferrous hydroxide oxidation influenced magnetization of the samples, just as it influenced their description. Slow oxidation with ammonium persulfate yielded a product of $\sigma_{\infty}(298) \cong 8$ gauss/gm. Even slower oxidation by air produced a non-magnetic product.

Hysteresis properties of the samples are even more dependent on the physical description of the samples than are the saturation properties. Samples of VMPS $< 600\text{\AA}$ exhibit no hysteresis losses at room temperature. Such samples are superparamagnetic. Plots of $\sigma(T)$ versus H/T superimpose for temperatures above the sample blocking temperature (T_b). Figure 19 shows an example of this overlap for one sample. At temperatures below T_b the superparamagnetic samples developed hysteresis in their magnetization curves. Samples of VMPS $> 600\text{\AA}$ had well-developed hysteresis properties at room temperature. In figures 20 and 21 the coercive field (H_c) and the ratio of remanent magnetization at zero applied field to saturation magnetization ($R = \sigma_R(T)/\sigma_{\infty}(T)$) for samples 1-12 are plotted against VMPS for $T = 298, 100, \text{ and } 40^\circ\text{K}$. At 298°K H_c and R increase sharply with VMPS to broad maxima. The front edge of these maxima is usually associated with the onset of single domain magnetic behavior. The particle size at which these maxima occur is the critical dimension at which a single magnetic domain is stabilized in the particle. Typically, the dimension determined from plots of R versus VMPS is somewhat smaller than that determined from H_c versus VMPS. In view of the narrow particle-size distributions in the samples of

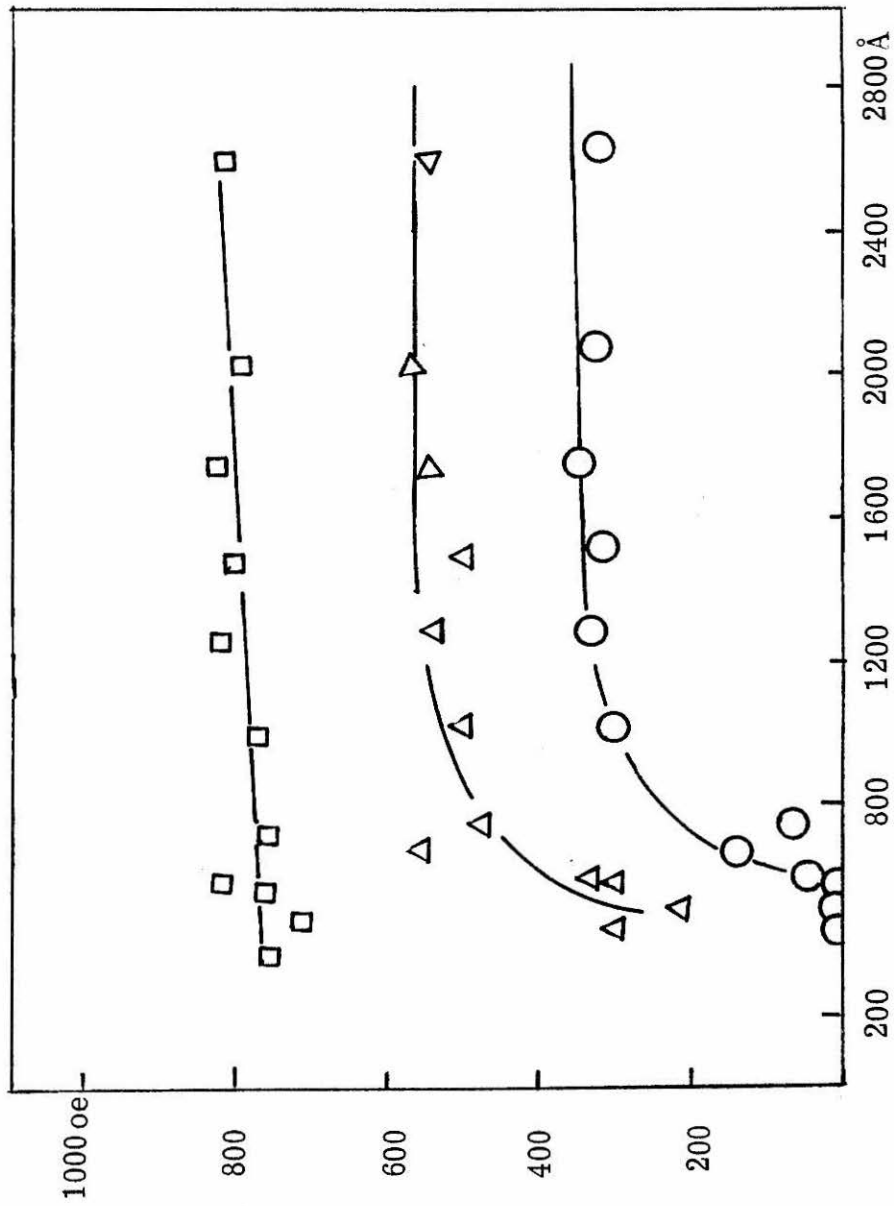


Figure 20. Coercive field versus VMPS at 298°K (○), 100°K (△), and 40°K (□).

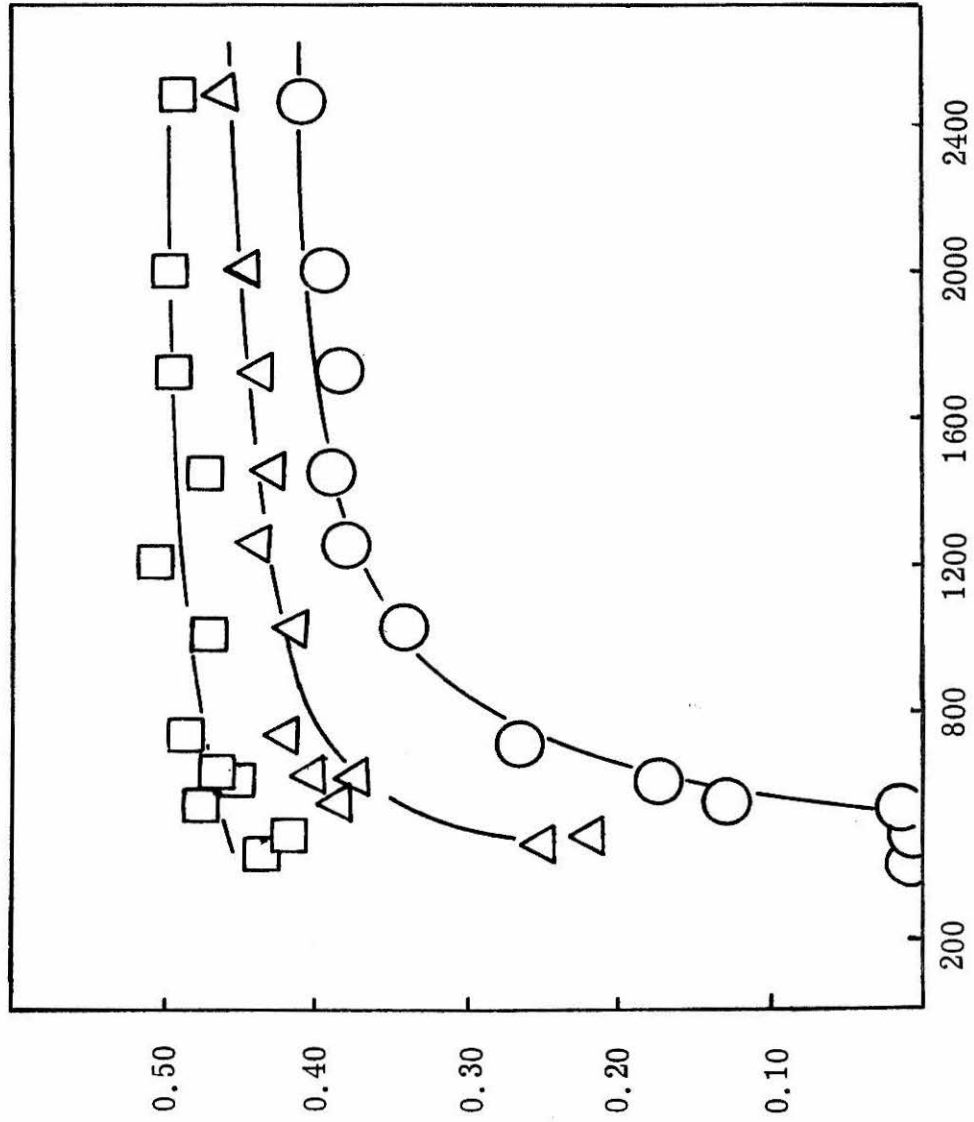


Figure 21. $R = \sigma_R(T)/\sigma_\infty(T)$ versus VMPS at 298°K (○), 100°K (△), and 40°K (□).

Table 3

Sample No.	Linear Least Squares Fit			Linear Least-Squares			Linear Least-Squares			Nonlinear Least-Squares		
	$\sigma_{O,x}$ (emu-gm)	a ($^{\circ}\text{K}^{-2}$)	T_c ($^{\circ}\text{K}$)	$\sigma_{O,x}$ (emw./gm)	a (K^{-2})	T_c ($^{\circ}\text{K}$)	$\sigma_{O,\omega}$ (emw./gm)	a ($^{\circ}\text{K}^{-2}$)	T_c ($^{\circ}\text{K}$)	$\sigma_{O,\omega}$ (emu/gm)	a ($^{\circ}\text{K}^{-2}$)	T_c ($^{\circ}\text{K}$)
	$\sigma_{O,x}(1.0\text{-aT}^{1.5})$			Fit to $\sigma_{O,x}(1.0\text{-aT}^2)$	Fit to $\sigma_{O,\omega}(1.0\text{-aT}^{2.5})$	Fit to $\sigma_{O,\omega}(1.0\text{-aT}^{2.5})$	Fit to $\sigma_{O,x}(1.0\text{-aT}^2)$	Fit to $\sigma_{O,\omega}(1.0\text{-aT}^{2.5})$	Fit to $\sigma_{O,x}(1.0\text{-aT}^2)$	Fit to $\sigma_{O,\omega}(1.0\text{-aT}^2)$	Fit to $\sigma_{O,x}(1.0\text{-aT}^2)$	Fit to $\sigma_{O,\omega}(1.0\text{-aT}^2)$
1	20.42	3.37×10^{-5}	959	20.16	1.96×10^{-6}	715	19.99	1.15×10^{-7}	596	20.19	3.18×10^{-6}	745
2	18.22	3.00×10^{-5}	1037	17.99	1.94×10^{-6}	718	17.84	2.00	631	18.01	2.80×10^{-6}	736
3	20.57	3.36×10^{-5}	959	20.30	2.05	698	20.13	1.21	585	20.34	3.34×10^{-6}	747
4	21.53	3.12×10^{-5}	960	21.25	1.89	727	21.07	1.03	624	21.28	2.87×10^{-6}	738
5	19.31	3.08×10^{-5}	1018	19.06	1.84	737	18.50	1.00	631	19.08	2.80×10^{-6}	736
6	24.85	3.34	964	24.52	2.02	703	24.32	1.02	629	24.55	2.63×10^{-6}	732
7	25.07	2.99	1038	24.74	2.02	703	24.54	1.09	610	24.77	2.63×10^{-6}	732
8	26.13	3.00	1037	25.79	2.08	693	25.57	1.14	599	25.82	2.70×10^{-6}	734
9	24.26	3.41	951	23.95	1.96	715	23.74	1.20	587	23.99	3.30×10^{-6}	747
10	26.64	3.02	1031	26.30	1.84	737	26.08	1.04	621	26.33	2.66×10^{-6}	732
11	24.68	2.99	1038	24.36	2.02	703	24.16	1.09	610	24.40	2.80	736
12	25.48	3.34	964	25.15	1.97	721	24.94	1.14	595	25.18	2.55×10^{-6}	730

this study, this interpretation of the maximal behavior of H_c and R seems valid. The critical dimension determined from Figures 20 and 21 at 298°K are ~ 1200 and $\sim 1100\text{\AA}$, respectively. As temperature decreases, the front-edge of the maxima moves to smaller VMPS until near 40°K no maxima can be definitely detected.

Figure 22 shows the temperature dependence of H_c for two samples of $\delta\text{FeO(OH)}$. One sample (VMPS = 585 \AA) is superparamagnetic at room temperature. The other (VMPS = 1284 \AA) has well-developed hysteresis properties at 298°K. H_c approaches zero fairly slowly. At lower temperatures it increases linearly with decreasing T to a broad shoulder. The position of this shoulder was dependent on particle size. For samples of smallest VMPS the shoulder was barely detectable at 50°K. At temperature below the shoulder point, H_c again increases fairly linearly with decreasing T , but at a rate much slower than before.

R increases smoothly with temperature as shown in Figure 23. The approach of R to zero is not marked by the "tailing-off" seen in the temperature dependence of H_c . For this reason extrapolation of R to zero was used to determine T_b for the samples in Table 5.

Electron micrographs show that the particles of $\delta\text{FeO(OH)}$ are best approximated as oblate spheroids. Such a particle shape will not give rise to hysteresis effects.¹³ Similarly, the temperature dependence of H_c is not directly proportional to $\sigma_\infty(T)$ as would be expected if shape anisotropy were the source of the hysteresis

Table 9

Effect of Hydrothermal Treatment

of $\delta\text{FeO(OH)}$ on $\sigma_{\infty}(298)$

Temperature of Treatment (°C)	Time of Treatment (days)	$\sigma_{\infty}(298)$ (gauss/gm)	VMPS (Å)
100	0	22.07	1284
100	1	17.95	--
100	2	16.89	--
100	3	14.90	--
100	4	14.95	--
100	5	13.17	--
100	7	10.78	1333
80	1	22.00	--
80	2	19.85	--
80	3	18.80	--
80	4	17.22	--
80	6	15.70	--
80	7	15.65	1302
50	1	22.23	--
50	2	22.13	--
50	3	21.95	--
50	4	22.00	--
50	5	21.50	--
50	6	20.44	--
50	7	20.54	1273

properties.^{13, 28} The hysteresis effects of $\delta\text{FeO}(\text{OH})$ must then arise from magnetocrystalline anisotropy. Further, the particle shapes make a uniaxial description a good approximation of the form of the anisotropy.

Anisotropy constants at 0 °K were calculated from the Stoner Wohlfarth formula.¹³

$$K(0) = \frac{1}{2} H_c(0) \sigma_\infty(0)$$

Anisotropy constants at other temperatures were determined by the method of Asti and Rinaldi.¹⁴ These values were then fitted to the expression

$$\frac{K(T)}{K(0)} = \left[\frac{\sigma_\infty(T)}{\sigma_\infty(0)} \right]^s$$

Fits for samples 1-13 could be made to 95% confidence for values of s between 7.5 and 8.7. Fits to the expression with $s = 8.0$ could be made for all samples with a minimum confidence of 85%.

Discussion

The results indicate that the physical description of an individual sample of $\delta\text{FeO}(\text{OH})$ is intimately related to the nature of the intermediate ferrous hydroxide from which the sample is produced. This intimacy is consistent with the topotactic relationship between the $\delta\text{FeO}(\text{OH})$ and $\text{Fe}(\text{OH})_2$ structures suggested by their X-ray powder diffraction patterns^{5, 15} and the well-known stability of the ferrous hydroxide structure to oxidation.¹⁶ The tremendous insolubility of $\text{Fe}(\text{II})$ and $\text{Fe}(\text{III})$ ions in the preparative medium which prevents

dissolution and reformation of the structure during oxidation may well be the source of this simple relationship between structures.

Certainly, when base concentration in the preparative medium drops below 1F, and the solubility of the ions is greater, the products of oxidation cannot be topotactically related to ferrous hydroxide.

Rapid oxidation is also essential to the formation of the $\delta\text{FeO}(\text{OH})$. Slower oxidation processes allow structural transformations to thermodynamically more stable phases such as $\alpha\text{FeO}(\text{OH})$ and $\text{Fe}(\text{OH})_3$. Speedy oxidation assists in quenching the structure and yields a kinetically stable, topotactically related oxidation product.

The variation in particle size with solute concentration of the preparative medium is unusual. As a rule, precipitates decrease in particle size with increasing reagent concentration. The opposite behavior is encountered only among a few very insoluble precipitates such as silver chromate,¹⁷ silver thiocyanate,¹⁸ nickel gloxime,¹⁹ and BaSO_4 at reagent concentrations comparable to the Fe^{2+} concentrations used in this study.²⁰ Often it was found that initially these precipitates are metastable and alter upon aging. The dependence of $\delta\text{FeO}(\text{OH})$ particle size on sodium ion concentration is difficult to rationalize. The contamination of all samples of $\delta\text{FeO}(\text{OH})$ with sodium ion suggests that this ion may be more directly involved in the precipitation process than merely contributing to the viscosity of the medium. This point is explored in greater detail in Chapter 5.

The thermal effects on particle size are more classical in aspect. VMPS increases with both increasing preparative temperature and aging time. Extrapolation of the regression lines in Figures 10 and 11 to zero aging time and to the freezing point of the medium ($\sim -15^\circ\text{C}$) predicts finite particle sizes (170 and 184\AA , respectively). For very short aging times, dendritic particles form. Such behavior has been interpreted by Turnbull²¹ as indicative of the formation of nucleating particles by a process high order in concentration. The ferrous hydroxide precipitate may nucleate from particles of about $170 \pm 50\text{\AA}$ in size. The insolubility of the precipitate in the medium constrains particle growth to follow an aggregation and cementation mechanism. Figure 11 shows that some limitation in particle growth occurs after a fairly short period of aging. Oxidation apparently terminates all particle growth.

Log-normal particle-size distributions are often found among particle assemblages subjected to some mechanical process. Normal distributions are encountered among precipitation products. The cementation and aggregation growth process will yield a log-normal size distribution such as found in the samples of this study. Alternatively, the extensive washing process each of the samples underwent may be the distribution determining event in their preparative history.

The magnetic behavior of $\delta\text{FeO}(\text{OH})$ is consistent with the behavior expected for fine-particulate ferrimagnets possessing uniaxial anisotropy. Exponential parameters in the temperature dependencies of magnetization and the anisotropy constants are consistent with those found for other ferrimagnets.^{25, 29}

The small Bohr magneton numbers found for the samples indicate that only 10% of the ferric ions have uncompensated spins. (It is interesting to note in this regard that the breakdown of the ferrous hydroxide structure during slow oxidation occurs at about 10% conversion.¹⁶) Hydrothermal treatment anneals these uncompensated spins probably by supplying the energy necessary for the ions to relocate in more favorable sites. The hydrothermal treatment is then much like thermal decomposition of $\delta\text{FeO}(\text{OH})$, though it proceeds at a much slower rate. This behavior is consistent with either of the two models of the $\delta\text{FeO}(\text{OH})$ structure which have been proposed based on X-ray powder diffraction evidence.^{1, 22} Magnetic phenomena are not by themselves sufficient to choose between these models as implied by other authors.²³ But, the quantitative aspects of the magnetic behavior and the chemical behavior of the phase favor the model proposed by S. Okamoto²² in which all magnetic ions are randomly distributed in octahedral sites.

The dependence of the magnetic moment of $\delta\text{FeO}(\text{OH})$ on particle size cannot be rationalized in terms of a homogeneous magnetic species. If, instead, it is assumed that each particle of $\delta\text{FeO}(\text{OH})$ is surrounded by a nonmagnetic layer, then the saturation magnetization of a particle assemblage of VMPS = D will be described by equation 4,

$$\frac{\sigma_{\infty}(\text{D}, 0^{\circ}\text{K})}{\sigma_{\infty}(\infty, 0^{\circ}\text{K})} = \left(1.0 - \frac{6\ell}{\text{D}} + \frac{12\ell^2}{\text{D}^2} - \frac{8\ell^3}{\text{D}^3} \right) \quad \text{eqn 4}$$

where $\sigma_{\infty}(\infty, 0^{\circ}\text{K})$ is the saturation magnetization of an infinitely large particle, and ℓ is the thickness of the magnetically dead region.

The data in Figure 15 can be fit to equation 4 with $\ell = 31 \pm 4\text{\AA}$ and $\sigma_{\infty}(\infty, 0^{\circ}\text{K}) = 28.43 \pm 0.11$ gauss/gm with a confidence of at least 95%. This magnetically dead layer corresponds to a layer 6 to 10 unit cells thick. The dead layer effect will be discussed in greater detail in Chapter 5.

Rationalization of the dependence of magnetization on the thermal treatment of the intermediate ferrous hydroxide is more complicated. The concept of a magnetically dead region surrounding each of the particles well accounts for the initial portions of Figures 16 and 17 where magnetization increases with preparative temperature and aging time. The dashed lines in these figures are best-fit polynomial expressions in terms of the independent variable. The solid lines are derived from equation 4 using $\ell = 31\text{\AA}$, $\sigma_{\infty}(\infty, 0^{\circ}\text{K}) = 38.4$ gauss/gm and the linear regressions of Figures 10 and 11 to

define particle size. Tables 6 and 7 include magnetizations calculated for the samples with this model.

To account for the maximizing behavior of magnetization, an additional effect must become significant at temperatures greater than 40-50°C and for aging times greater than 8 minutes at 50°C. The decline in magnetization in Figures 16 and 17 is reminiscent of the thermal annealing of the magnetic moment of $\delta\text{FeO}(\text{OH})$ described above. Evidence from the physical descriptions of the samples shows that the intermediate ferrous hydroxide precipitates in a metastable structure. Other authors have also noted this behavior of ferrous hydroxide.² The medium of precipitation prevents dissolution processes such as Ostwald ripening from being a pathway for the perfection of the structure. The medium will not, however, prevent ion migration within the lattice to more favored sites, which will occur after sufficient aging times or at sufficient temperatures. The evidence herein indicates that upon oxidation the ions in the thermodynamically favored sites will have compensating spins. To the extent that thermally induced ion migration occurs, the magnetization will be reduced, and the maximal behavior in the figures would be expected.

Hysteresis behavior of the samples of $\delta\text{FeO}(\text{OH})$ is consistent with the behavior of fine particulate ferromagnets outlined by Jacobs and Bean.¹¹ Particles of the smallest size have their magnetic moments disoriented by thermal effects. Such particles cannot develop hysteresis losses in their magnetization curves since they are in thermodynamic equilibrium. Once the particle exceeds a critical

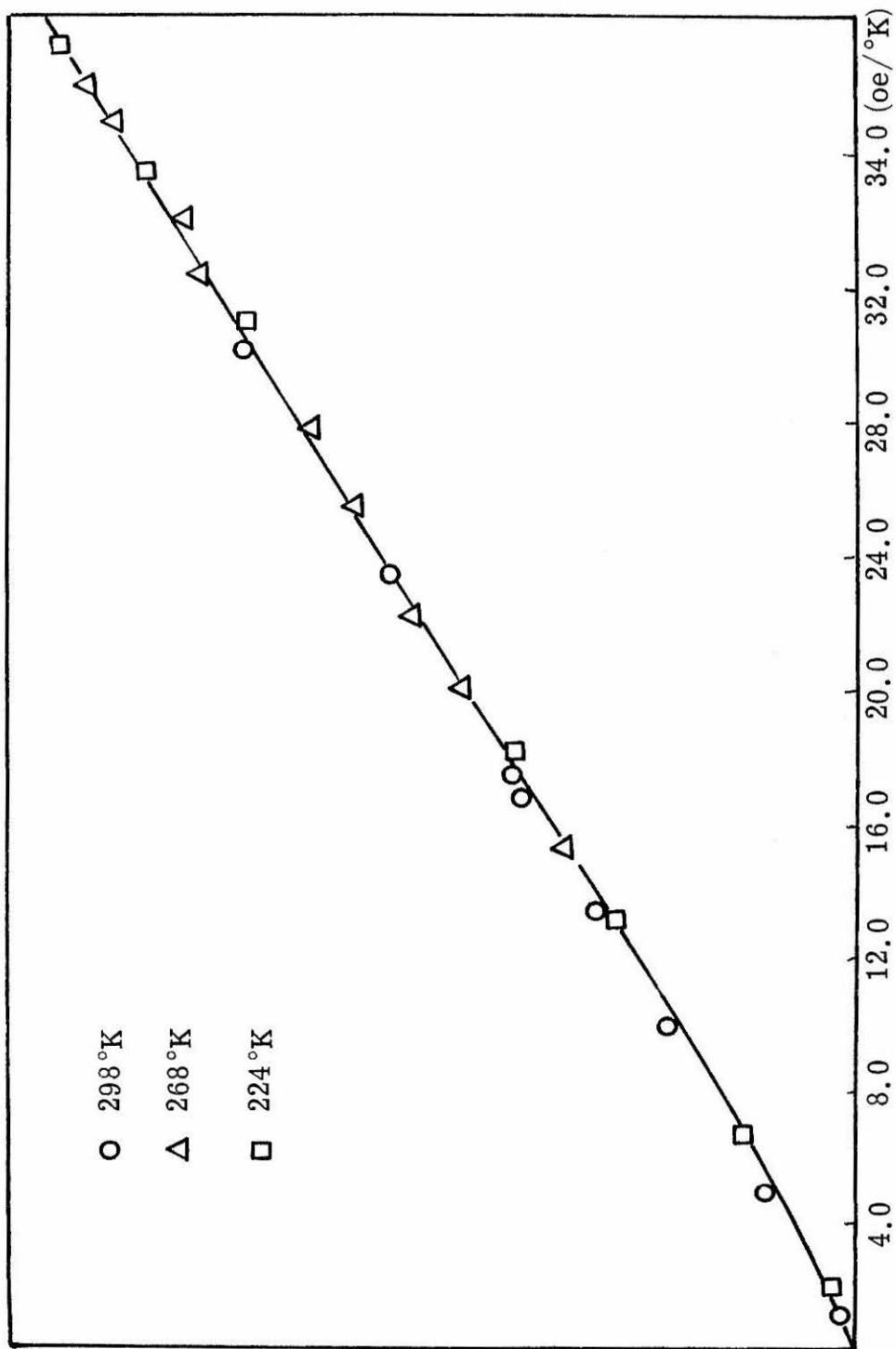


Figure 19. Plot of H/T versus magnetization (arbitrary units) for a sample of VMPS = 485 Å

above the sample blocking temperature ($T_b \approx 200^\circ\text{K}$).

dimension, a single magnetic domain develops. Since there is only one domain within the particle, no easy mechanisms such as domain wall movement exist for reversal of the moment of the particle in a reversed magnetic field. Reversal of the moment of an immobilized single-domain particle must occur by rotation, either coherent or incoherent, of the magnetization vector. Such reversal is opposed by an energy barrier. In $\delta\text{FeO}(\text{OH})$ this barrier is due to the magnetocrystalline anisotropy. A finite applied field (H_c) is necessary to expedite the reversal process within experimental times, and remanent magnetization is observed. Experimentally, the critical dimension for $\delta\text{FeO}(\text{OH})$ particles is 1100\AA . This value is similar to that found for cobalt and nickel ferrites²⁵ as well as other ferri-magnetic phases.²⁶ It is in good agreement with the lower-bound estimate for critical size from the Wohlfarth expression²⁷:

$$D_c = 2b \left(\frac{A}{K}\right)^{\frac{1}{2}} \cong 1000 \text{\AA}$$

where D_c is the critical dimension, b is factor to convert from a geometric measure of length to the volumetric measured used in this study, $A = 10^{-6}$ ergs/cm, and K is the anisotropy constant.

As temperature is decreased, the critical dimension for single domain behavior also decreases. The ratio $2R = 2\sigma_R(T)/\sigma_\infty(T)$ is a measure of the fraction of particles within a sample which are single domain in size.¹³ The thermal dependence of $2R$ shows that subdomain particles exist in all of the samples down to 70°K . For samples of

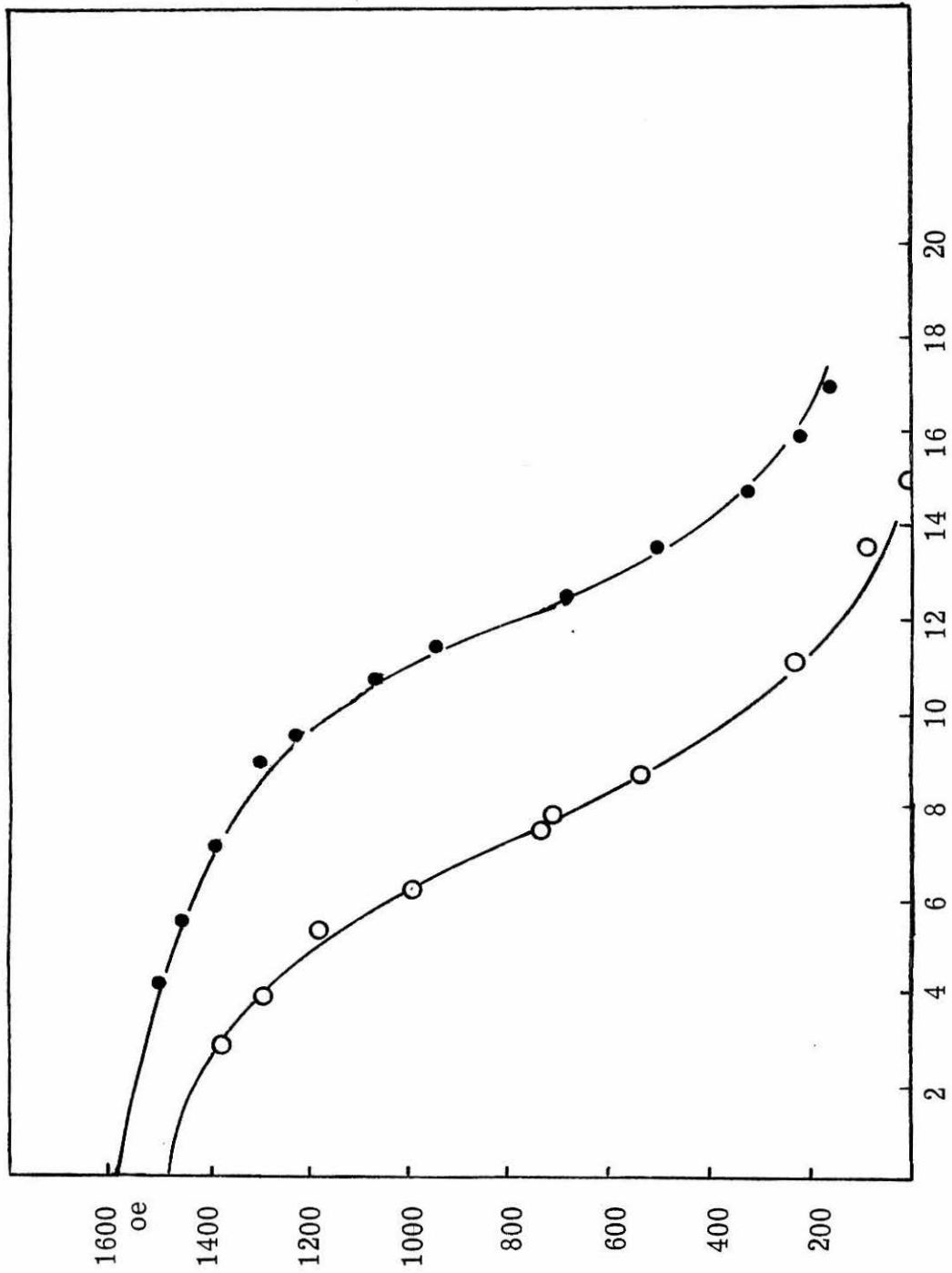


Figure 22. $H_c(T)$ versus $T^{1/2}$ for a sample of $VMPS = 1284 \text{ \AA}$ (dark circles) and a sample of $VMPS = 501 \text{ \AA}$ (open circles).

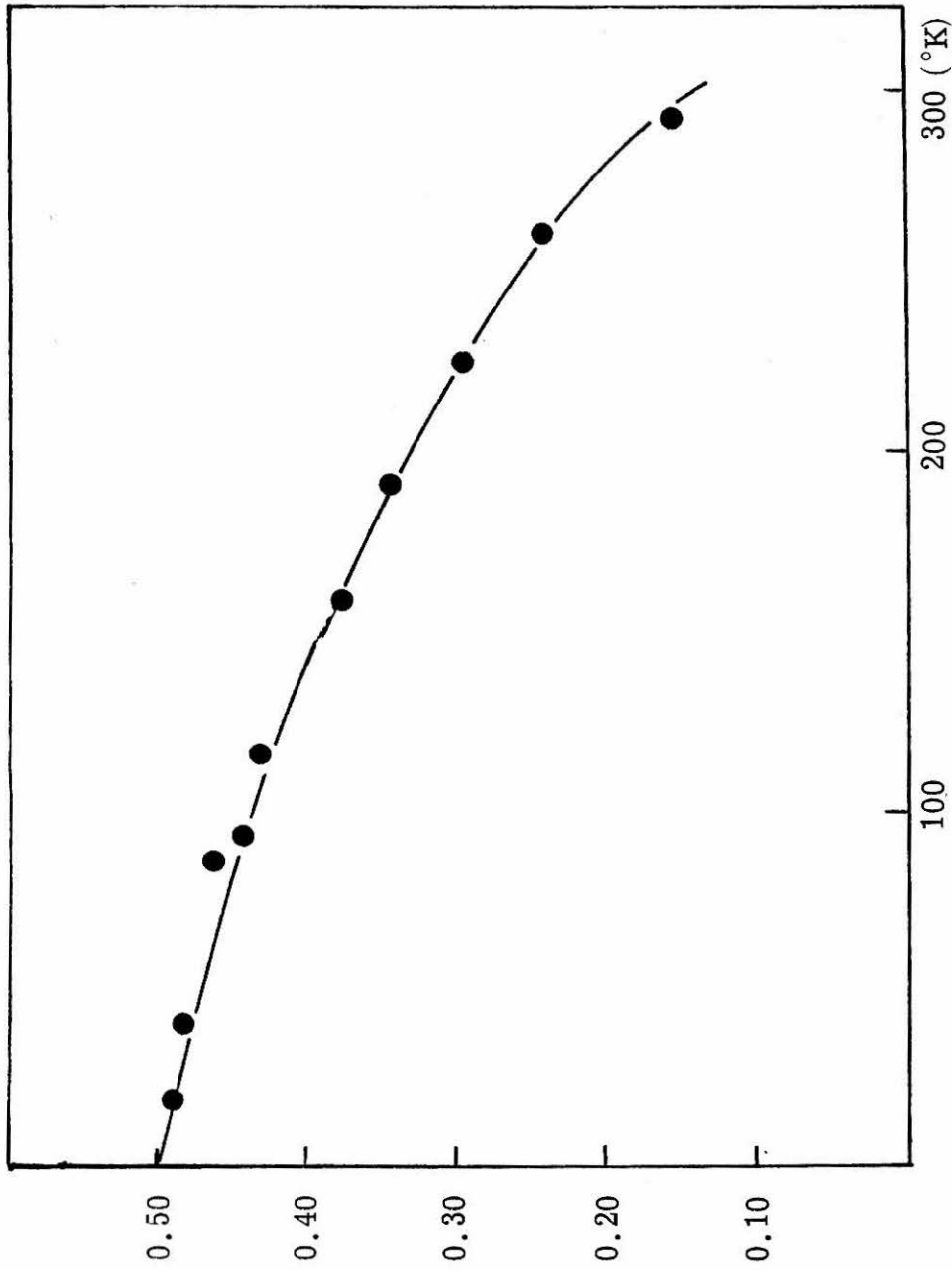


Figure 23. Plot of the ratio of magnetization at zero field and at infinite field versus temperature for a sample of VMPS = 1284\AA .

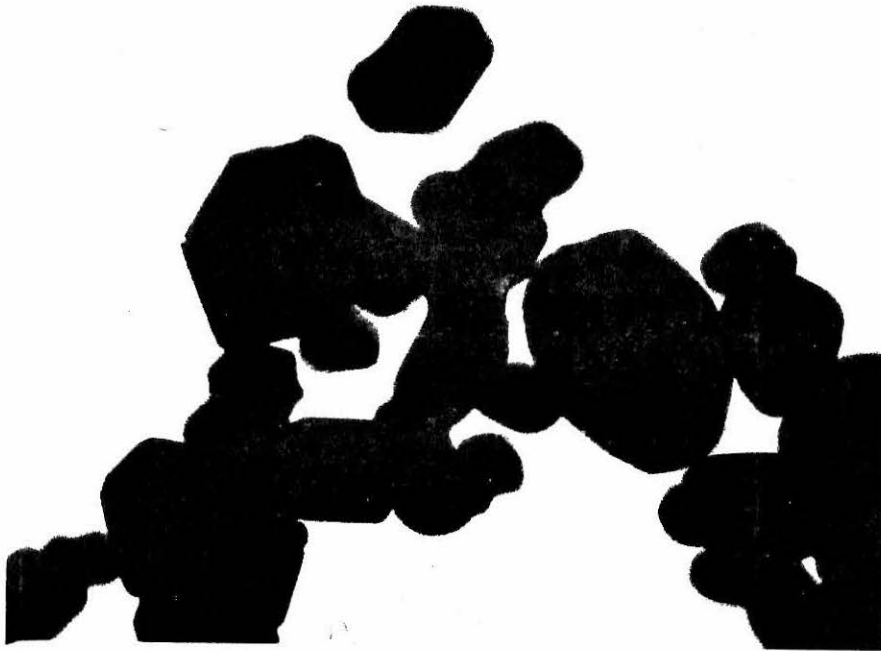


Figure 24. δ FeO(OH) hydrothermally aged at 100 °C for 7 days.
Magnification = 184,460 \times .

small VMPS some superparamagnetic particles exist to at least 40°K, though at this temperature all the samples were made up of predominantly single-domain particles.

Particles of sufficient size ought to develop multiple domains. The appearance of many domains in a particle would present easy mechanisms for reversal of the particle magnetization. Coercive field would then decrease. No such decrease in H_c was observed in the samples even among those of largest VMPS. Particle interactions are well known to prevent the nucleation of multiple magnetic domains²⁰ and are probably so operating in the samples of $\delta\text{FeO}(\text{OH})$ of this study.

References

1. M. Francombe and H. Rooksby, Clay Minerals Bulletin, 4, 1 (1959).
2. L. A. Welo and O. Baudisch, Chem. Revs., 15, 45 (1934); and references therein.
3. F. Treadwell and W. T. Hall, "Analytic Chemistry," Vol. 2, 1963, John Wiley and Sons, Inc., New York.
4. Schwartzkopf Microanalytic Laboratories.
5. J. Bernal, D. Dasgupta, and A. Mackay, Clay Minerals Bulletin, 4, 15 (1959).
6. G. Herdon, "Small Particle Statistics," (196), p. 45.
7. R. A. Robinson and H. S. Harned, Chem. Revs., 28, 429 (1941).
8. R. H. Stokes and R. A. Robinson, J. Amer. Chem. Soc., 70, 1870 (1948).
9. H. A. Laitinen, "Chemical Analysis," McGraw-Hill Book Co., New York, 1960.
10. C. F. Wells, J. Chem. Soc. (A), 2740 (1969).
11. I. S. Jacobs and C. P. Bean, "Magnetism," Vol. III, G. T. Rado and H. Suhl, eds., Academic Press, 1963, New York.
12. W. H. Meiklejohn and C. P. Bean, Phys. Rev., 102, 1413 (1956); 105, 904 (1957).
13. E. C. Stoner and E. P. Wohlfarth, Philos. Trans. Roy. Soc., A240, 599 (1948).
14. G. Asti and S. Rinaldi, Phys. Rev. Letters, 28, 1584 (1972).

15. D. R. Dasgupta, Indian J. Phys., 35, 401 (1961).
16. G. Keller and W. Feitknecht, Z. anorg. Chem. 262, 61 (1950).
17. E. A. Gulbransen, R. T. Phelps, and L. Langer, Ind. Eng. Chem., Anal. Ed., 17, 646 (1945).
18. R. B. Fischer, J. Chem. Ed., 24, 484 (1947).
19. R. B. Fischer and S. H. Simonsen, Anal. Chem., 20, 1107 (1948).
20. P. P. VonWeimarn, Chem. Revs., 2, 217 (1926).
21. D. Turnbull, J. Appl. Phys., 20, 817 (1949).
22. S. Okamoto, J. Amer. Ceramic Soc., 51, 594 (1968).
23. P. Kulgawczuk, A. Obuszko, and A. Szytula, Phys. Status Solidi, 26, K83-85, (1968).
24. C. P. Bean and J. D. Livingston, J. Applied Phys., 30, 120S (1959).
25. W. J. Schuele and V. D. Deetsereck, Fine Partile Ferrites in "Ultrafine Particles," W. E. Kuhn, ed., John Wiley and Sons, New York, 1963, p 218.
26. R. Tebble and D. Craik, "Magnetic Materials," John Wiley and Sons, New York, 1969.
27. E. P. Wohlfarth, Chapter 7, "Magnetism," Vol. III, G. T. Rado, and H. Suhl, eds., Academic Press, New York, 1963.
28. D. F. Eagle and J. C. Mallinson, J. Appl. Phys., 28, 995 (1967).
29. H. Shenker, Phys. Rev., 107, 1246 (1957).
30. A. H. Morrish and L. A. K. Watt, Phys. Rev., 105, 1476 (1957).
31. G. F. Huttig and H. Moldner, Z. Anorg. Allgem. Chem., 184, 180 (1929).

CHAPTER 5

INFLUENCE OF CATIONIC IMPURITIES AND
MAGNETICALLY DEAD LAYERS ON THE
MAGNETIC BEHAVIOR OF $\delta\text{FeO}(\text{OH})$ Abstract

Impurities in $\delta\text{FeO}(\text{OH})$ are discussed. Excess water is shown to be an adsorbed species. Cationic impurities are shown to be more tenaciously entrained by the solid. The magnetic behavior of $\delta\text{FeO}(\text{OH})$ prepared in LiOH-LiCl and KOH-KCl media is described. Saturation magnetization of the samples is used to postulate the existence of a magnetically dead region surrounding the $\delta\text{FeO}(\text{OH})$ particles. The approach to saturation and hysteresis properties of the samples are found to be consistent with this model.

Chapter 4 described the magnetic behavior of $\delta\text{FeO}(\text{OH})$ and how that behavior is influenced by the preparative history of individual samples of the material. It did not, however, shed light on the structural alterations that must inevitably be the source of the variations in magnetic behavior. Chapter 4 did suggest that cationic impurities and possibly non-magnetic layers surrounding the particles may be the origin of many of the variations. It is the purpose of this chapter to pursue these two possibilities in greater detail.

The impact of impurities and magnetic "dead" layers on the behavior of $\delta\text{FeO}(\text{OH})$ increases with decreasing particle size. For this reason, superparamagnetic samples of $\delta\text{FeO}(\text{OH})$ with varying types and concentrations of impurities were used in this investigation.

Experimental

(A) Preparation of Samples. Samples of $\delta\text{FeO}(\text{OH})$ prepared in NaOH-NaCl media discussed in the chapter were those prepared in the previous investigation. Analytic data for samples 1-40 and magnetic data for samples 1-13 of the previous chapter are used in this study.

Samples of $\delta\text{FeO}(\text{OH})$ prepared in LiOH-LiCl media and KOH-KCl media were prepared by procedures completely analogous to those described in Chapter 4. They were prepared with 0.0034F Fe^{2+} and the intermediate ferrous hydroxide was aged 5.0 minutes at 50°C prior to oxidation to $\delta\text{FeO}(\text{OH})$. Concentrations of the solutes in the precipitation media were used to control the particle size. The preparative behavior in the lithium and potassium media was quite

Table 1

Preparative and Analytic Data for
 $\delta\text{FeO}(\text{OH})$ Samples Produced in KOH-KCl Media

Sample Number	Condition of Preparative Medium ^a			Analytic Data				
	[K ⁺] ^b	[OH ⁻] ^c	[Cl ⁻] ^c	GMPS [Å]	σ_g	VMPS [Å]	for Product [K ⁺] ^d	H ₂ O
1	1.22F	1.22F	0.00F	162	1.47	253	0.040	5.25
2	2.78	2.78	0.00	176	1.46	270	0.045	4.51
3	5.31	5.31	0.00	270	1.43	396	0.130	3.80
4	5.11	0.985	4.12	342	1.44	510	0.175	2.70
5	6.35	3.07	3.28	376	1.43	552	0.18	2.50
6	6.89	6.89	0.00	327	1.43	480	0.175	3.11
7	9.35	9.35	0.00	526	1.44	784	0.245	1.68
8	10.22	5.03	5.19	498	1.45	754	0.265	2.12
9	13.21	13.21	0.00	580	1.41	826	0.296	1.75

^a Samples were prepared in 0.0034F Fe²⁺, aged 5 minutes prior to oxidation at 50°C.

^b By summation of [OH] + [Cl⁻]. Error = ± 1.5%.

^c Error = ± 1.0%.

^d Error = ± 0.01%.

^e Water in excess of that expected from stoichiometry. Error = ± 0.2%.

Table 2

Preparative and Analytic Data for
 $\delta\text{FeO}(\text{OH})$ Samples Produced in LiOH-LiCl Media

Sample Number	Condition of Preparative Medium ^a			GMPS (Å)	σ_g	VMPS (Å)	Analytic Data for Product	
	[Li ⁺] ^b	[OH ⁻] ^c	[Cl ⁻] ^c				[Li ⁺] ^d (%)	H ₂ O ^e (%)
10	1.00F	1.00F	0.00F	183	1.48	290	0.215	4.2
11	0.91	0.91	0.00	137	1.49	221	0.29	4.8
12	1.86	0.53	1.33	122	1.43	179	0.30	4.8
13	2.75	2.75	0.00	349	1.44	250	0.22	2.65
14	3.07	3.07	0.00	418	1.45	632	0.281	2.20
15	2.25	0.93	1.32	292	1.44	435	0.24	3.15
16	5.26	2.99	2.27	573	1.43	841	0.33	1.60
17	4.04	4.04	0.00	584	1.41	832	0.325	1.90

^a Samples were prepared in 0.0034F Fe²⁺, aged 5 minutes prior to oxidation at 50°C.

^b By summation of [OH⁻] + [Cl⁻]. Error = ± 1.5%.

^c Error = ± 1.0%.

^d Error = ± 0.01%.

^e Water in excess of that expected from stoichiometry. Error = ± 0.2%.

similar to that previously noted for preparation in NaOH-NaCl media. Particle size increased fairly linearly with alkali metal ion concentration as shown in Figures 1 and 2. The concentration range used for the LiOH-LiCl media was limited by the low solubility of these salts. No difficulty was encountered in the oxidation of ferrous hydroxide at maximum concentrations of alkali metal hydroxides such as was observed in the NaOH-NaCl media. Again it was noted that when base concentration was less than $\sim 1.0F$ products of inferior quality were prepared regardless of total alkali metal ion concentration.

Samples prepared in LiOH-LiCl media were difficult to free of excess alkali metal salts. These samples required more extensive washing than samples prepared in other media. Lithium carbonate, formed during the washing process was especially difficult to remove. Electron microscopy was especially useful for monitoring the washing process of these salts. Figure 3 shows an electron micrograph of a sample contaminated with lithium carbonate. Samples used in this study were entirely free of lithium carbonate as indicated by electron microscopy and infrared spectroscopy. It was noted that acidification of the sample to pH 3 with acetic acid greatly accelerated the washing process. No samples so purified were used in this investigation.

Numerous attempts were made to prepare δ FeO(OH) from ferrous hydroxide precipitated with bases other than alkali metal bases. Ammonium hydroxide, pyridine, tetramethyl ammonium hydroxide,

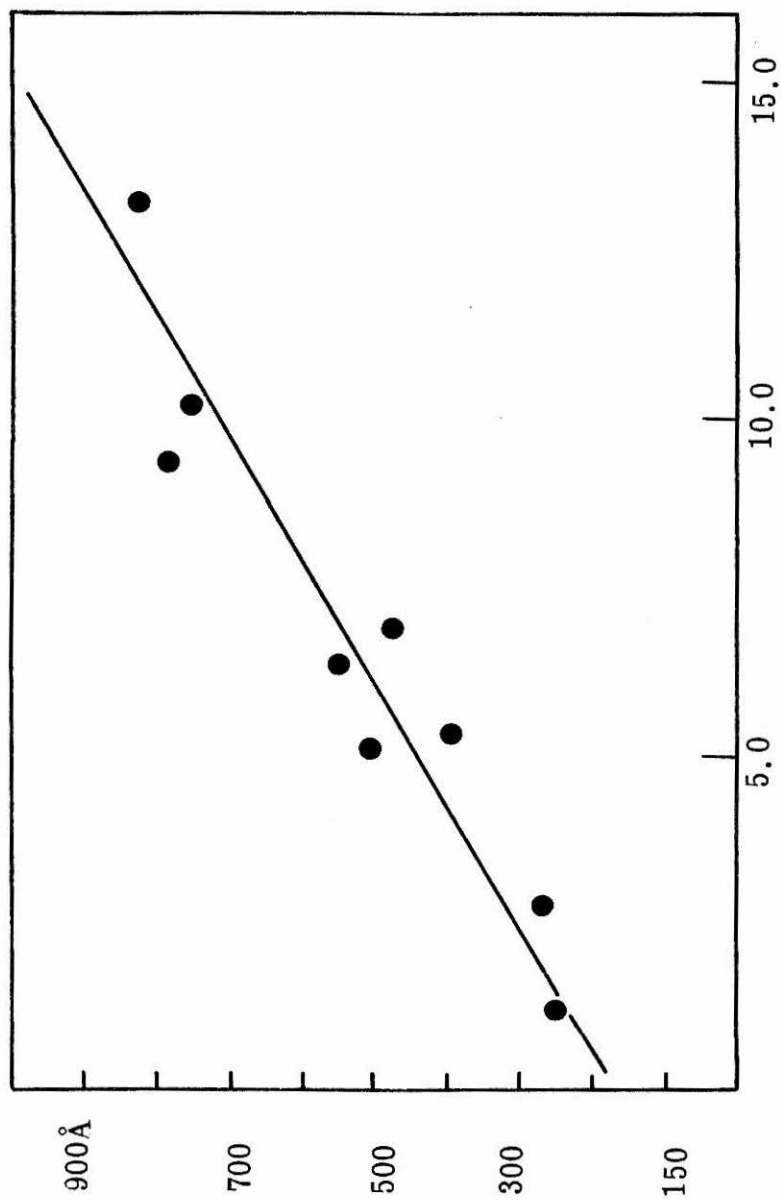


Figure 1. Formal concentration of potassium ion versus VMPS (Å) of $\delta\text{FeO}(\text{OH})$ prepared in KOH-KCl media. Linear regression line is $VMPS = (168 + 54 [K^+])/A$.

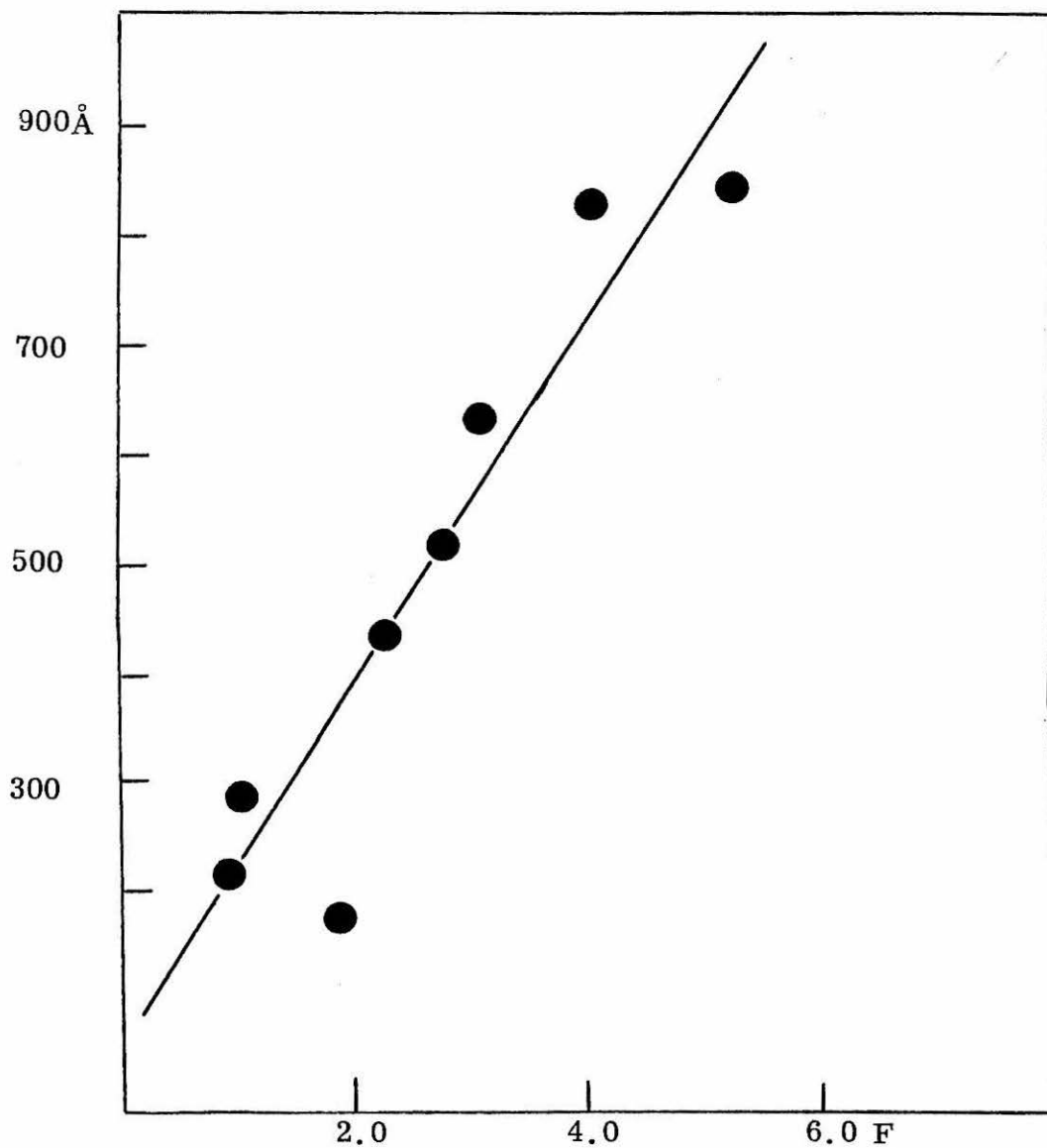


Figure 2. Formal concentration of lithium versus VMPS(Å) of δ FeO(OH) prepared in LiOH-LiCl media. Linear regression line is $VMPS = (63 + 163 [Li^+])\text{Å}$.

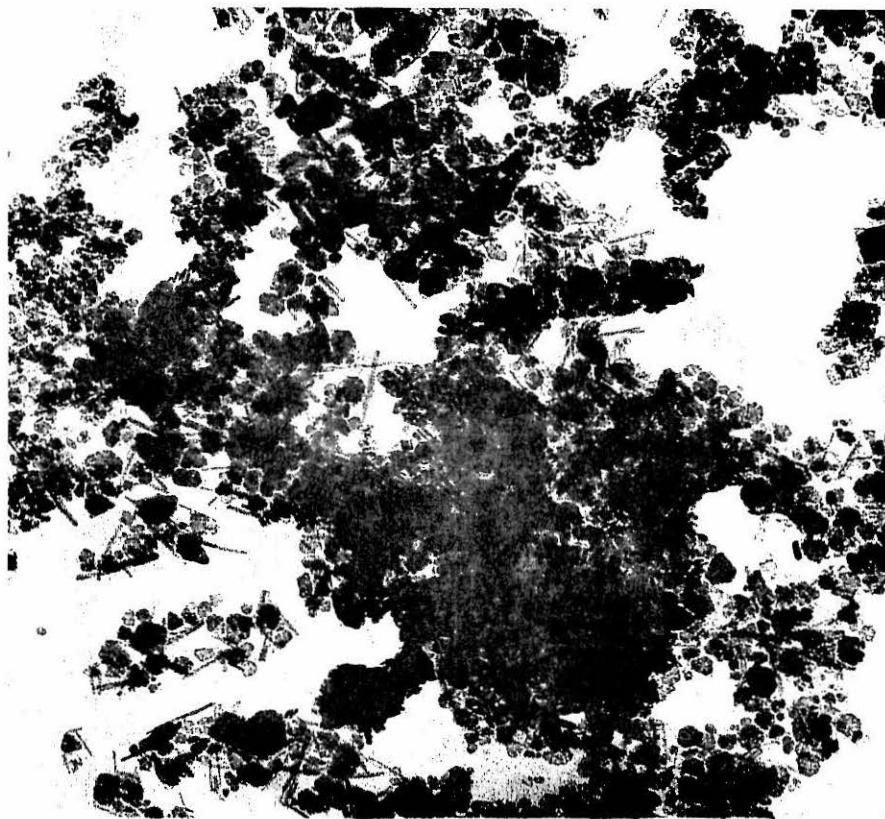


Figure 3. δ FeO(OH) prepared in LiOH-LiCl medium contaminated with lithium carbonate. Magnification = 106,850 \times .

and triethyl ammine were tried. In every case only a flocculent non-magnetic oxidation product which yielded no X-ray powder diffraction lines was obtained. Figure 4 shows an electron micrograph of the product obtained from ferrous hydroxide precipitated with ammonium hydroxide.

Attempts were made to prepare $\delta\text{FeO}(\text{OH})$ from ferrous hydroxide precipitated with concentrated ammonium hydroxide from a medium of concentrated (5N) NaCl. The product bore all the physical aspects of ferric hydroxide but was feebly magnetic $\sigma_{\infty}(297^{\circ}\text{K}) = 1.2$ emu/gm. This magnetic character disappeared over a period of one month. Electron micrographs of the product were much like that of Figure 4, and no hexagonal platelets of $\delta\text{FeO}(\text{OH})$ were observed. Again the product yielded no X-ray powder diffraction lines.

It was concluded that alkali metal cations were essential for the formation of $\delta\text{FeO}(\text{OH})$.

The samples of $\delta\text{FeO}(\text{OH})$ were authenticated by their X-ray powder diffraction patterns. The small particle size of samples used in this study greatly reduced the quality of these patterns. The breadths of the [101] and [102] reflections were such that d-spacings could not be measured. D-spacings for the other three reflections were, within experimental error, identical to those found for $\delta\text{FeO}(\text{OH})$ prepared in NaOH-NaCl media in Chapter 4. No additional reflections which might be attributable to other oxides of iron or other impurities were noted, nor did electron micrographs of the samples show evidence for impurity phases.

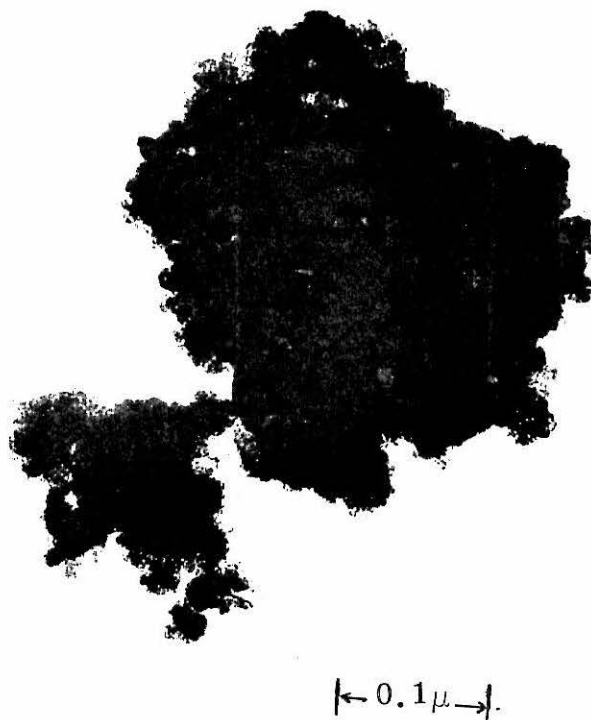


Figure 4 . Product of oxidation of ferrous hydroxide prepared in concentrated ammonia solution. Magnification 188850X.

All samples were ferrous iron-free when tested with potassium ferricyanide solution. Similarly, no evidence for chloride or sulfate ions was found when the samples were tested with AgNO_3 and BaCl_2 solutions, respectively. All samples were completely soluble in dilute hydrochloric acid. Analytic data are tabulated for the samples in Tables 1 and 2.

(B) Physical Characterization of the Samples. ESCA spectra of several of the samples were provided by Dr. Frank Grunthner of the Jet Propulsion Laboratory, Pasadena, California. I gratefully acknowledge Dr. Grunthner for his assistance in the acquisition and interpretation of these spectra.

Instrumental analysis and characterization of the samples were done as described in the previous chapter.

Electron micrographs of the samples prepared in LiOH-LiCl and KOH-KCl media were quite similar to those prepared in NaOH-NaCl media. The particle size distributions were log-normal with relatively constant σ_g . Particle size data were quite difficult to collect for samples of smallest mean particle size ($< 200 \text{ \AA}$). Consequently, plots of the cumulative number density versus the log of the particle diameter deviated somewhat from linear at the lower extreme of particle sizes ($< 50 \text{ \AA}$).

For some parts of this investigation the surface-area-mean particle size (SMPS) is a more meaningful quantity than either GMPS or VMPS. SMPS is readily computed from the geometric data by the

relationship

$$\log_{10} \left[\frac{\text{SMPS}}{\text{GMPS}} \right] = 4.605 \log_{10}^2 \sigma_g$$

Again, it was noted that occasional edge-on particles were about one-sixth as thick as they were long. However, no statistical data on thickness could be acquired. The method of particle size measurement treats the particles as if they were round discs for statistical purposes. For these reasons the volume factor used in the calculations in this study was taken to be $\pi/3$.

Results

(A) Analysis of Impurities in the Samples. All the samples of $\delta\text{FeO}(\text{OH})$ described in this thesis were contaminated with alkali metal cations and water in excess of that expected from the equivalent stoichiometry $\text{Fe}_2\text{O}_3 \cdot \text{H}_2\text{O}$. Where available, analytic data from previous investigations of $\delta\text{FeO}(\text{OH})$ also show persistent impurities of these types. A real stoichiometry for the δ phase is $[\text{FeO}(\text{OH})]_y \cdot 3/2y \text{M}_2^{\text{I}}\text{O} \cdot (x + y/2)\text{H}_2\text{O}$ where M^{I} is an alkali metal cation. Among the samples used in this thesis typical values of x and y are 0.125 and 0.005, respectively.

$\delta\text{FeO}(\text{OH})$ is formed only as extremely fine-particulate matter with tremendous surface area ($3200 \text{ m}^2/\text{gm}$). A most obvious source of impurities is surface adsorbed species. The amount of surface adsorbed impurity in a specimen ought to have a marked particle size dependence given by equation 1.

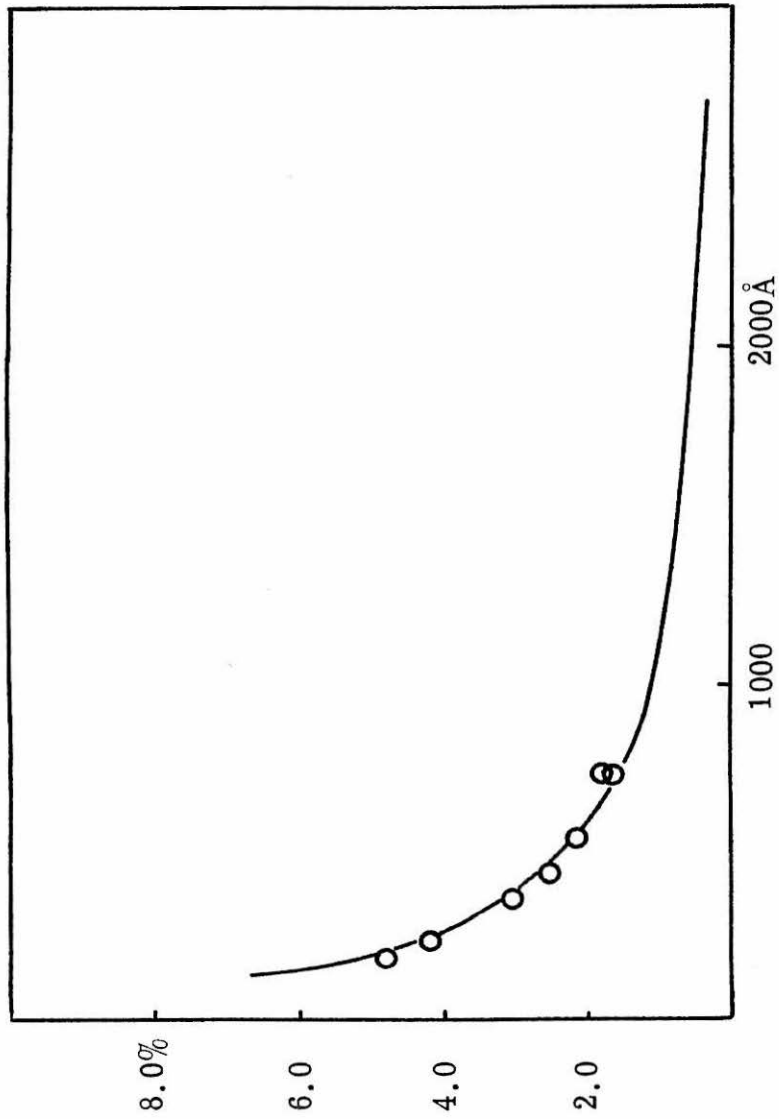


Figure 5. Weight percent excess water in samples of δ FeO(OH) prepared in LiOH-LiCl media versus SMPS (\AA) of samples.

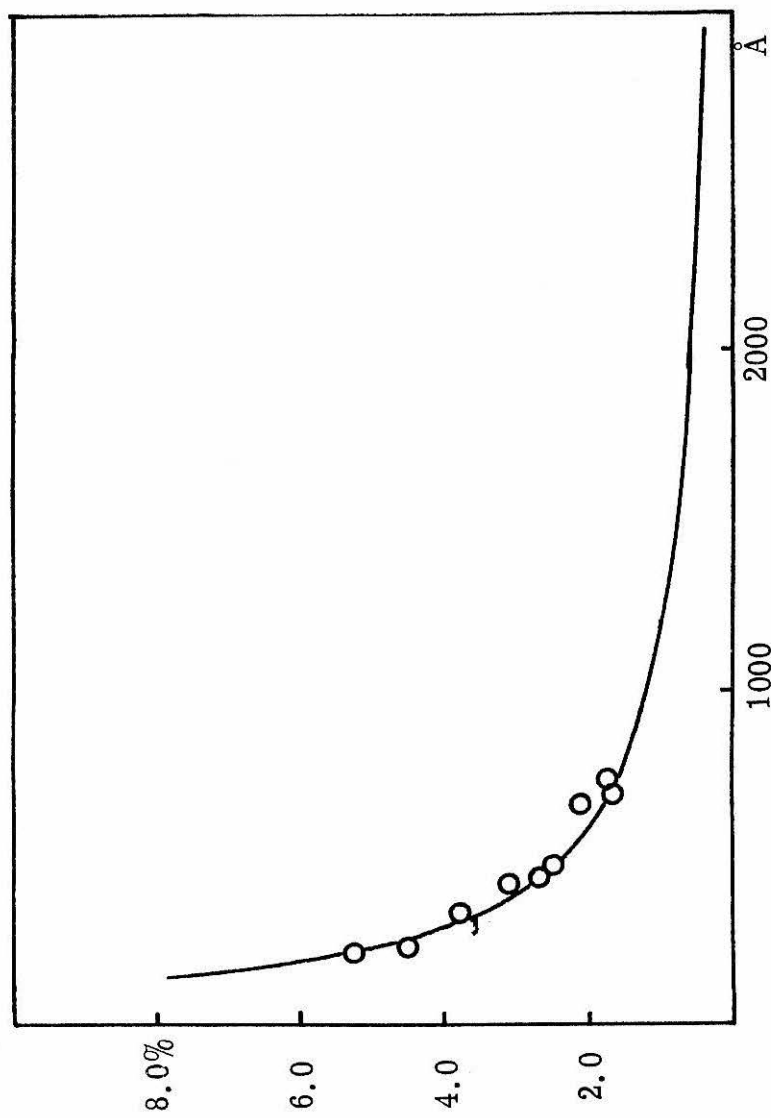


Figure 6. Weight percent excess water in samples of δ -FeO(OH) prepared in KOH-KCl media versus SMPS (\AA) of samples.

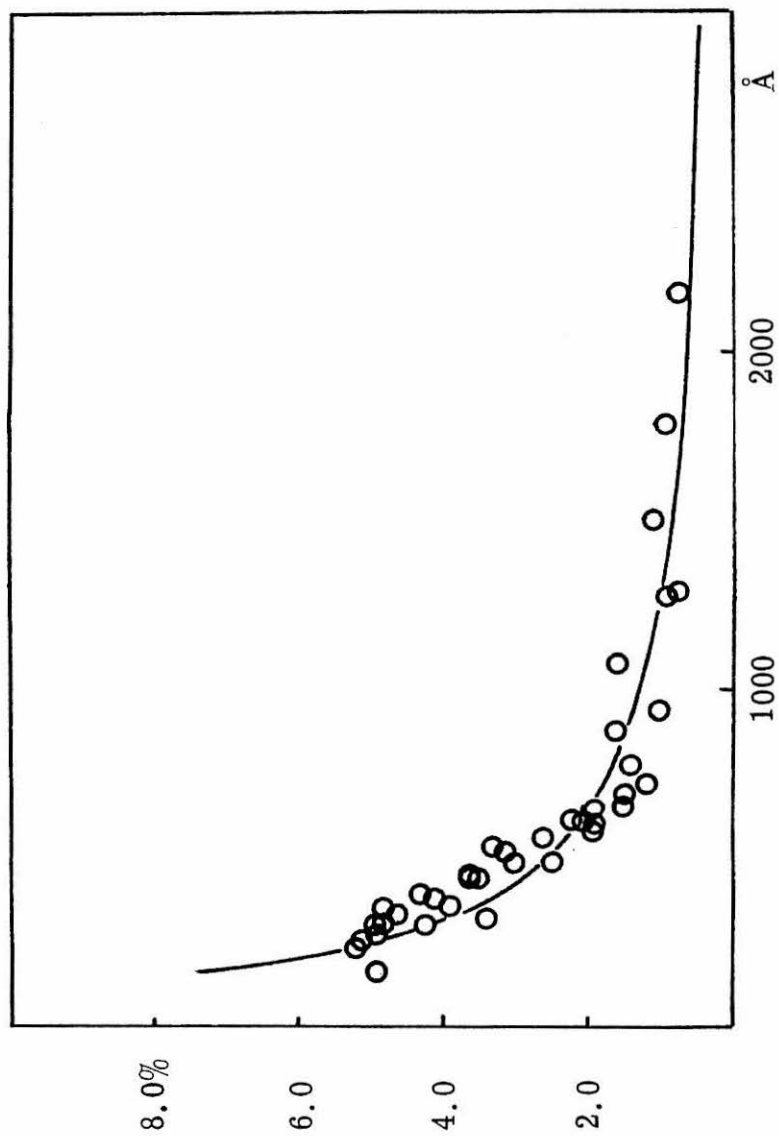


Figure 7. Weight percent excess water in samples of $\delta\text{FeO}(\text{OH})$ prepared in NaOH-NaCl media versus SMPS (\AA) of samples.

$$\text{weight \% impurity} = \frac{8 B/A f \cdot 100}{\rho N r}$$

B = molecular weight of impurity species

a = effective surface area occupied by a molecule of adsorbed species

f = fractional coverage of surface by adsorbed species.

ρ = density of particle

N = Avogadro's number

r = radius of particle

The amount of excess water in the $\delta\text{FeO(OH)}$ samples conforms well with this model. In figures 5, 6, and 7 the weight percent excess water for samples prepared in LiOH-LiCl, KOH-KCl, and NaOH-NaCl media, respectively, are plotted against sample SMPS. The solid line in these figures is the best least-squares fit of equation 1 to the data in the figures. Parametric values from the least squares fit were used to calculate the fractional coverage of the particle surface by water cited in Table 3. Errors in f correspond to the upper and lower

Table 3

Fractional Coverage of $\delta\text{FeO(OH)}$ Particles by Water*

<u>Media in Which Samples were Prepared</u>	<u>Fractional Coverage</u>
LiOH-LiCl	0.93 \pm 0.08
KOH-KCl	0.89 \pm 0.06
NaOH-NaCl	0.98 \pm 0.07

*Effective surface area of an adsorbed water molecule was taken to be 8.4\AA^2 (see reference 2).

support planes of the fits. Within the limits of uncertainty, the fractional coverage of the samples amounts to one mono-molecular layer of water.

The weight percent of cationic impurities in the samples is not at all described by equation 1. Figures 8 and 9 show the dependence of the weight percent of alkali metal cations in samples of $\delta\text{FeO}(\text{OH})$ prepared in KOH-KCl and NaOH-NaCl media on the VMPS of the samples. The marked dependence is obviously described by positive powers of VMPS. This type of dependence is difficult to rationalize in terms of a homogeneously contaminated phase. Models describing the contamination in terms of homogeneously distributed islands of entrapped species or coprecipitates also fail to describe the observed behavior.

Several heterogeneous models can be imagined which will predict the observed behavior. One of the simplest of these postulates that each particle contains a central core of impure material. Surrounding this core is a layer of material in which the impurities have been depleted. A most likely mechanism by which depletion might occur is the extensive washing each of the samples undergoes prior to analysis. Several descriptions of the $\delta\text{FeO}(\text{OH})$ particle can be formulated that are in keeping with the above postulate. The data of figures 8 and 9 were fit to the following descriptive models:

- (1) Uniform model: A uniform depletion layer of thickness g surrounds the particle. The weight percent impurity within the core is $C(\infty)$. The weight percent impurity in

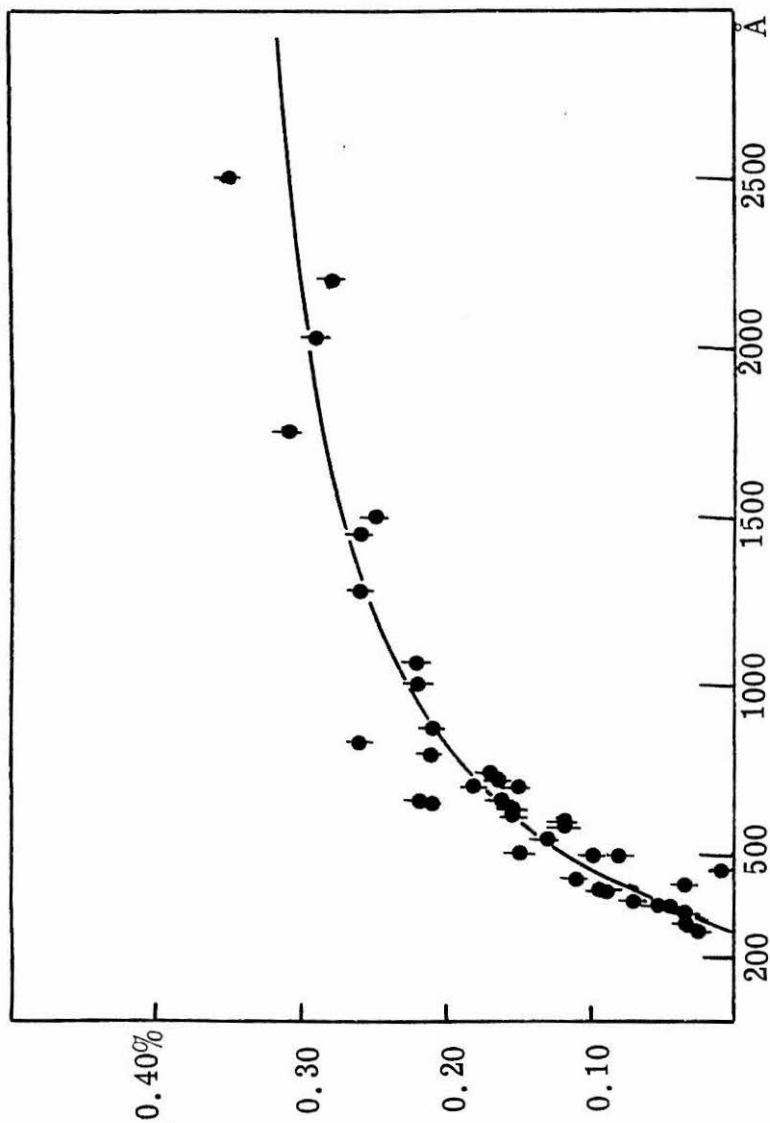


Figure 8. Weight % Na⁺ impurity in δ FeO(OH) prepared in NaOH-NaCl media versus VMPS. Solid line calculated for Uniform Depletion Layer Model.

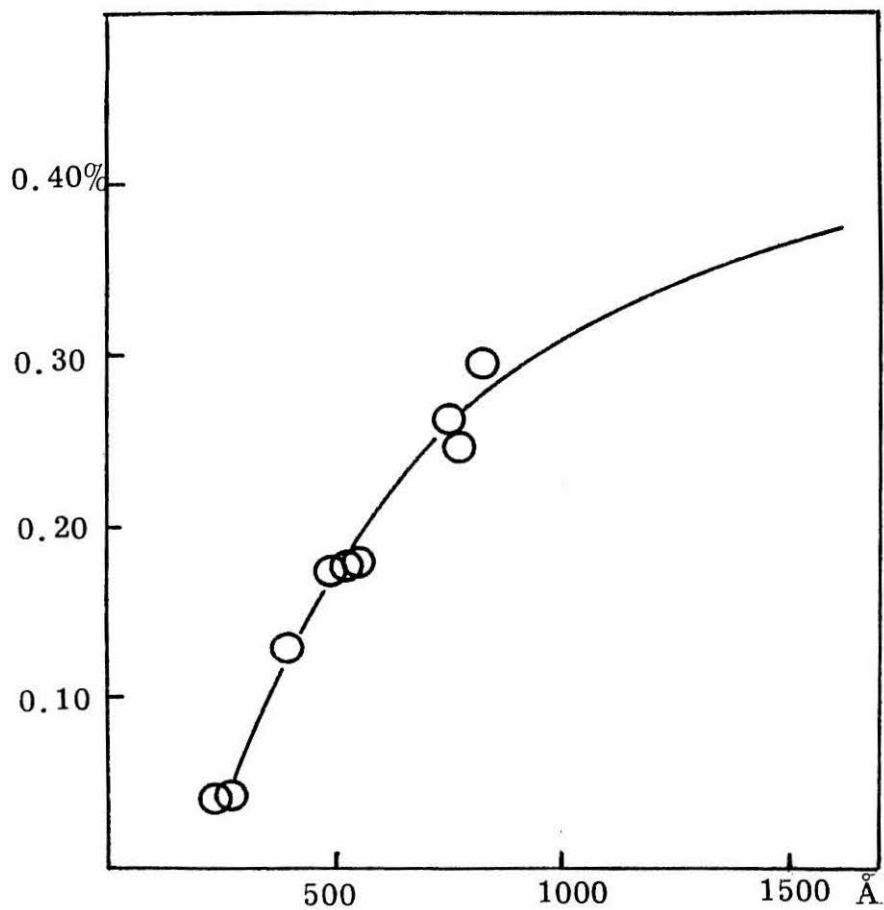


Figure 9. Weight percent cationic impurity versus VMPS of samples of $\delta\text{FeO}(\text{OH})$ prepared in KOH-KCl media. Solid line calculated from Uniform Model.

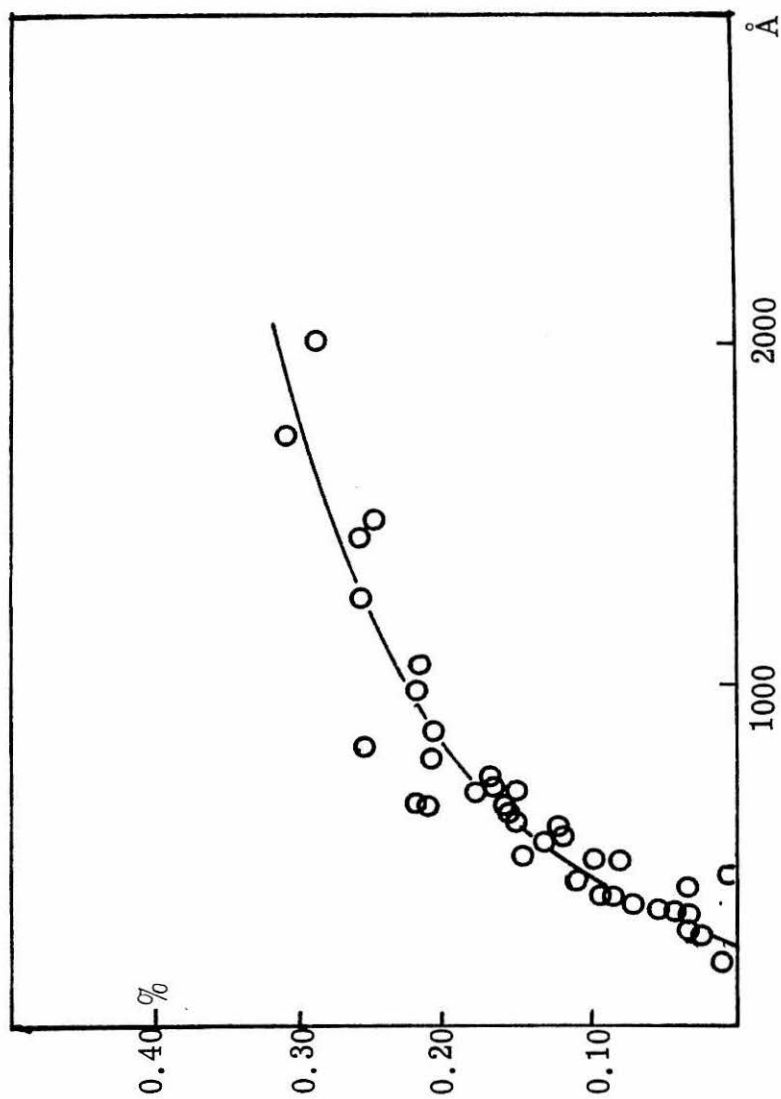


Figure 10. Weight percent cationic impurity versus VMPS (Å) of samples of $\delta\text{FeO}(\text{OH})$ prepared in NaOH-NaCl media. Solid line calculated from Anisotropic Model.

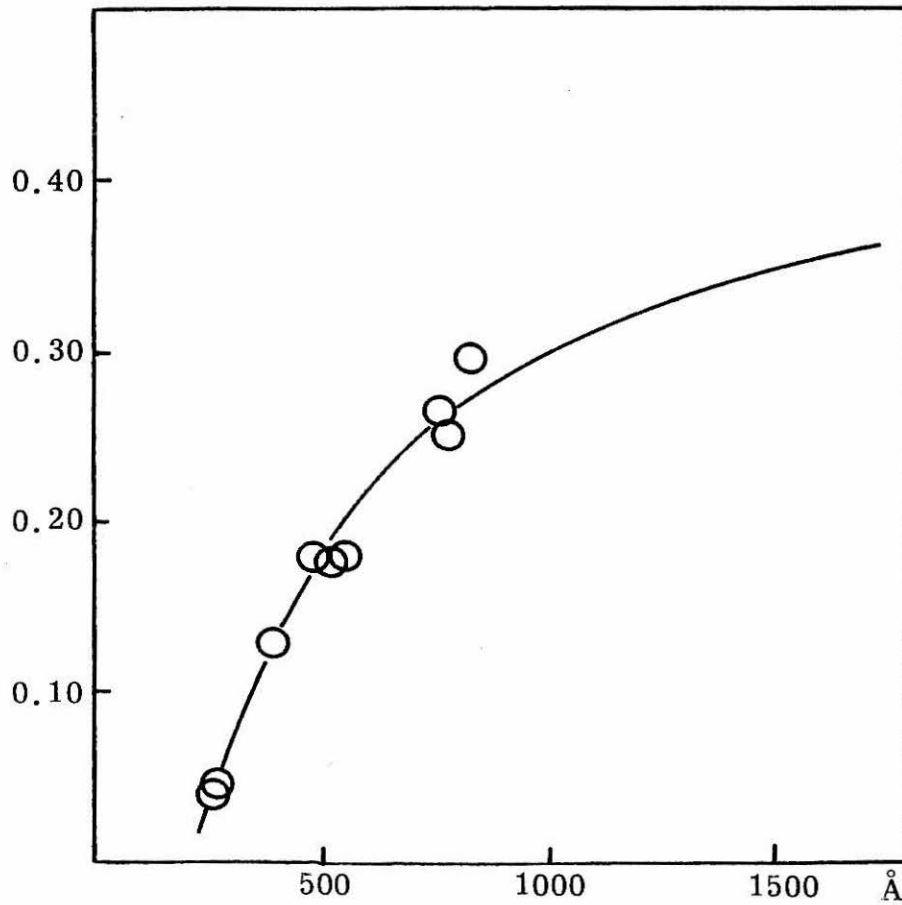


Figure 11. Weight percent cationic impurity versus VMPS (Å) of samples of δ -FeO(OH) prepared in KOH-KCl media. Solid line calculated from Anisotropic Model.

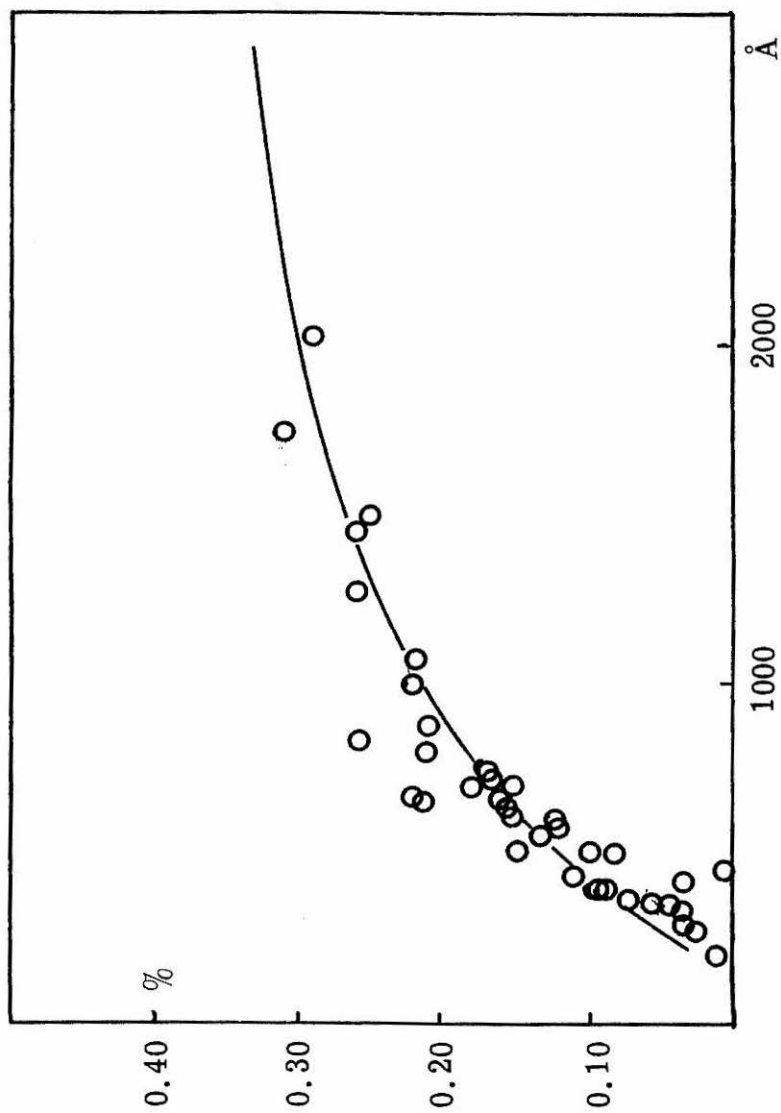


Figure 12. Weight percent cationic impurities versus VMPS (Å) of samples of δ -FeO(OH) prepared in NaOH-NaCl media. Solid line calculated from Gradient Model.

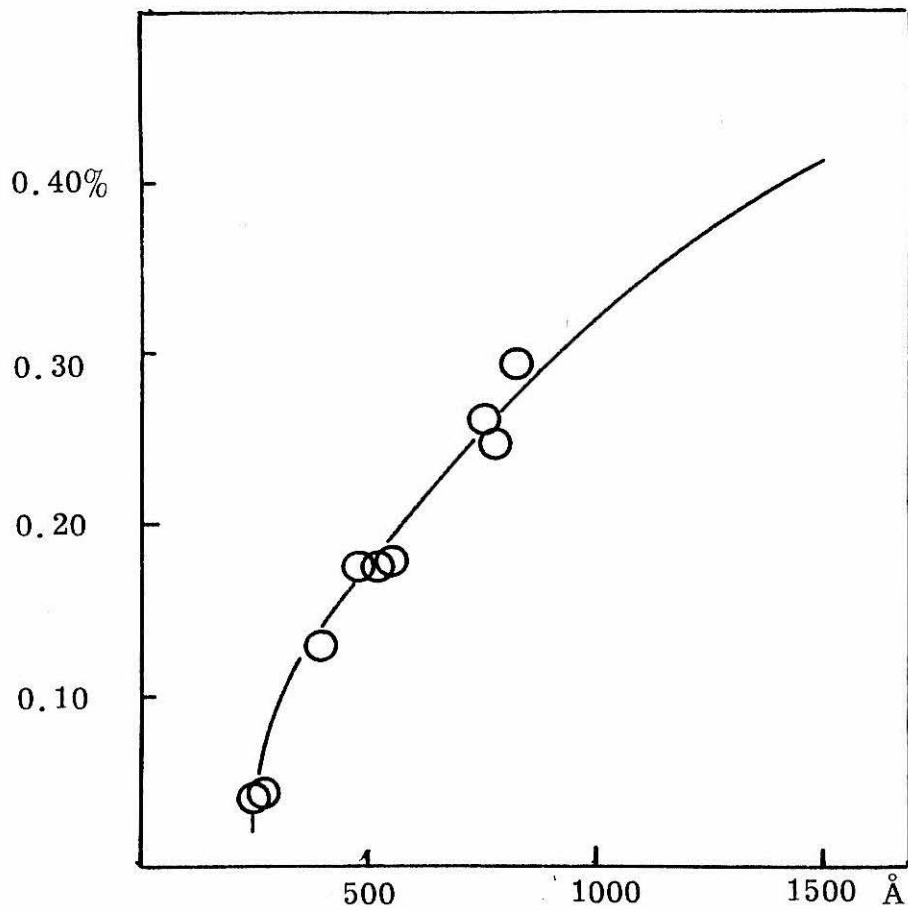


Figure 13. Weight percent cationic impurity versus VMPS (Å) of samples of $\delta\text{FeO}(\text{OH})$ prepared in KOH-KCl media. Solid line calculated from Gradient Model.

the depletion layer is 0. Then, the weight percent impurity for a bulk sample of VMPS = D is given by the expression

$$C(D) = C(\infty) (1.0 - 10 g/D + 28 g^2/D^2 - 24 g^3/D^3)$$

The solid lines in figures 8 and 9 were computed from a least-squares best fit of the data to this expression.

- (2) Anisotropic model: The morphology of the $\delta\text{FeO}(\text{OH})$ particle is quite anisotropic as is the unit cell of $\delta\text{FeO}(\text{OH})$. It would not be surprising to find that the thickness of the depletion layer is also anisotropic. This model sets the thickness of the depletion layer along the c-axis (g') equal to one-third the thickness of the layer along the a- or b-axes. The bulk weight percent impurity for a sample of VMPS = D is given by

$$C(D) = C(\infty) (1.0 - 6 g/D + 12 g^2/D^2 - 8 g^3/D^3)$$

The solid lines in figures 10 and 11 were computed for a least-squares fit of the impurity data to this expression.

- (3) Totally Anisotropic Model: This model is similar to the preceding except g' , the thickness of the depletion layer along the c- axis is set to zero. The particle size dependence of impurity concentration is then given by $C(D) = C(\infty) (1.0 - 4.0 g/D + 4.0 g^2/D^2)$.

- (4) Gradient Model: This model is quite similar to the uniform model. The thickness of the depletion layer is assumed to be uniform along all the particle axes. However, the concentration of impurity within the particle is not taken as zero. Instead, it is assumed that there is a linear gradient of concentration. Near the surface of the particle the concentration is zero. The concentration increases linearly with penetration into the particle until it is $C(\infty)$ at a penetration g . The bulk weight percent impurity is then described by

$$C(D) = C(\infty) (1 - 3g/D + 4g^2/D^2 - 2g^3/D^3)$$

The solid lines in figures 12 and 13 were computed from best least-squares fit of the data to this expression.

Schematic diagrams of the models are shown in figures 14 and 15. Dotted portions of these drawings indicate the contaminated portion of the particle. Parametric values derived from least-squares fit of impurity data for δ FeO(OH) samples prepared in NaOH-NaCl and KOH-KCl media are cited in Table 4. Errors in the parameters correspond to upper and lower support planes of the fits.

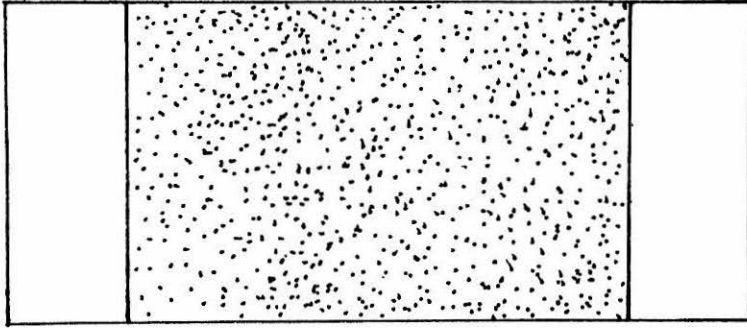
The differences between the models and the limited amount of data available prevent clear choice among the models. Based on the confidence levels of the fits, the Totally Anisotropic and Gradient Models are poorer representations of the data. The Uniform model accounts best for the overall data.

Table 4

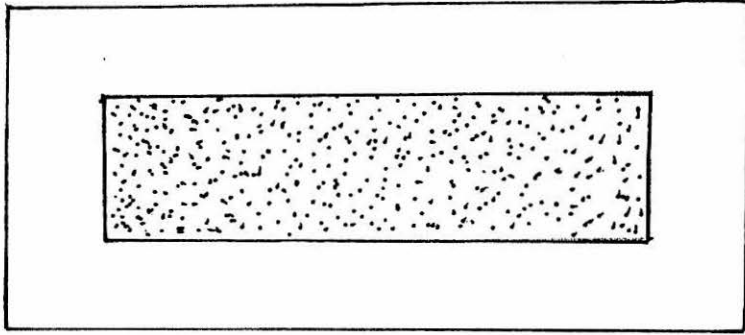
Parametric Values of Best Least-Squares Fit of
Cationic Impurity Data to Various Models

<u>Model</u>	<u>Cationic Impurity</u>	<u>Thickness of Depletion Layer (Å)</u>	<u>Weight % Impurity of an Infinite Diameter Particle (%)</u>
Uniform	K ⁺	73 ± 4	0.495 ± 0.060
	Na ⁺	88 ± 4	0.408 ± 0.038
Anisotropic	K ⁺	73 ± 8	0.495 ± 0.060
	Na ⁺	87 ± 10	0.399 ± 0.035
Totally Anisotropic	K ⁺	93 ± 7	0.453 ± 0.040
	Na ⁺	116 ± 10	0.389 ± 0.030
Gradient	K ⁺	240 ± 12	0.665 ± 0.045
	Na ⁺	212 ± 22	0.412 ± 0.040

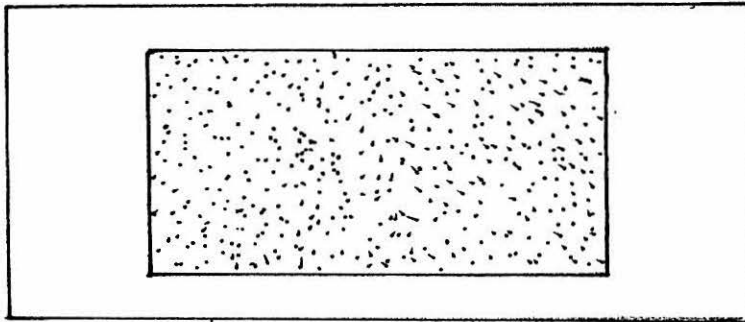
Figure 14. Impurity models described in text. (A) Totally Anisotropic Model, $g' = 0$; (B) Uniform Model, $g' = g$; (C) Anisotropic Model, $g' = 1/3g$.



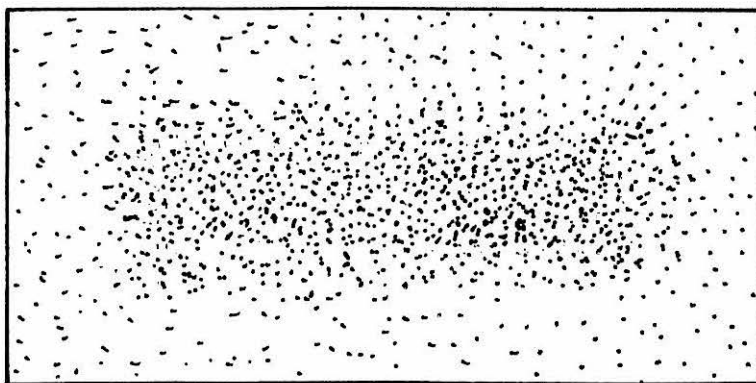
(A) Totally Anisotropic Model



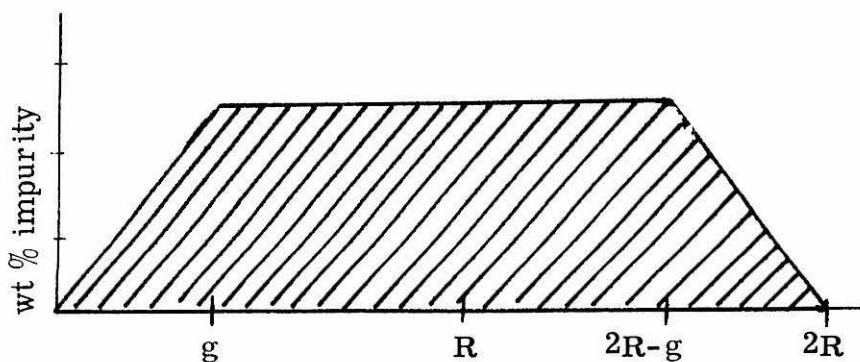
(B) Uniform Model



(C) Anisotropic Model



Gradient Model. Depletion layer is uniform along all axes. Concentration increases linearly from zero at the surface of particle to $C(\infty)$ at and throughout the core.



Concentration profile postulated in Gradient Model.

Figure 15. Gradient Model.

The lithium ion impurity in samples of $\delta\text{FeO}(\text{OH})$ prepared in LiOH-LiCl media cannot be well represented by any of the models. In view of the difficulty encountered in washing these samples, it may be that the observed dependence of lithium impurity on VMPS (figure 16) is a combination of adsorbed surface species and entrained ions such as found in other samples of $\delta\text{FeO}(\text{OH})$. The available data are insufficient to attempt any separation of these effects.

A presumption that might be drawn from the above discussion of cationic impurities is that prolonged washing of the samples might eventually reduce the impurity level to zero. To test this hypothesis a sample of $\delta\text{FeO}(\text{OH})$ prepared in 7F NaOH (VMPS = 1185Å; Na % = 0.090) was slurried in 5N NaCl for 3 days. The sample was filtered, washed free of excess halide solution and dialyzed against distilled water for several weeks. Periodically a sample was removed for analysis. The results are shown in figure 17. The weight percent sodium ion content of the sample dropped rapidly in the first day of washing. After about one week, the sodium content stabilized at $0.084 \pm 0.002\%$. This content was quite similar to that of the original sample. Prolonged washing of the material produced no significant decrease in the ion content. Apparently, any surface absorbed sodium ions are rapidly removed from the particles. Sodium ions within the particle are effectively entrained and simple washing fails to leach them away.

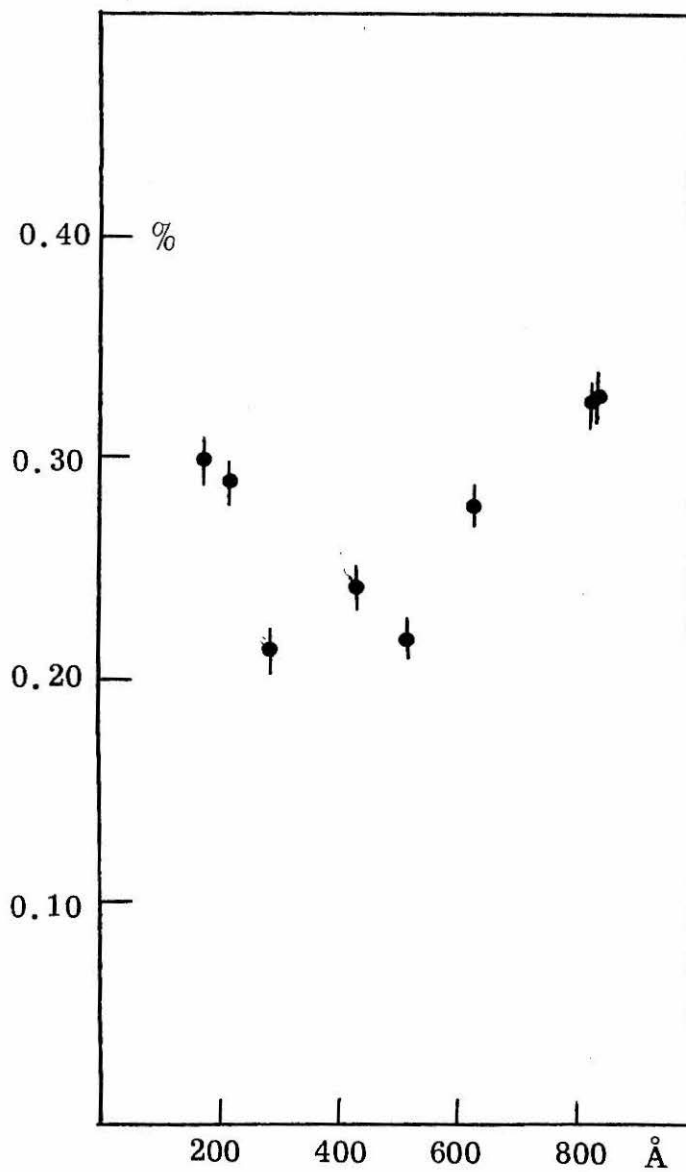


Figure 16. Weight % Li^+ impurity in $\delta\text{FeO}(\text{OH})$ prepared in LiOH-LiCl media versus VMPS.

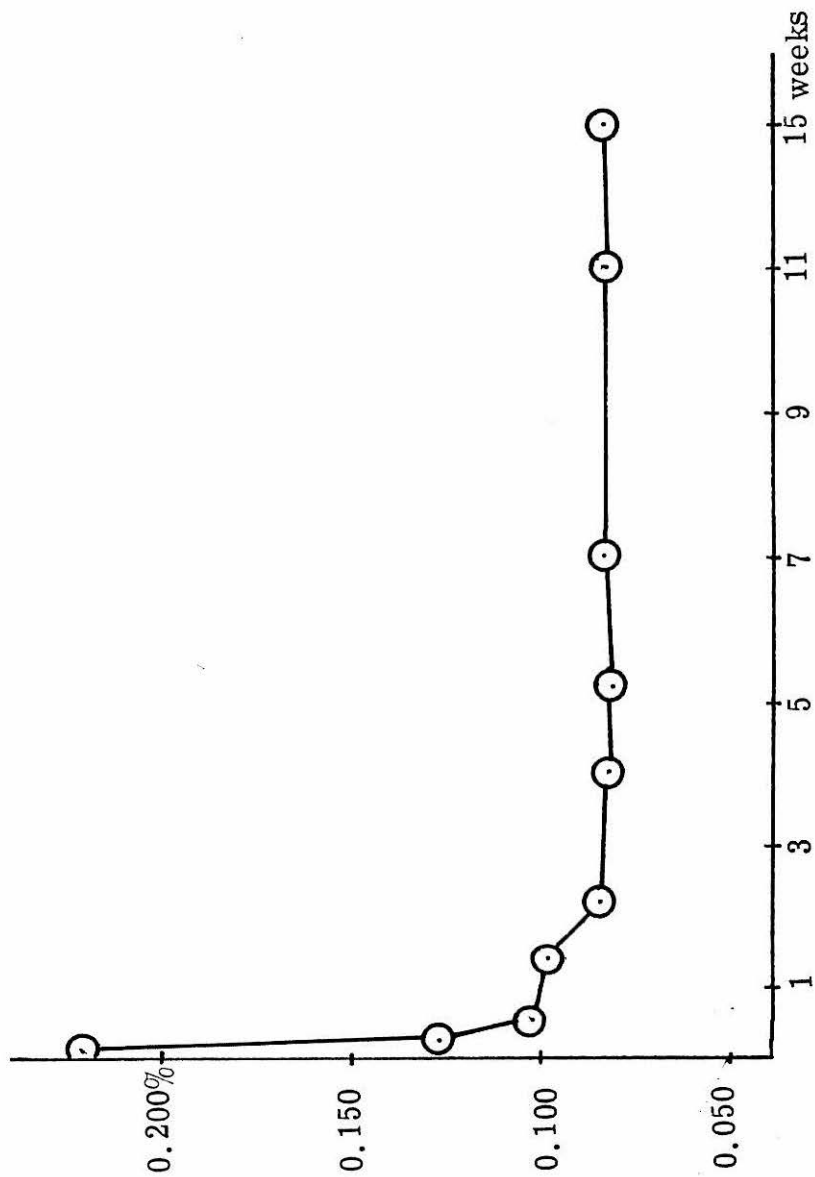


Figure 17. Results of prolonged washing of $\delta\text{FeO}(\text{OH})$. Plot of wt. % Na versus washing time in weeks.

The surface of δ FeO(OH) particles does exhibit considerable affinity for cations. The above sample of δ FeO(OH) was slurried with solutions of various ions at room temperature and at 100°C for two days. The samples were then removed from the baths by filtration and washed by a procedure completely analogous to that used in the preparation of δ FeO(OH) samples. Analyses of the samples yielded the results in Table 5.

Intuitively the moles of ions adsorbed ought to be proportional to the charge on the ion divided by the cube of its radius. A plot of the data taken for samples held at room temperature is shown in figure 18.

The lithium content is considerably removed from the general trend line in this figure. This result is in keeping with the general difficulty in removing excess lithium salts discussed in the Experimental section.

The adsorptivity data taken at 100°C are not nearly so well behaved. The cation content seems to parallel the decreasing solubility of the oxides of the cation. Zinc oxide was definitely precipitated in the course of the experiment.

The adsorbed cations produced negligible changes in the magnetic behavior of the sample. The original sample of δ FeO(OH) had a room temperature saturation magnetization of 20.17 emu/gm and a coercive field of 450 ± 20 gauss. Samples exchanged at room temperature had saturation magnetizations of 20.10 ± 0.10 emu/gm and coercive fields of 450 ± 20 gauss. The saturation magnetization of

Table 5

Ion Exchange in $\delta\text{FeO}(\text{OH})$

Exchange Solution	Room Temperature Bath			100° C Bath			radius of cation ^c ($\frac{r}{\text{Å}}$) ^b
	wt % Na	wt % M^{n+}	$\frac{\text{Moles } \text{M}^{n+}}{\text{gm}} (\times 10^2)$	wt % Na	wt % M^{n+}	$\frac{\text{Moles } \text{M}^{n+}}{\text{gm}} (\times 10^4)$	
5N LiCl	0.82	2.90	0.0414	0.066	0.052	0.742	0.60
5N NaCl	0.180 ^a	0.180 ^a	a	0.083	0.083	--	0.95
5N KCl	0.078	0.030	0.008	0.084	0.027	0.069	1.33
5N AgNO_3	0.078	0.120	0.0011	0.063	0.063	0.058	1.26
Satd CaCl_2	0.080	0.260	0.0065	0.096	0.072	0.180	0.99
Satd BaCl_2	0.083	0.211	0.0015	0.067	0.053	0.038	1.35
3N NiNO_3	0.081	0.98	0.0166	0.073	0.140	0.237	0.72
2N ZnCl_2	0.075	1.72	0.0267	0.072	0.370	0.566	0.74
5N $\text{Cd}(\text{NO}_3)_2$	0.081	0.430	0.0038	0.070	0.070	0.062	0.97
2N CuCl_2	0.081	1.460	0.0230	0.056	0.310	0.488	0.69

^a Original wt % Na content of solid was 0.084%. Therefore 0.095% Na was added = 4.13×10^{-5} moles/gm at room temperature. ^b Charge of ion divided by the cube of the ionic radius in units of eÅ^{-3} .

^c Ionic radii of cations.

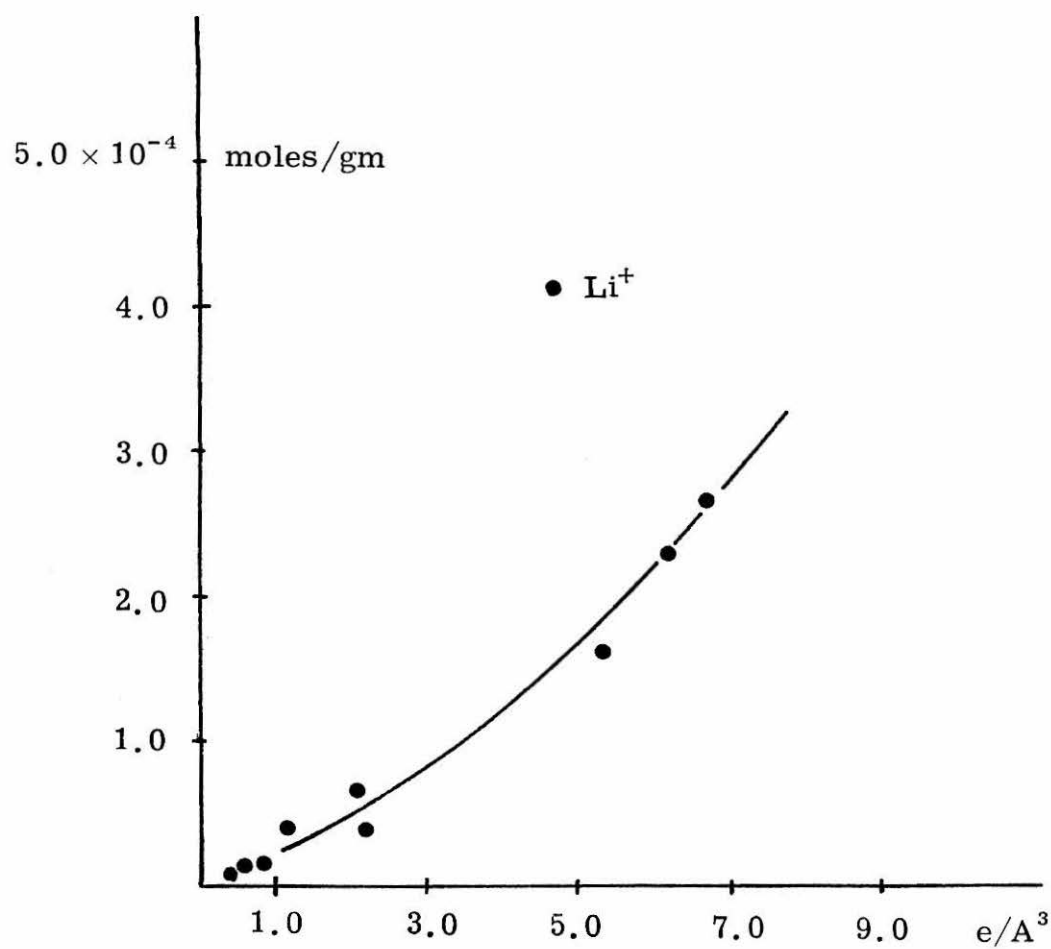


Figure 18. Moles of cations adsorbed per gram of $\delta\text{FeO}(\text{OH})$ versus charge density of cations in units of $e\text{\AA}^{-3}$.

samples exchanged at 100°C was of course greatly reduced from that of the original material to 8.35 gauss/gm. Coercive field was also greatly increased to 950 ± 50 gauss. Within experimental error all of the samples exchanged at 100°C had these values for their magnetic properties.

(B) Magnetic Results. The qualitative aspects of the magnetic behavior of $\delta\text{FeO(OH)}$ samples prepared in LiOH-LiCl and in KOH-KCl media are entirely similar to the magnetic behavior of samples prepared in NaOH-NaCl media. For the most part, the samples are superparamagnetic or exhibit minute hysteresis losses at room temperature. Saturation magnetization data, obtained by the means described in Chapter 4, were easily fit to the expression

$$\sigma_{\infty}(T) = \sigma_{0,\infty} (1 - a T^n)$$

The parametric values obtained from this expression are listed in Table 6.

Hysteresis effects develop for all the samples at sufficiently low temperatures. Figures 19 and 20 show plots of coercive field versus temperature for two samples $\delta\text{FeO(OH)}$ prepared in LiOH-LiCl and KOH-KCl media, respectively. Similar plots of the temperature dependence of the ratio of remanent magnetization to saturation magnetization are shown in figures 21 and 22. The temperature dependences shown in these figures are typical of mixtures of superparamagnetic and single domain particles.¹⁹

Pertinent magnetic data for the samples are shown in Table 7.

Table 6

Saturation Magnetization Data for $\delta\text{FeO}(\text{OH})$ Samples

Prepared in LiOH-LiCl and KOH-KCl Media

VMPS (\AA)	$\sigma_{0, \infty}$ (emu/gm)	n	^a $(^{\circ}\text{K})^{-2} \times 10^6$	T_c ($^{\circ}\text{K}$)	μ^a (BM)
Samples prepared in KOH-KCl media					
270	21.26	1.96	4.66	532	0.34
253	17.76	1.78	11.96	578	0.28
396	23.15	1.94	4.56	524	0.37
480	22.95	1.90	5.60	577	0.36
510	22.85	1.78	10.70	616	0.36
552	24.77	1.96	4.54	530	0.39
754	25.44	2.03	1.58	525	0.405
784	25.27	1.86	8.15	540	0.40
826	25.54	2.03	2.77	532	0.41
Samples prepared in LiOH-LiCl media.					
179	28.33	1.76	16.33	517	0.45
221	30.49	1.89	7.27	527	0.485
435	34.30	1.96	4.54	530	0.55
520	41.44	2.05	1.59	526	0.66
632	42.37	1.94	5.96	535	0.67
832	44.75	1.96	4.55	530	0.71
841	44.45	1.89	7.77	510	0.71

$$^a \mu = MW \cdot \sigma_{0, \infty} / N\beta.$$

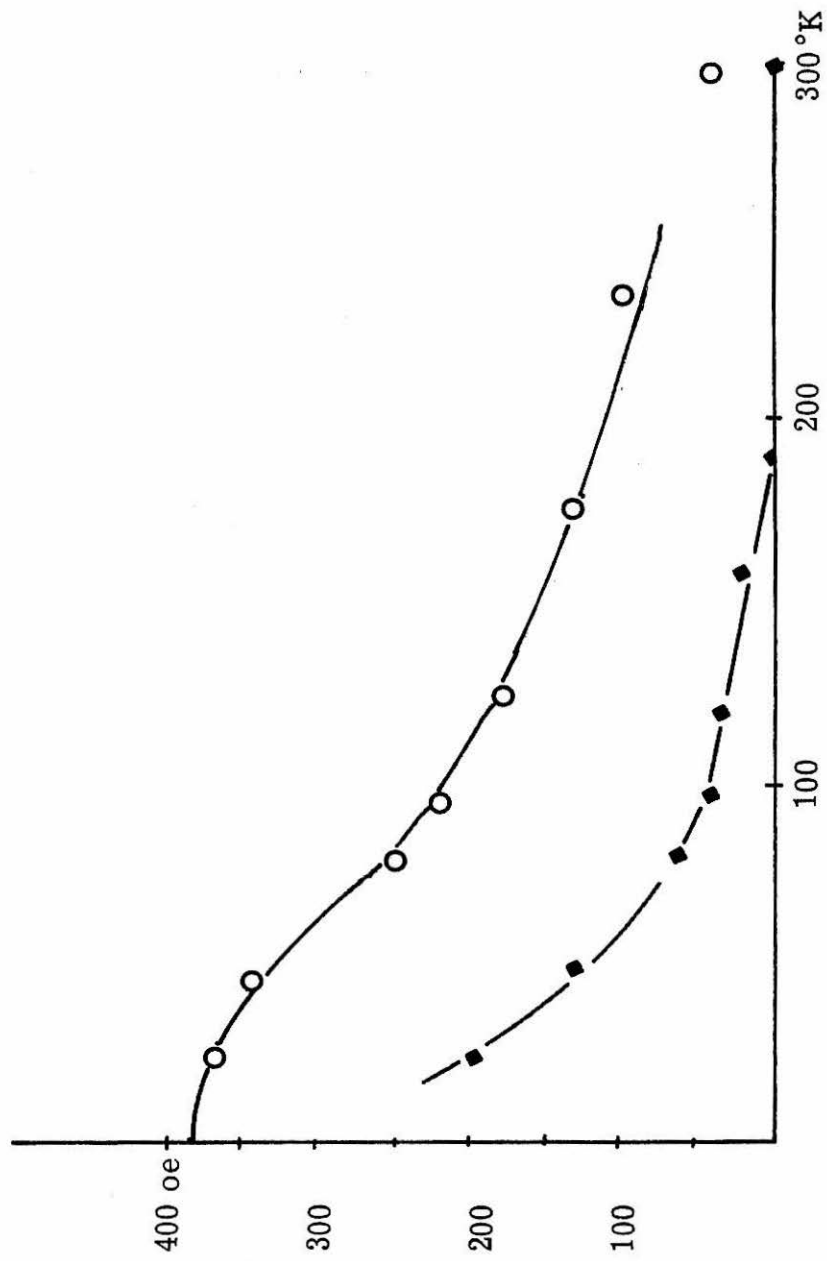


Figure 19. Temperature dependence of coercive field of δ FeO(OH) samples prepared in LiCl-LiOH media with VMPS = 841 Å (O) and VMPS = 179 Å (◆).

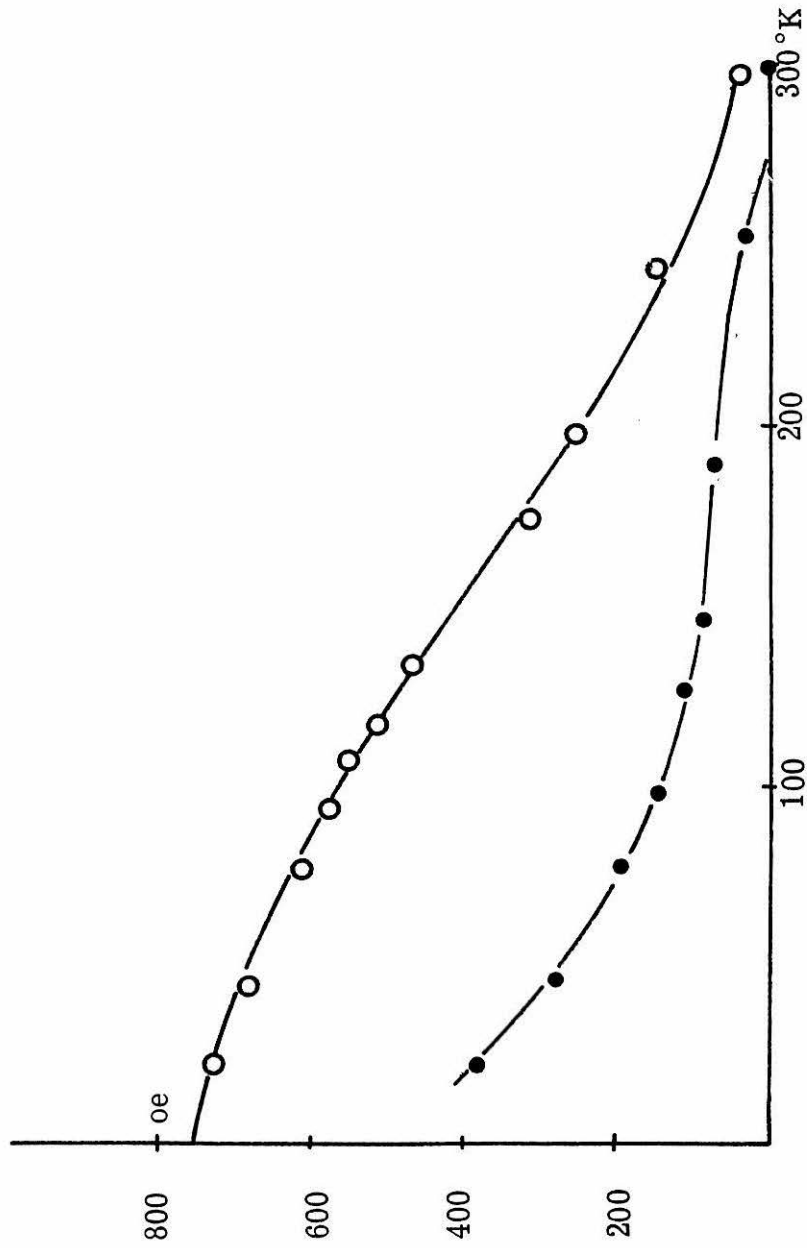


Figure 20. Coercive field versus temperature for samples of $\delta\text{FeO}(\text{OH})$ prepared in KOH-KCl media with VMPS = 270 Å (●) and VMPS = 826 Å (○).

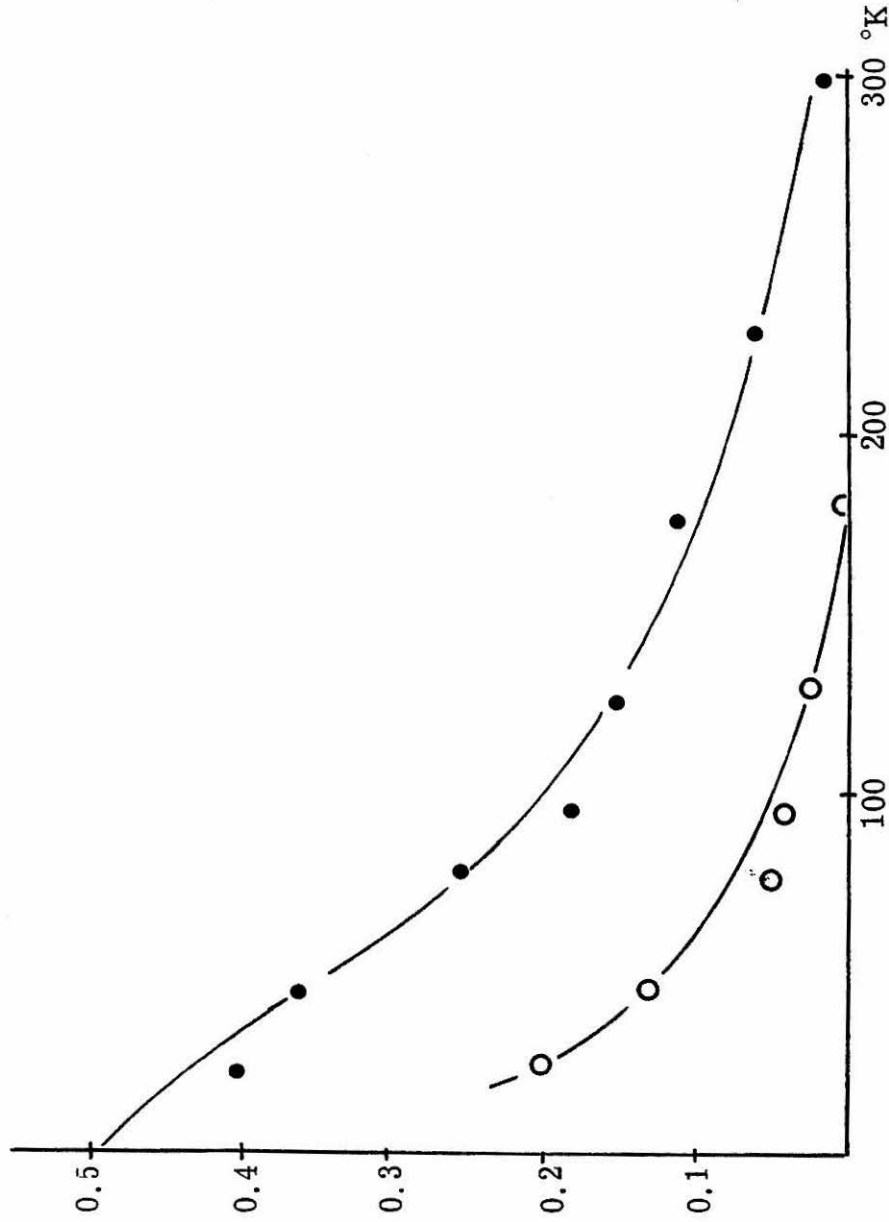


Figure 21. Temperature dependence of the ratio of remanent magnetization to saturation magnetization for δ -FeO(OH) samples prepared in LiOH-LiCl media with VMPS = 841 Å (●) and VMPS = 179 Å (○).

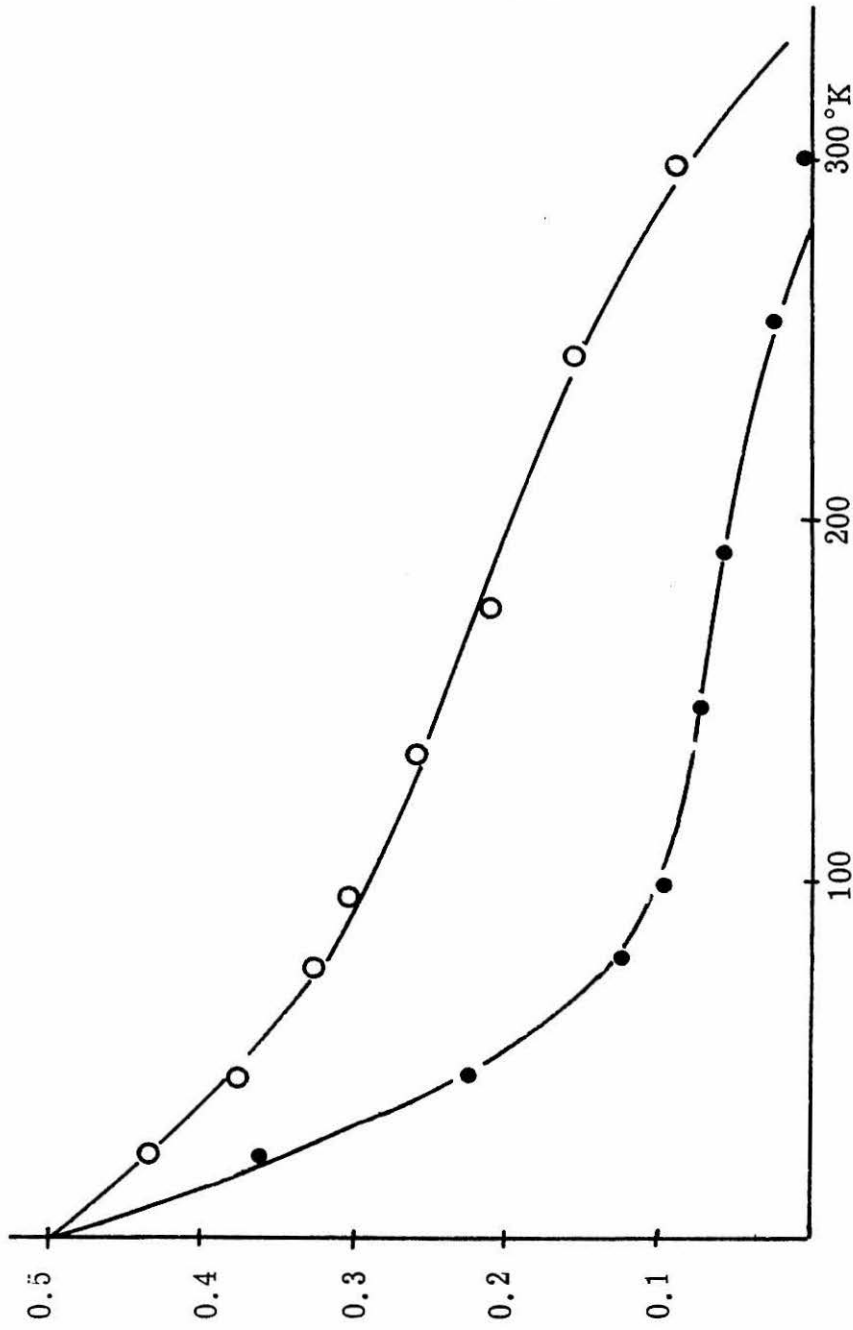


Figure 22. Ratio of remanent magnetization to saturation magnetization versus temperature for samples of $\delta\text{FeO}(\text{OH})$ prepared in KOH-KCl media with VMPA = 270 Å (●) and VMPS = 826 Å (○).

Table 7

Hysteresis Data for Samples of $\delta\text{FeO}(\text{OH})$ Prepared in

LiOH-LiCl and KOH-KCl Media

VMPS (\AA)	T_b ($^\circ\text{K}$)	$H_c(\text{O})$ (gauss)	298 $^\circ\text{K}$			77 $^\circ\text{K}$			22.5 $^\circ\text{K}$		
			$H_c(\text{T})$ (gauss)	$R(\text{T})^a$	$H_c(\text{T})$ (gauss)	$R(\text{T})$	$H_c(\text{T})$ (gauss)	$R(\text{T})$			
Samples prepared in KOH-KCl media											
270	273	420	0.0	0.0	120	0.123	370	0.240			
253	262	340	0.0	0.0	90	0.06	310	0.330			
396	288	480	0.0	0.0	315	0.157	665	0.55			
480	278	520	40	0.0	400	0.225	687	0.330			
510	300	523	25	0.008	440	0.245	695	0.400			
552	308	570	10	0.011	460	0.275	712	0.396			
754	334	695	45	0.015	605	0.320	725	0.432			
784	332	720	25	0.008	600	0.322	730	0.430			
826	(338) ^b	780	30	0.009	620	0.325	732	0.435			
Samples prepared in LiOH-LiCl media											
179	175	275	0.0	0.0	60	0.05	200	0.207			
221	220	290	0.0	0.0	100	0.115	237	0.280			

Table 7 (Continued)

VMPS (Å)	T _b (°K)	298°K			77°K		22.5°K	
		H _c (O) (gauss)	H _c (T) (gauss)	R(T) ^a	H _c (T) (gauss)	R(T)	H _c (T) (gauss)	R(T)
435	273	320	27	0.035	175	0.175	355	0.385
520	290	360	42	0.017	190	0.215	355	0.405
632	(300) ^b	375	40	0.025	220	0.220	368	0.417
832	(310) ^b	380	50	0.015	245	0.270	365	0.415
841	(310) ^b	375	45	0.015	245	0.255	365	0.415
290	240	310	10	0.005	122	0.143	305	0.38

^a Ratio of remanent magnetization at zero applied field to saturation magnetization.

^b By extrapolation.

The particle size dependence of the coercive field of the samples are shown in figures 23 and 24 for temperatures of 297, 200, 77, and 22.5°K. Similar plots of the ratio of remanent to saturation magnetization are shown in figures 25 and 26. The single domain size at 22.5°K is about 320Å. This size increases to ~900Å at 77°K and is somewhat greater than 900Å at room temperature. Such values of the critical particle dimension are similar to those found in Chapter 4 for samples of $\delta\text{FeO}(\text{OH})$ prepared in NaOH-NaCl.

The single domain size of $\delta\text{FeO}(\text{OH})$ prepared in LiOH-LiCl is similar to that found for $\delta\text{FeO}(\text{OH})$ prepared in other media, yet the saturation magnetization is nearly twice that of samples prepared in other media. Such a result is possible only if the ultimate coercive field ($H_c(O)$) of samples prepared in LiOH-LiCl is much lower than that found for $\delta\text{FeO}(\text{OH})$ prepared in other media. The value $H_c(O)$ for single domain particles of $\delta\text{FeO}(\text{OH})$ prepared in LiOH-LiCl is 420 oe. For samples prepared in KOH-KCl, $H_c(O)$ is ~1300 oe and for NaOH-NaCl it is ~1360 oe. Uniaxial magnetocrystalline anisotropy constants calculated from the Stoner Wohlfarth equation¹⁷ for these species are 34,100, 72,800, and 86,800 ergs/cm³, respectively.

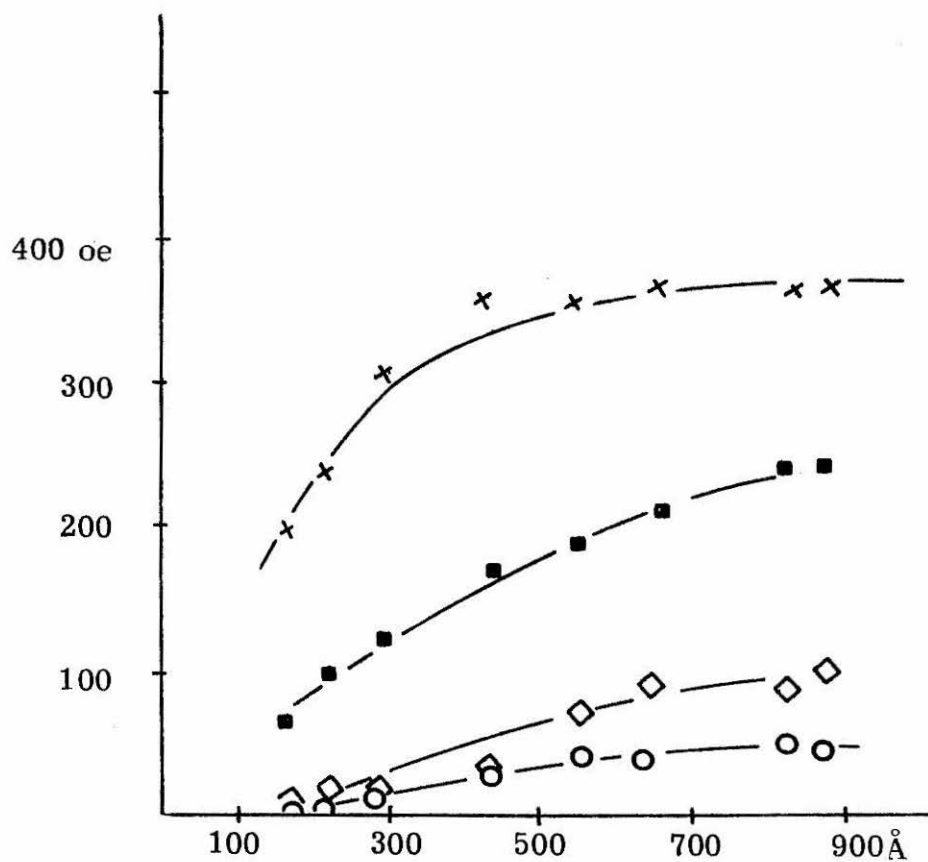


Figure 23. Coercive field at 297°K (○), 200°K (◇), 77°K (■), and 22.5°K (x) plotted versus VMPS of samples of $\delta\text{FeO}(\text{OH})$ prepared in LiOH-LiCl media.

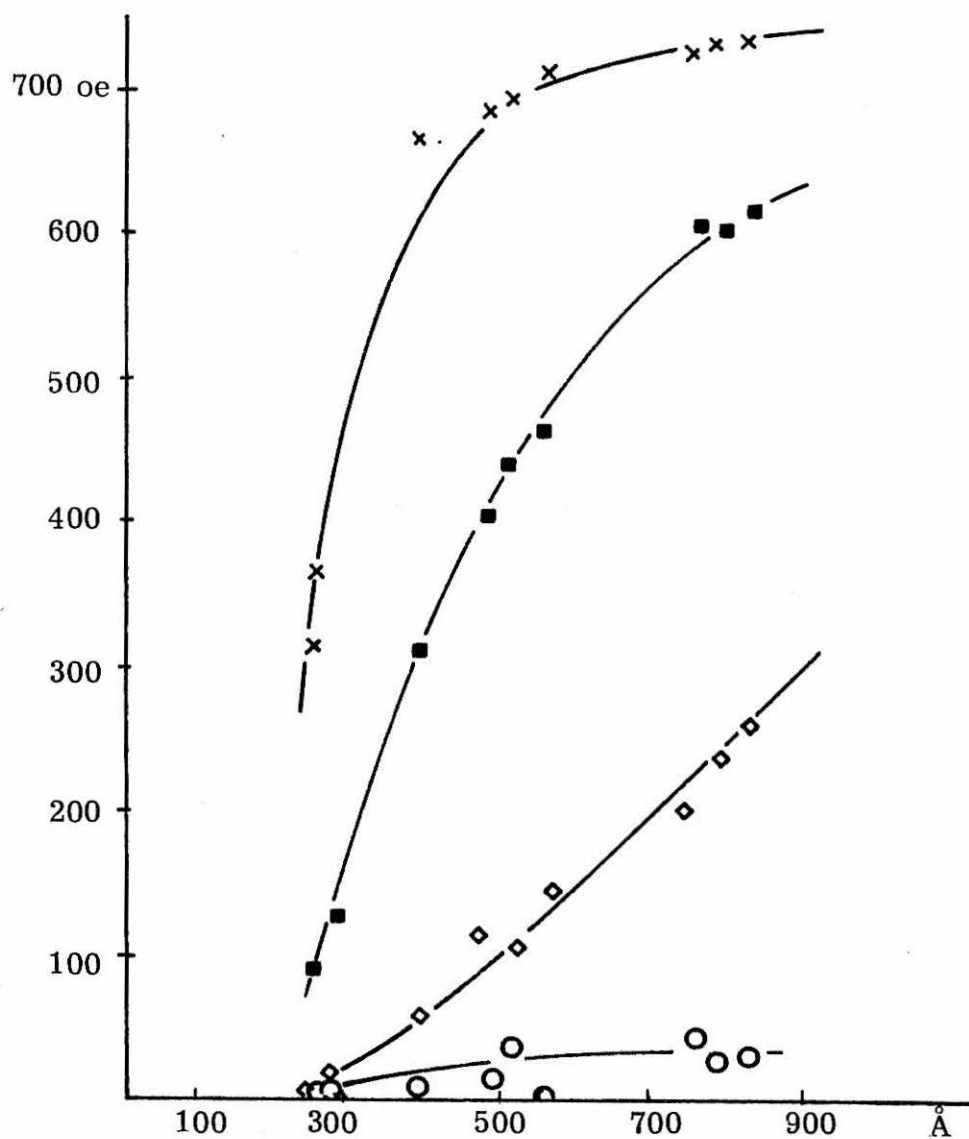


Figure 24. Coercive field at various temperatures versus VMPS of samples of $\delta\text{FeO}(\text{OH})$ prepared in KOH-KCl media. (273°K = \circ , 200°K \diamond , 77°K \blacksquare , 22.5°K = x.)

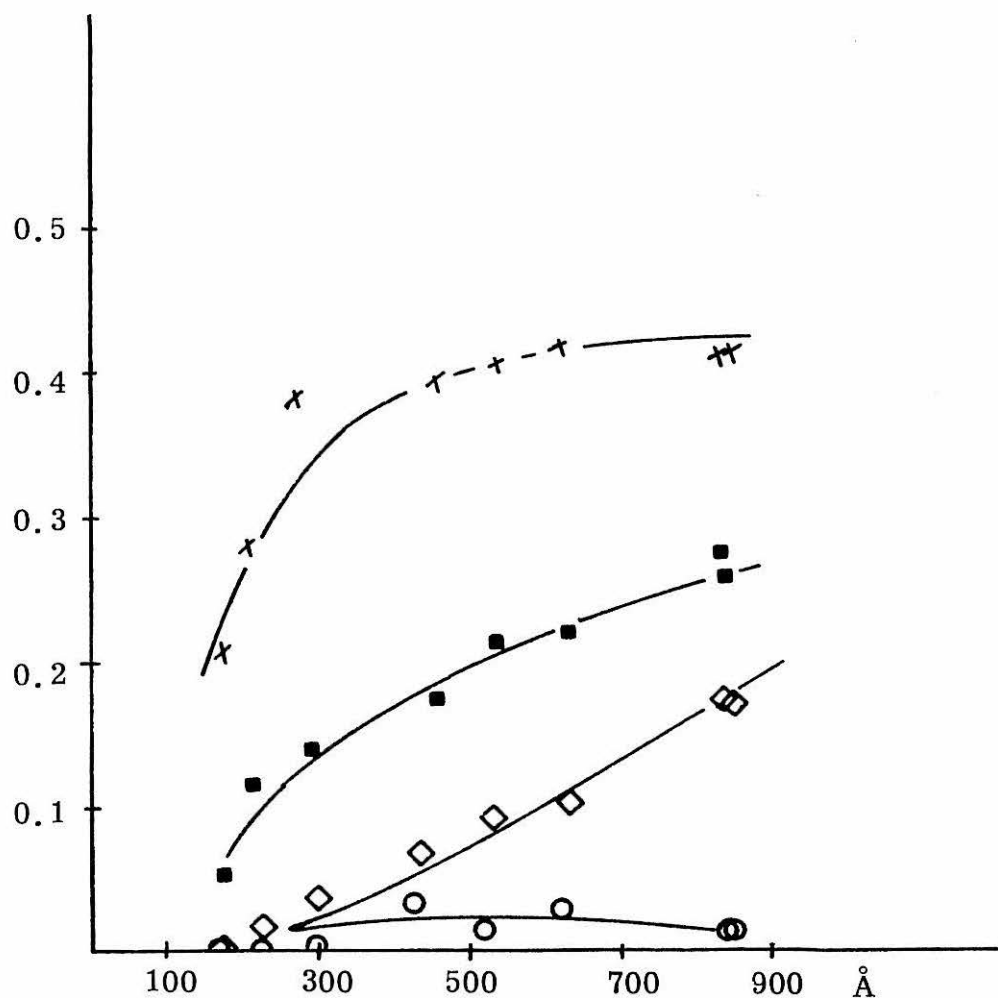


Figure 25. Ratio of remanent magnetization to saturation magnetization at several temperatures versus VMPS of $\delta\text{FeO}(\text{OH})$ samples prepared in LiOH-LiCl media. (297°K = \circ , 200°K = \square , 77°K = \blacksquare , 22.5°K = x.)

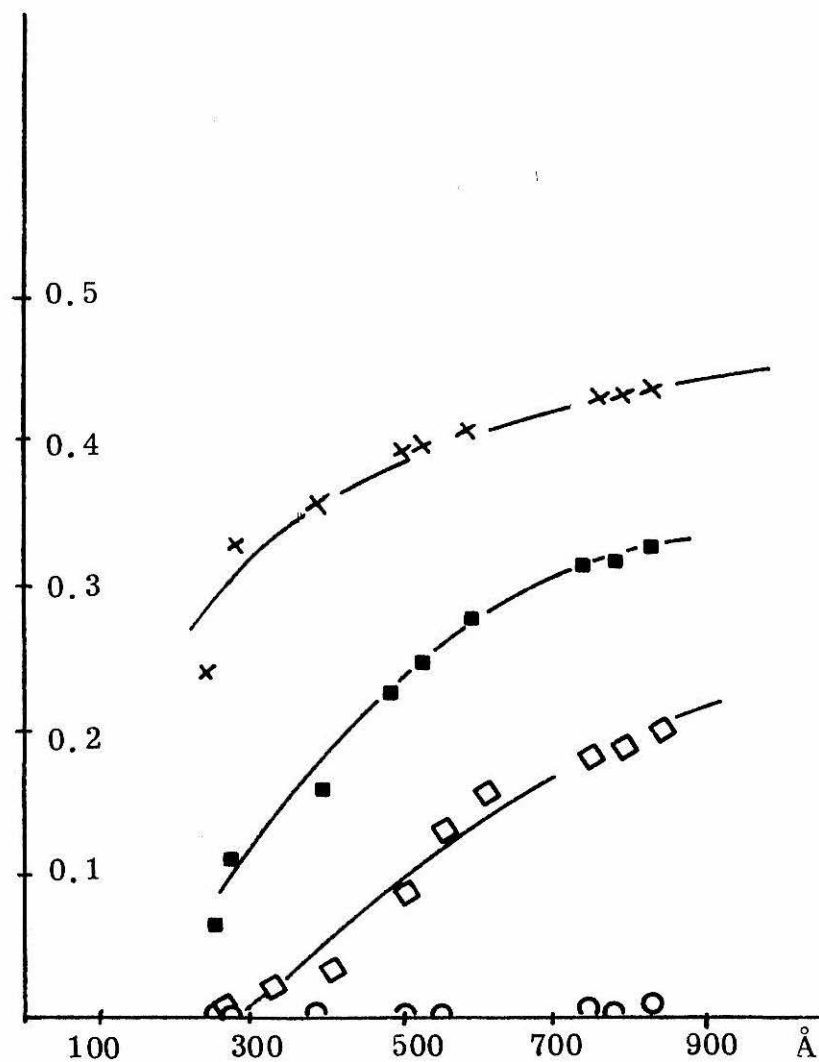


Figure 26. Ratio of remanent magnetization to saturation magnetization versus VMPS of samples of $\delta\text{FeO}(\text{OH})$ prepared in KOH-KCl media at temperatures of 298°K (○), 200°K (◇), 77°K (■), 22.5°K (x).

Discussion

The particle size dependence of the saturation magnetization of $\delta\text{FeO}(\text{OH})$ is difficult to rationalize in terms of homogeneous magnetic particles. A size dependence might be expected if the fields used in this study were insufficient to permit the linear extrapolation of magnetization data in the determination of $\sigma_s(T)$. However, for all samples used in this study, plots of $\sigma(T)$ versus $1/H$ were linear for fields greater than 7000 oersteds. It can only be concluded that the size dependence is endemic to the system and not a result of data treatment.

Rationalization of the size dependence requires a certain inhomogeneity exist in particles of $\delta\text{FeO}(\text{OH})$. An intuitively simple means of introducing inhomogeneity is the postulation of a magnetically inactive layer surrounding each of the magnetic particles. This layer need not be completely inactive, rather it must be less magnetic than the core of the particle. Nevertheless, the terminology "dead-layer" will be used in this discussion.

Magnetic dead-layers have been postulated to explain the magnetization of thin films.³⁻⁵ Though there has been some criticism of this proposal,⁶ theoretical treatments of magnetic films have been developed which do predict dead-layers.⁷

Experimental evidence of dead-layers in fine particulate magnetic material is not extensive. Such layers apparently do not exist in fine particulate iron⁸ or cobalt.⁹ A size dependence in the saturation

magnetization of nickel and cobalt ferrites has been observed.¹⁰ The investigators did not explain its origin except to allow that it might be due to surface effects. Fine particulate magnetic materials coated with surface-active agents also have size dependent magnetization.^{11,12} Coordination of the surface-active agent with surface ions reduces the magnetic contribution of these ions. The particle size dependence of the saturation magnetization of $\gamma\text{Fe}_2\text{O}_3$ has been explained in terms of a magnetically dead-layer $5.7 \pm 2.0\text{\AA}$ thick.¹³

(A) Size Dependence of Saturation Magnetization of $\delta\text{FeO(OH)}$.

The observed size dependence of the saturation magnetization of all samples of $\delta\text{FeO(OH)}$ is well explained by the postulation of a magnetically inactive layer. A precise description of the magnetization depends on the morphology of the layer. Data for $\delta\text{FeO(OH)}$ have been analyzed in terms of four layer models. The models are quite similar to those used above to describe the cationic impurities in $\delta\text{FeO(OH)}$.

(1) Uniform Model: The dead-layer is assumed to be uniformly thick along all axes of the particle. This is the model used in the description of the saturation magnetization of $\gamma\text{Fe}_2\text{O}_3$ cited above. The saturation magnetization of an assemblage of particles of mean diameter D is given by equation (2)

$$\frac{\sigma_{O,\infty}(D)}{\sigma_{O,\infty}(\infty)} = (1 - 10 g/D + 28 g^2/D^2 - 24 g^3/D^3) \quad \text{eqn 2}$$

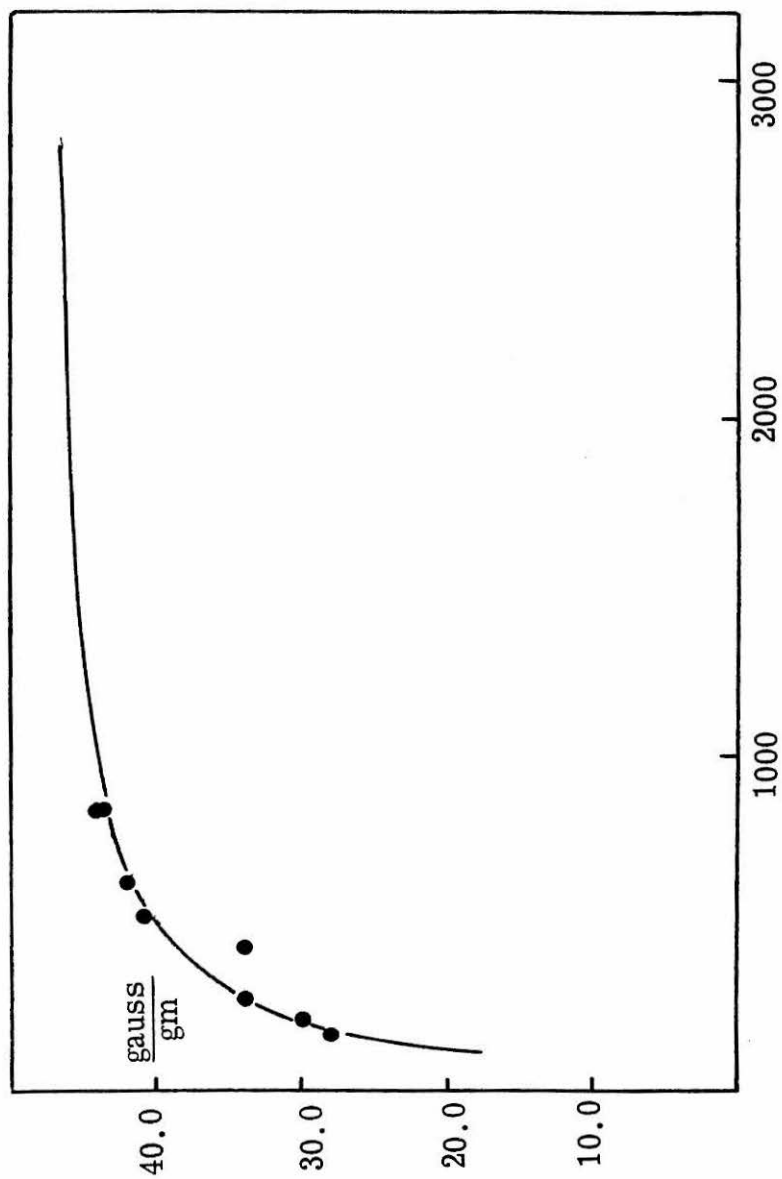


Figure 27. $\sigma_{O, \infty}^{(b)}$ versus VMPS of samples prepared in LiOH-LiCl media. Solid line calculated for Uniform Model.

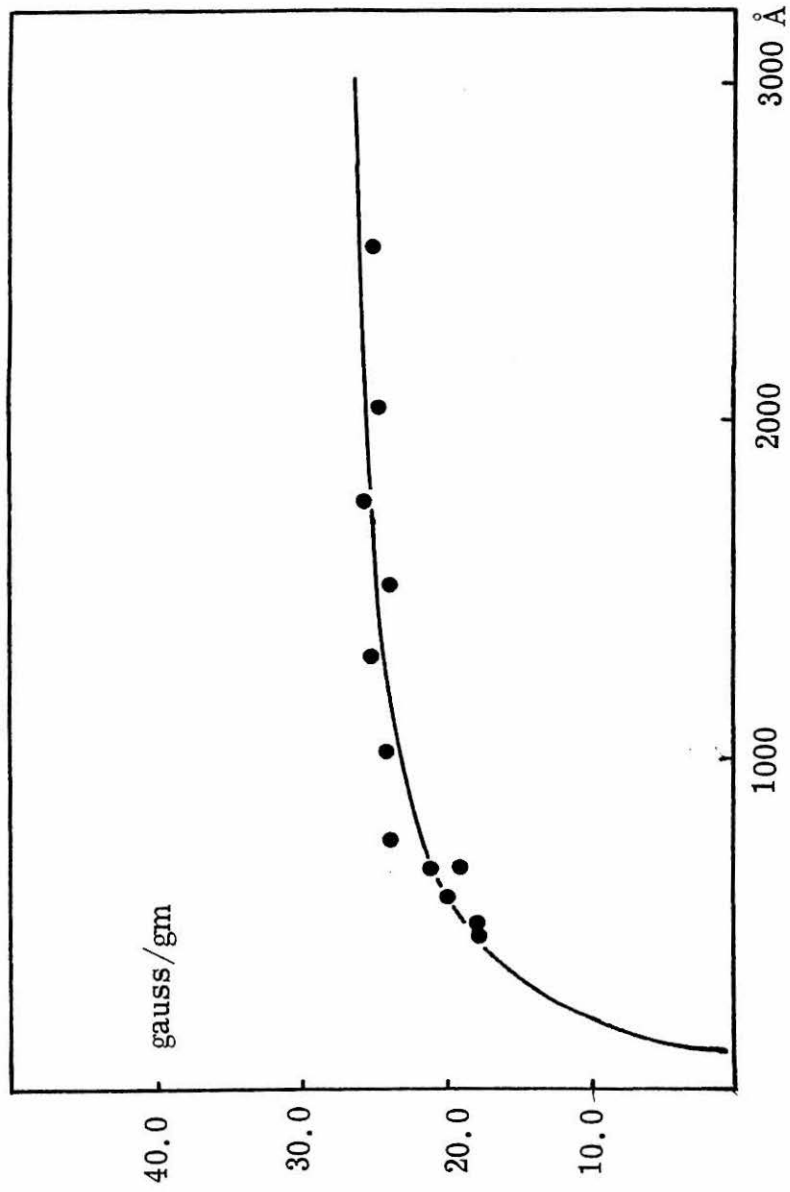


Figure 28. $\sigma_{O, \infty}$ (D) versus VMPs of samples prepared in NaOH-NaCl media. Solid line calculated for Uniform Model.

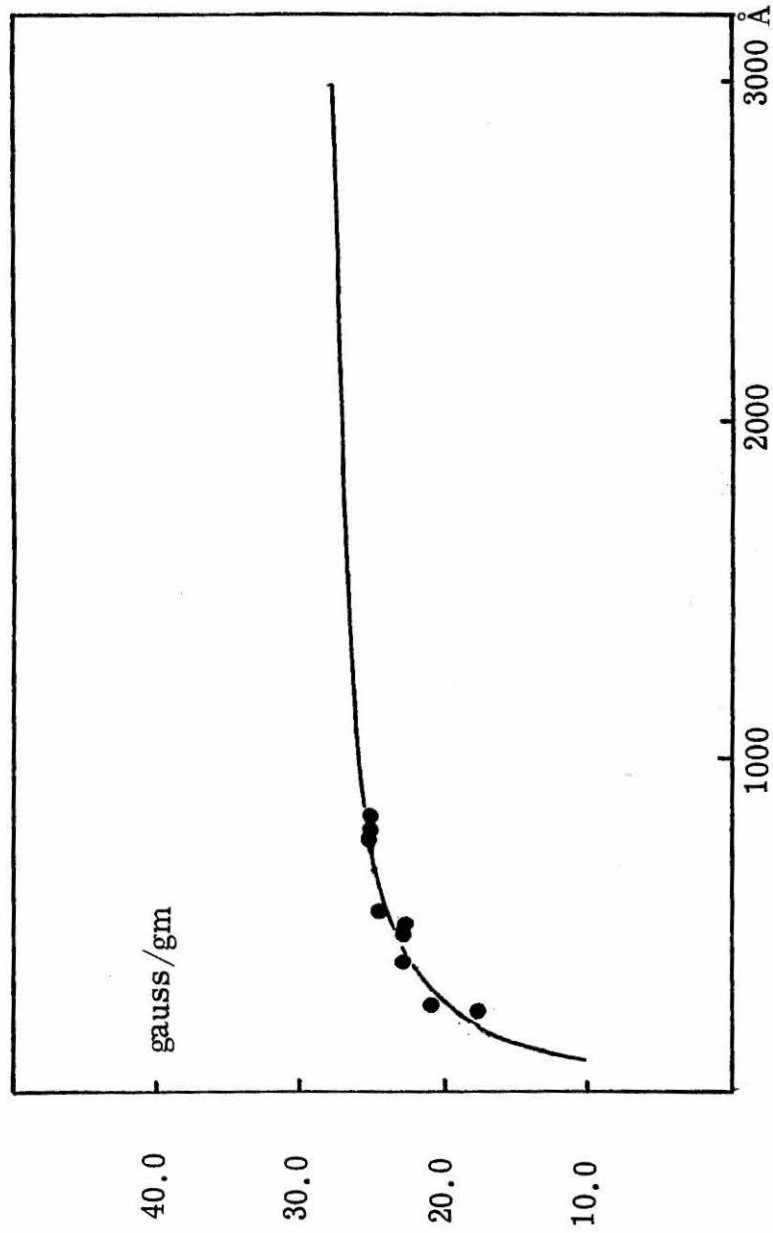


Figure 29. $\sigma_{0, \infty}$ versus VMPS of samples prepared in KOH-KCl media. Solid line calculated for Uniform Model.

where $\sigma_{O,\infty}(D)$ is the saturation magnetization at infinite applied field and 0°K, g the thickness of the dead-layer, and $\sigma_{O,\infty}(\infty)$ is the saturation magnetization of an infinite size particle--the bulk saturation magnetization. The dead-layer is assumed to be completely non-magnetic. Figures 27, 28, and 29 show the best least squares fit of magnetization data of $\delta\text{FeO}(\text{OH})$ prepared in different media to equation 2.

- (2) Anisotropic Model: $\delta\text{FeO}(\text{OH})$ particles are platelets whose easy axis of magnetization probably lies within the platelet. It is reasonable to assume then that the dead-layer, too, is anisotropic. In this model the dead-layer measured along the c axis of the particle is 1/3 as thick as along the a or b axes.

$$\frac{\sigma_{O,\infty}(D)}{\sigma_{O,\infty}(\infty)} = (1 - 6g/D + 12g^2/D^2 - 8g^3/D^3)$$

Figures 30, 31, and 32 show best least-squares fit of magnetization data to the Anisotropic Model.

- (3) Totally Anisotropic Model: In this model even greater account is taken of the particle anisotropy. The dead-layer is taken to exist only along the a and b axes.

$$\frac{\sigma_{O,\infty}(D)}{\sigma_{O,\infty}(\infty)} = (1 - 4g/D + 4g^2/D^2)$$

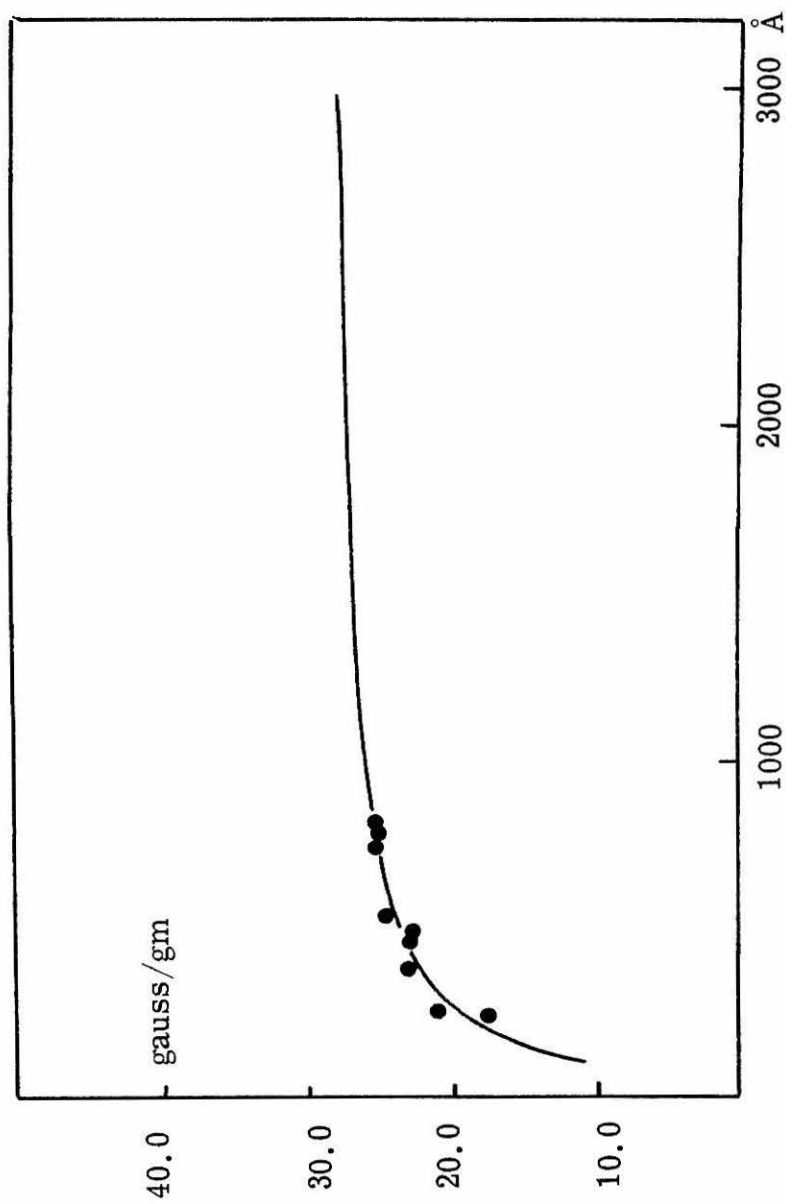


Figure 30. $\sigma_{O, \infty}(D)$ versus VMPS of samples prepared in KOH-KCl media. Solid line calculated for Anisotropic Model.

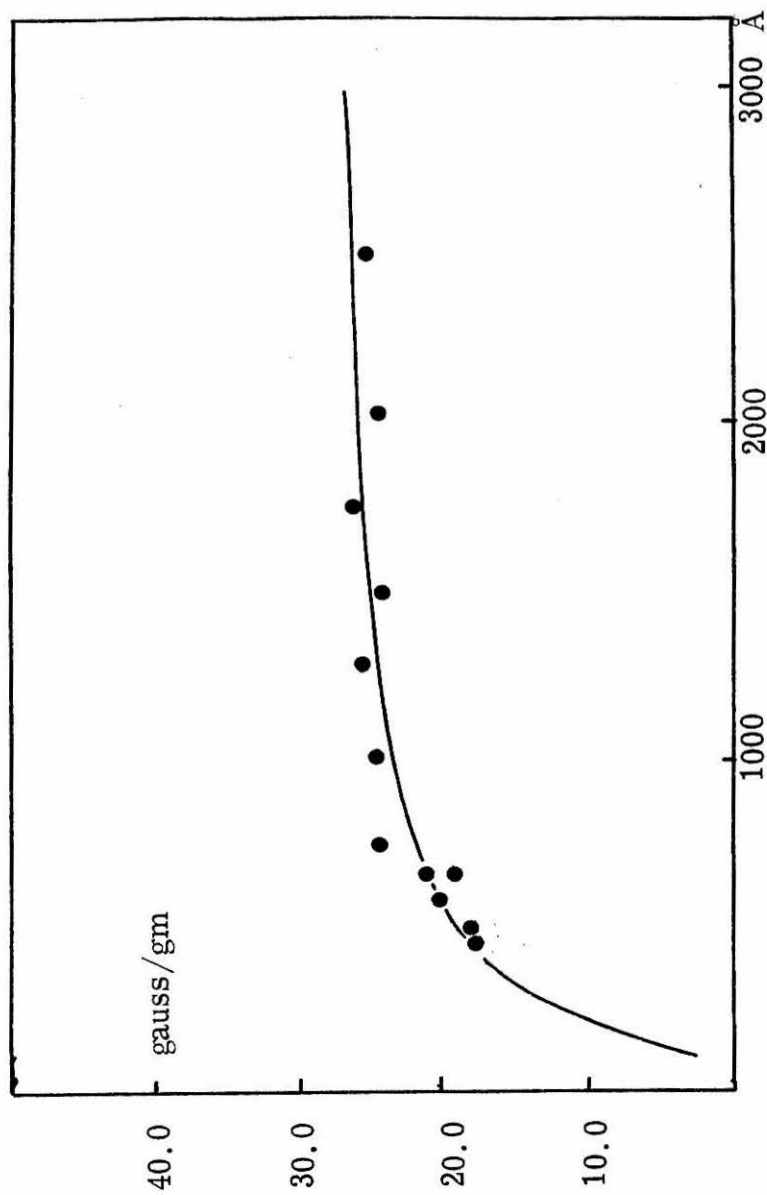


Figure 31. $\sigma_{0,\infty}(D)$ versus VMPS of samples prepared in NaOH-NaCl media. Solid line calculated for Anisotropic Model.

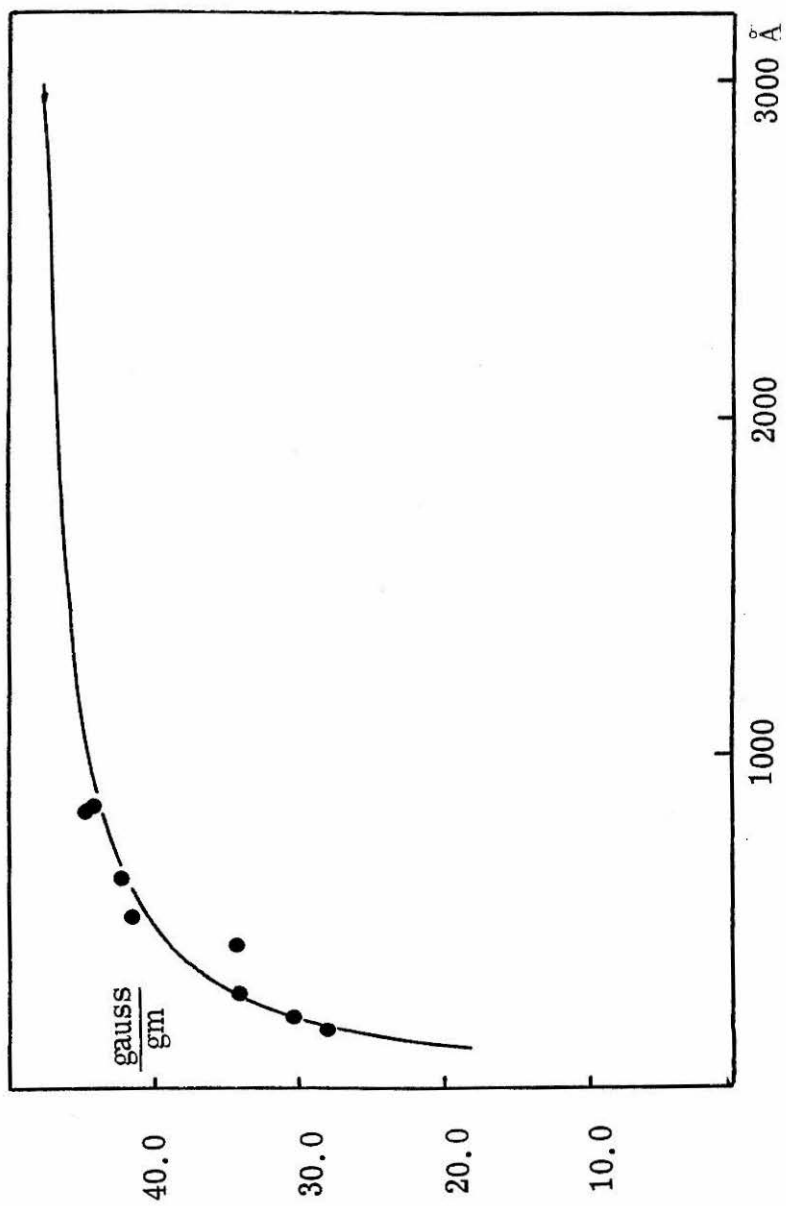


Figure 32. $\sigma_{0,\infty}(D)$ versus VMPS of samples prepared in LiOH-LiCl media. Solid line calculated for Anisotropic Model.

- (4) Gradient Model: The dead-layer need not be completely non-magnetic as assumed in the previous models. In this model it is assumed that a linear gradient of magnetic activity exists in the dead-layer. The magnetization increases from zero at the surface to a maximum at the the edge of the magnetic core.

$$\frac{\sigma_{0,\infty}^{(D)}}{\sigma_{0,\infty}^{(\infty)}} = (1 - 3g/D + 4g^2/D^2 - 2g^3/D^3)$$

Figures 33, 34, and 35 show the best least squares fit of magnetization data of $\delta\text{FeO}(\text{OH})$ prepared in different media to this model.

Schematic representations of the models are shown in figures 14 and 15. Parametric values obtained from the best least-squares fit of the models to the data for $\delta\text{FeO}(\text{OH})$ are given in Table 8. The dead-layers found for $\delta\text{FeO}(\text{OH})$ prepared in NaOH-NaCl media by all four models is much thicker than the layer found for samples produced in either KOH-KCl or LiOH-LiCl. This may reflect either the greater amount of data available for the NaOH-NaCl system or the different preparative conditions used to prepare these samples (see previous chapter). In all cases the dead layer found is several unit cells thick. Statistics of the model fits to the data do not permit clear-cut choice among the models. Errors in the parameters are greatest for the Totally Anisotropic and Gradient models. It is likely that either the Uniform or Anisotropic models is the best description of the system.

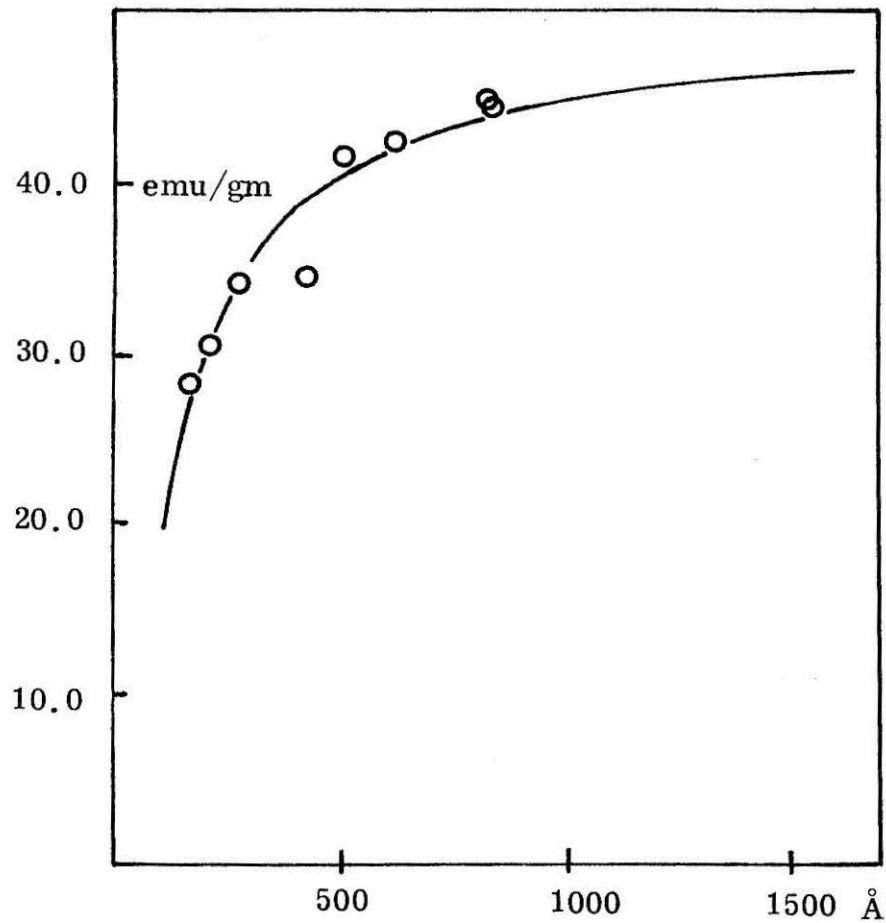


Figure 33. $\sigma_{O, \infty}(D)$ versus VMPS for samples of $\delta\text{FeO(OH)}$ prepared in LiOH-LiCl media. Solid line calculated from Gradient Model.

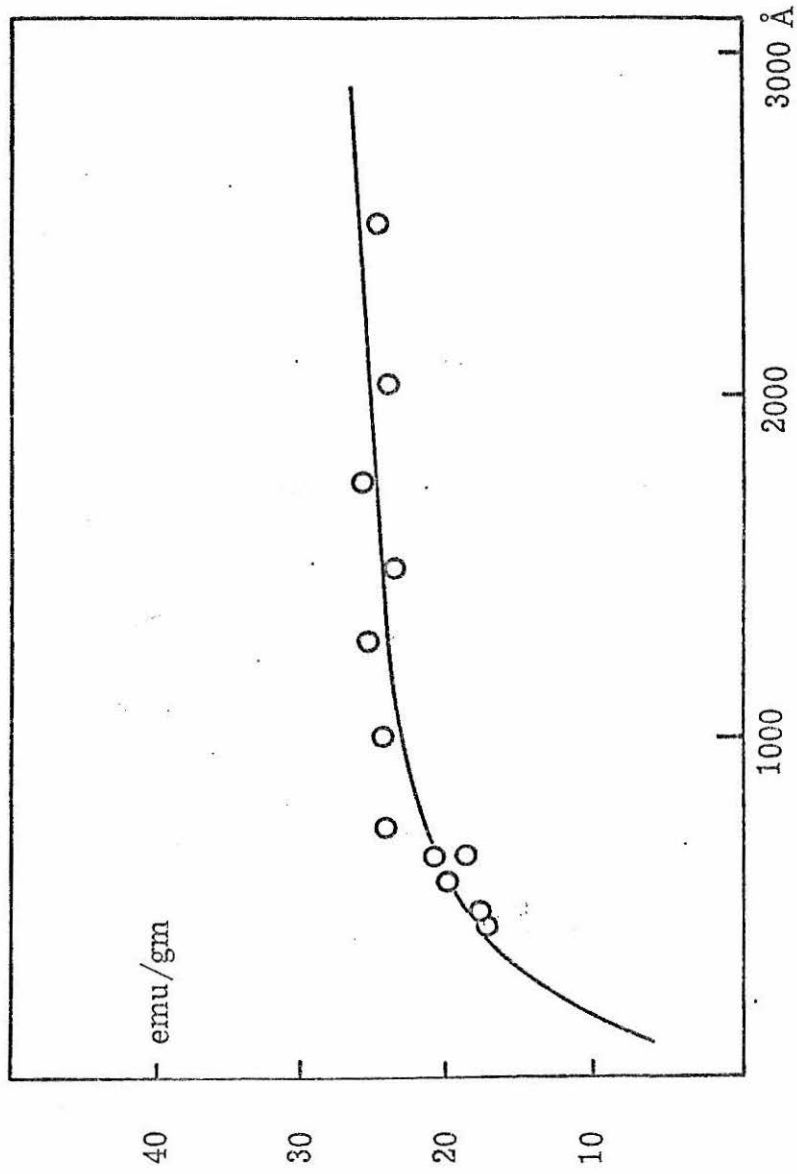


Figure 34. $\sigma_{o, \infty}(D)$ versus VMPS for samples of $\delta\text{FeO}(\text{OH})$ prepared in NaOH-NaCl media. Solid line calculated from Gradient Model.

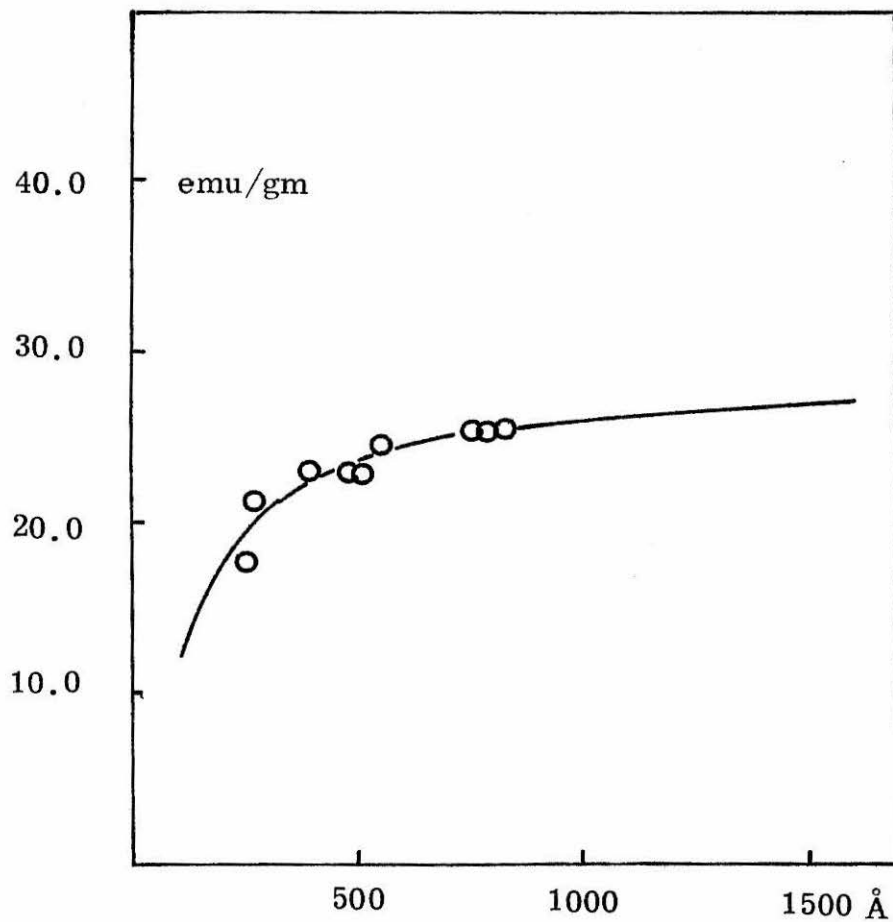


Figure 35. $\sigma_{O,\infty}(D)$ versus VMPS for samples of $\delta\text{FeO}(\text{OH})$ prepared in KOH-KCl. Solid line calculated from Gradient Model.

Table 8

Parametric Values from Best Least-Squares Fit of Saturation Magnetization Data
for $\delta\text{FeO}(\text{OH})$ to Dead Layer Models

Model	Media in Which Samples were Prepared			NaOH-NaCl			LiOH-LiCl			
	KOH-KCl	NaOH-NaCl	LiOH-LiCl	$\sigma_{0,\infty}^b$ (emu/gm)	μ^c (BM)	g^a (Å)	$\sigma_{0,\infty}^b$ (emu/gm)	μ^c (BM)	g^a (Å)	$\sigma_{0,\infty}^b$ (emu/gm)
Uniform	28.39	28.38	28.38	0.45	0.45	9.3	48.76	0.45	48.76	0.78
	± 1.40	± 2.00	± 2.00			± 2.2	± 3.60			
Anisotropic	28.47	28.43	28.43	0.45	0.45	15.85	49.03	0.45	49.03	0.78
	± 1.50	± 2.10	± 2.10			± 5.4	± 3.50			
Totally	28.28	28.36	28.36	0.45	0.45	22.9	48.68	0.45	48.68	0.78
Anisotropic	± 1.45	± 2.90	± 2.90			± 4.5	± 3.50			
Gradient	28.98	28.56	28.56	0.46	0.45	33.8	49.75	0.45	49.75	0.79
	± 2.00	± 2.30	± 2.30			± 10.3	± 3.75			

^a Thickness of dead layer. For anisotropic model this is the thickness of the layer along the a and b axes. The thickness along the c axis is 1/3 g.

^b Saturation magnetization of an infinite sized particle or the bulk saturation magnetization at 0 °K and infinite applied field.

^c Magnetic moment calculated from $\mu = \sigma_{0,\infty}(\infty) \cdot MW/N\beta$.

(B) Magnetic Dead-Layers and the Approach to Saturation.

Magnetic inhomogeneity should have a definite impact on the magnetic behavior of a sample of fine particulate magnetic species. This impact should be reflected in all parts of the magnetization curve. Particle volume is a controlling parameter of magnetization curves. A comparison between particle volume calculated from magnetization data (magnetic volume) and particle volume found from other data (physical volume) should yield information concerning the magnetically depleted volume.

Magnetogranulometry has been a much investigated aspect of fine particulate magnetic species. Cahn¹⁴ and Becker¹⁵ have developed a simple scheme by which the volume (and consequently size) distribution of an assemblage of superparamagnetic species can be derived from magnetization data. The procedure takes advantage of the fact that initial portions of magnetization curves are controlled by larger particles while the approach to saturation is controlled by the smallest particle in a distribution.

Let the volume distribution of particles in an assemblage be given by a function $n(v)$ such that N , the total number of particles per unit volume is $\int_0^{\infty} n(v)dv$. The magnetic moment per unit volume is

$$I = I_S^{(T)} \int_0^{\infty} V n(v) dv$$

where $I_S^{(T)}$ is the saturation magnetization at temperature T . The initial volume susceptibility is then given by

$$\chi_i = \lim_{H \rightarrow 0} I/H = \frac{I_s^2}{kT} \int_0^\infty V^2 n(v) dV$$

and the approach to saturation is

$$\frac{I}{I_0} = 1 - \frac{kT}{I_0 H} \int_0^\infty n(v) dV$$

where I_0 is the magnetic moment of the assemblage at saturation and H is the applied field. The quantities H_h and H_l are defined in figure 36. Then, the mean volume and root mean square volume of the particles in the assemblage are given by

$$\bar{V} = \frac{1}{N} \int_0^\infty V n(v) dV = \frac{kT}{I_s H_h}$$

$$(\bar{V}^2)^{\frac{1}{2}} = \frac{1}{N} \left(\int_0^\infty V^2 n(v) dV \right)^{\frac{1}{2}} = \frac{kT}{I_s} \left[\frac{3}{H_l H_h} \right]^{\frac{1}{2}}$$

Notice that to this point no assumption has been made concerning the nature of the distribution function $n(v)$.

The mean volume \bar{V} and $(\bar{V}^2)^{\frac{1}{2}}$ are related by the standard deviation of the volume distribution. Once the standard deviation of the assemblage is known, a complete description of the size distribution of particles in the assemblage is at hand. The root-mean square deviation is given by

$$(\nabla \bar{V}^2)^{\frac{1}{2}} = [\bar{V}^2 - (\bar{V})^2]^{\frac{1}{2}} = \frac{kT}{I_s H_h} \left[\frac{3H_h}{H_l} - 1 \right]$$

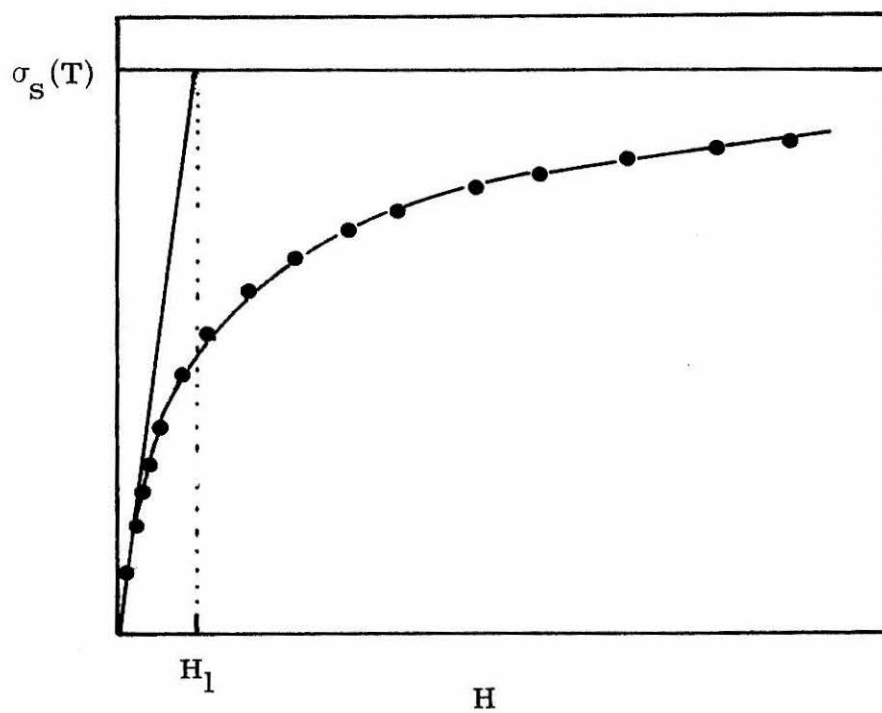
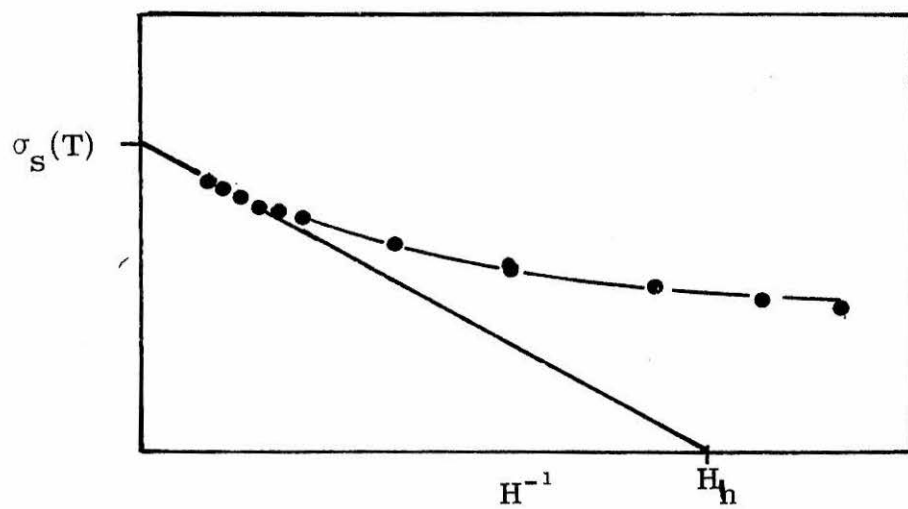


Figure 36. Definitions of H_h and H_1 .

Table 9

Cahn-Becker Analysis of Superparamagnetic $\delta\text{FeO}(\text{OH})$

Samples Prepared in Various Media

VMPS ^a	H_n	H_1	\bar{V}	$\langle \bar{V}^2 \rangle^{\frac{1}{2}}$
(\AA)			($\text{\AA}^3 \times 10^5$)	($\text{\AA}^3 \times 10^5$)
Samples prepared in KOH-KCl media				
253	1400	2350	4.56	6.10
270	1250	2135	5.11	6.77
396	1050	1370	6.08	9.22
480	755	1195	8.46	11.65
510	820	1215	7.79	11.08
552	540	765	11.83	17.21
Samples prepared in LiOH-LiCl media				
179	1190	1650	3.11	4.57
221	1087	1520	3.40	4.97
290	945	1420	3.92	5.53
435	560	1090	6.61	8.20
520	440	1000	8.41	9.66
632	390	900	9.49	10.82
Samples prepared in NaOH-NaCl media				
456	1.44	545	765	11.75
502	1.43	530	740	12.08
585	1.53	500	715	12.80

^a VMPS derived from microscopic data. ^b Samples not cited contained a significant percentage of single domain particles at room temperature.

Table 10
Results of Cahn-Becker Analysis of
Superparamagnetic Samples of $\delta\text{FeO}(\text{OH})$
Prepared in Various Media

Physical Data ^a		Magnetic Data				
VMPS (\AA)	σ_g	$\left(\frac{\bar{V}}{f}\right)^{\frac{1}{3}}$ (\AA)	$\left(\frac{\bar{V}}{f}\right)^{\frac{1}{5}}$ (\AA)	σ_g	VMPS _M (\AA)	g^b (\AA)
Samples prepared in KOH-KCl media						
253		151	167	1.25	1.75	40
270		157	173	1.25	182	44
396		167	192	1.30	206	95
480		186	208	1.27	220	130
510		182	204	1.27	216	147
552		208	236	1.28	251	150
Samples prepared in LiOH-LiCl media						
179		132	152	1.30	163	8
221		137	156	1.29	166	28
290		145	162	1.27	171	60
435		172	184	1.20	190	122
520		186	196	1.18	201	160
632		199	208	1.16	213	210
Samples prepared in NaOH-NaCl media						
456	1.44	208	236	1.29	251	102
502	1.43	210	238	1.28	253	125
585	1.53	214	242	1.28	257	164

^aData from electron micrographs. ^bDead layer thickness.

Most of the samples of $\delta\text{FeO}(\text{OH})$ considered in this study are superparamagnetic at room temperature. Application of Cahn-Becker analysis to these samples will yield descriptions of the effective magnetic volumes of the samples which can be compared to the known physical volume. To maintain the continuity of analysis in this study, it is convenient to convert the volume description above into a size distribution. From the physical data concerning the samples it is known that the particle size in the samples is well described by a log-normal distribution function. Higher moments of the log-normal function are also log-normal. Therefore, it is assumed that $n(v)$ is the log-normal distribution. Then

$$\ln \left[\frac{(\bar{V}^2/f)^{1/6}}{(\bar{V}/f)^{1/3}} \right] = 2 \ln^2 \sigma_g$$

where f is the volume factor (see above). Therefore the magnetic volumetric-mean particle size (VMPS_M) is given by

$$\text{VMPS}_M = (\bar{V}/f)^{1/3} \exp(3 \ln^2 \sigma_g)$$

The results of Cahn-Becker analysis of the samples are shown in Tables 9 and 10. As can be seen the VMPS_M of all samples is smaller than the VMPS determined from electron micrographic data. Further, the size distribution calculated from magnetic data is much sharper than that found from electron microscopic data. A comparison of the size distribution found from magnetic and from physical data for one sample is shown in Figure 37 in terms of frequency and particle diameter.

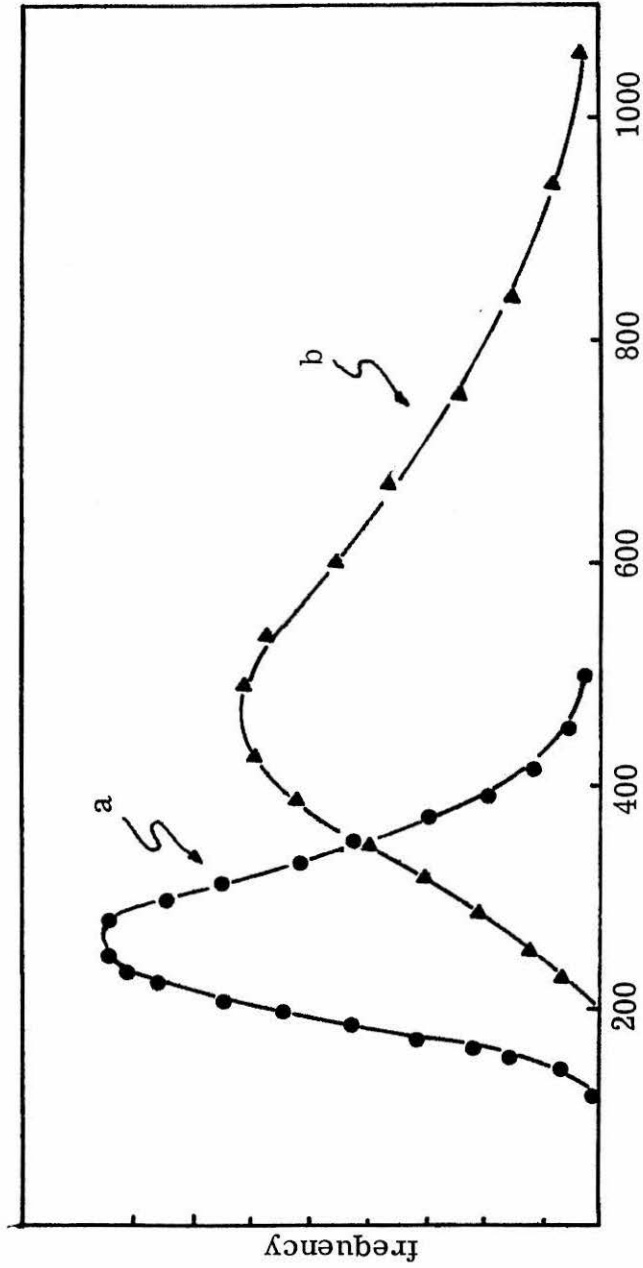


Figure 37. VMPS distributions (a) calculated from magnetic data - · - ·, and (b) found from electron micrographic data.

A disquieting feature of the results is the particle size dependence of the calculated magnetic dead-layer. Rather than being uniform, the dead-layer increases in size with particle size. This effect may not be altogether real. Cahn-Becker analysis presupposes that the magnetic particles are isotropic superparamagnets whose approach to saturation is described by the Langevin equation

$$\frac{\sigma(T)}{\sigma_s(T)} = 1 - \frac{kT}{\mu H}$$

The approach to saturation of all samples of $\delta\text{FeO}(\text{OH})$ used in this study was linear for fields greater than 7000 oe. However, the $\delta\text{FeO}(\text{OH})$ particles are definitely anisotropic. Their approach to saturation is described by

$$\frac{\sigma(T)}{\sigma_s(T)} = f\left(\frac{kT}{KV}, \frac{H\sigma_s V\rho}{kT}\right)$$

where f is a complex function of the anisotropy energy as well as the field energy. The contribution of the anisotropy energy would be expected to increase with particle size. Consequently, only dead-layers found for particles much smaller than the single domain particle size can be viewed with confidence. Dead layers for the smallest particles are on the order of 25\AA , in good agreement with those calculated from the size dependence of the saturation magnetization.

(C) Magnetic Dead-Layers and the Hysteresis Properties of Magnetization Curves. Bean and Jacobs¹⁶ have suggested that the

coercive force of a single domain, uniaxial, magnetic particle can be related to particle volume by

$$H_c = \frac{2K}{\rho\sigma_s(T)} \left(1 - 5 \left(\frac{kT}{KV}\right)^{\frac{1}{2}}\right)$$

where H_c is the coercive force, K the anisotropy energy, k the Boltzmann constant, and V the volume of the single domain particle. (See Appendix 1 for a possible derivation of the relation.) Little has been done analytically with this expression, though it seems to contain all the elements necessary for magnetic granulometry. Consider an assemblage of particles with a distribution of particle sizes centered about a mean which is near the single domain particle size at temperature T_i . As the temperature is lowered some of the particles become single domain particles and develop hysteresis properties. The smaller particles remain superparamagnetic. As the temperature is lowered still further a larger fraction of the particles convert from their original superparamagnetic state to the single domain state. Finally at some T_f the entire assemblage consists of single domain particles.

From the above expression, the mean volume of the single domain particles at any given temperature between T_i and T_f could be calculated. Since the ratio of the magnetization of the assemblage of particles at zero applied field to the magnetization at infinite field is equal to one half the single domain fraction of particles, at T_f a complete description of the volume distribution of particles in the assemblage could be made. Comparison between this distribution and

the distribution found from physical data could then be used to determine the magnetic inhomogeneity of the particles in the assemblage. In this section this application of the relation is made to the magnetic behavior of the $\delta\text{FeO}(\text{OH})$ samples.

Figure 38 shows the behavior of the Bean and Jacobs relationship for several particle sizes. The striking similarity of these curves and those experimentally found for $\delta\text{FeO}(\text{OH})$ should be noted.

Use of the above relationship requires knowledge of not only the temperature dependence of the saturation magnetization of the assemblage, but also the temperature dependent anisotropy energy. Determination of the anisotropy energy from powder magnetic data is no easy matter. The following procedure has been used. The anisotropy energy at 0°K was calculated from the Stoner-Wohlfarth equation¹⁷

$$K(0) = \rho \sigma_{0,\infty}(0) H_c(0)$$

where $H_c(0)$ is the coercive field of the samples at 0°K . The temperature dependence of K was then found by the method of Asti and Rinaldi.¹⁸

Asti and Rinaldi have related the discontinuity in the second derivative of the magnetization curve of powder samples to the anisotropy field (see Appendix 2). No faith, however, was placed in the results of this method. Instead, the data found by the second derivative method was used to fit the anisotropy energy to the expression

$$\frac{K(T)}{K(0)} = \left[\frac{\sigma_s(T)}{\sigma_s(0)} \right]^n$$

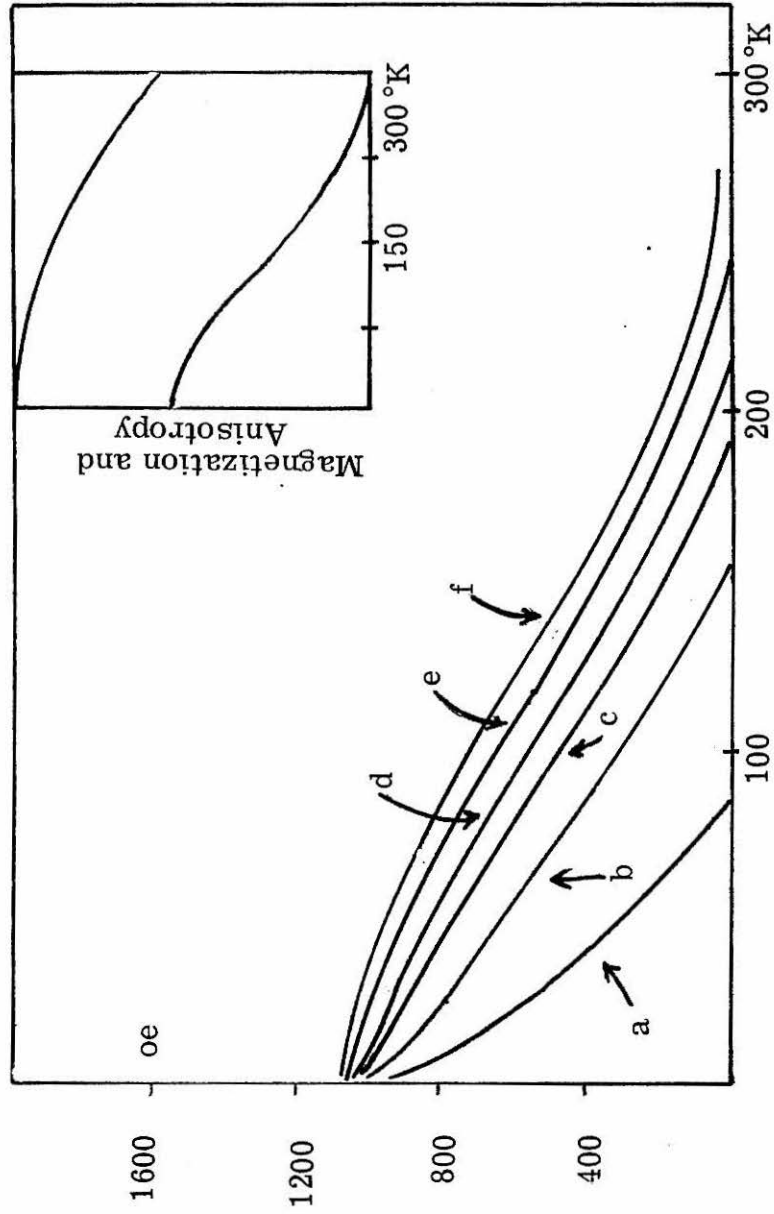


Figure 38. Behavior of Bean-Jacobs Relationship for particles of varying size--(a) 200Å, (b) 300Å, (c) 400Å, (d) 600Å, (e) 800Å, (f) 1000Å. Insert shows temperature dependence of anisotropy and saturation magnetization.

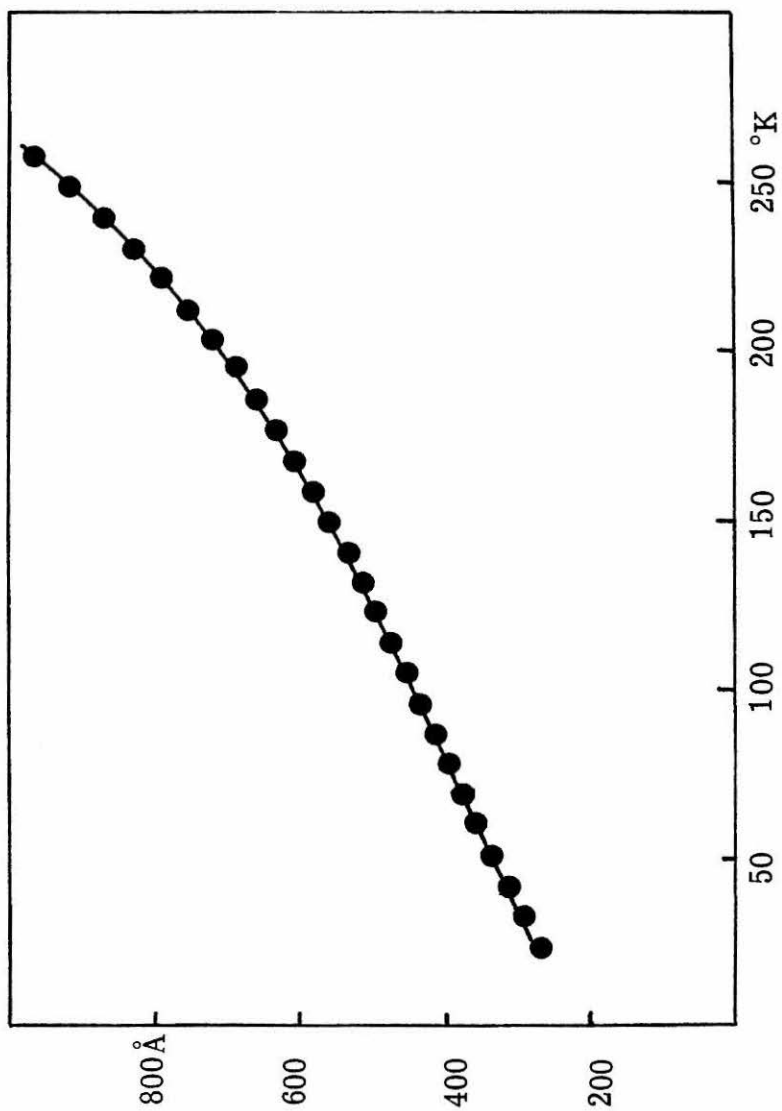


Figure 39. Particle size as function of temperature calculated from Bean-Jacobs relationship.

The fit was typically fairly insensitive to the parameter n . Best fits were obtained with $n = 8.0 \pm 1.5$.

In figure 39 the variation in mean particle diameter calculated from the Bean-Jacobs relation and the above expression for the anisotropy energy with temperature is shown for a single sample of $\delta\text{FeO}(\text{OH})$. The mean particle diameter at first falls rapidly with temperature and then begins to asymptotically approach a finite value.

If the system being interrogated is a system whose size distribution is log-normally distributed, then plots of the log of particle diameter versus twice the ratio of the remanent to saturation magnetization (that is the cumulative percent number density of active particles) can be used to determine the size distribution of the assemblage. A plot of this type drawn from the data in Table 11 is shown in figure 40. Results of similar analysis for other samples of $\delta\text{FeO}(\text{OH})$ are shown in Table 12. From these results it is apparent that the analysis is tracing out a log-normal distribution whose mean is universally smaller than that found from electron micrographic data and whose standard deviation is larger. The difference between physical and magnetic volumes is variable, but of the same order as that calculated from the size dependence of the saturation magnetization.

Computational note: The laborious process of acquiring magnetic data suitable for this analysis was relieved by spline fitting data from 11 to 16 magnetization curves and using the fit to interpolate intermediate points. The spline fit was created to match first and second derivatives at the experimental points.

Table 11

Data Used in the Preparation of Figures 40 and 41

Temperature (°K)	H_c (oe)	Calculated Mean Diameter (Å)	$2R^a$
24	730	339	0.86
33	715	376	0.81
42	699	407	0.76
51	680	433	0.72
60	659	457	0.698
69	638	481	0.672
78	620	505	0.65
87	604	531	0.632
96	587	557	0.609
105	563	580	0.583
114	527	595	0.546
123	501	617	0.526
141	484	647	0.52
150	458	672	0.51
159	422	690	0.488
168	382	703	0.462
177	342	716	0.436
186	310	736	0.412
195	287	765	0.396
204	268	800	0.392

Table 11 (Continued)

Temperature (°K)	H _c (oe)	Calculated Mean Diameter (Å)	2R ^a
213	249	838	0.372
222	229	876	0.362
231	208	913	0.352
240	186	950	0.34
249	164	986	0.326
258	142	1023	0.31

^a Ratio of remanent to saturation magnetization.

Table 12

Magnetic Size Distributions

Calculated from Bean Jacobs Relation

Physical Data		Magnetic Data		
VMPS (\AA)	σ_g	VMPS _M (\AA)	σ_g	g (\AA)
Samples prepared in LiOH-LiCl media				
179		123	2.15	28
221		133	2.82	44
290		182	3.26	54
520		384	2.15	68
632		517	2.17	62
841		699	2.16	70
Samples prepared in KOH-KCl media				
253		141	2.06	56
270		152	1.87	59
396		286	1.98	55
510		386	1.95	62
784		688	1.94	48
826		676	1.86	75
Samples prepared in NaOH-NaCl media				
456	1.44	338	1.88	59
660	1.43	490	1.90	85
746	1.44	598	1.94	74
1284	1.52	1062	1.87	111
2030	1.42	1878	1.85	76

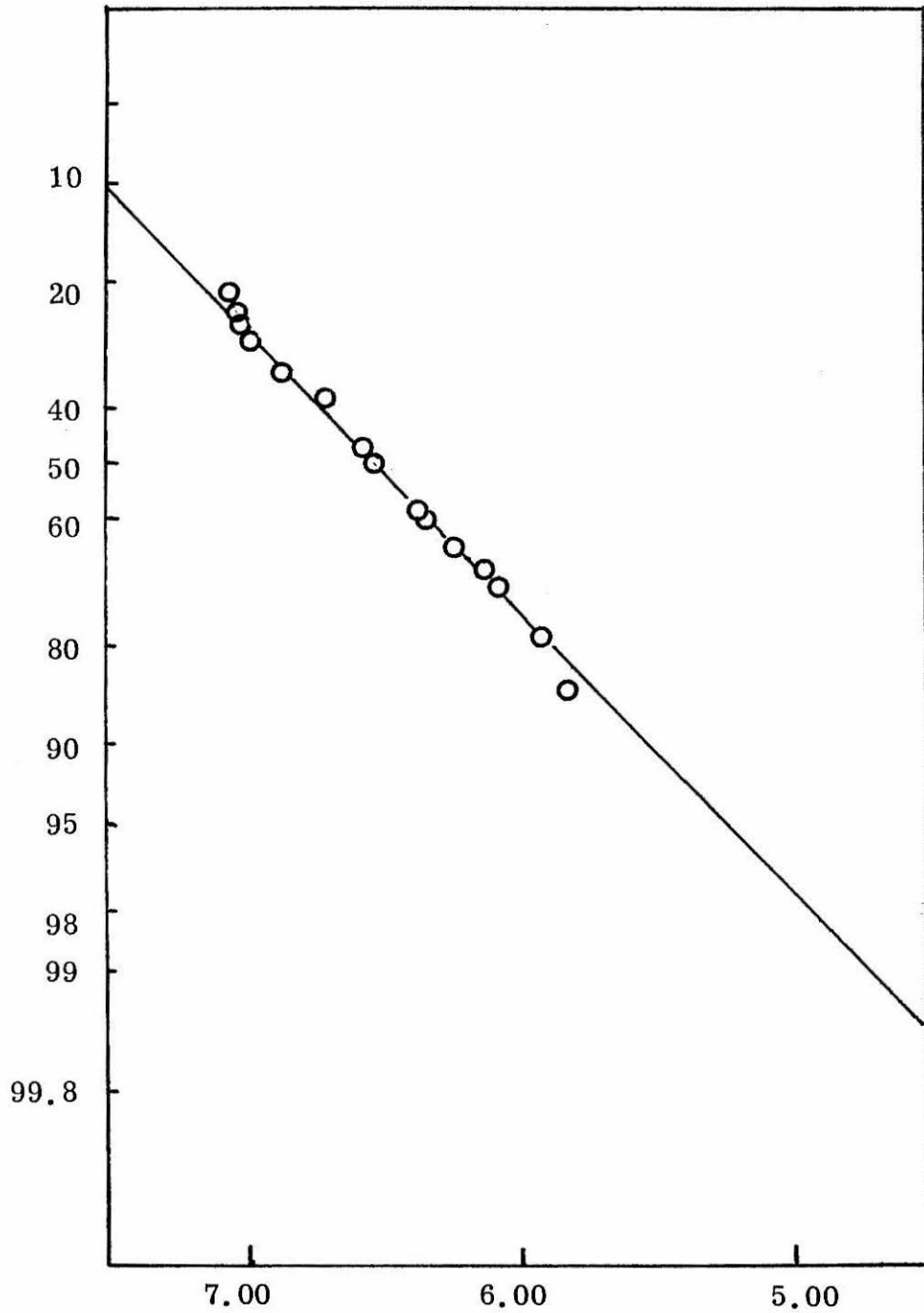


Figure 40. Plot of cumulative number percent versus $\ln D$ calculated from fit of hysteresis data to Bean and Jacobs relationship.

Conclusions

It is apparent that the magnetization data for particles of $\delta\text{FeO}(\text{OH})$ are indeed consistent with the idea that each particle of material is surrounded by a layer of magnetically depleted material. This layer is apparently several unit cells thick. It is tempting to equate the magnetically active material with that material which is not depleted of alkali metal cations. Several observations auger in favor of this conclusion:

- (1) A magnetic phase could not be produced when the intermediate ferrous hydroxide was precipitated with bases other than those derived from alkali metals.
- (2) Depletion layers account well for the observed dependence of magnetization and alkali metal ion contamination of the phase.
- (3) The intensity of magnetization of $\delta\text{FeO}(\text{OH})$ is strongly dependent on the alkali metal base used to precipitate the intermediate ferrous hydroxide.
- (4) Complete removal of alkali metal cations was not possible, indicating strong interactions between the lattice and the ions.

The temptation to make this equation is inhibited by the very low level of alkali metal ion concentration in the samples. This inhibition is mitigated by the observation that an allotrope of $\delta\text{FeO}(\text{OH})$, $\beta\text{FeO}(\text{OH})$ is structurally stabilized by as little as one part in four thousand of

halide ion. In the absence of a more conclusive link between the cationic impurities and magnetic behavior of $\delta\text{FeO}(\text{OH})$ no correlation can be positively drawn. The inference, however, is strongly made.

References

1. G. Herdan, "Small Particle Statistics," 2nd. ed., Academic Press, New York, 1960.
2. International Critical Tables, Vol. 1, p. 92.
3. M. J. Kelin and R. S. Smith, Phys. Rev., 81, 378 (1951).
4. R. Coren and H. J. Juretschke, J. Appl. Phys., 28, 806 (1957).
5. E. C. Crittenden and R. W. Hoffman, Revs. Modern Physics, 25, 310 (1953).
6. J. C. Walker, C. R. Guarnieri, and R. Semper, Amer. Phys. Soc., 17, 545 (1972)
7. L. N. Libermann, J. Clinton, D. M. Edwards, and J. Mathon, Phys. Rev. Letters, 22, 539 (1969).
8. F. E. Luborsky, Phys. Rev., 109, 40 (1958).
9. J. J. Becker, J. Metals, 209, 59 (1957).
10. W. J. Schuele and V. D. Deetscreek in "Ultrafine Particles," W. E. Kuhn, H. Lamprey, and C. Sheer (eds), p. 218, John Wiley and Sons, New York, 1963.
11. R. Kaiser and G. Miskolczy, J. Appl. Phys., 41, 1064 (1970).
12. A. E. Berkowitz and J. A. Lahut, private communication.
13. A. E. Berkowitz, W. J. Schuele, and P. J. Flanders, J. Appl. Phys., 39, 1261 (1968).
14. J. Cahn, Trans. AIME, 209, 1309 (1957).
15. J. J. Becker, Trans AIME, 209, 59 (1957).

16. C. P. Bean and I. S. Jacobs in "Magnetism," Vol. III, G. T. Rado and H. Suhl, eds., Academic Press, New York, 1963.
17. E. C. Stoner and E. P. Wohlfarth, Philos. Trans. Roy. Soc., A, 240, 74 (1948).
18. G. Asti and S. Rinaldi, Phys. Rev. Letters, 28, 1584 (1972).
19. C. P. Bean, J. Appl. Phys., 26, 1381 (1955).

APPENDIX 1
DERIVATION OF THE RELATION BETWEEN
PARTICLE SIZE AND THE
COERCIVE FIELD OF A PARTICLE ASSEMBLAGE

The following derivation is provided for the reader who might be unfamiliar with micromagnetics. The result is well-known in the literature, but seems never to be specifically derived. For more complete accounts of the implications of this result, one should consult the references.

Consider an assemblage of single-domain magnetic particles. Allow that the particles are immobilized and are not free to mechanically rotate. Further, the particles possess a uniaxial magnetic anisotropy completely specified by the parameter K which may be temperature dependent. Anisotropy may be due to either shape or crystalline effects. The volume of a particle is V . In real situations there will be a volume distribution. The parameter V will then be the mean volume and the derivation will still apply provided the distribution is reasonably sharp and unimodal. Experimental methods for the determination of coercive field of particle assemblages are sufficiently crude to negate any error associated with a spread in particle volume. Let the saturation magnetization of the assemblage be M_s which is also temperature dependent.

Since the particles are immobilized, reversal of the magnetization of the assemblage with a reversal of field must occur by reversal of the magnetic moment of the particle, $\mu = VM_s$. This moment will in fact behave much like a particle. The orientation of the magnetic moment will be dictated by (1) the applied magnetic field, (2) the magnetic anisotropy, and (3) thermal fluctuations analogous to Brownian motion. The first two influences will act to align the moment in a magnetic field. Let θ be the angle between the easy axis of magnetization of the particle and the applied field, H . The energy of the moment will then be

$$E_M = KV\sin^2\theta - \mu H\cos\theta$$

Thermal effects will act to eliminate the alignment of the magnetic moments. The combination of influences will produce a Boltzmann distribution of moments.

$$\bar{u} = \text{average moment} = \frac{u \int \frac{(\vec{u} \cdot \vec{H})}{\mu H} \exp\left(\frac{-E_M}{kT}\right) d\Omega}{\int \exp\left(\frac{-E_M}{kT}\right) d\Omega}$$

where k = Boltzmann constant

$d\Omega$ = incremental solid angle

When the field is removed, de-alignment of the assemblage of moments will be impeded by an energy barrier KV . The size of KV may be sufficient that rotation of the moments by thermal fluctuations is indetectably slow. To reverse the orientation of such moments, it is

necessary to apply a reverse field to the assemblage. This acts to reduce the energy barrier. To find the barrier, one must examine the angular functional behavior of the above energy expression. The barrier will be equal to the maximum of this expression less the initial energy of the reverse oriented particles. (Note, since a reverse field has been applied, the moments are initially completely reverse oriented, $\theta = \pi$.)

The first derivative of E_M with respect to θ is

$$\frac{dE_M}{d\theta} = 2KV \sin \theta \cos \theta + uH \sin \theta$$

This derivative is zero at $\theta = 0$ (oriented position), $\theta = \pi$ (reverse oriented position), and $\theta = \arccos(-uH/2KV)$. The oriented and reverse oriented positions must correspond to global and relative minima in the energy expression. Therefore, from the second derivative, E_M is a maximum at $\theta = \arccos(-uH/2KV)$.

$$E_M(\theta = \arccos \frac{-uH}{2KV}) = KV + \frac{u^2 H^2}{4KV}$$

$$E_M(\theta = \pi) = uH$$

Then the barrier, $E_b(H)$, is $KV + \frac{u^2 H^2}{4KV} - uH$

The probability that a particle moment will have sufficient energy to surmount the barrier is given by the Boltzmann probability expression:

$$p = \exp(-E_b(H)/kT)$$

where k is the Boltzmann constant and ought not to be confused with the magnetic anisotropy constant K .

As the moments de-align, the magnetization of the particle assemblage will be reduced from the saturation value. The kinetics of this process is described by

$$\frac{dM}{dt} = f_0 p M$$

where f_0 is a frequency factor approximately equal to 10^9 sec^{-1} .

Integration then gives

$$M = M_s \exp(-t f_0 p) = M_s \exp\left(-t f_0 \exp\left(\frac{-E_b}{kT}\right)\right)$$

Magnetic measurements are usually done on a time scale of 10^2 seconds. Reversal on this time scale will be perceptible only if $E_b(H) \leq 25kT$. Magnetization curves then are generated by decreasing the applied field until H is sufficient to lower $E_b(H)$ to $25kT$. The field at this point is the coercive field, $H_c(T)$. The relation between this field and the particulate volume can be derived as follows:

$$KV + \frac{\mu^2 H_c^2}{4KV} - \mu H_c = 25kT$$

$$4K^2 V^2 + \mu^2 H_c^2 - 4\mu H_c KV = 25 kT(KV)4$$

$$(2KV - \mu H)^2 = 100 kT(KV)$$

$$\mu H_c = 2KV - [100kT(KV)]^{\frac{1}{2}}$$

$$\mu H_c = 2KV [1 - 5 \left(\frac{kT}{KV}\right)^{\frac{1}{2}}]$$

$$H_c = \frac{2KV}{\mu} [1 - 5 \left(\frac{kT}{KV}\right)^{\frac{1}{2}}]$$

$$H_c(T) = \frac{2K(T)}{M_s(T)} [1 - 5 \left(\frac{kT}{KV}\right)^{\frac{1}{2}}]$$

With this expression, the mean volume of single-domain particles in a given assemblage at a particular temperature can be calculated. By knowing the temperature behavior of H_c , M_s , and K , and the fraction of single-domain particles in a given sample at every temperature, one can derive a volume distribution of the sample as shown in the preceding chapter.

References

1. I. S. Jacobs and C. P. Bean, "Magnetism," Vol. III, Chapter 6, G. T. Rado and H. Suhl eds., Academic Press, New York, 1963.
2. L. Néel, Compt. rend. acad. sci., 228, 664 (1949).
3. W. F. Brown, Jr., J. Appl. Phys., 50, Suppl., 130S (1959).
4. E. H. Frei, S. Shtrikman, and D. Trevers, Phys. Rev., 106, 446 (1957).

APPENDIX 2
 DERIVATION OF MAGNETIC ANISOTROPY FROM
 BULK MAGNETIZATION DATA

Consider a single-domain, uniaxial particle oriented with its symmetry axis along the x-axis and its "hard" axis of magnetization along the y-axis of a coordinate system. In a field H applied at an angle φ to the symmetry axis, the magnetic moment of this particle will orient at some angle θ to the symmetry axis as shown in Figure 1.

Stoner and Wohlfarth¹ have shown that as the applied field H approaches H_A and the angle φ approaches 90° , a discontinuity occurs in the magnetization curve $M(H)$. The curves for $\varphi \neq 90^\circ$ are smooth functions of H . The curvature of these functions increases without limit as φ approaches 90° (see Figure 2). The field at which this discontinuity occurs, H_A , is the anisotropy field which is related to the anisotropy energy, $E_K = K_1 \sin^2 \theta + K_2 \sin^4 \theta$ by the expression

$$-H_A = (2K_1 + 4K_2)/M_S$$

The angle between the applied field and the magnetic moment will be dictated by energy minimization. The energy per unit volume for the particle in an applied field is

$$E = K_1 \sin^2 \theta + K_2 \sin^4 \theta - M_S H \cos(\theta - \varphi)$$

where $\theta - \varphi$ is the angle between \vec{H} and \vec{M}_S . As shown above, interesting behavior occurs only for $\varphi \approx \pi/2$ and $H \approx H_A$. Therefore the following definitions are substituted into the above energy expression:

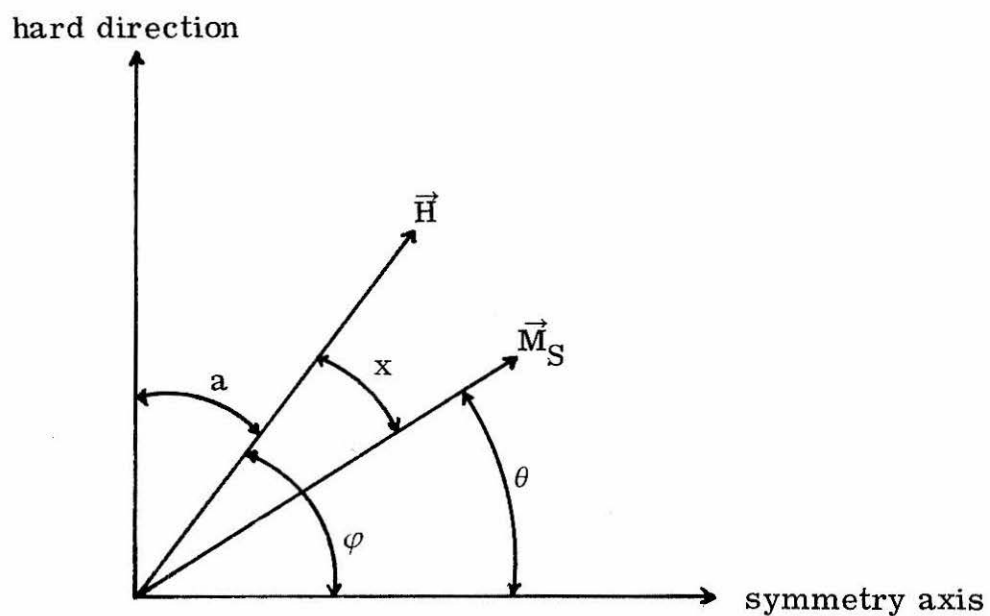


Figure 1. Orientation of applied field, \vec{H} , and the magnetic moment, \vec{M}_S , of a single particle with its symmetry along horizontal axis.

$$\chi = \theta - \varphi ; \quad a = \frac{\pi}{2} - \varphi ; \quad H = -(\gamma + 1)H_A$$

$$\gamma = \frac{H - |H_A|}{|H_A|}$$

Then

$$E = K_1 \cos^2(x - a) + K_2 \cos^4(x - a) + M_S H_A (\gamma + 1) \cos x$$

Then the equilibrium condition for x is

$$\begin{aligned} \frac{\partial E}{\partial x} &= -2K_1 \cos^2(x - a) \sin(x - a) - 4K_2 \sin(x - a) \cos^3(x - a) - \\ &M_S H_A (\gamma + 1) \sin x = 0 \end{aligned}$$

Again, interest centers on this expression only for small values of x and a . This expression can be simplified by expanding the trigonometric functions in algebraic expansions and by noting that $M_S H_A = -2(K_1 + 2K_2)$. Then to third order,

$$\begin{aligned} \frac{\partial E}{\partial x} &= K_1(-2x + 2a + \frac{4}{3}x^3 - 4ax^2 + 4xa^2 - \frac{4}{3}a^3) + K_2(-4x + 4a + \frac{20}{3}x^3 \\ &- 20x^2a + 20xa^2 - \frac{20}{3}a^3) + 2(K_1 + 2K_2)(\gamma + 1)(\frac{x^3}{6} - x) \\ &= 2(K_1 + 2K_2)(a + \gamma x) + (K_1 + 6K_2)x^3 - (K_1 + 2K_2)\gamma \frac{x^3}{3} \\ &+ (K_1 + 5K_2)(-\frac{4}{3}a^3 - ax^2 + xa^2) = 0 \end{aligned}$$

Maintaining the level of approximation, the equilibrium expression defining x is

$$\frac{(K_1 + 6K_2)}{(2K_1 + 4K_2)} x^3 + \gamma x + a = 0 = Lx^3 + \gamma x + a$$

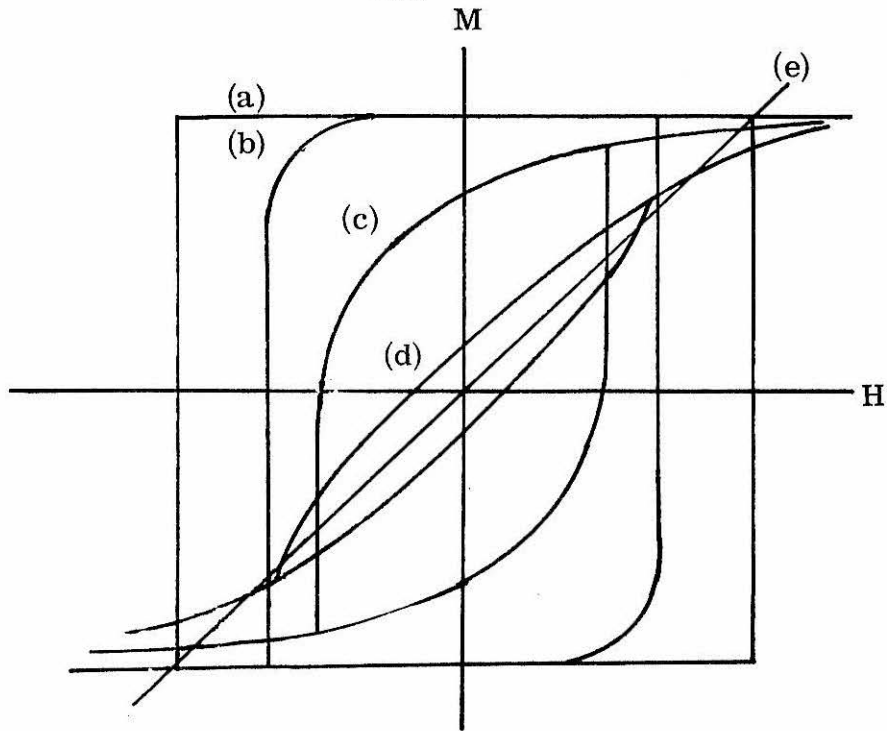


Figure 2. Magnetization curve for a single particle with its symmetry axis inclined to the applied field by an angle (a) 90° , (b) 80° , (c) 45° , (d) 10° , (e) 0° . Discontinuity in (a) occurs at $H = H_A$. (After reference 1)

In polycrystalline samples all possible orientations of the particles occur. A rigorous analysis would have to deal with all orientations of the particles in the interval $-90^\circ \leq \varphi \leq 90^\circ$. Asti and Rinaldi² have shown that by considering only those particles oriented at angles in the neighborhood of $\varphi = 90^\circ$ simple procedures for deriving the anisotropy of the particles can be derived. The theoretical derivation provided by these authors is fraught with several errors. This appendix follows the course of their theoretical development and hopefully corrects the errors in their presentation.

Define the dimensionless magnetization parameter $t = (M_S - M(H))/M_S$ which in the level of approximation described above is

$$t = 1 - \cos x \cong \frac{x^2}{2}$$

For an assemblage of particles oriented such that φ is nearly 90° ($-a_0 \leq a \leq a_0$) the average value of t is

$$\bar{t}(\gamma) = 2 \int_{a_0}^0 t(\gamma, a) da \cong 2 \int_{a_0}^0 x^2/2 da$$

Differentiate $\bar{t}(\gamma)$ by γ

$$\frac{d\bar{t}(\gamma)}{d\gamma} = 2 \int_{a_0}^0 x \frac{\partial x}{\partial \gamma} da.$$

From the equilibrium expression defining x above it is known that

$$\frac{\partial x}{\partial \gamma} = -x \frac{\partial x}{\partial a}$$

Then,

$$\frac{d\bar{f}}{d\gamma} = -2 \int_{a=a_0}^{a=0} x^2 dx = \int_{x=x_0}^{x_1} x^2 ds = \frac{-2}{3} (x_1^3 - x_0^3)$$

$$\text{where } x_0 = x(\gamma, a_0) = \left[\frac{a_0}{2L} + \left(\frac{a_0^2}{4L} + \frac{\gamma^3}{27L} \right)^{\frac{1}{2}} \right]^{\frac{1}{3}}$$

$$+ \left[\frac{a_0}{2L} - \left(\frac{a_0^2}{4L} + \frac{\gamma^3}{27L} \right)^{\frac{1}{2}} \right]^{\frac{1}{3}}$$

(Notice that this is but one root of the cubic equilibrium condition. Other roots are complex.)

$$x_1 = \left\{ \begin{array}{ll} (-\gamma/L)^{\frac{1}{2}} & \text{for } \gamma < 0 \\ 0 & \text{for } \gamma > 0 \end{array} \right\} = \left(\frac{-\gamma + |\gamma|}{2L} \right)^{\frac{1}{2}}$$

The integral has a singular point at $\gamma = 0$. This singular point stems directly from the discontinuity in the magnetization curves of an isolated particle oriented such that $\varphi = 90^\circ$ when $H = H_A$. This singularity will give rise to a cusp in the functional dependence of the second derivative of \bar{f} with respect to γ .

$$\frac{d^2 \bar{f}}{d\gamma^2} = -2 x_1^2 \frac{\partial x_1}{\partial \gamma} + 2 x_0^2 \frac{\partial x_0}{\partial \gamma} =$$

$$\frac{1}{L} \left(\frac{-\gamma}{L} \right)^{\frac{1}{2}} + 2 x_0^2 \frac{\partial x_0}{\partial \gamma} \quad \text{for } \gamma < 0$$

$$= \left\{ \begin{array}{ll} 0 & + 2 x_0^2 \frac{\partial x_0}{\partial \gamma} \quad \text{for } \gamma > 0 \end{array} \right.$$

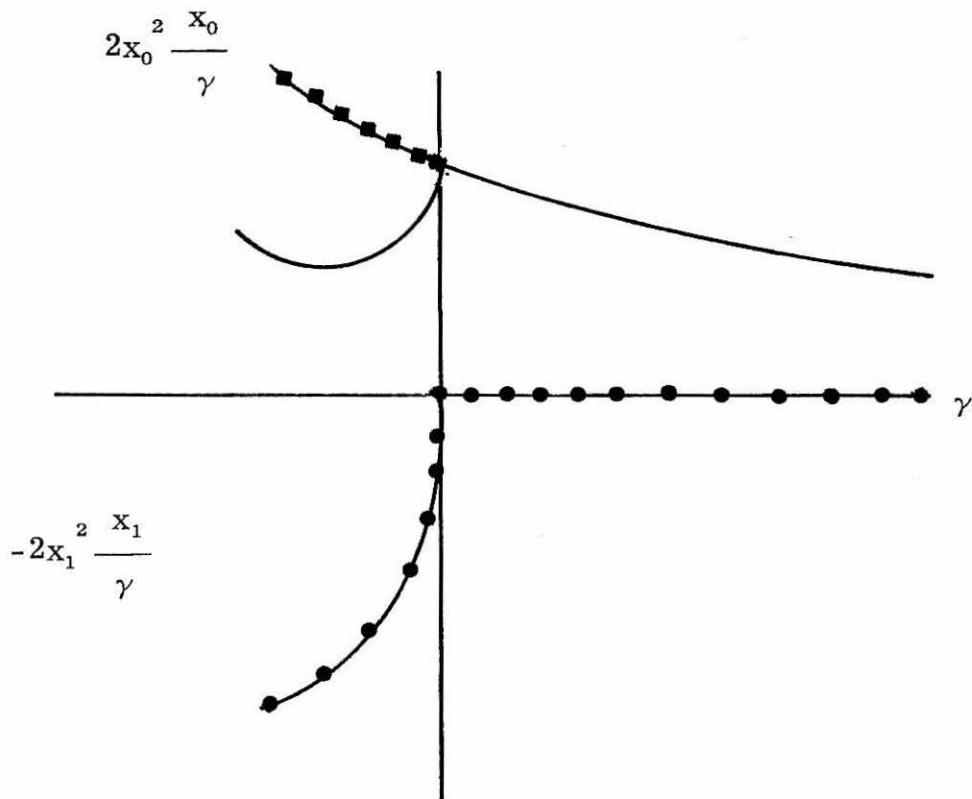


Figure 3. Function behavior of $-2x_1^2 \frac{x_1}{\gamma}$ ($\bullet\text{---}\bullet\text{---}\bullet\text{---}\bullet\text{---}\bullet$), $2x_0^2 \frac{x_0}{\gamma}$ ($\blacksquare\text{---}\blacksquare\text{---}\blacksquare\text{---}\blacksquare\text{---}\blacksquare$), and their sum (---). Note that for $\gamma > 0$, $2x_0^2 \frac{\partial x_0}{\partial \gamma}$ and the sum of the terms are coincident.

The functional dependences of the two terms in the expression for $\frac{d^2 \bar{t}}{\gamma^2}$ and their sum are shown in Figure 3.

When dimensional units are used, the cusp at $\gamma = 0$ becomes a cusp in the second derivative of the magnetization curve and is located at $H = H_A$. The procedure then for determining magnetic anisotropy constants is simply to search for the cusp in the second derivative of the magnetization curve. Only the reversible portion of the magnetization curve need be examined. The field at which the cusp occurs is the negative of the anisotropy field.

References

1. E. C. Stoner and E. P. Wohlfarth, Philos. Trans. Roy. Soc., A240, 74 (1948).
2. G. Asti and S. Rinaldi, Phys. Rev. Letters, 28, 1584 (1972).

PROPOSITIONS

PROPOSITION I
PRICING OF NEW PRODUCTS

Abstract: The economic effect of the introduction of a new product to the market is reviewed with emphasis on the choosing of a price for such a new commodity. The welfare economics of innovation and the distortions of the competitive system caused by the patent system are discussed. The simplified Lancaster model of consumer behavior with one-to-one correspondence between consumer activities is described. The Multi-Attribute Choice theory is related to the Lancaster formulation. A possible mechanism of introducing consumer uncertainty into the theory is suggested and a method of deriving clues to the appropriate price for a new product is derived. No general algorithm for pricing is presented, but the need to correctly formulate a price is shown. Considerable evidence is marshalled to suggest that prices for new products are set too high. It is proposed that an effort be made to formulate a method consistent with economic theory to fix a price for a new product.

In this proposition, the economics of innovation are discussed with an eye toward pricing inventions. The reader is asked to consider the position of an entrepreneur (or firm) who is about to introduce a wholly new product onto the market. This entrepreneur is faced with the problem of setting a price for his new product. He is protected by the patent system and is, therefore, a monopolist who wants to maximize his revenue from the sale of his invention. The patent system allows the owner of an invention to create an artificial scarcity of the product. The owner is then free to charge "what the market will bear" taking into account the price elasticity of demand and the marginal costs of promotion and production. Pricing considerations are primarily with the value of the invention to the consumer and not the costs to the seller. At the same time the seller must be aware of the

constraints placed on his price by emulation of his product and alternatives to it.

The question of what exactly is a "new" product has been discussed.^{1,2} New products can be divided into three classes:

(1) Products that are completely innovative such that no similar product exists on the market.

(2) Products which are emulative; that is, they are new to the producer but not new to the market.

(3) Products that are adaptive and represent modifications or refinements to existing products.

This proposition is concerned with the innovative product. Such a product does not serve a totally new function in the society. Rather, it fills a gap in the range of substitutes formerly available to the society.³ It will later be asserted that the prices of these substitutes will largely delineate the range of prices available for a new product.

In a technological society such as ours, the introduction of a new product is a frequent occurrence, and the problem of estimating its demand and consequently its price is often faced. Firms that do this are fairly closed-mouthed about their pricing procedures. They may have no formal procedure and rely, instead, on the experience intuition of their personnel in setting prices for innovations. As a whole, the process of forecasting demand and profitable prices has not been terribly successful, and there is a high rate of failure among new products. In a study of 63 new products produced by 28 firms,

Tull⁴ found the absolute mean error between forecasted sales and actual sales to be 65%.^{*} Forecasts of sales for new products were found to have a systematic upward bias. That is, if F_i is the forecasted sales per unit time of product 'i' and A_i the actual sales, then in the regression

$$F_i = a + b (A_i)$$

the parameter 'a' is greater than zero and 'b' > 1.0. Perhaps even more surprising is that the mean relative error in sales forecasting is the same for innovative products as it is for emulative or adaptive products where there ought to be clearer pricing and sales restrictions.

It is clear that in practice firms tend to underestimate the price elasticity of demand for innovative products. They tend to discount use by marginal users who have relatively good substitutes available. Consequently, they set prices too high and resist efforts to lower them. This was especially true in the case of penicillin, ball-point pens, and jet freight-transport.⁵

The adoption of a new product, particularly an emulative product, by consumers has been of immense interest to the advertising industry. Recently Bass⁶ has offered a model of this process based on epidemic growth which seems better able to predict future sales but which is not particularly useful for predicting prices.

Resistance to price change has long been recognized as a major source of difference between our real economy and an economy based on

^{*} Absolute mean error = ame = $(F_i - A_i)/A_i \times 100$.

free competition. Such resistance is most unwise in the case of new products. There may be greater demand for, and consequently greater revenue from, the new product at a lower price. The entrepreneur must consider not only price but also price elasticity. However, even more fundamentally, upon introduction of a new product one can anticipate that monopoly profits will draw out competitive products. The price of the commodity will be forced to evolve by market pressures.⁷ Clearly there is great need to predict the future demand of a product if this evolution is to proceed in an optimal fashion.

An often suggested, and seldom used technique for finding a price for a new product is to introduce the new product in one area of the country and see how it sells at various prices. This merely begs the question discussed in this proposition. One still has no good way to choose a trial price. If the trial price is badly chosen the innovator will lose much potential revenue. If the product is destined for national distribution, the optimal price found in an isolated area of the country may be distorted relative to the optimal price in the national market.

In the next section, the welfare economics of innovation is discussed. The central role played by a profitable innovation in this discussion must be considered in light of the high failure rate of new products on the market. The discussion is in terms of the quantities demanded, and prices are treated as given parameters, as is typical in such arguments. In real situations, the prices of new products are

not known. The whole discussion might be more useful for the purpose of forecasting demand if it were recast in terms of prices.

Welfare Economics of Innovation

An innovation is the product of knowledge. And knowledge is a most unusual commodity. Investment in knowledge is unlike investment in any other commodity. Once acquired, knowledge is never used up. Its optimum price is therefore zero. Consequently, there should be no incentive to acquire it. The patent system acts to create an artificial scarcity of knowledge so there can be reward for those who possess it, and a profit incentive to acquire it. The patent system then makes the economic system operate in a non-optimal way toward the products of knowledge. In the following, the welfare economics of invention and the non-optimality of the economy is reviewed following a treatment by Usher.⁸

Assume that the ideas for inventions spring spontaneously into the heads of inventors. The research necessary to produce inventions consists solely of acquiring the knowledge needed to implement these ideas. Further assume that research is of no other use than for the invention it is dedicated to. Let inventors be very small factors in the economy and the tastes of the society. Assume that initially the society is a one commodity world and that all prices, etc., are measured in units of that commodity, Q_1 .

Invention of a new commodity, Q_2 , will transform that society into a two-commodity world and a production possibility curve will appear (Figure 1).

Initially the society consumed q_1 units of Q_1 per unit time. After the appearance of Q_2 , it can consume at most q_1^2 units of Q_1 . The difference $(q_1^1 - q_1^2)$ represents the cost of the research to produce Q_2 . The concave nature of the production possibility curve guarantees that $q_1^1 - q_1^2 > 0$. The society can also trade off units of Q_1 for units of Q_2 . If the society locates itself at L on the production possibility curve it will consume the commodity bundle (q_1^3, q_2^3) . The difference $(q_1^2 - q_1^3)$ is the direct alternative cost of production of q_2^3 units of Q_2 .

The inventor is granted the right to be a monopolist and restrict the available quantity of Q_2 . He will choose to produce a quantity (or equivalently charge a price) of Q_2 which will maximize the difference between the marginal rate of transformation between Q_1 and Q_2 , which is the price he pays the factors of production, and the marginal rate of substitution in use of Q_1 and Q_2 , which is the price the consumer pays. This difference is the inventor's revenue.

Let C_1 in Figure 2 be the indifference curve for the society. It intersects the Q_1 axis at q_1^6 . The inventor chooses an output of q_2^4 of Q_2 . He pays for this output at the marginal rate of transformation between Q_1 and Q_2 indicated by line Lq_1^3 tangent to the production possibility curve at q_2^4 . His total cost is $(q_1^3 - q_1^4)$. The convexity of C_1 insures that $q_1^6 > q_1^3$. The inventor sells q_2^4 units of Q_2 at the highest price the society is willing to pay. This is the marginal rate of substitution in use of Q_1 and Q_2 indicated by the line q_1^3M tangent to

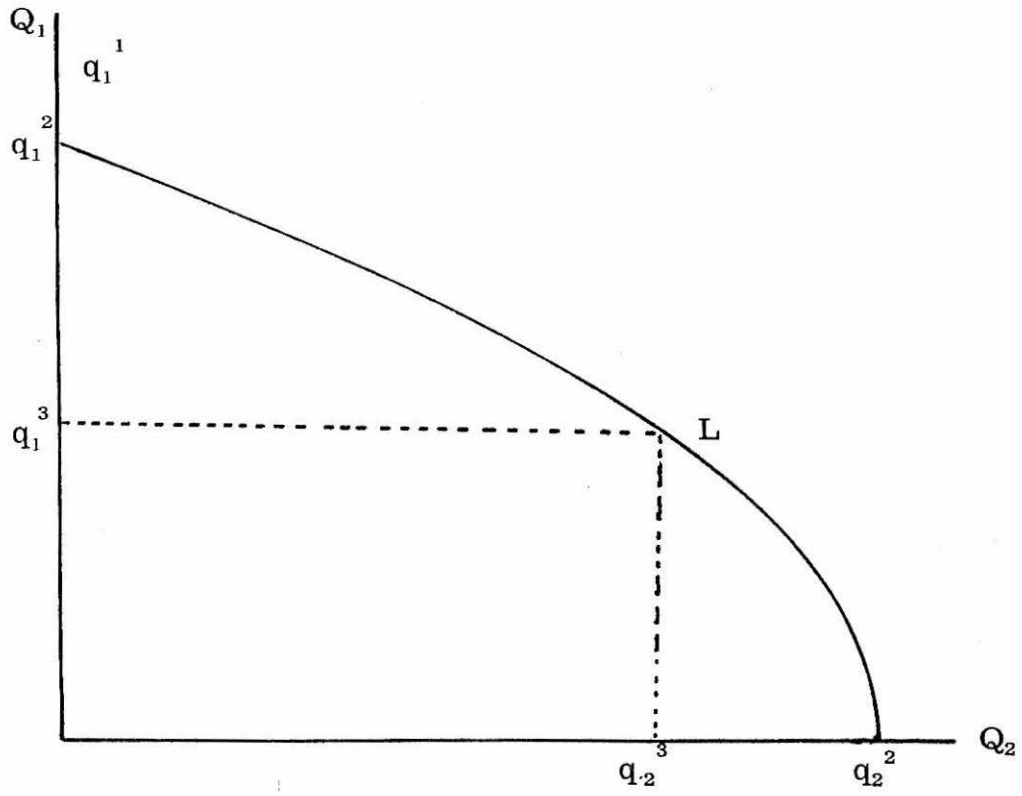


Figure 1

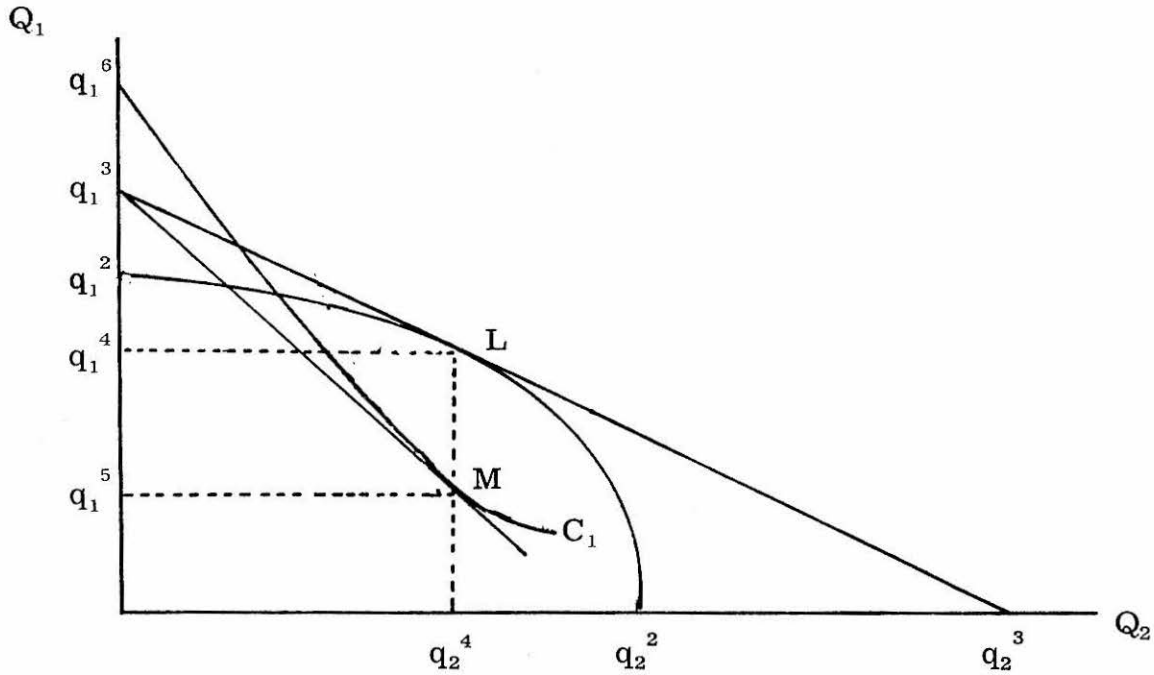


Figure 2

C_1 at M and the intersection of C_1 with line Lq_2^4 . The inventor will try to maximize the difference $L-M$. The criterion for rational invention--a profitable invention--is then

$$(L - M) \geq (q_1^1 - q_1^2)$$

That is, the inventor must realize more revenue from the invention than it costs to acquire the knowledge to implement the invention. It should be noted at this point that in the highly simplified economy used in this discussion that interest rates, etc., are ignored. There are no opportunity costs associated with diverting money to research save the loss of this money from the production of Q_1 .

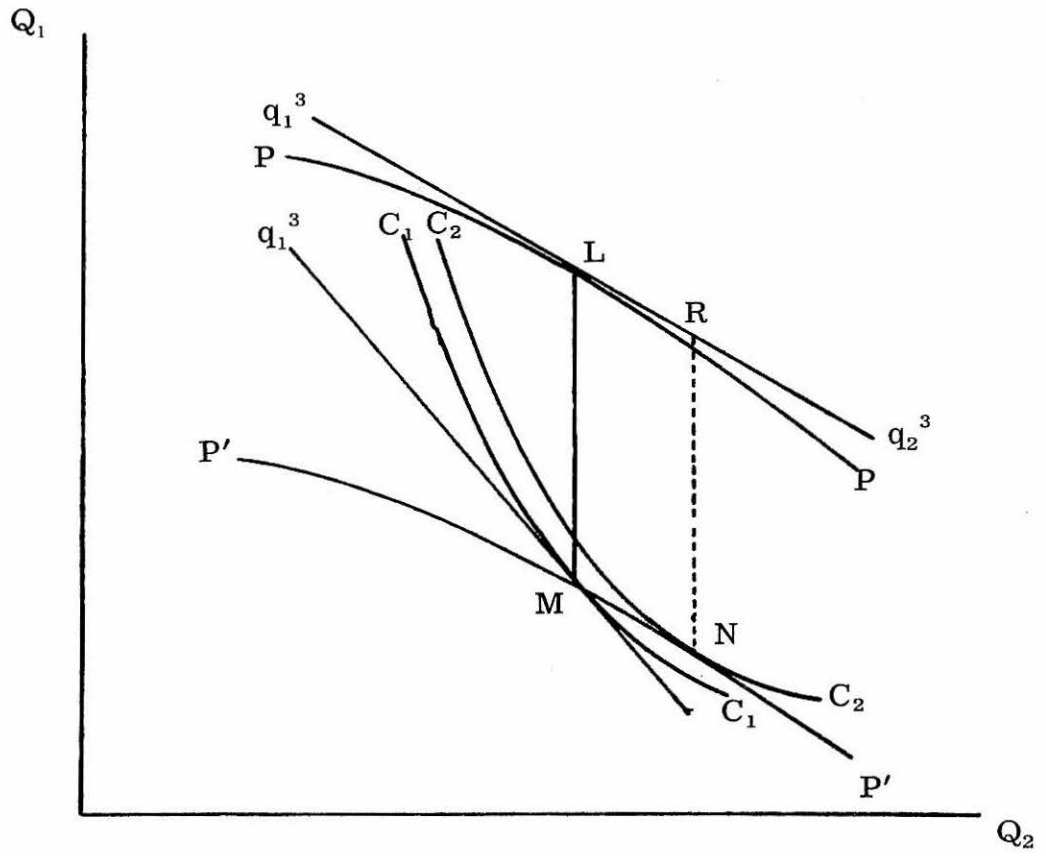


Figure 3

Several propositions concerning social welfare of invention can now be demonstrated.

- (1) Any profitable invention confers a net benefit on the whole community. Since C_1 cuts the Q_1 axis at q_1^6 , then the commodity bundle $(q_1^6, 0)$ is indifferent to the point (q_1^5, q_2^4) . The society is better off by $(q_1^6 - q_1^2)$ units after invention. The shapes of the production possibility curves and the indifference curve insure that for a profitable invention this quantity is always positive.
- (2) The patent system introduces monopolistic elements into the economy so that there is underproduction of the new product and the equilibrium position is NOT a Pareto optimum. As is shown in Figure 3, it is possible to make the society better off and the inventor no worse off. The curve P'P' is the production possibility curve less the revenue the inventor derives at an output q_2^4 . This curve necessarily has the same slope as the production possibility curve PP above it. At any point on this curve the inventor is as well off as he would be under the patent system. The indifference curve C_1 cuts this lower curve at M. There must be a higher indifference curve C_2 which is tangent to P'P' at R. This higher indifference curve cuts the Q_1 axis at q_1^7 . The difference $(q_1^7 - q_1^6)$ represents the social welfare loss under the patent system.

- (3) Some inventions may result in a net gain for the community, but be unprofitable for an inventor to undertake under the patent system. An invention is valuable to an inventor only if

$$(L - M) \geq (q_1^1 - q_1^2)$$

Let C_3 in Figure 4 be the community indifference curve which leaves the community just as well off after invention as before. The curve $q_1^2 q_2^2$ is the production possibility curve. The community will gain by undertaking an invention if $R - S \geq q_1^1 - q_1^3$. However, if

$$(R - S) \geq (q_1^1 - q_1^2) \geq (L - M)$$

they will have to pay the inventor to do the research to devise the new product since he will be unwilling to do it on his own.

- (4) The patent system causes under-investment in productivity.

There may be several ways to produce a given product which results in several alternative production possibility curves as shown in Figure 5. Greater productivity can be had at greater research cost. Curve 'e' represents a production possibility curve of greatest productivity and greatest research cost. Curve 'a' is cheaply reached but is lowest in productivity. Choice among the curves will depend on the society. If the marginal utility of Q_2

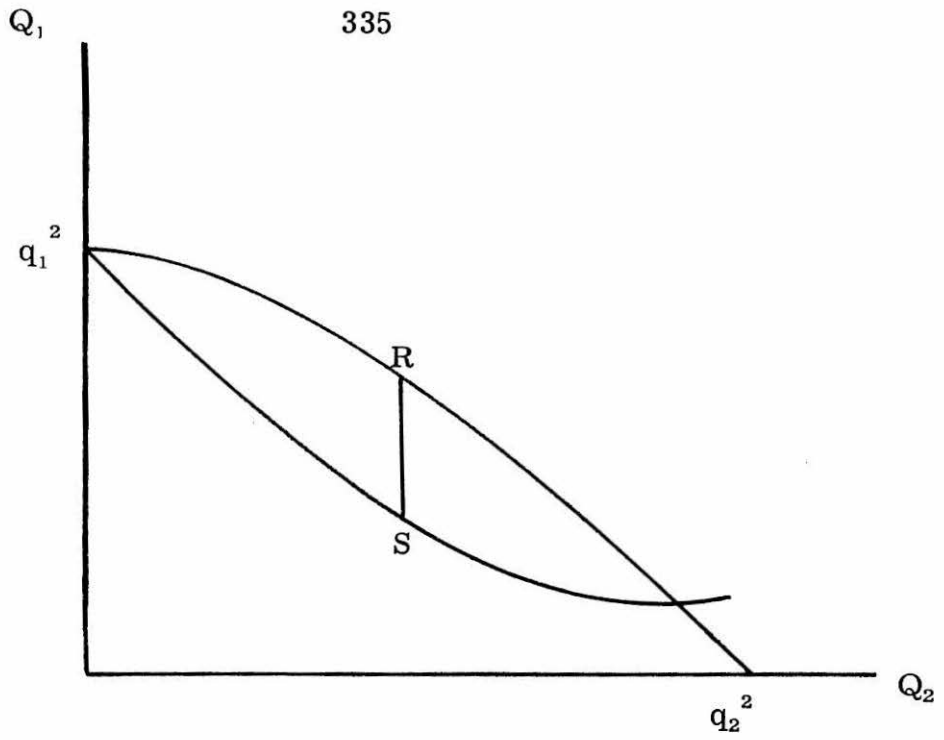


Figure 4

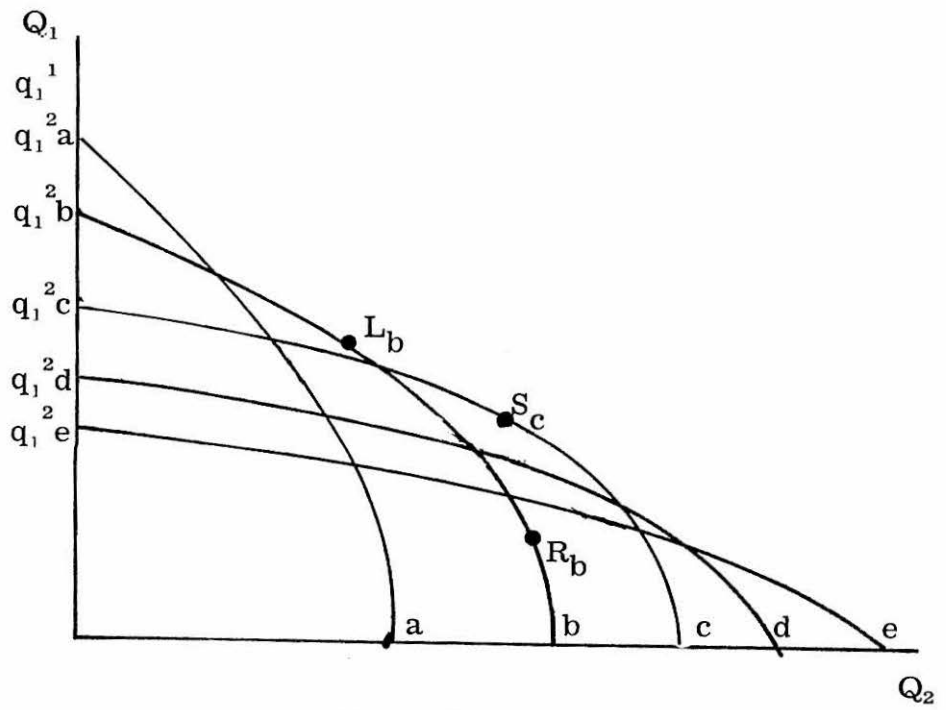


Figure 5

diminishes rapidly a curve of low productivity and low cost will be chosen. If large amounts of Q_2 are useable by the society, the greater productivity curves would be more desirable.

Once a curve is chosen, say b , society will locate itself at L_b . From proposition 2 it is known that L_b is inferior to some point R_b (also on b) with respect to the welfare of the society. But R_b is outside the envelope curve and is therefore inferior to some point S on a curve of greater productivity since this point will involve consumption of more Q_1 and Q_2 than R . Society would be better off by investing in a curve of greater productivity.

Usher does not analyze the effects of competition in research in detail, though he certainly realizes there are real, important effects. The tremendous gains yielded by monopoly profits by some inventions will draw many innovators into research. However, the patent system allows monopoly only for the first successful inventor. The competition will reduce the expected value of research seen by each inventor because it is possible that another inventor could acquire the knowledge to implement the invention first. The criterion for profitable invention

$$(L - M) \geq (q_1^1 - q_1^2)$$

is overly simplified, since a factor dealing with uncertainty is not included.

Usher's model assumes, as is typical of such arguments, perfect foresight on the part of all parties to the economy. His analysis can not then be used to treat the question of pricing or the demand for a new commodity. The empirical study by Tull suggests that risk and uncertainty in new product introduction is centrally important. This factor and the importance of competition in research may make the competitive solution under the patent system more nearly an optimum.

In spite of the simplifying assumptions required by the model, the results of proposition 2 fit well with with experimental data from the market. Proposition 2 indicates that the inventor chooses to overly restrict output and charge too high a price for his innovation. The upward bias of demand forecasts made by inventors mentioned above is not identical to this proposition but in an intuitive way it is in keeping with this result. The importance of proposition 2, cannot be underestimated. It will color any results concerning pricing that are later derived. Also, the importance of competition in research needs more careful investigation. This analysis suggests that efforts by the federal government to promote cooperation in research and efforts by the courts to further competition in the market place rather than in the research lab are miss-directed.

In the following pages three pathways by which the problem of pricing new products are discussed. All rely on the idea of product characteristics (vide infra).

Lancaster Formulation of Consumer Behavior

The classical theory of consumer behavior based on commodities and their prices is ill-equipped to handle a "new" commodity. The appearance of an innovation requires the expansion of the commodity space from n dimensions to $n + 1$ dimensions. Even a complete map of consumer preferences for n goods will generally give no information concerning the ranking of $n + 1$ goods. The effect of the introduction of a new product will be difficult to predict from this theory. For a new product there hasn't been time for consumer attitudes to evolve, and such an evolution has been postulated to be a necessary aspect of classical consumer theory.⁹

Simply examining the response to consumers to advertizing or education concerning a product is one way of evaluating market response to such a new product.^{10, 11} Such an approach has all the values of empirical studies. That is, it gives hard data concerning specific examples. But it lacks all the features of a theoretical model--one cannot assess the optimality of the solution found by the market.

Haines¹² has attempted to use Markov chains and game-like approaches to determine market response to new products. Haines himself admits that assessing the maximizing nature of optimality of his model is not readily done.

Lancaster¹³ has recast consumer behavior theory by postulating that a consumer derives utility not from a commodity, but rather, from the characteristics or attributes of that commodity. This model

is reviewed below to the extent that it applies to new products. The theory is remarkably advantageous for handling innovations. As was stated before, no invention fulfills a completely new function. An invention merely has characteristics in a different mix from its substitutes. If the consumer preference map is formulated in terms of characteristics, the introduction of a new product requires no changes in the dimension of this map. A new product which is profitable allows the consumer to acquire his old characteristics bundle more efficiently.

In the discussion below, the simplified Lancaster model is outlined. It is assumed that there is a one-to-one correspondence between individual consumption activities and available commodities. This assumption is fairly stringent. In general, the relationship between consumption activities ($X_1 \dots X_T$) and the commodities is fairly complex and is expressed by the matrix equation

$$X = By$$

However, for the purposes of this discussion the possibility of composite goods is disregarded, and B is assumed to be diagonal.

In the Lancaster model, there are n goods, ($y_1 \dots y_n$), each good possessing one or more of m characteristics ($z_1 \dots z_m$). The relationship between the goods and their characteristics can be quite complex. Two commodities in conjunction may have characteristics that neither good possesses alone. The relationship between the two sets is given by the matrix equation

$$Z = Ay$$

The elements of A are assumed to be constant and objectively defined. Plott¹⁴ has expressed concern that the elements of A may be indeterminant. However, for technical products which are devoid of consumer-oriented frills, the elements of A could be easily estimated.

It is assumed that there are no negative characteristics or goods

$$Z, y \geq 0$$

The model postulates that the consumer derives utility from the characteristics of goods rather than from the goods themselves. The consumer utility function is defined over characteristics space. The consumption problem then becomes:

$$\text{Maximize } U(z) \quad \text{subject to} \quad \sum_{i=1}^n p_i y_i \leq I \quad (\text{budget constraint})$$

$$z = Ay \quad (\text{model constraint}), \text{ and}$$

$$z, y \geq 0 \quad (\text{non-negativity constraint})$$

The observational features of the model are the quantities of goods demanded and their prices. The budget constraint is defined over the observed goods space. Transformation of this convex constraint into characteristics space leaves it convex because matrix A is constant and the relationship between goods and characteristics is linear.

In general, the number of goods does not equal the number of characteristics. There are three possible cases:

- (i) $m = n$ A is a square matrix. This is the easiest system to handle mathematically. If A is a permutation of a diagonal matrix, the Lancaster model is equivalent to the commodity-oriented consumer theory, and corresponds to a very primitive market.
- (ii) $m > n$ The number of characteristics exceeds the number of goods. This problem lacks the necessary observable data for solution of the problem of deriving information about characteristics.
- (iii) $m < n$ The number of goods exceeds the number of characteristics. This is probably a good description of a complex economic entity such as the United States. This is the problem concentrated on in this discussion.

When $m < n$, a consumer can reach every point in his characteristics space by several commodity vectors. The choice among these vectors is made based on the efficiency criterion of cost minimization. The efficiency problem is then:

$$\text{Minimize } \sum_{i=1}^n p_i y_i \quad \text{subject to } Ay = z^*$$

This is a linear program which will have a solution y^* for some z^* and I^* . Once a solution is obtained, a scalar multiple will fit the solution to any level of income I and characteristics vector $(I/I^*)z^*$. By varying z^* keeping the budget constraint $py = I$ fixed a convex characteristic frontier is mapped out. The frontier expands

isostructurally with income if prices are constant. The consumer's choice activity then takes two aspects. There is an objective efficiency choice followed by a private subjective choice among the characteristics bundles.

To demonstrate the treatment this model affords to new commodities, consider a two characteristic world with three "old" goods. Figure 6 shows the initial situation.

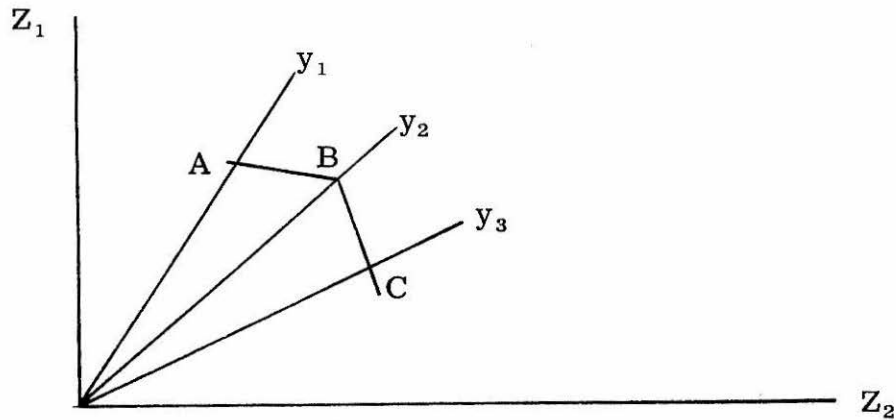


Figure 6

The curve ABC is the characteristic frontier. Some consumers will purchase combinations of y_1 and y_2 , and some combinations of y_2 and y_3 .

A new good, which is innovative, is a product with a different mix of characteristics than previously available goods. If the characteristics in a new good were present in the same proportion as an old good, it would fail to sell if its price were too high. It would completely replace the old good if its price were lower. When the characteristics are different, the effect of the good on the economy will again be determined by price. This is demonstrated in Figure 7.

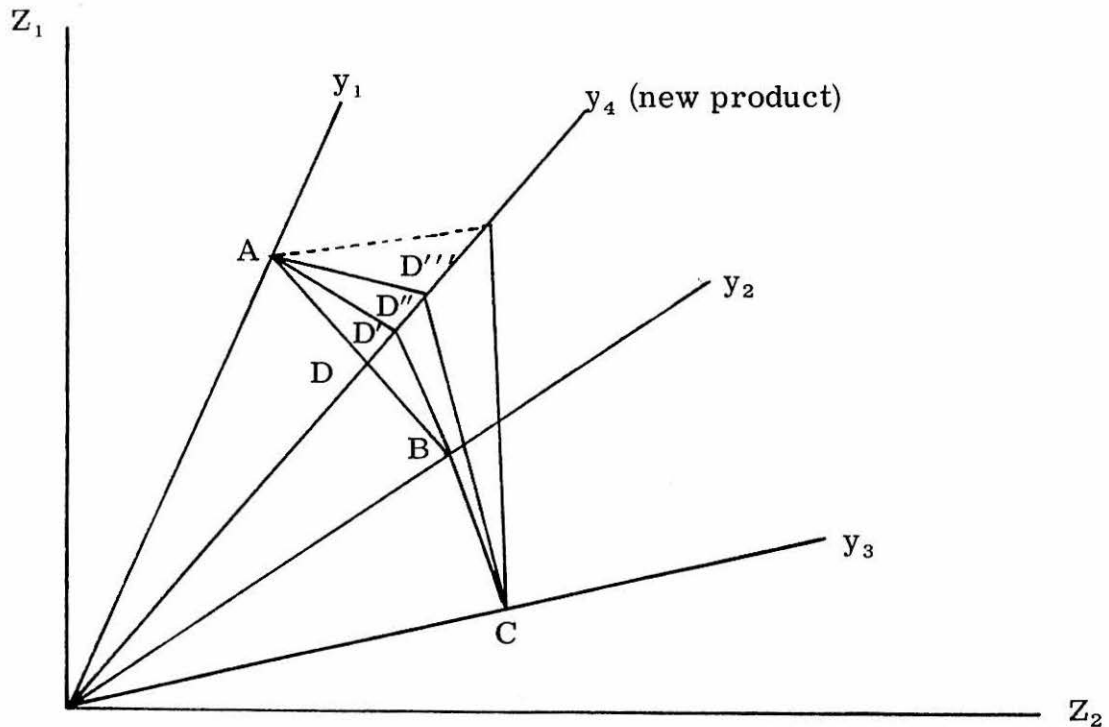


Figure 7

Figure 7

If the price of the new product (y_4) places it at D, consumers who purchase combinations of y_1 and y_2 will be indifferent to its introduction. Some may change their habits and purchase combinations of y_1 and y_4 , or y_2 and y_4 . If price is reduced to D', a new frontier will be available. Combinations of y_1 and y_4 or y_2 and y_4 will replace combinations of y_1 and y_2 . The new product will not dominate either y_1 or y_2 since these goods will still be purchased. At a still lower price D'', combinations of y_4 and y_3 will dominate y_2 and no more y_2 will be purchased. At D''' combinations of y_4 and y_3 will still dominate y_2 . The corner

solution y_4 will dominate all combinations of goods y_1 and y_4 since AD''' has positive slope. At D''' , y_4 will replace both y_1 and y_2 . At this point, this innovation will have completely replaced its close substitutes. The Lancaster model clearly shows how prices of competitive goods will affect the choice of a price for the innovative product. Choosing among the prices (D , D' , D'' , D''') will, of course, require a great deal of information. The model certainly indicates the hazard of setting the price to be greater than D .

The Lancaster model still requires a considerable amount of foresight on the part of the owner of an invention. Uncertainty and risk are still ignored. Uncertainty can be explicitly incorporated into the model by modifying an empirical model used by advertizers to correlate market data. The need for evolution of consumer attitudes toward a new product is not explicitly considered in the model. This evolution has been an area of some research.¹⁵⁻¹⁷

The Multi Attribute Choice Theory is a linear model which has been amazingly successful at predicting consumer choice among brands and their reactions to new brands. (A new brand may be thought of as an emulative innovation.) The theory has been much reviewed.¹⁵⁻¹⁷

In this model, an "attitude score" (A_{jk}) toward a brand by a consumer is formulated as

$$A_{jk} = \sum_{i=1}^n I_{ik} \cdot B_{ijk}$$

i = attribute or characteristic of products

j = brand

k = consumer

I_{ik} = the importance consumer K attaches to characteristic i

B_{ijk} = consumer K 's belief as to the extent to which
characteristic i is offered by brand j .

The model is based on product characteristics much as is the Lancaster formulation of consumer theory. It seems but a simple step to modify the model to apply to innovative new products. To make it conceptually fit consumer theory, it is necessary to redefine parts of the model.

Let utility be defined by

$$U_k = \sum_{i=1}^n I_{ik} \cdot \sum_{j=1}^n P_{ijk}$$

U_k = utility of consumer K

I_{ik} = importance that consumer K attaches to characteristic i

P_{ijk} = distribution of characteristic i delivered by commodity j .

P_{ijk} can be further refined by making an assumption concerning its form. Since negative quantities of a characteristic are not allowed in the Lancaster formulation, a likely form might be the log-normal distribution

$$P_{ijk} = \frac{1}{\log \sigma_{ij} \sqrt{2\pi}} \exp \left\{ -\frac{1}{2} \left(\frac{\log z_i - \log z_{ij}^0}{\log \sigma_{ij}} \right)^2 \right\}$$

Where σ_{ij} and z_{ij}^0 are parameters associated with the particular commodity. Because the probabilities are dependent on both characteristics and the commodities through the parameters, they will take into account consumer attitudes toward "new" products.

It is important to note that these probabilities are those seen by the consumer and are not objectively found. In dealing with consumer theory of the Lancaster form, it is imperative that objective evaluations of characteristics in commodities be confined in the matrix A and subjective evaluation be confined to the utility function.

Once models have been formed, the question arises about what to do with them. One would like to have prices that could be attached to the characteristics. The price of an innovative product could then easily be found as:

$$P_{\text{new}} = \sum_{i=1}^n P_i Z_{i, \text{new}}$$

$$P_i = f(p_1, \dots, p_m, I)$$

where P_i = characteristic price per unit characteristic

p_j = commodity price

$Z_{i, \text{new}}$ = units of characteristic i per unit of new commodity

This formula will hold identically. Should it ever not hold, one would simply "invent" a new characteristic to attribute to the commodity.

Unfortunately, resolution of characteristic prices is not a particularly easy problem. An alternate procedure is to examine the change in demand of existing products with changes in the amount of

the characteristics in the commodity

$$dy_j = \sum_{i=1}^n \left(\frac{\partial y_j}{\partial a_{ij}} \right) da_{ij}$$

Otani and Plott have taken this course.¹⁸

Let $y_j = y_j(P_1, \dots, P_n, I, \{a_{ij}\}_{m_j})$ be the consumer demand function for product j . The set (a_{ij}, \dots, a_{mj}) are parameters which describe the amounts of the characteristics in j . Initially these parameters are held constant. The utility function is then derived so that the functional form of the demand function in terms of these parameters can be found. This is done by solving the problem

$$\begin{aligned} & \text{maximize} && U(z_1, \dots, z_n) \\ & \text{subject to} && \sum_{j=1}^n P_j Y_j = I && \text{budget constraint} \\ & && Z = AY && \text{Lancaster model constraint} \end{aligned}$$

In this treatment A is assumed to be square which differs from the assumption in the discussion of the Lancaster model above. When the number of commodities exceeds the number of characteristics, the analysis is done with a square submatrix of A . The authors do not try to treat the case of the number of characteristics exceeding the number of commodities.

Using the Lagrangian treatment, the first order conditions for a maximum are:

$$(1) \frac{\partial L}{\partial z_i} = U_i + \rho_i = 0 \quad i = 1(1)n$$

$$(2) \frac{\partial L}{\partial y_i} = 2P_j + \sum_{i=1}^n \rho_i a_{ij} = 0 \quad \kappa = 1(1)n$$

$$L = U(z) + \lambda \left(\sum_j p_j y_j - I \right) + \sum_{i=1}^n \rho_i \left(\sum_{j=1}^n a_{ij} y_j - Z_i \right)$$

where λ and $\{\rho_1, \dots, \rho_n\}$ are Lagrangian multipliers.

From (1) one derives

$$\frac{U_i}{U_n} = \frac{\rho_i}{\rho_n} \quad i = 1(1)n-1$$

From (2)

$$-\lambda \begin{bmatrix} \rho_1 \\ \cdot \\ \cdot \\ \cdot \\ \rho_n \end{bmatrix} = \begin{bmatrix} a_{11} & \dots & a_{1n} \\ \cdot \\ \cdot \\ \cdot \\ a_{n1} & \dots & a_{nn} \end{bmatrix} \begin{bmatrix} \rho_1 \\ \cdot \\ \cdot \\ \cdot \\ \rho_n \end{bmatrix}$$

$$\Rightarrow \begin{bmatrix} \rho_1 \\ \cdot \\ \cdot \\ \cdot \\ \rho_n \end{bmatrix} = \frac{-\lambda}{|A|} \begin{bmatrix} C_{11} & & C_{1n} \\ \cdot & & \cdot \\ \cdot & & \cdot \\ \cdot & \dots & \cdot \\ C_{n1} & \dots & C_{nn} \end{bmatrix} \begin{bmatrix} \rho_1 \\ \cdot \\ \cdot \\ \cdot \\ \rho_n \end{bmatrix}$$

where C_{ij} is the cofactor of a_{ji} in A and $|A|$ is the determinant of A .

$$\text{Then } \frac{P_i}{P_n} = \frac{\sum_{j=1}^n C_{ij} P_j}{\sum_{j=1}^n C_{nj} P_j} = F^i \left(\frac{P_1}{P_n} \dots \frac{P_{n-1}}{P_n} \right) \quad i = 1(1)n$$

The demand functions are by hypothesis homogeneous of degree zero in prices

$$y_i = y_j \left(\frac{P_1}{P_n}, \dots, \frac{P_{n-1}}{P_n}, 1, \frac{I}{P_n} \right) \quad j = 1(1)n$$

These functions can be inverted to give

$$\frac{P_i}{P_n} = g^i (y_1 \dots y_n) \quad i = 1(1)n-1$$

Since

$$y = A^{-1} x$$

$$\begin{aligned} \frac{P_i}{P_n} &= g^i \left(\frac{1}{|A|} \sum_{j=1}^n C_{nj} Z_j \dots \frac{1}{|A|} \sum_{j=1}^n C_{nj} Z_j \right) = \\ &= G^i (Z_1, \dots, Z_n) \end{aligned}$$

Then

$$\begin{aligned} \frac{U_i}{U_n} &= F^i (G^1 (Z_1, \dots, Z_n) \dots G^{n-1} (Z_1, \dots, Z_n)) \\ & \quad i = 1(1)n-1 \end{aligned}$$

If this function satisfies the integrability condition

$$\frac{\partial F^j}{\partial Z_k} - F^k \frac{\partial F^j}{\partial Z_m} = \frac{\partial F^k}{\partial Z_j} - F^j \frac{\partial F^k}{\partial Z_m} \quad m > k \neq j < m$$

the utility function which yields the observed prices and demands can be derived. The first order conditions for a maximum and the constraints can be directly differentiated to yield

$$\frac{\partial Y_k}{\partial A_{ij}} .$$

This result would be most useful in cases where the new product had fairly close substitutes. It yields clues to consumer demand which would not be available from commodity-oriented consumer theory. Specific account of consumer attitude to new products could be taken by constraining the utility function to be of the Multi Attribute Choice form. Perhaps more useful results could be obtained by considering the seller's objective of maximizing revenue. The result one would really like to see is still prices for characteristics of existing products which could then be used to set the price of the new commodity. If the maximizing revenue approach is used, the result will not represent a social optimum as was pointed out before. Such an approach will still ignore consumer uncertainty which is obviously an essential aspect in assessing demand for a new product.

Acknowledgment

I wish to thank Dr. Charles Plott and Dr. James Quirk for fascinating discussions concerning Multi Attribute Choice Theory, the Lancaster Model, and their interest in the pricing problem.

References

1. Chester Wasson, "What is 'New' About a New Product?" Journal of Marketing, 25, 52 (1960).
2. E. B. Weiss, "What is a New Product?", Advertising Age, 29, 112 (1958).
3. Joel Dean, "Pricing Pioneering Products," Journal of Industrial Economics, 17, 165 (1968).
4. D. S. Tull, "The Relationship of Actual and Predicted Sales and Profits in New-Product Introduction," Journal of Business, 40, 233 (1967).
5. Burton Klein, private communication.
6. John V. Nevers, "Market Response to Innovation," Paper No. 283, Herman C. Krannert Graduate School of Industrial Administration, Purdue University, Lafayette, Indiana, July, 1970.
7. Ole C. Nord, "Growth of a New Product," MIT Press, Cambridge (1963).
8. D. Usher, "Welfare Economics of Innovation," Economica, 123, 279 (1964).
9. A. Alchian, "Uncertainty, Evolution, and Economic Theory," Journal of Political Economy, June 1950.
10. F. J. Francombe, "Estimating a Mixed Exponential Response Law," Journal of the American Statistical Society, September 1961.
11. B. Benjamin, W. P. Jolly, and J. Maitland, "Operations Research and Advertising: Theories of Response," Operations Research Quarterly, 11, 186 (1960).

12. G. H. Haines, Jr., "A Theory of Market Behavior After Innovation," Management Science, 10, 634 (1964).
13. K. L. Lancaster, "A New Approach to Consumer Theory," Journal of Political Economy, 74 (1966).
14. Charles Plott, private communication.
15. E. A. Pessamier and W. L. Wilkie, "Multi-Attribute Choice Theory," Paper No. 372, Herman C. Krannert Graduate School of Industrial Administration, Purdue University, Lafayette, Indiana, September 1972.
16. E. A. Pessamier and W. L. Wilkie, "Issues in Marketing's Use of Multi-Attribute Attitude Models," Paper No. 365, Herman C. Krannert Graduate School of Industrial Administration, Purdue University, Lafayette, Indiana, August 1972.
17. J. L. Ginter and F. M. Bass, "An Experimental Study of Attitude Change, Advertising, and Useage in New Product Introduction," Paper No. 358 Herman C. Krannert Graduate School of Industrial Administration, Purdue University, Lafayette, Indiana, July 1972; and references therein.
18. Y. Otani and C. R. Plott, "Demand Response to Product Characteristic Changes," unpublished results privately communicated.

PROPOSITION II

THE STRUCTURE OF ZEOLITE PAULINGITE

Abstract: It is proposed that a detailed structure refinement of Paulingite and its modifications be done to resolve the locations of all cations and protonated species. Further experiments are proposed to elucidate other features of this zeolite structure.

Zeolites are, without a doubt, the most outstanding discovery in catalytic chemistry of the last half century. Consideration of their catalytic activity relative to previously used systems, tonnage of catalyst used, and economic impact shows that zeolites are without peer as catalysts.¹ Catalytic activity represents only one area in which the potential utility of zeolites has been developed. Application of zeolites to processes of purification, separation and effluent scrubbing is still in its infancy.² As might be expected in light of their tremendous commercial value, zeolites have been the focal point of a major scientific effort which has proceeded along these four basic lines:

- (a) structure of zeolites
- (b) synthesis of zeolites
- (c) catalytic activity of zeolites
- (d) absorption and ion exchange capacity of zeolites.

In each of these research categories there has been a continuing need for more detailed structural information.³ Progress in the structure determination of zeolites has been retarded by the polycrystalline and amorphous nature of most natural zeolites. The use of bulk techniques and X-ray powder diffraction methods for the study of zeolites have often been criticized.^{2, 3, 99} These techniques are often subject to erroneous interpretation.^{3, 98, 99} The advent of synthetic processes which allow the preparation of zeolite crystals of up to 100 microns in size has somewhat relieved this situation.² Many single-crystal X-ray structure determinations have appeared in recent years. There are now some 43 zeolite frameworks whose structures are known to vary degrees of refinement and confidence.⁹⁹ However, the small size of the target crystals used in these studies has prevented refinement of the data to a sufficient level of detail to facilitate correlations between bulk properties and zeolite structure. Further, insufficient attention has been paid during the course of these structure determinations to the pretreatment and environment of the zeolite. Many of the studies have been made on poorly described and characterized zeolites.³ The lack of detailed structural information has been a great handicap to the interpretation of spectroscopic and physical chemical data.

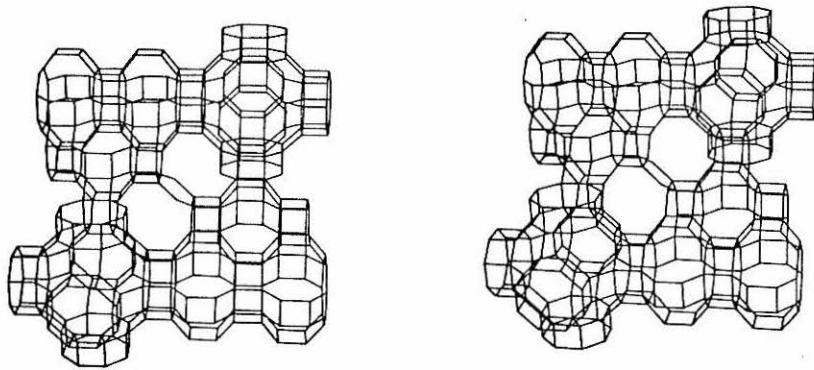
There are now available single crystals many tenths of millimeters in size of the natural zeolite, Paulingite.^{4, 105} Discovery of these crystals makes it possible to propose an X-ray structure

determination of Paulingite of detail comparable to that commonly available for simple inorganic and organic compounds. To take proper advantage of these large crystals, considerably more than a single structure determination is proposed.

This proposal is divided into three parts. In the first, the proposed X-ray experiments are described, and the techniques which will be necessary for refining the X-ray data are discussed. The second part reviews the structural features of zeolites that deserve the greatest attention. A structure determination of this complexity and significance cannot be done in isolation as demonstration of the crystallographer's skill. This section is offered as an outline of how the results of the proposed X-ray experiments might relate to the vast body of experimental data dealing with zeolites. The body of literature pertinent to this discussion is indeed large. Over 1100 patents and publications dealing with zeolites appeared in 1972 alone.¹⁰⁰ It was, of course, not possible to review the entirety of zeolite literature. Some attempt was made to be thorough for the years 1966-1972. The third section of the proposal describes some non-crystallographic experiments which, when related to the structural information provided by the experiments of the first section, would further probe the structure of the zeolite.

Paulingite crystallizes in a cubic structure ($a = 35.1 \text{ \AA}$) of probable space group $\text{Im}\bar{3}\text{m}$ (O_n^9)⁴ which is the largest known unit cell of any inorganic compound. The empirical formula is $\text{K}_{68} \text{Ca}_{36}$

Figure 1. Stereoscopic projection of Paulingite framework viewed along $[100]$ from reference 112.



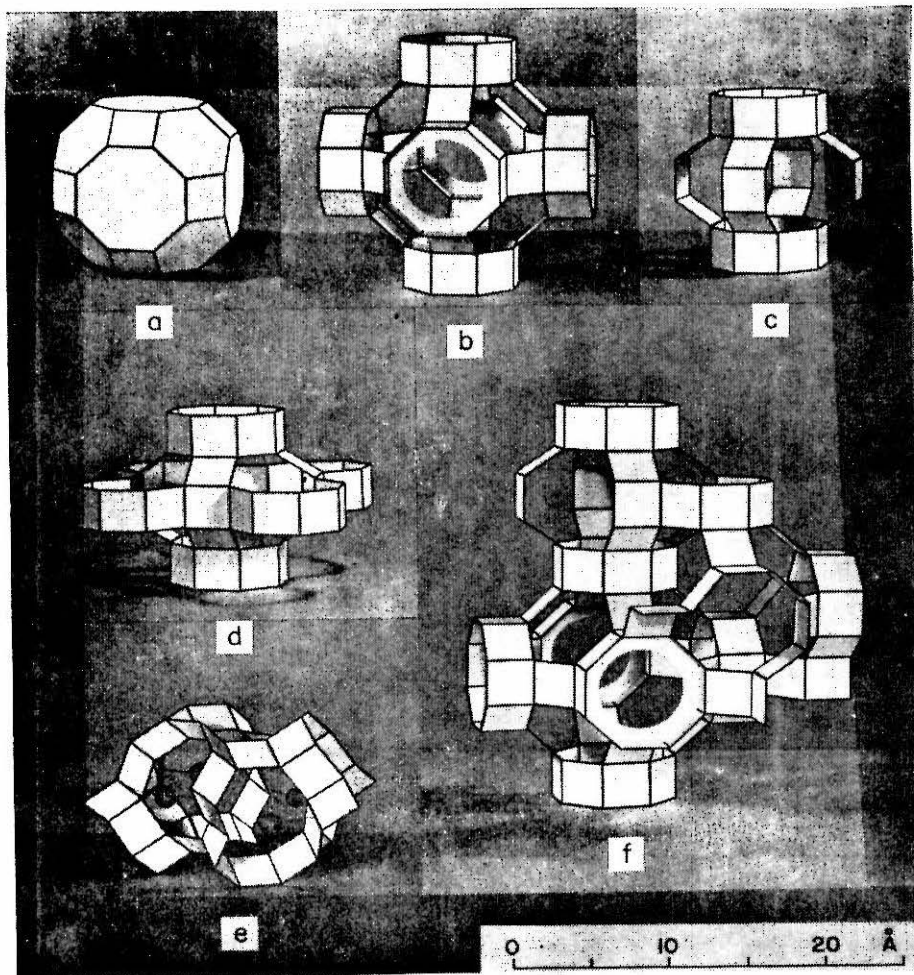


Figure 2. Representations of the structural units of the Paulingite framework. (a) An idealized truncated cubo-octahedron; (b) α cage; (c) γ or B cage; (d) γ cage with appendeges which when connected to δ or C cage and toroidal channel of (e) and (a) form a representation of the Paulingite framework (f). Notice that certain of the appendeges have been removed in (f) to clarify the relationship between the cages.

$\text{Na}_{13}\text{Ba}_{1.5}(\text{SiO}_2)_{520}(\text{AlO}_2)_{152} \cdot 705 \text{H}_2\text{O}$. An initial structure determination located all but 30 cations and 250 water molecules, and established the framework structure of the zeolite.¹² Figure 1 shows a stereoscopic projection of this framework. Figure 2 displays the important secondary building units of the Paulingite framework. The framework is formed by three supercages-- α (26-hedron or truncated cubo-octahedron), γ (18-hedron) and δ (10-hedron). There are three channels of minimum free aperture 3.9\AA in the hydrated form. The void fraction (0.48) is quite large and is typical of many catalytically active zeolites.¹²

Paulingite belongs to a general structural class of zeolites which includes some of the most common as well as quite rare zeolites:

- (1) Analchime
- (2) Phillipsite
- (3) Ugawaralite
- (4) Gismondine
- (5) Hamotome
- (6) Kehoeite
- (7) Laumontite
- (8) Viseite
- (9) Synthetic Gismondine
- (10) Wairakite
- (11) ZK-19

Further, the secondary building units in Paulingite are found in many commercially important zeolites. The α cage is found in zeolites ZK-5 and Linde A. Similar, though not identical cages, are found in the faugasites. The 18-hedron also occurs in ZK-5 and zeolite Ω .² These similarities of structure in Paulingite and other zeolites add tremendously to the significance of the study proposed below.

(I) X-Ray Experiments

The following structural determinations of Paulingite and its modifications are proposed:

(A) The structure of Paulingite should be refined to a level that would locate all cations and protonated species. The coordination spheres of the cations within the zeolite framework are of particular interest.

Modern techniques of X-ray crystallography make it possible to obtain a structure of this refinement on a suitable crystal. The determination will be done with $\text{MoK}\alpha$ radiation monochromatized with graphite filters.¹⁰¹ Forty-thousand independent reflections will be required to sufficiently "overdetermine" the structure. Approximately 100 days of diffractometer time would be required to collect this amount of data. Absorption effects are relieved when spherical crystals are used.

From an X-ray structural viewpoint zeolite crystals are quite pathological. Refinement of the data will be impeded by:

- (1) Pseudosymmetry
- (2) Twinning

(3) Positional disorder

(4) Thermal motion of some atoms

Major advances in crystallography allow each of these impediments to be resolved. The treatment of pseudosymmetry has been discussed by several authors.^{5,6} Meier and coworkers¹⁰³ have developed effective techniques for surmounting twinning in zeolite crystals. Positional disorder and thermal motion of atoms in zeolites and procedures for treating these difficulties have been described.⁷⁻¹⁰ Thermal motion and disorder of the liquid-like zeolitic water (*vide infra*) has been successfully treated in the case of synthetic faujasites.¹¹⁻¹³ Statistical tests for the evaluation of model structures of zeolites and the applicability of refinement techniques are well known.¹⁰²

Acquisition of the X-ray data from crystals cooled to liquid nitrogen or even liquid helium temperatures may tremendously aid in the refinement of the structure. Some caution is incumbent on the use of this technique. Bulk studies of the conductivity of zeolites have intimated that interactions between the cations and the zeolite framework vary abruptly at low temperature.⁵⁹ Certainly, in view of the extensive hydrogen bonding that must occur within a zeolite, one would anticipate second order phase transitions when zeolites are cooled.

Once this first structural determination is completed, subsequent determinations of modified Paulingite can be done by difference techniques.

(B) Surface and zeolite water will be removed from the zeolite by thermal means or by prolonged evacuation. The structure will then be redetermined. Thermal pretreatment is especially attractive, since most catalytic applications of zeolites involve high temperatures, and zeolites are often activated thermally. The thermal stability of zeolites increases with the silicon-aluminum ratio. In Paulingite this ratio is quite high ($S_i/Al = 3.4$) which suggests that the zeolite framework would easily withstand the thermal pretreatment.

Structural determinations of Paulingite or its modifications maintained elevated temperatures would be of immense interest. Unfortunately thermal motions would, in all probability, preclude intensive data refinement.

(C) As will be demonstrated below, cation valence, concentration, and location are of central importance in the structure of zeolites. The structural role of divalent cations have proven to be particularly enigmatic. It is further proposed that Paulingite be treated with divalent cations--in particular Ca^{2+} --and the structure determinations of (A) and (B) be repeated. The relatively mild conditions necessary for the ion exchange of zeolites and the large pore size of Paulingite suggest that an exchanged product can be easily obtained. Ion microprobe analysis will be used to determine the extent of exchange. Alternatively, Weissenburg photos can be used to monitor the zeolite. When reflection intensities cease to change, it can be assumed an equilibrium product is in hand.

(D) Differences in cation location with changing valence are also important factors in the application of zeolites. Trivalent cation exchanged zeolites are currently the most popular catalyst in petroleum cracking. Paulingite crystal can be exchanged with La(III) ion and the structural determinations of (A) and (B) repeated. It may be necessary to use virgin crystals for this exchange treatment--considerably complicating data collection.

(E) The use of metal loaded zeolites as catalysts is becoming increasingly common. The need for detailed structural information concerning these metal loaded zeolites is similarly becoming increasingly clear. It is proposed that a crystal of Paulingite be exchanged with a reducible metal ion. From an applications point of view, the ions Ni(II), Cu(II), Co(II), Pt(II), or Pd(II) are of greatest interest. From a chemical and crystallographic standpoint, the Pt(II) ion is easiest to handle. The exact choice of ion will be dictated by the experiments discussed in the third part of this proposition. Pt(II) exchange will be assumed in this proposition. Once exchange has occurred, structural determinations of (A) and (B) will be repeated.

Exchange of Pt(II) into a zeolite is a fairly tricky operation shrouded in priority considerations. Commercial platinum compounds are often quite acidic and accelerate the hydrolysis of the zeolite. Greatest success has been had by use of freshly prepared tetra-ammine platinate(II) ion.^{106,111,112} Ammonia coordinated ions are, alas, not particularly satisfactory. Ammonia and nitrogen

containing bases are known to poison the catalytic sites of some zeolites³⁹ and may introduce structural changes entirely independent of the metal ion.

It is unfortunate that the rate of ion exchange cannot be predicted in advance. Following an exchange reaction crystallographically would yield considerable data concerning ion site preferences and the alteration of those preferences with concentrations. Such studies may best be done spectroscopically (vide infra).

Once the structure of the ion-loaded zeolite is known, the ion will be reduced to the metal. In the case of Pt(II) and Pd(II), only mild conditions are necessary.¹⁰⁶ For these ions, metal atom migration and agglomeration ought to be minimal. The harsher conditions necessary to reduce transition metal ions will be necessarily lead to complications.

(II) Structural Impact of Cations and Protonated Species on the Behavior of Zeolites

The following discussion serves to further justify this detailed investigation of a zeolite, to illustrate the structural problems that a structural refinement may bear on, and to present data which must be considered in the analysis of the results of the proposed experiments.

The focal point of interest in zeolites has been their catalytic activity. The non-empirical research in zeolite catalysis has been devoted to:

- (1) identification and optimization of the source of catalytic activity,
- (2) description and optimization of the absorption capacity of zeolites,
- (3) improvement of the thermal stability of zeolites.

The vast body of physical and spectroscopic studies on bulk zeolites, as well as the available structural information, indicates that the cations and the protonated species within the zeolite framework are of central importance in each of these categories.^{2,3,108,110}

The protonated species with a zeolite are present as water and hydroxide. Water is present as a variety of structural entities:

(a) absorbed water. This type of water is of little importance and is usually completely removed at temperatures above 60°C.¹¹¹

(b) zeolitic water. Water is readily absorbed into the channels and pores of the zeolite framework. It can be removed without structural damage to the framework. Thermal loss of zeolitic water usually occurs quite sharply between 100 and 120°C.^{111,113} Nmr results indicate that the density of zeolitic water is about that of ordinary water, but that its viscosity is some 20 to 30 times greater.⁵⁸ These thermal and spectroscopic results indicate that bonding interactions involving zeolitic water are present though not strong. Recent evidence has shown that zeolitic water is sufficiently ordered to be susceptible to X-ray structural determination.¹¹⁻¹³

(c) constitutional water bound to framework. Constitutional water is bound very tightly to the silica-alumina zeolite framework and can be removed only by extensive thermal treatment. This water is well-ordered.⁷⁴

(d) constitutional water coordinating cations. The coordination sphere of cations within the zeolite framework without a doubt must include water. This aspect of the structure of zeolites has been significantly neglected in the past. Yet, as described below, cation-water interactions may have profound influence on catalytic activity of zeolites.

A wide variety of studies have intimated that the catalytic activity of zeolites is distinctly dependent on tightly bound water present, presumably, at the active site.²⁹⁻³³ The effect of water in zeolite catalysis of reactions involving carbonium ions such as cracking,⁴⁵ alkylation,⁴⁶ isomerization,⁴⁷ and disproportionation⁴⁸ has been emphasized in the literature. However, in some reaction water has been found to both inhibit catalytic activity.¹³⁶ Water is known to promote the activity of decationized zeolites and zeolites containing monovalent cations.^{110,115}

Water dramatically affects the thermal stability of zeolites.¹⁹⁻²⁸ Removal of all constitutional water often initiates collapse of the zeolite framework.^{111,114} The preparation of "ultrastable faujasites" requires treatment of the zeolite with water at 700-800°C.¹⁵⁻¹⁷ On the other hand, zeolite Y was found to be stable to temperatures above 500°C, yet no water could be detected in the zeolite above 150°C.¹⁴⁻¹⁶

Several natural zeolites are structurally stable well beyond the temperature of complete dehydration.¹²⁹ The structural role of water is clearly complex. Bulk studies have only illustrated paradoxes. Only detailed structural analysis can hope to resolve the discrepancies in the reported behavior of zeolites.

As in the case of water, many structural types of hydroxide have been identified in zeolites, principally by infrared spectroscopy. Some hydroxide types are peculiar to a specific zeolite. Those common to nearly all zeolites are:

- (a) terminal or silica residue hydroxides which absorb at 3745 cm^{-1} in the infrared,^{5, 84, 96}
- (b) bridging hydroxides which absorb at $3642\text{-}3630\text{ cm}^{-1}$,⁶⁵
- (c) framework hydroxides absorbing at 3540 cm^{-1} ,^{32, 51, 52, 65}
- (d) and hydroxides coordinated to cations which absorb at variable frequencies between $3500\text{ and }3600\text{ cm}^{-1}$.⁶⁵

The hydroxide groups, known in the jargon of zeolite chemistry as Brönsted acid sites, were the first identified sources of catalytic activity.^{34, 168} The great number of these sites was assumed to be the source of the enhanced catalytic activity of zeolites relative to conventional silica-alumina catalysts.³ Certainly when Brönsted acid sites are absent there is no catalytic activity.⁵⁷ The considerable body of literature surrounding the carboniogenic activity of the hydroxides seems to be associated primarily with those hydroxide groups absorbing at $3630\text{-}3652\text{ cm}^{-1}$ in the infrared.^{3, 45, 116-118}

Terminal hydroxides and hydroxides coordinated to cations appear to be catalytically passive.^{14, 109, 131}

Lewis acid sites have also been identified as active sites.^{51, 52} The proportion of Lewis and Brönsted sites critically affects catalytic activity. Maximum activity occurs when there are approximately equal numbers of these sites.^{18, 19} This proportion is directly affected by the thermal pretreatment of the zeolite,⁴¹⁻⁴⁵ as well as the number and type of cations present.^{36, 66}

It must be pointed out that the acid sites may be symptomatic of the enhanced activity of zeolites relative to silica-alumina, and not its source. Enhanced activity may be due to (a) enhanced electrostatic fields present at the active site, (b) greater absorption capacity of zeolites, (c) longer retention time of reactants at the active site, (d) superior geometry of the active site as well as the higher acidity of the zeolite. Structural analysis of the proposed resolution will definitely aid in determining which of these effects is predominant.

The number, type, and proportion of acid sites and consequently catalytic activity are affected by the cations present within the zeolite framework. Some attempts to explain the variation in acidity have focused on ionizations of the type:



But, since the hydroxide groups coordinated to cations are generally viewed as inert, such arguments seem incomplete. Nevertheless, it is obvious that the structural role of protonated species cannot be isolated from the cations.


Cations within the zeolite framework may be expected to:

- (a) alter the geometry of the active site of the zeolite,
- (b) alter the absorption and diffusion capacities of the zeolite,
- (c) alter the electrostatic fields present within the zeolites,
- (d) as well as alter the acidity of the zeolite.

Attempts to examine these effects and their impact on the catalytic activity of the zeolite have, in the main, relied heavily on bulk studies. The general course of these investigations has been to exchange a zeolite with particular cations and then examine its activity. These studies usually involve a minimum of characterization of control of the ion exchange. Even stoichiometry is often unmonitored! A sampling of the results of such investigations is offered in Table 1. In light of the numerous alterations that ion exchange might provoke, it is not surprising to find that the rationalizations of the orderings of catalytic activity presented in Table 1 are indeed complex.^{49, 74, 82-91} Effects as diverse as atomic radius,⁹⁴ electrostatic potential, ionic strength,^{36, 37} electronegativity and ammine complex formation constants⁶⁹ have been invoked in these rationalizations. This diversity is directly attributable to the lack of detailed structural data concerning the cations. The need for this detailed information is emphasized by

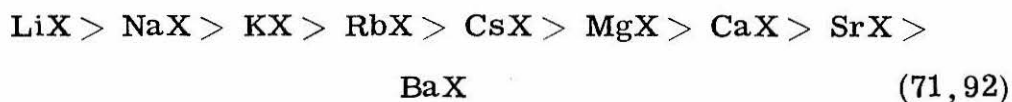
Table 1

Effect of Cations on the Catalytic Activity of Zeolites

Zeolite	Reaction Catalyzed	Order of Catalytic Activity	Ref.
X	Isomerization of butenes	NaCoX > NiThX > NaNiX > NaCrX	120
Y	Isomerization of butenes	HNaY > NaNiY > NaCoY > NaCrY > NaY	120
Y, A	$C_2H_4 \xrightarrow{H_2O} CH_3CH_2OH$	LaY > CaY > MgA > CdA > ZnA > AgA > SrA > CaA ~ CeA	121, 122
X	Cracking n paraffins	CaX > NaX	123
Y	$HC \equiv CH \longrightarrow$ 	Ca, Na = O < Mn ²⁺ << Co ²⁺ = Ni ²⁺ <<< Cu ²⁺ = Zn ²⁺ = O	3
Y	Dehydration of cumene to α methylstyrene	K, Na = O <<< Li < Ba ~ Sr ~ Ca ~ Mg	18
X	Oxidation of alkanes	Cu > Pd > Cr > Ni > Zn > Ag	124
X	Cracking of hexanes	CaX > MnX > NaX	125
Y	$C_6H_6 + NH_3 \longrightarrow NH_2C_6H_5$	Cu > Ni > Zn > Cr > Co > Cd > Mn > Mg, Ca, Na \approx O	69
Y	Cumene cracking	CuKY < CuMgY	40

recent results that indicate that cations adjacent to the active site as well as those within the active site influence catalytic activity.⁸³

Cations affect not only catalytic activity, but also nearly every other physical property of the zeolite.¹³⁶ Absorption capacities are definitely sensitive to cations.^{94, 97, 156} This effect has been correlated with cation size, charge, and polarization.^{70, 71, 97} Heats of absorption of water by exchanged zeolite X have been shown to follow the ordering:



Similarly, cation size affects the diffusion¹⁶⁷ and chromatographic properties of a zeolite.^{70, 93, 94}

The impact of cations on the thermal stability of zeolites is second only to catalytic affects in commercial importance.^{146, 147, 154} The thermal stability of zeolites is a matter of some consequence since most processes using zeolite catalysts proceed at temperatures well above ambient. Unfortunately, the effect of cations on stability is an area of more confusion than understanding. In general monovalent cations are generally removed from the zeolite framework to enhance stability.⁹⁶ On the other hand, ammonium ions are often exchanged into the framework to enhance stability.² Barium ions generally stabilize the zeolite framework.⁷² However, three different patterns of stability have been observed with other divalent cations:

Table 2

Hydration Numbers in Water Solution for Ions Commonly
Found in Zeolites¹⁶²

<u>Ion</u>	<u>Hydration Number</u>
Li	7.1
Na	4.15 - 5.05
K	1.9
Mg	13.9
Ca	11.9
Sr	10.8
Ba	8.4

- (a) stability passes through a maximum at 20-40% exchange
- (b) stability monotonically increases with exchange
- (c) stability monotonically decreases with exchange with divalent cations^{72, 73, 126}

Trivalent and tetravalent cations seem to universally enhance the stability of zeolites.⁶⁸ Rare-earth exchanged zeolites are now used in million-pound quantities for exactly this reason.

Water hydrating the cations has been proposed to be a major factor in determining the stabilizing/destabilizing effect of the cation.^{20, 21} The position and ordering of cations has been shown to be dependent on the water content of the zeolite.⁷⁷ The hydration of cations within the zeolite is still largely a matter of conjecture. Presumably the hydration number of the cations cannot be greater than that of the ion in solution. Some solution hydration numbers for common zeolite cations are shown in Table 2. The interactions between the cations and the water in zeolites have been established as strong and complex.^{24, 25, 73} Nmr analysis of ²³Na exchanged zeolite has shown that cation site preference and mobility are drastically affected by water content.⁵⁶ Further, exchange studies have shown that some cations readily exchange, while others resist exchange even over prolonged times and harsh conditions.^{75, 76, 95} This behavior considerably complicates bulk studies of the exchange properties of zeolites. For instance, Sr²⁺ exchange of Na⁺ Linde X appears to violate thermodynamics.⁷⁵

During the process of exchange it appears that the cations occupy sites within the voids of the zeolite where they can remain fully hydrated. Cations in such positions would little affect the catalytic activity or physical properties of the zeolite. Only during heat treatment and/or with a high cation population do the ions migrate into the zeolite active site where they can interact with the framework structure.¹⁵³ The higher valent cations show a greater preference for the active site²³⁻²⁵ for reasons unknown. Correspondingly, the zeolites exchanged with higher valent cations are less affected by further hydrothermal treatment.^{110, 115} Framework-cation interactions are deepest of mysteries at present. In LaX and LaY the La³⁺ ions are freely mobile and reversibly relocated in the fully dehydrated, active, zeolite.²⁵ Trivalent cations are known to be the cations most tightly bound to the zeolite framework, yet this result is indicative of very weak cation framework interactions. On the other hand, infrared and bulk studies have attributed framework distortions to interactions with the cations^{62, 119} and cation selectivity and site preference have been related to such interactions.^{2, 3} The discrepancies in these descriptions are particularly striking, and call into question a number of the precepts of synthetic zeolite chemistry. Only careful resolution of the structural interplay between cations, protonated species and the zeolite framework can this problem be resolved. Framework interactions must play some role in the effects of the zeolite on the ionization of polyvalent ions described below.

The extensive work with transition-metal-loaded zeolites is a natural extension of similar work with silica-alumina catalysts. Virtually every known transition metal and transition metal ion has been loaded into zeolites.^{86, 115} Examples typical of this work are shown in Table 3. The zeolite seems to stabilize unusual oxidation states. Ions such as Ni(I), Pd(I), and Pt(III) have been identified in zeolites.^{60, 63} This stabilizing capability contributes to the extreme efficiency of metal-ion loaded zeolites as oxidation catalysts. Metal-ion loaded zeolites of this type have been little exploited.

Of greater commercial interest are the zeolites loaded with reduced metal. The zeolite is an attractive metal substrate since it assures great disbursement of the metal ions. The cage structure of the zeolite inhibits metal atom migration and agglomeration which are principal sources of deactivation of silica-alumina supported catalysts.¹³⁷⁻¹⁴⁰

Structural work on metal loaded zeolites has been slow in the face of the rapid growth of empirical studies on such systems. Some attempts have been made to characterize the location of Pd before and after reduction using X-ray powder diffraction.¹⁴¹ The palladium ions were found to agglomerate in groups of 4 to 10. The specific coordination structure of these aggregations was not resolved. After reduction, migration of metal ions occurred only at temperatures greater than 200°C. At lower temperatures the atoms were reported to be isolated. Aggregation in Ni⁰ loaded zeolites has been reported to be more extensive.^{44, 143}

The need for more structural information on such systems as well as zeolite cations in general is manifest. The following headings illustrate the type of structure information concerning cations and metal atoms in zeolites that would be desirable:

- (a) Cation location and its variation with temperature, valence state, and cation population.
- (b) Coordination geometry and stoichiometry of the cations and its variation with location.
- (c) Water content, location, and its effects on cation location.
- (d) Interaction between the cations and the zeolite framework.
- (e) Effect of cation valence on the structural units present in the adjacent zeolite framework.
- (f) Effect of cations on pore and channel size.
- (g) Intercation interactions and the occurrence of clusters.
- (h) State of atomic metals in zeolites, their variation with temperature, water content, and their interaction with the zeolite framework.

Paulingite presents an excellent choice of zeolite for a structural study to elucidate these points. Within the Paulingite framework there are four different cations (K^+ , Na^+ , Ca^{2+} , Ba^{2+}). Each of them commonly occurs in other zeolites. It will be possible to examine the "natural" site preference of both mono and divalent cations. The comparison between these natural sites and the more forced sites of exchanged cations will be most revealing. The structural diversity of

Table 3
Examples of Metal Ion Exchanged Zeolite Systems

Zeolite	Metal Ions	Reference
X	Cu, Pd, Cr, Ni, Zn, Ag, Co, Cd, Mn, Th	120, 124, 125
Y	Cu, Ni, Zn, Cr, Co, Cd, Mn, La	3, 69, 121, 122
A	Ce, An, Ag, Cd	121, 122
X	Te	133
Y	Cu	124, 142, 159
X	Fe	120
Faujasite	Ni, Cr ₂ O ₃	150
Y	Pt	151
Y	Cu	40
X	Mn	125
Faujasite	Ni	152
Y	Ag ⁺	153, 157, 165
Y, X	Pt	154
NH ₄ Y	Co ²⁺ , Ni ²⁺ , Pt ²⁺ , Pd ²⁺	111, 112
NaX	various rare earths	155, 156, 158
A	Ni	54
Y	Pd	141

Paulingite will yield a more complete portrait of cation site preferences than would a simpler zeolite. Extension of the Paulingite results to a wide range of other zeolites including those of commercial interest will be possible.

III. Additional Studies

Pinpointing the source of catalytic activity in any inhomogeneous system is a difficult and frustrating task. The acid sites in zeolites have received by far and away the most attention as the active sites in these structures. But, as mentioned above, a number of other features of the zeolite structure may be responsible for its activity. Of these other possibilities, the electrostatic fields present within the zeolite cavities are the most intriguing. Such fields cannot possibly be estimated from X-ray diffraction results alone.

Theoretical calculations by Dempsey²⁶ indicate electrostatic fields within zeolite supercages of millions of volts per centimeter. Fields of this magnitude would, of course, be sufficient to literally rip any chemical species apart. Zeolite catalysts, moreover, are most efficient in ionic reactions,^{3, 45-48, 145} which suggest that this theoretical result might at least be qualitatively accurate.

Several attempts have been made to probe the fields inside the zeolite. Boudart, et al.¹⁴⁰ used absorbed krypton to probe zeolite Y. They found that the free energy of absorption was indicative of fields of only 5.3 kcal/mole. Unfortunately, these results were done on poorly characterized systems at extremely low coverages (about one

krypton per 64 cages) and this result may be greatly in error. Further, inert gases such as krypton and argon as well as active gases such as methane and oxygen are known to disrupt the hydroxide structure of the zeolite cage which would adversely affect thermodynamic results.¹⁸⁴ Neikam¹⁴⁶ reported that Ce^{IV} exchanged zeolites were capable of ionizing small molecules whose ionization potentials were 7.5 electron volts or less. Some high energy sites produced 9.0 electron volt potentials. Heat of immersion data has been used to estimate field intensities in zeolites NaX and CaX of 1.5×10^5 esu/cm² and 6.5×10^5 esu/cm².¹⁶³ The stability of unusual species such as Na₄³⁺, Na₆⁵⁺, Pd(I) and Ni(I) within the zeolite framework further attests to the strange electrostatic fields that must be present within the structure. Experimental examination of these fields has been plagued by poorly characterized and controlled systems. Without adequate structural information derivations of the field intensities must be largely a matter of guesswork. The results to date may safely be presumed to be inaccurate.

Once extensive structural information concerning the geometry and stoichiometry of cation sites is available, spectroscopic studies may possibly be more successful in probing the electrostatic fields present in these sites. Optical, ultraviolet, and epr spectroscopy of single-crystal, transition-metal-ion exchanged zeolites would be particularly powerful techniques for this type of examination.

The spectra of Co(II) and Ni(II) are quite sensitive to coordination geometry and the electrostatic field produced by the coordination sphere of the ions. An extensive background of theoretical and experimental results is available for the interpretation of this sensitivity. The X-ray crystallographic experiments proposed in part one of this proposition would detail the coordination geometry of an exchanged ion. Intuitively, an ion in a zeolite cage fits well within the framework of ligand field theory. Consequently, with spectra in hand it ought to be possible to assess the electrostatic field surrounding the ion in a straightforward way.

Some attempt has been made in this direction with powdered material. Kleir, et al. examined the optical spectra of Ni(II) and Co(II) exchanged zeolite X.^{53-56, 135} After exchange of these ions into the zeolites, little change was observed in the spectra from that of the hexaquo ion. Heat treatment, which from the discussion above might be expected to drive the ions into active sites, caused some change in the spectra. The absence of structural information precluded interpretation of these changes in terms of field strengths.

Esr spectra of zeolites have largely been confined to spectra of free radical species absorbed into the zeolite. Nitric oxide has been a popular absorbate.^{128-130, 164} Free radicals generated from alkylbenzen derivatives¹⁶¹ and alkenes¹⁶² absorbed on commercially important zeolites have also been studied. Esr studies of mobility and geometry of absorbed NO₂, CO₂, and O₂⁻^{131, 161} have also appeared. Conclusions were drawn from the spectra under the

assumption that only moderate electrostatic fields occurred at the absorption site. ESR spectra of transition-metal-ion loaded zeolites have been largely confined to Cu^{2+} containing zeolites.¹³²⁻¹³⁴ Here, again, the spectra of the freshly exchanged species was little different from that of the aquated ion. Heat treated material gave no detectable signal--a significant result in light of the possibility of large electrostatic fields.

Magnetic susceptibility has been used to examine metal-loaded zeolites.^{143, 147-149, 166} Unusual results have appeared which most authors have attributed to extraordinary electronic structures of the metal atoms in the zeolite sites.

These experimental results obtained from powdered and bulk, structurally uncharacterized zeolites are disturbing, but largely uninterpretable. It seems clear that only single crystal studies of zeolites that are structurally well understood will produce quantitative data concerning the electrostatic potentials within zeolite active sites.

References

References from "Advances in Chemistry Series," Vol. 101 (1971) will be marked by H* following the page number. Those from "Advances in Chemistry Series," Vol. 102 (1971) will be marked by K* following the page number and those from "Advances in Chemistry Series," Vol. 104 (1973) W. M. Meier, ed., will be marked by L* following the page number.

1. D. P. Bruke, Chemical Week, Nov. 1, 1972, p. 23.
2. D. W. Breck, p. 1, H*.
3. J. A. Rabo and M. L. Poutsma, 284, K*.
4. E. K. Gordon, S. Samson, and W. B. Kamb, Science, 154, 1004 (1966).
5. K. F. Fisher, p. 31, and references therein, H*.
6. W. M. Meier and H. Villiger, Z. Krist., 129, 411 (1969).
7. R. M. Barrer and H. Villiger, Ibid., 128, 353 (1969).
8. V. Gramlich and W. M. Meier, Ibid., 133, 134 (1971).
9. V. Schramm and K. F. Fischer, p. 259, H*.
10. Ch. Baerlocher and W. M. Meier, Z. Krist., 136, 245 (1972).
11. H. Steinfink and H. D. Simpson, Acta Cryst., A26, 158 (1970).
12. H. Steinfink and H. D. Simpson, J. Amer. Chem. Soc., 92, 6225 (1969).
13. H. Steinfink and H. D. Simpson, Ibid., 91, 6229 (1969).
14. J. W. Ward, Trans. Faraday Soc., 67, 1489 (1971).
15. G. T. Kerr, J. Phys. Chem., 71, 4155 (1967).

16. G. T. Kerr, J. Catalysis, 15, 200 (1969).
17. P. K. Maher, F. D. Hunter, and J. Scherzer, p. 266, H* .
18. J. T. Richardson, J. Catalysis, 9, 182 (1967).
19. J. T. Richardson, Ibid., 11, 275 (1968).
20. H. S. Sherry, J. Phys. Chem., 72, 4086 (1968).
21. E. Dempsey and D. H. Olson, J. Phys. Chem., 74, 633 (1968).
22. J. V. Smith, J. M. Bennett, and E. Flanigen, Nature, 215, 241 (1967).
23. T. I. Barry and L. A. Lay, J. Phys. Chem. Solids, 29, 1395 (1968).
24. J. M. Bennett and J. V. Smith, Mat. Res. Bull., 3, 865 (1968).
25. J. M. Bennett, J. V. Smith, and C. L. Angell, Mat. Res. Bull., 4, 77 (1969).
26. E. Dempsey, J. Phys. Chem., 73, 3660 (1969).
27. D. H. Olson, J. Phys. Chem., 72, 1400 (1968).
28. R. C. Hansford and J. W. Ward, J. Catalysis, 13, 316 (1969).
29. L. Bertsch, H. W. Hapgood, J. Phys. Chem., 67, 1621 (1963).
30. H. Matsumoto, K. Yasui, and Y. Morita, J. Catalysis, 12, 84 (1968).
31. H. A. Benesi, J. Catalysis, 8, 368 (1967).
32. D. A. Hickson and S. M. Csicsery, J. Catalysis, 10, 27 (1968).
33. P. D. Hopkins, Ibid., 12, 325 (1968).
34. J. W. Ward, Ibid., 9, 225 (1967).
35. J. W. Ward, Ibid., 9, 396 (1967).
36. J. W. Ward, Ibid., 10, 34 (1968).

37. J. W. Ward, Ibid., 11, 328 (1968).
38. J. W. Ward, Ibid., 11, 259 (1968).
39. J. T. Richardson, Ibid., 9, 50 (1967).
40. J. T. Richardson, Ibid., 9, 178 (1967).
41. J. T. Richardson, Ibid., 21, 122 (1971).
42. K. M. Minachev, V. I. Garanin, V. V. Khardamor, and T. A. Isakova, Kinetics and Catalysis, 13, 1101 (1972).
43. O. Grubner, Z. Phys. Chem., 216, 287 (1961).
44. V. Panchev, H. Minchev, I. Bakusdjier, and I. Tsolovski, p. 434, K*.
45. C. J. Plank, Proc. Intern. Congr. Catalysis, 3rd, 1, 726 (1965).
46. P. B. Venuto and P. S. Landis, Advan. Catalysis, 18, 259 (1968).
47. H. A. Benesi, J. Catalysis, 8, 368 (1967).
48. H. Matsumoto and H. Morita, J. Chem. Soc. Japan, 71, 1496 (1968).
49. J. W. Ward, J. Catalysis, 13, 321 (1969).
50. R. Beaumont, D. Barthomeuf, and Y. Tranboize, p. 327, K*.
51. S. E. Tung and E. McIninch, J. Catalysis, 10, 166 (1968).
52. S. E. Tung and E. McIninch, Ibid., 10, 175 (1968).
53. K. Klier, Catalysis Rev., 1, 207 (1967).
54. K. Klier and M. Ralek, J. Phys. Chem. Solids, 29, 951 (1968).
55. R. Polak and V. Cerny, Ibid., 29, 945 (1968).
56. R. Polak and K. Klier, Ibid., 30, 2231 (1969).
57. A. P. Bolton and R. L. Bujalki, J. Catalysis, 23, 331 (1971).

58. H. A. Resing and J. K. Thompson, p. 473, H*.
59. F. J. Jansen and R. A. Schoonheydt, p. 96, L*.
60. J. A. Rabo, C. L. Angell, P. H. Kasai, and V. Schomaker,
Disc. Faraday Soc., 328 (1966).
61. P. B. Weisz and V. J. Frilette, J. Phys. Chem., 64, 382 (1960).
62. H. Lechert, p. 74, L*.
63. C. Naccache, M. Primet, and M. V. Mathieu, p. 266, L*.
64. E. F. Vansant and J. H. Lunsford, p. 441, L*.
65. R. M. Barrer and I. M. Galabora, p. 365, L*.
66. J. W. Ward, J. Catalysis, 14, 365 (1969).
67. K. V. Topchieva, B. V. Romanovskii, L. T. Thoang, H. Shi,
and Y. W. Bizreh, Proc. 4th Intern. Congr. Catalysis, 2, 135
(1968).
68. D. Balliret, P. Pichat, and D. Barthomeuf, p. 469, L*.
69. K. Hatada, Y. Ono, and T. Keii, p. 501, L*.
70. G. V. Tsitsishvili and T. G. Andronikashvili, p. 217, H*.
71. N. N. Augul, A. G. Bezus, and O. M. Dzhigit, p. 284, H*.
72. A. Dyer, W. Z. Celler, and M. Shute, p. 436, H*.
73. E. Dempsey and D. H. Olson, J. Phys. Chem., 74, 305 (1970).
74. D. H. Olson and E. Dempsey, J. Catalysis, 13, 221 (1969).
75. D. H. Olson and H. S. Sherry, J. Phys. Chem., 74, 305 (1970).
76. R. M. Barrer, W. Buser, and W. F. Gruetle, Helv. Chim Acta,
39, 518 (1956).
77. D. H. Olson, G. T. Kokotailo, and J. F. Charnell, J. Colloid
Interface Science, 28, 305 (1968).

78. L. Moscov, p. 337, K*.
79. C. Hansford and J. W. Ward, p. 354, K*.
80. J. W. Ward, J. Phys. Chem., 72, 4211 (1968).
81. J. B. Uytterhoeven, R. S. Shoonheydt, B. V. Liengme, and W. K. Hall, J. Catalysis, 13, 425 (1969).
82. J. Bandiera, Y. Ben Taaril, and C. Naccache, Bull. Soc. Chim. France, 349 (1969).
83. R. Beaumont and D. Marthomeuf, Compt. Rend., 269C, 617 (1969).
84. Y. Tranbouze, R. Beaumont, and D. Barthomeuf, p. 327, K*.
85. Ya. I. Isakov, A. L. Klyachko-Gurvich, A. T. Khudier, and A. M. Rubinstein, Intern. Congr. Catalysis Moscow, paper no. 56, (1968).
86. J. A. Rabo, P. E. Pickert, D. N. Stamines, and J. E. Boyle, Proc. Intern. Congr. Catalysis Paris, 2, 2055 (1960).
87. H. S. Sherry, J. Phys. Chem., 70, 1158 (1966).
88. J. Turkevich, Catalysis Rev., 1, 1 (1967).
89. J. B. Uytterhoeven, P. Jacobs, M. Makay, and R. Schoonheydt, J. Phys. Chem., 72, 1768 (1968).
90. P. B. Venuto, L. A. Hamilton, and P. S. Landis, J. Catalysis, 5, 484 (1966).
91. J. W. Ward and C. R. Hansford, J. Catalysis, 13, 364 (1969).
92. P. J. Cram and R. M. Barrer, p. 105, K*.
93. D. P. Timotejer and I. T. Evashko, Izv. Akad. Nauk SSR Ser. Khim, 1192 (1961) (English translation).

94. F. Wolf, F. Danes, and K. Pilchowski, p. 229, K*.
95. Y. Nishimura and H. Takahashi, Kolloid Z. u. Z. Polymere, 245, 415 (1971).
96. W. C. Ambs and W. H. Flank, J. Catalysis, 14, 118 (1969).
97. Y. Nishimura and H. Takahashi, Kolloid Z. u. Z. Polymere, 245, 415 (1971).
98. J. A. Gard and J. M. Tait, p. 230, H*.
99. W. M. Meier and D. H. Olson, p. 155, H*.
100. Molecular Sieve Abstracts, Union Carbide Corp., N.Y. (1972).
101. I am indebted to Drs. Sten Samson and Richard Stanford, Jr., for discussions concerning this point.
102. H. Hamilton, Acta Cryst., 18, 502 (1965).
103. W. M. Meier, p. 39, L*.
104. E. L. Wu, G. H. Kühl, T. E. Whyte, and P. B. Venuto, p. 490, H*.
105. W. B. Kamb and W. C. Oke, Amer. Mineralogist, 45, 79 (1960).
106. A. Schwitzer, private communication.
107. G. T. Kerr, J. Phys. Chem., 72, 2594 (1968).
108. M. Minachev and Ya. I. Iszkov, p. 451, L*.
109. G. T. Kerr, J. Phys. Chem., 73, 2780 (1969).
110. P. B. Venuto, p. 260, K*.
111. G. T. Kerr and A. W. Chester, Thermochimica Acta, 3, 113 (1971).
112. W. W. Wendlandt and L. A. Funes, J. Inorg. Nucl. Chem., 26, 1879 (1969).

113. A. Grobler and T. Kado, Proc. Anal. Chem. Conf., 3rd, Budapest, Vol. 2, 335 (1970).
114. R. Otsuka, H. Hayashi and N. Imai, Memoirs of the School of Sci. and Eng. Waseda University, 34, 107 (1970).
115. P. E. Pickert, J. A. Rabo, E. Dempsey, and V. Schomaker, Proc. Intern. Congr. Catalysis, 3rd, Amsterdam, 714 (1965).
116. A. E. Hirschler, J. Catalysis, 2, 428 (1963).
117. C. F. Heylen and P. A. Jadobs, p. 490, L*.
118. P. E. Eberly, Jr., J. Phys. Chem., 72, 1042 (1968).
119. J. V. Smith, p. 177, L*.
120. L. V. Skalkima, Bull. Acad. Sci. USSR Chem., 5, 929 (1970).
121. N. Nitta, H. Hatlori, C. Matsudzaki, and K. Tanabe, J. Catalysis, 13, 103 (1971).
122. N. Nitta, K. Tanabe, H. Hattori, and S. Gakkaishi, J. Japan Petrol. Instit., 15, 113 (1972).
123. V. J. Frilette, P. B. Weiss, and R. L. Golden, J. Catalysis, 1, 301 (1962).
124. I. Mochida, S. Hayate, A. Kato, and T. Seiyama, Ibid., 19, 405 (1970).
125. A. L. Aqudo, F. R. Badcock, and F. S. Stone, Intern. Congr. Catalysis Moscow, paper no. 59 (1968).
126. H. Bremer, W. Mörke, R. Schöded, and F. Vogt, p. 249, L*.
127. H. S. Sherry, J. Phys. Chem., 74, 2710 (1970).
128. K. M. Wang and J. H. Lunsford, J. Phys. Chem., 75, 3475 (1971).

129. C. L. Gardner and M. A. Weinberger, Canadian J. Chem., 48, 1317 (1970).
130. R. L. Corio and S. Shih, J. Phys. Chem., 75, 3475 (1971).
131. K. M. Wang and J. H. Lunsford, J. Phys. Chem., 75, 1165 (1971).
132. I. R. Leith, C. Kembull, and H. F. Leach, Chem. Comm., 407 (1971).
133. C. M. Naccache and Y. Bentaart, J. Catalysis, 22, 171 (1971).
134. I. D. Mikheikin, V. A. Shuets, and V. B. Kazanskii, Kinetics and Catalysis, 11, 609 (1970).
135. K. Klier, p. 480, H*.
136. H. Matsumoto, M. Tokuno, H. Futami, Y. Morita. Bull Chem. Soc. Japan, 43, 1899 (1970).
137. C. S. Brooks and G. L. M. Christopher, J. Catalysis, 10, 211 (1968).
138. W. G. Keman, A. H. Ali, and G. G. A. Schuit, J. Catalysis, 20, 374 (1971).
139. T. Kubo, H. Arai, H. Tominaga, and T. Kunugi, Bull Chem. Soc., Japan, 45, 607 (1972).
140. R. A. Dalla Betta, and M. A. Boudart, Intern. Cong. Catalysis, 5, 100 (1972).
141. P. Gallezot and B. Imekil, p. 66, L*.
142. R. J. Mikovsky, A. J. Silvestri, E. Dempsey and D. H. Olson, J. Catalysis, 22, 371 (1971).

143. W. Romanowski, Roczniki Chemi. Ann. Soc. Chem., 45, 427 (1971).
144. J. M. Andre and J. J. Fripiat, Trans. Faraday Soc., 67, 1821 (1971).
145. J. H. Block and M. S. Zei, Surface Science, 27, 419 (1971).
146. W. C. Neikam, J. Catalysis, 21, 102 (1971).
147. W. Trzebiatowski, "Catalysis and Chemical Kinetics," Academic Press, New York, 1964.
148. F. Figueras, R. Gomez, and M. Primet, p. 480, L*.
149. W. Romanowski, Z. anorg. allg. Chem., 351, 180 (1967).
150. J. P. Lawson and H. F. Rose, Ind. Eng. Roc. Res. and Dev., 9, 317 (1970).
151. I. M. Keene, p. 409, K*.
152. D. H. Olson, J. Phys. Chem., 72, 4366 (1968).
153. L. Riekert, Z. Elektrochemie, 73, 331 (1969).
154. S. W. Weller and A. A. Montagna, J. Catalysis, 20, 394 (1971).
155. L. L. Ames, Jr., J. Inorg. Nucl. Chem., 27, 885 (1965).
156. H. S. Sherry, J. Colloid and Interface Sci., 28, 288 (1968).
157. K. Narrita, J. Luminescence, 4, 73 (1971).
158. F. P. Hunter and J. Scherzer, J. Catalysis, 23, 31 (1971).
159. I. Mochida. S. Hayata, A. Kato, and T. Seiyama, J. Catalysis, 23, 31 (1971).
160. Y. Kurita, T. Sonoda, and M. Sato, J. Catalysis, 19, 82 (1970).
161. T. M. Pietrzak and D. E. Wood, J. Chem. Phys., 53, 2454 (1970).

162. Data taken from R. H. Stokes and R. A. Robinson, J. Amer. Chem. Soc., 70, 1870 (1948); as cited in H. A. Laitinen, "Chemical Analysis," McGraw-Hill Book Co., New York, 1960, pp 15-17.
163. K. Tsutsumi and H. Takahashi, J. Phys. Chem., 74, 2710 (1960).
164. P. H. Kasai and R. J. Bishop, Jr., J. Amer. Chem. Soc., 94, 5560 (1972).
165. K. Tsutsumi, H. Takahashi, Bull. Chem. Soc. Japan, 45, 2332 (1972).
166. T. A. Egerton and J. C. Vickerman, J. Chem. Soc. Faraday Transactions, 1973, p 39.
167. K. F. Loughlin and D. M. Ruthuen, Chem. Eng. Sci., 27, 1401 (1972).
168. J. W. Ward, Preprint Vol. 16, pB6 (1971).

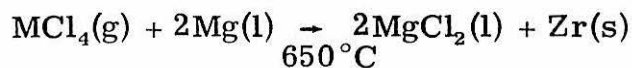
PROPOSITION III
STRUCTURE OF ZIRCONIUM THIOCYANATES
AND THE SEPARATION OF ZIRCONIUM AND HAFNIUM

Abstract: It is proposed that the zirconium and hafnium isothiocyanato species involved in the Fischer process deserve detailed structural investigation. It is further proposed that the structure of species of the stoichiometry $MO(SCN)_2 \cdot CsSCN \cdot 2H_2O$ ($M = Zr(IV), Hf(IV)$) involves seven-coordinate metal ions linked in polymeric units by dihydroxy bridges. As such, the extraction of hafnium in the Fischer process may involve an eight-coordinate intermediate species.

It is now apparent that the large neutron capture cross-section of zirconium metal (3.5 barns) is in fact due to a small percentage of hafnium impurity (the thermal neutron capture cross-section of hafnium is > 115 Barns versus 0.18 Barns for pure zirconium).^{1,2} Recent pressure to develop fission capability for the production of electrical energy has greatly enhanced the demand for both uncontaminated zirconium metal and uncontaminated hafnium metal. Demand for hafnium free of zirconium has recently become especially heavy. This metal is corrosion and failure resistant in both high and low temperature environments, as well as under high radiation conditions. Its thermal conductivity is twice that of either titanium or zirconium.¹ Unfortunately the separation of Hf and Zr is one of the most difficult of all elemental chemistry.

Typical ores of zirconium (zircon, baddelyite, alvite, thortveite) are all contaminated with 1-14% hafnium.³ The refinement process is laborious and expensive. The ore is first fluxed

with carbonates or hydroxides, fired and leached to yield the metal oxides. The oxides are then chlorinated to give the metal tetrachlorides.⁴ At this point separation of hafnium and zirconium is initiated. Once separated, the pure metals are formed by the Kroll process.⁵



Because of the "Lanthanide" contraction the atomic and ionic radii of hafnium and zirconium are very nearly the same. The chemical and physical properties of these metals are therefore nearly identical. All separation processes are laborious since they must rely on quirks, often quite subtle, in the properties of the metal and their compounds.

Separation of the metals by distillation of the tetrachlorides has proved very unsatisfactory. The process is plagued by the need for high pressures (10-30 atms) and numerous theoretical plates. Consequently, the process has low recovery and low efficiency. Today, it is used primarily for the preparation of hafnium concentrates and "reactor-grade" zirconium.

Other processes for the separation involve a considerable detour from the above refinement process. The most successful process, the Fischer process,⁶ involves fractional extraction of hafnium thiocyanates into ketonic or organophosphonate media.

The organic fraction is distilled, the hafnium salt is left as the oxide. The oxides are reconverted to the tetrachlorides and returned to the refinement process.

In spite of the obvious inefficiency of the Fischer process, it has been the object of no fundamental research, though empirical studies abound.⁷

It is the thesis of this proposition that the enhanced solubility of hafnium thiocyanates in the organic phase must ultimately stem from some difference in the structures of hafnium and zirconium thiocyanates. Further, to optimize the Fischer process or to design a process which will narrow the difference between the separation and refinement processes, it is essential that the structures of these species be understood.

The chemical species involved in the extraction have been variously reported as $M(\text{SCN})_6^{2-}$, $M(\text{SCN})_4$,¹ $M(\text{OH})_2(\text{SCN})_2 \cdot 2\text{R}$ (where R is a ketone used in the extraction), $M(\text{OH})_2(\text{SCN})_2 \cdot 2\text{R} \cdot 2\text{HSCN}$,⁸ or $M(\text{SCN})_n^{4-n}$ ($n = 1-8$).⁹ However, none of these species have been isolated as more than tars or oils and their formulation is based solely on elemental analyses. I. V. Tananaev and coworkers were able to isolate species of the stoichiometry $\text{ZrO}(\text{SCN})_2 \cdot \text{MSCN} \cdot 2\text{H}_2\text{O}$ ($M = \text{NH}_4^+$, K^+ , Cs^+)¹⁰ from solutions of zirconium(IV) and thiocyanate ion. Later, similar hafnium species were prepared.¹¹

Infrared spectra of the zirconium salts show a sharp absorption at 913 cm^{-1} .¹² The hafnium salts absorb at 940 cm^{-1} .¹³

These absorptions were assigned to the stretching vibration of the zirconyl and hafnyl group, respectively. The structure of the salts was then proposed to be represented by the stoichiometry $M^+[ZrO(SCN)_3 \cdot H_2O]^- \cdot H_2O$. These arguments have been criticized and the above infrared absorptions have been reassigned to vibrational modes of the thiocyanate ion.¹⁴

Both assignments are patently ridiculous. Assume the vibrations of the zirconyl and hafnyl model are well described by a diatomic model. From the 913 cm^{-1} absorption in the zirconium salt, the force constant for the metal oxygen stretch is calculated to be $6.7 \text{ md}/\text{\AA}$. For the reasons cited above the force constant for the $Hf = O$ stretch must be the same. The absorption of the hafnyl stretch is then predicted to be 880 cm^{-1} ! It is unlikely that the assumptions of the diatomic model in this instance would produce such an error between predicted and observed absorption frequencies. The shift of an absorption in a zirconium salt to higher energies in a hafnium salt is much more likely the behavior of a deformation mode than a stretching mode. Deuteration of the species in question verifies this prediction (figure 1). The 913 cm^{-1} band is shifted to 695 cm^{-1} upon deuteration while the 940 cm^{-1} absorption shifts to 715 cm^{-1} ($\nu_H/\nu_D = 1.31$). Such shifts are, of course, typical only of protonated species. The sharp absorptions are easily assigned to the deformation of bridging hydroxide groups.¹⁶ Certainly, such an assignment is far more consistent with the known structural chemistry of zirconium(IV) and hafnium(IV).^{14, 15}

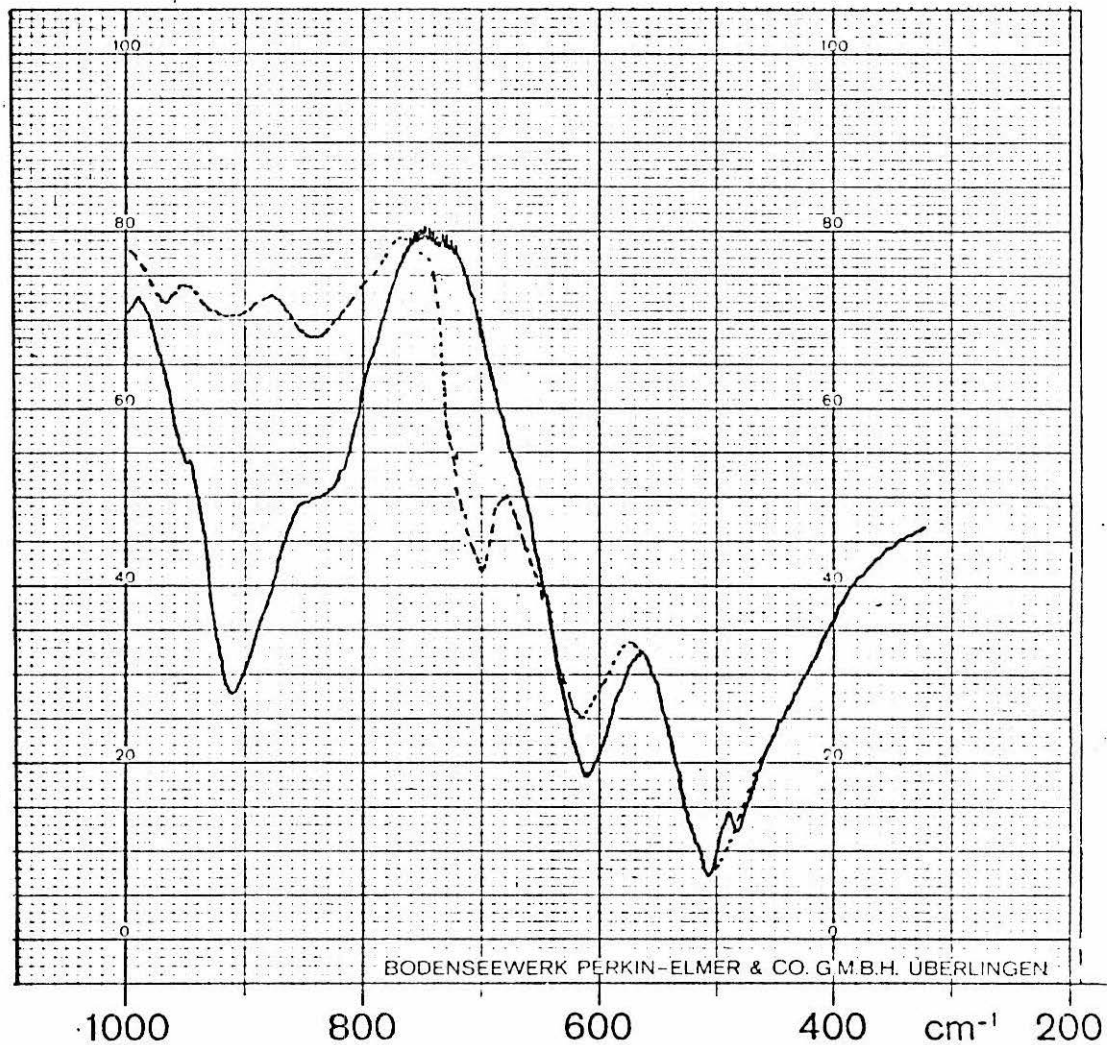
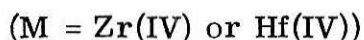
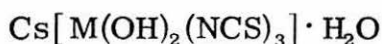
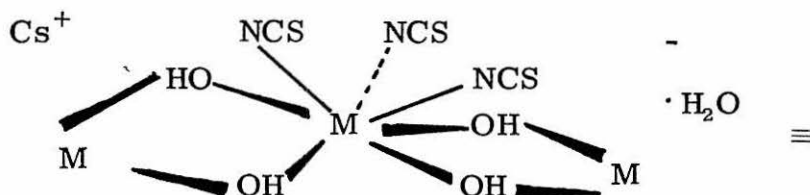


Figure 1. Infrared spectra of (a) $\text{CsZr(OH)}_2(\text{NCS})_3 \cdot \text{H}_2\text{O}$ (solid line) and (b) $\text{CsZr(OD)}_2(\text{NCS})_3 \cdot \text{D}_2\text{O}$ (dashed line). (From D. Powers, unpublished work.)

Inspection of the infrared spectra of the salts further shows:

- (1) no bands due to rocking or wagging modes of coordinated water,
- (2) no evidence for uncoordinated thiocyanate ion,
- (3) thiocyanate is N-coordinated,
- (4) spectra of hafnium and zirconium salts are nearly identical.

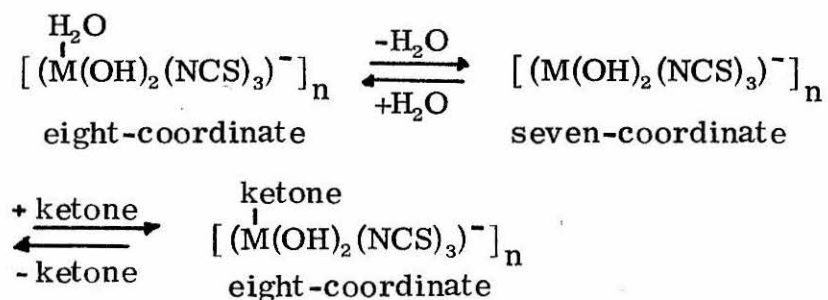
This evidence suggests that the structure of the above species consists of seven-coordinate zirconium(IV) or hafnium(IV) ions linked in a polymeric array with dihydroxy bridges.



Though other structures are possible, this formulation is in good accord with known structures of zirconium(IV) salts.

If differences in structure are responsible for the differences in solubility in the Fischer process, these differences are not apparent in the species described above. They may in fact manifest themselves only in solution or when the organic extraction phase is present. The structural chemistry of zirconium and hafnium is

predominated by eight-coordinate structures. A seven-coordinate species, such as above, would have a site available for an oxygen donor, such as the extracting solvent to attack. A coordination extraction mechanism is definitely suggested by the many empirical investigations of the Fischer process. Extraction species described in reference 8 are also compatible with this process. Ketonic complexes of zirconium(IV) are well known.¹⁵ The preliminary steps of the extraction may then be described by the equilibria:



In aqueous solution it has been assumed that water occupies the eighth coordination site. No speculation on subsequent steps in the extraction can be made. The differences in solubility of the hafnium and zirconium complexes may be due to:

- (1) differing extents of polymerization of the species,
- (2) varying ketonic coordination,
- (3) varying intraligand interactions.

To completely understand the extraction process, it will be essential to investigate the structure of the solution species. Infrared spectroscopy will be of limited utility in these investigations. Raman

spectroscopy may indeed yield a limited amount of useful information.

A host of experimental techniques have been applied to problems of polymerization of dissolved zirconium salts. Equilibrium studies¹⁷⁻¹⁹ often yield useful information. In the case of $\text{ZrOCl}_2 \cdot 8\text{H}_2\text{O}$ solution, they have shown that the nature of the dissolved species is dependent in very complex ways on pH and concentration. Further, zirconium solutions sometimes take years to come to equilibrium. In the case of thiocyanate species, even greater complications can be anticipated. Other techniques which have been applied to zirconium, such as ultracentrifugation,²⁰⁻²² low-angle X-ray scattering,²³ light scattering,²⁴ electromigration,²⁵ dialysis and diffusion kinetics,²⁶ and chromatography²⁷ may yield information. But the difficulties in interpretation associated with these techniques, and the type of information they yield make these studies at best supplemental. What is really needed is information dealing with structure and bonding of the species.

Fortunately, the species in question are well disposed for investigation with nuclear magnetic resonance. Proton magnetic resonance may be of limited utility, though not totally impractical. Resonance of other nuclei will be of greatest interest. O^{17} nmr, while expensive, will yield greatest information about the zirconium-oxygen framework of any polymeric species. Further, water dissociation rates can be measured by this technique. Resonances due to N^{15} , C^{13} , and S^{31} will yield information about the nature of

the thiocyanate groups and their interactions with other species. C^{13} and F^{19} nmr might be useful in the investigation of ketonic interactions when fluorinated ketones are used.

Nearly all the nuclear species in the zirconium and hafnium thiocyanates will yield nmr spectra. Fortunately, the natural abundance of nmr active nuclei in each case is small. Consequently, by use of isotopically labelled species, the massive spin-spin coupling that would otherwise result can be excluded. The chemical environment of each species can then be investigated with a minimum of complication.

References

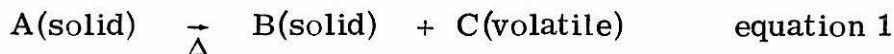
1. I. V. Vinarov, Russian Chem. Revs., 36, 522 (1967).
2. Handbook of Chemistry and Physics.
3. F. P. Venable, "Zirconium," ACS Monograph Chem. Catalog Co., New York, 1922.
4. J.W. Mellor, "Inorg. Theor. Chem." vol. 7
5. W. J. Kroll, J. Less Common Metals, 8, 361 (1965).
6. W. Fischer and W. Chalybaeus, Z. anorg. Chem., 255, 79 (1947).
7. W. Fischer and H. P. Pohlmann, Z. anorg. Chem., 328, 252 (1964); for an excellent review of Russian work in the field, see reference 1.
8. O. A. Sinegribova and G. A. Yagodin, Russ. J. Inorg. Chem., 10, 675 (1965).
9. A. M. Golub and V. N. Sergun'kin, Russ. J. Inorg. Chem., 11, 419 (1966).
10. I. V. Tananaev and I. A. Rozanov, Russ. J. Inorg. Chem., 7, 957 (1962).
11. I. V. Tananaev, I. A. Rozanov, and A. G. Kolgushkina, Russ. J. Inorg. Chem., 8, 522 (1963).
12. Yu. Ya. Kharitonov and I. A. Rozanov, Izv. Akad. Nauk. SSR, 3, 373 (1962); translated to English.
13. Yu. Ya. Kharitonov, I. A. Rozanov, and I. V. Tananaev, Izv. Akad. SSR, 4, 538 (1963); translated to English.

14. A. Clearfield, Rev. Pure and Applied Chem., 14, 91 (1964)
and later by D. L. Kepert, "The Early Transition Metals,"
Academic Press, New York, 1972, p 109.
15. E. M. Larsen, Advances Inorg. Radio. Chem., V. 13, p 1.
16. D. A. Powers and H. B. Gray, Inorg. Chem., 12, 2721 (1973).
17. R. Connick and W. McVey, J. Amer. Chem. Soc., 71, 3182
(1949).
18. R. Connick and W. Reas, J. Amer. Chem. Soc., 73, 3182 (1949).
19. J. A. Connor and E. A. Ebsworth, Advan. Inorg. Radiochem.,
6, 279 (1964).
20. J. Johnson and K. Kraus, J. Amer. Chem. Soc., 78, 3937(1956).
21. J. Johnson and K. Kraus, J. Amer. Chem. Soc., 75, 5766(1953).
22. J. Johnson, K. Kraus, R. W. Holmberg, J. Amer. Chem. Soc.,
78, 26 (1956).
23. G. M. Muha and P. A. Vaughan, J. Chem. Phys., 45, 4751 (1966).
24. R. L. Angstadt and S. Y. Tyree, J. Inorg. Nucl. Chem., 24,
913 (1962).
25. B. I. Nabivanets, Russ. J. Inorg. Chem., 6, 586 (1961).
26. A. K. Babko and G. I. Gridchina, Russ. J. Inorg. Chem., 6,
680 (1961).
27. A. M. Chekmarev, Russ. J. Inorg. Chem., 11, 792 (1966).

PROPOSITION IV
 NUMERICAL METHODS APPLIED
 TO THERMOGRAVIMETRIC ANALYSIS (TGA)

Abstract: It is proposed that numerical methods may permit significantly more accurate interpretation of thermogravimetric analysis in terms of kinetic parameters. A block diagram for a possible program for numerical analysis of TGA traces is proposed. An example of the use of numerical methods in interpretative TGA is given.

Thermogravimetric analysis (TGA) has been a useful analytic tool for well over two centuries.¹ Modern instrumentation has made such analysis both precise and convenient. Unfortunately, TGA is still used primarily for the determination of stoichiometry. Little attention has been applied to its potential for the kinetic analysis of solid state reactions. This is surprising since the TGA experiment is in reality a dynamic determination of the kinetics of a special class of solid-state reactions in which one of the products is volatile



The information density in a single TGA trace is far greater than that of any isothermal experiment. Not only is analysis carried out over a broad range of temperatures, but typically analysis is continued to completion of the reaction. Deconvolution of a TGA trace ought to yield kinetic parameters (activation energy, entropy, etc.) at the expense of far less labor than is involved in the host of isothermal experiments necessary to obtain these parameters.

Further, some criticism has been levelled at the use of isothermal methods for solid state reactions because of the problems of prior decomposition.^{2,3} The TGA experiment for kinetic analysis is not entirely free of objections. Careful attention to experimental conditions, reactor configuration and sample preparation, however, relieves most of these objections. As commonly performed, the TGA experiment presents integral data, whereas kinetic parameters have been derived in terms of differential results. Consequently, the deconvolution of a TGA trace requires considerable data treatment. Recent developments in differential thermogravimetric analysis (dtga) may relieve these difficulties. Currently, the expense of dtga equipment makes it unavailable to most experimenters.

It is the intent of this proposition to show that numerical methods can be used for high-precision deconvolution of TGA traces to yield kinetic parameters. The flexibility of numerical analysis will permit far better description of the solid-state reactions than current techniques will permit. The parameters derived from the TGA traces will permit a first step in the understanding of the mechanisms of the class of solid-state reactions described above.

A rate expression for the reaction in equation 1 is

$$\frac{d[A]}{dt} = - \sum R_i T^{n_i} \exp(-E_i/kT) [A]^{a_i}$$

where T^{n_i} is the temperature dependence of the pre-exponential rate factor; and a_i is the reaction order. Time is, of course,

related to the temperature program of the TGA experiment. For TGA purposes the above expression can be recast as

$$\frac{dA}{dT} = \frac{-1}{f'} \sum_i R_i T^{n_i} \exp(-E_i/kT) [A]^{a_i} \quad \text{equation 2}$$

where $T = f(t)$ and $f' = dT/dt$.

Some previous attempts have been made to understand TGA traces using analytic methods.^{2, 4-9} In all these attempts a vastly simplified form of equation 2 has been used for the rate expression, i. e. ,

$$\frac{dA}{dT} = -R \exp(-E/kT)A$$

Even so, the analytic methods used to deconvolute TGA traces in terms of this expression were laborious and imprecise. Most of these processes involved estimations of dA/dT in terms of finite differences, a process which theoretically may be carried to limitless precision, but experimentally yields only crude approximations. All the methods involve log, log-log, or semilog plotting which is well known to greatly truncate precision and obscure the inadequacy of the above rate expression.

The simplified rate expression is by far the most objectionable feature of previous attempts to deconvolute TGA traces. A typical TGA trace for an isolated weight-loss consists of an initial first-order portion which passes into a so-called second-order tail as the reaction nears completion. To accurately deal with such a trace, a minimum rate expression must be:

$$\frac{dA}{dT} = -R_1(T) \exp(-E_1/kT)[A] \\ -R_2(T) \exp(-E_2/kT)[A]^2$$

At least one author has recognized this necessity and restricted his deconvolution method to the initial weight loss, thereby considerably shorting the information available in a TGA trace.⁹ Of course, the above expression is not easily integrated by analytic means and has been avoided by previous authors.

Not only have reaction orders been simplified but the temperature dependence of the pre-exponential factors have been neglected in previous considerations. While such neglect has been satisfactory in isothermal kinetic analysis, it is unlikely to be so in TGA. All theoretical derivations ascribe a temperature dependence to the pre-exponential factor in rate expressions.¹⁰ This temperature dependence will definitely play a role in the determination of the shape of a TGA trace.

A block diagram for a computer program which will allow numerical analysis of TGA traces in terms of rate expressions such as equation 2 is shown in figure 1. Data necessary for the program are simply weight and temperature, both of which can be obtained from a TGA trace with errors within the bounds of experimental error. These data are converted to a spline which will imitate the behavior of the TGA trace and its derivatives up to third order. The derivative of the TGA trace-accurate to its second order

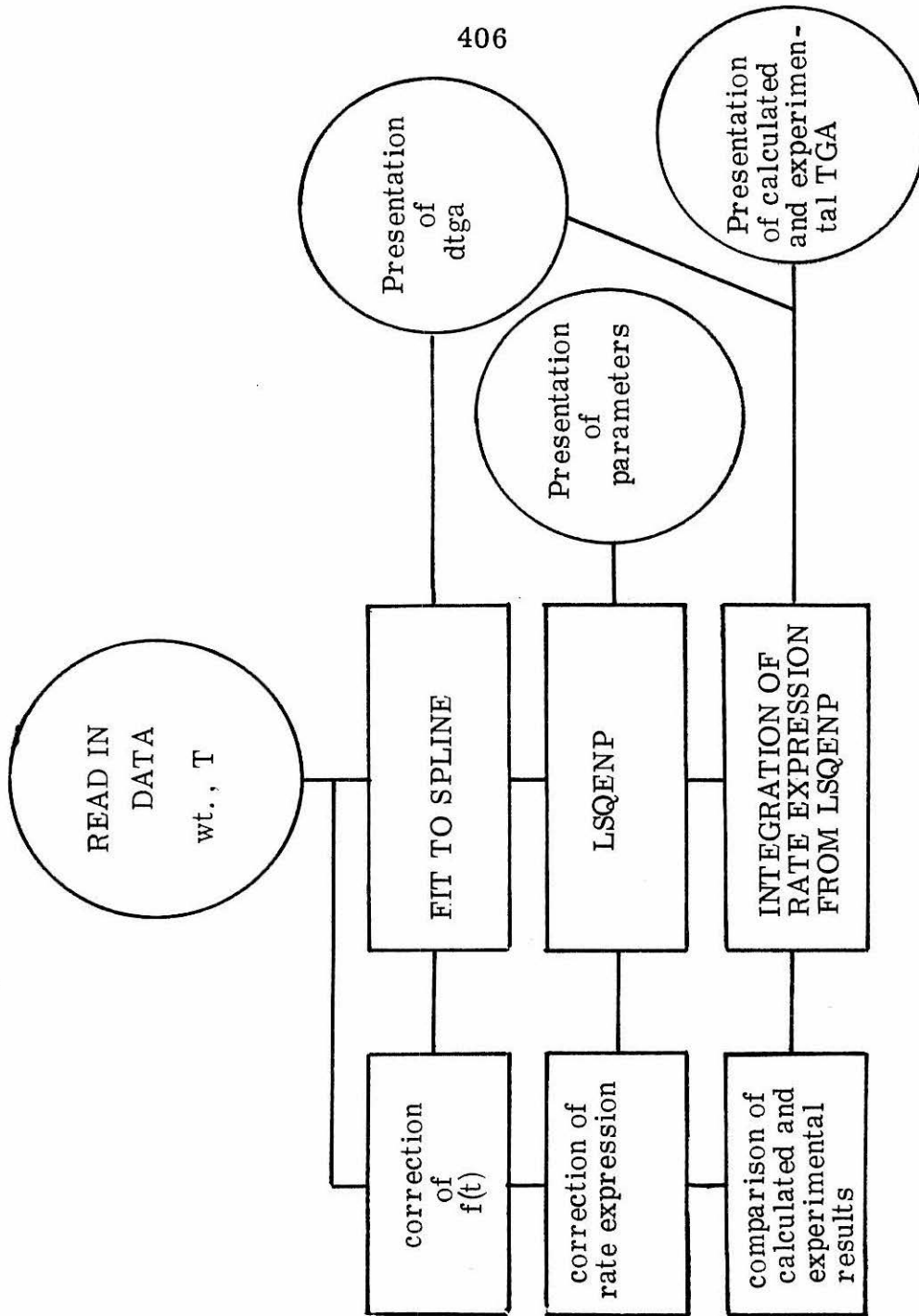


Figure 1. Block diagram for proposed computer program to derive kinetic parameters from TGA traces

derivative- is then fit to a rate expression by least squares estimation of non-linear parameters (LSQENP). The fit is done under the assumption that weight and temperature are precisely defined, but dA/dT is subject to random fluctuations.

A provision is included in the program for inclusion of higher-order terms from equation 2 should they be necessary. Some success in the deconvolution of TGA traces has been noted when the temperature program ($f(t)$) is varied.⁸ This can be done computationally without resorting to renewed experimentation, and a provision for this type of variation is included.

The parameters found from solid-state reactions may not be easily interpreted since they are likely to be out of any context based on solution kinetics. It will be necessary to compare the results to those of other experiments. For instance, parameters from dehydration reactions may be related to the vibrational frequencies of coordinated water (rocking, wagging, twisting, as well as the internal modes). These in turn are related to the coordination bond strength, hydrogen bonding, and other structural features of the phase in question.

Numerical methods may find application in the more classic use of TGA. One of the most difficult determinations in TGA experiments is the separation of the stoichiometry of two reactions occurring at similar temperatures.

A simplified version of the program in figure 1 was used to examine the behavior of the TGA trace as two identical independent weight-loss reactions approached each other in temperature. The form of the TGA trace for each weight-loss step was taken from the dehydration of calcium oxalate monohydrate. When the two reactions are separated by 90°C, the final weight of the sample is easily determined as w_1 (figure 2). As the separation between the reactions is narrowed to 50°C and 30°C, the TGA trace is altered as shown in figure 3. Computer drawn lines of maximum and minimum slope are shown in these figures. As can be seen in these figures, a general algorithm for estimation of the stoichiometry of the first reaction requires extrapolation of the slope lines AA and BB to intersection at P_1 . P_1 is quite close to w_1 . The temperature of completion of the first reaction is found as the midpoint of the line segment defined by the intersection of lines AA with BB and CC with BB--that is P_3 . Further work will be necessary to establish the generality of this algorithm in more complex situations.

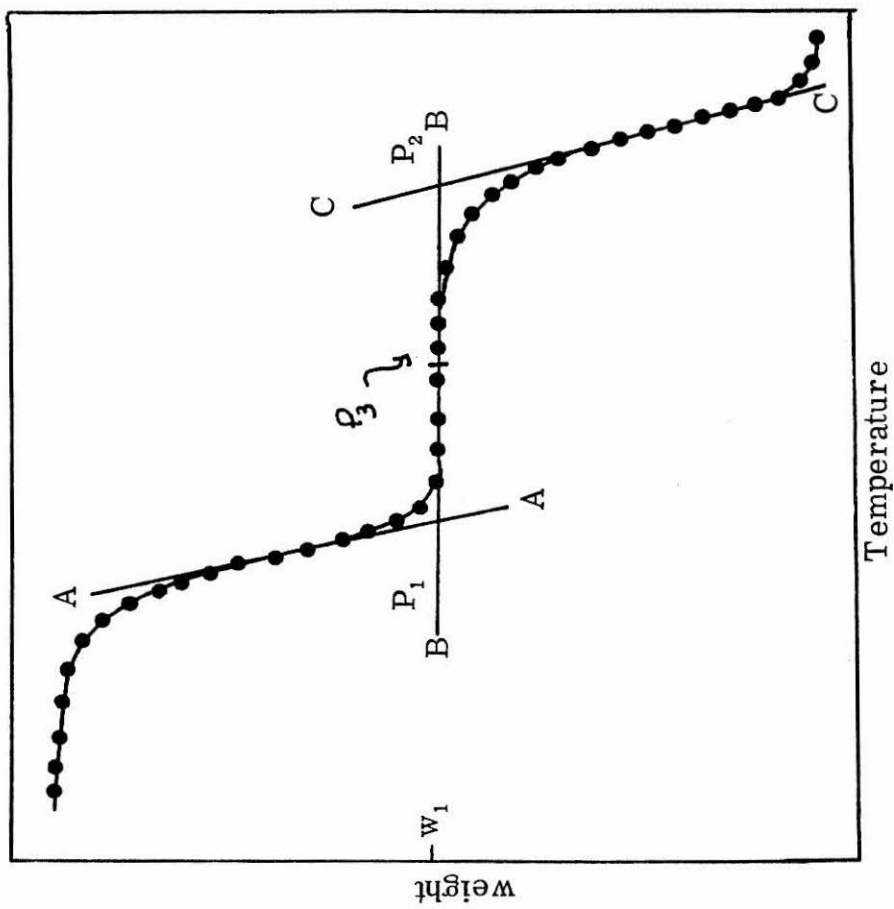


Figure 2. TGA trace of two identical reactions separated by 90°C. Lines of maximum and minimum slope are shown as AA, BB, CC.

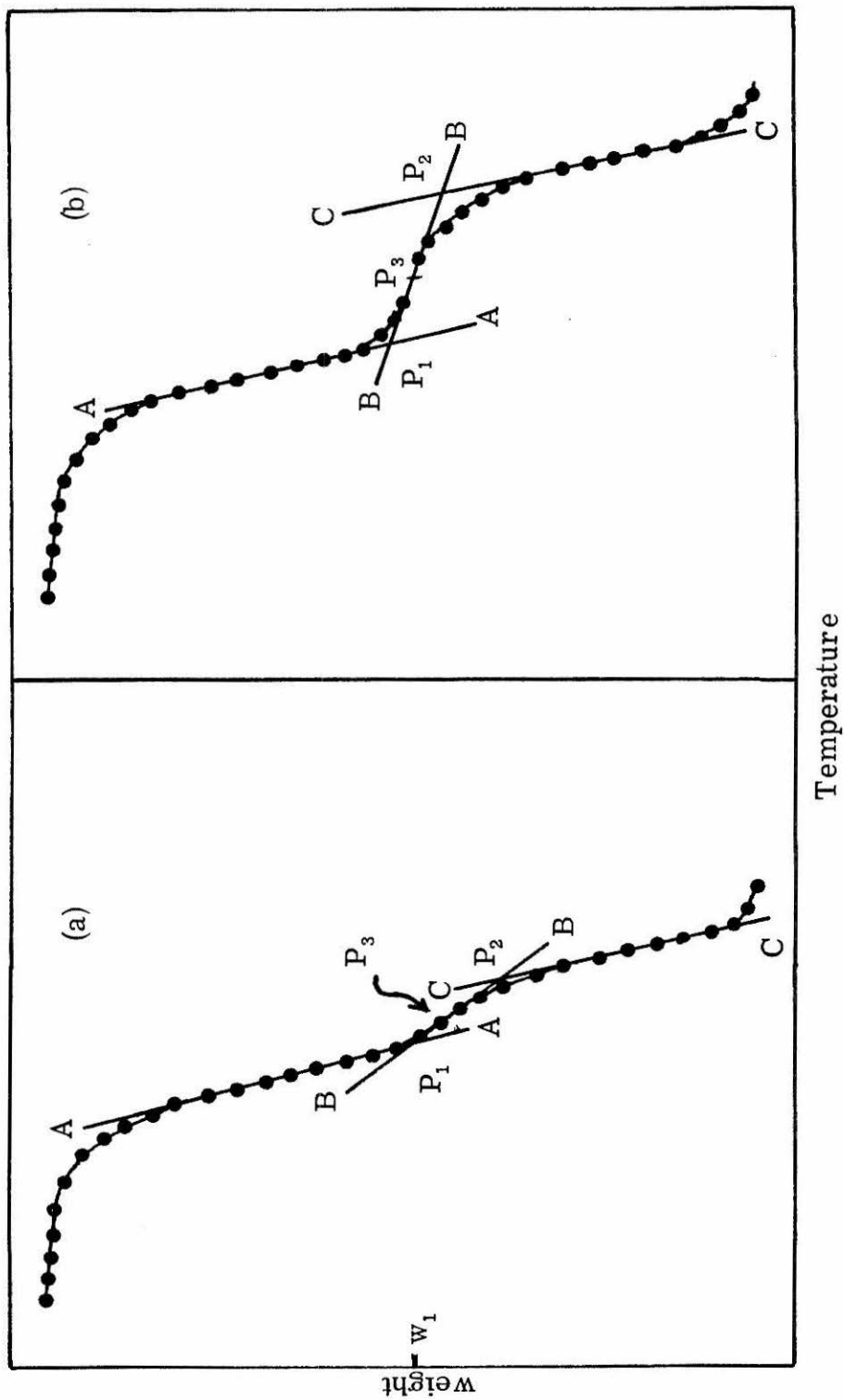


Figure 3. (a) TGA for two step process in which second step is initiated at a temperature 30°C higher than first. (b) Similar TGA with 50°C separation in weight loss steps.

References

1. C. Duval, "Inorganic Thermogravimetric Analysis," 2nd ed., Elsevier, Amsterdam, 1963.
2. E. S. Freeman and B. Carroll, J. Phys. Chem., 62, 394 (1958).
3. W. Wm. Wendlandt, "Thermal Methods of Analysis," Interscience Publishers, New York, 1964.
4. D. W. Van Krevelen, C. Van Heerden, and F. J. Huntjens, Fuel, 30, 253 (1951).
5. H. H. Horowitz and G. Metzger, Anal. Chem., 35, 1464 (1963).
6. C. D. Doyle, J. Appl. Polymer Sci., 5, 285 (1961).
7. R. M. Fuoss, I. O. Salyer, H. S. Wilson, J. Polymer Science, 2, 3147 (1964).
8. P. T. Davey and T. R. Scott, Nature, 179, 1362 (1957).
9. A. E. Newkirk, Anal. Chem., 32, 1558 (1960).
10. G. Gavalas, notes for Applied Chemical Kinetics, ChE 101, California Institute of Technology.

PROPOSITION V

REACTIONS OF COORDINATED NITRIC OXIDE

Abstract: The reactivity of coordinated nitric oxide has been largely ignored in the past. It is demonstrated that coordinated nitric oxide ought to be susceptible to chemical attack. Several potential reactions are described. Catalytic preparations of dinitrile compounds using transition metal nitrosyl are discussed.

The investigation of transition metal nitrosyl complexes has been dominated by structural and preparative studies.¹⁻³ In comparison, the reaction chemistry of coordinated nitric oxide has received little attention. Herein it is proposed that this aspect of the chemistry of metal nitrosyls merits closer scrutiny. The focus of this proposition is upon reactions that result in chemical transformation of the coordinated nitric oxide. Simple substitution and rearrangement reactions are ignored in the belief that such reactions are in reality reactions of the metal ion.

Investigations of the reactivity of coordinated nitric oxide may be expected to yield:

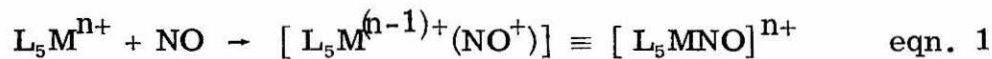
- (1) Novel complexes involving unusual ligands such as coordinated nitrenes,
- (2) New complexes with known ligands such as metal ion complexes of N_2O , NH_2OH , N_2 , etc.,
- (3) Convenient synthetic routes for the preparation of known complexes,
- (4) Catalytic nitration processes analogous to the Wacker process and the "oxo" process.

A rational course for the investigation of the reactions of coordinated nitric oxide would involve (a) determination of the susceptibility of the nitrosyl ligand to chemical attack, (b) reviewing the known reaction chemistry of nitrosyl complexes, (c) searching for possible reactions from among the known reactions of metal complexes with isoelectronic ligands and reactions of free nitric oxide. The bulk of this proposition follows this outline.

A. Susceptibility of the Nitrosyl Ligand to Chemical Attack

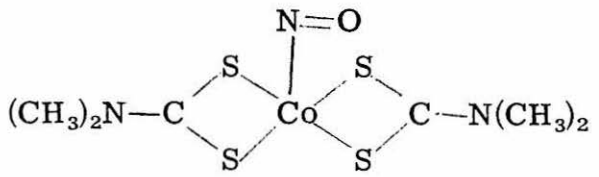
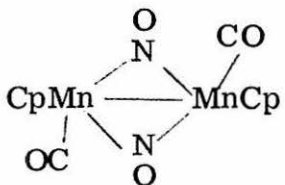
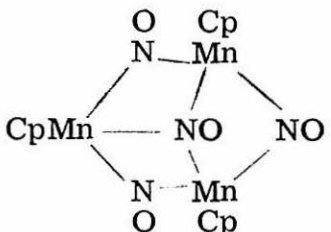
The known transition metal nitrosyl complexes obey the "eighteen-electron" rule to a great extent if it is assumed that coordination of the nitric oxide involves a three-electron bond and the proposition of metal-metal bonding is accepted in the case of a few polynuclear species. (For some exceptions see ref. 114). The structural diversity adopted by the nitrosyl ligand within the "eighteen electron" rule is illustrated in Table 1.

Infrared data have shown that the vast majority of metal nitrosyl complexes are best thought of as complexes of nitrosonium ion (NO^+).¹ The coordination reaction is then:

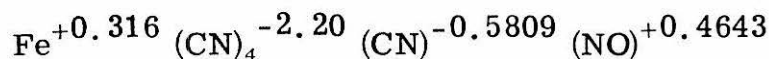


The molecular orbital description of the nitroprosside ion $((\text{NCS})_5\text{FeNO})^{2-}$ ⁴ has shown that the charge distribution (below) is consistent with this coordination reaction.

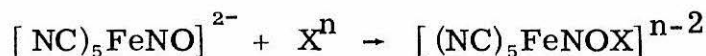
Table 1
 Various Structures Adopted by the Nitrosyl Ligand

<u>Structural mode of NO</u>	<u>Example</u>	<u>Reference</u>
terminal, linear	$\text{Na}_2\text{Fe}(\text{CN})_5\text{NO}$	5
terminal, bent ^a		54
bridging between two metal centers		51
bridging between three metal centers		51, 53

^a Also called "edge-on" in older literature.

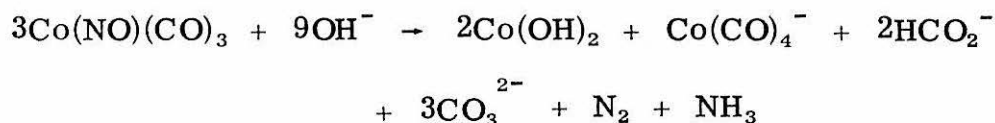


The large positive charge assigned to nitric oxide resides on the nitrogen, and this suggests that this atom ought to be susceptible to nucleophilic attack. This suggestion has been abundantly confirmed by a wide variety of reactions of nitroprusside of the type



where X^n is a nucleophile. Table 2 lists many examples of this type of reaction. Presumably all pentacyanonitrosyl metal complexes will undergo similar nucleophilic attack. Investigations of these reactions have produced most of the known reaction chemistry of coordinated nitric oxide.

There have been occasional reports⁶⁻⁸ of similar nucleophilic attack in other metal nitrosyl complexes such as



Nucleophilic attack on coordinated nitric oxide also occurs among ruthenium nitrosyls. For example, consider this reversible oxidation of nitric oxide³²:

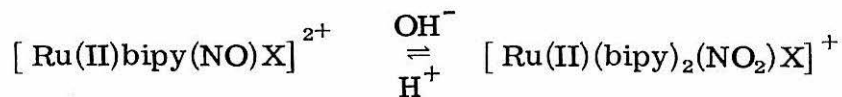
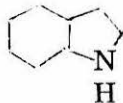
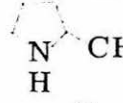
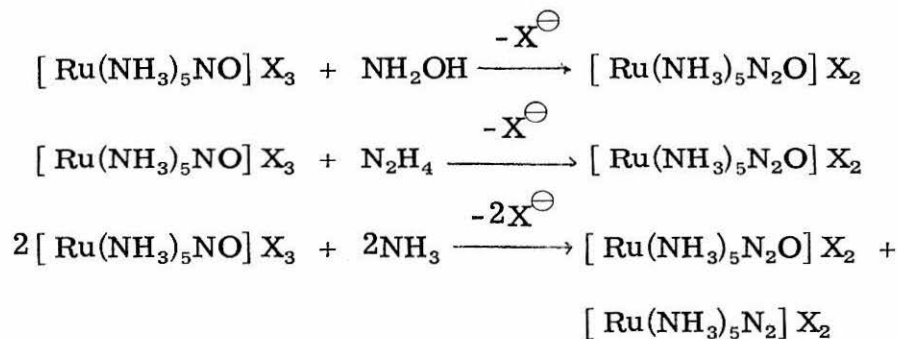
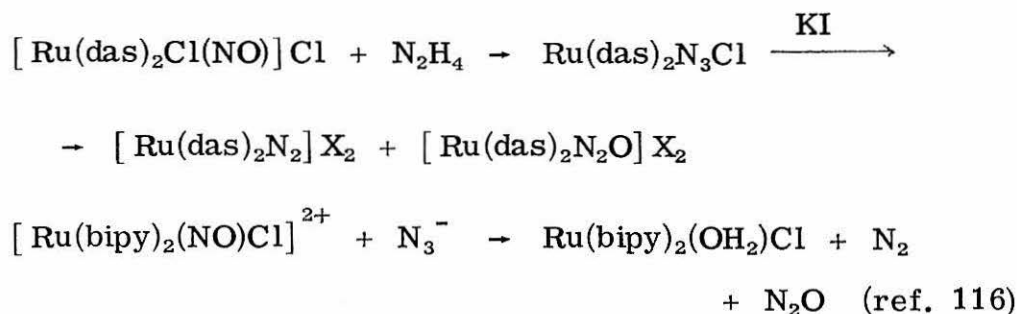


Table 2
Some Reactions of Nitroprusside Ion

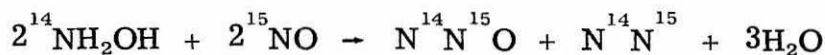
OH^-	$[(\text{NC})_5\text{FeNO}_2]^{4-}$	59, 60
H_2S	$[(\text{NC})_5\text{FeN} \begin{array}{l} \text{O} \\ // \\ \text{S} \end{array}]^{4-}$	61
SO_3^{2-}	$[(\text{NC})_5\text{FeN} \begin{array}{l} \text{O} \\ // \\ \text{OSO}_2 \end{array}]^{4-}$	62, 63, 64, 65
O CH_3CCH_3	$[(\text{NC})_5\text{FeN} \begin{array}{l} \text{O}^- \\ // \\ \text{CHCCH}_3 \end{array}] \rightarrow \text{CH}_3\text{CCH}=\text{NO}$ $+ \text{N}-\text{OH}$ $\text{CH}_3\text{C}-\text{CH}$ O	58, 66, 67
$\text{CH}_3\text{CH}_2\text{NO}$	ethyl nitrolic acid	57
$\text{CH}_3\text{C} \begin{array}{l} \text{O} \\ // \\ \text{CH}_2 \end{array} \text{C} \begin{array}{l} \text{O} \\ // \\ \text{CH}_3 \end{array}$	$[(\text{NC})_5\text{FeC}_5\text{H}_6\text{O}_3\text{N}] \rightarrow \text{CH}_3\text{C} \begin{array}{l} \text{O} \\ // \\ \text{C} \end{array} \begin{array}{l} \text{NOH} \\ // \\ \text{C} \end{array} \text{CH}_3$ O	69
SCN^-	$[2(\text{NC})_5\text{FeN} \begin{array}{l} \text{OH} \\ // \\ \text{O} \\ // \\ \text{CNS} \end{array}] \rightarrow (\text{NC})_5\text{FeN} \begin{array}{l} \text{CNS} \\ // \\ \text{O} \\ // \\ \text{CNS} \end{array} \text{N}-\text{Fe}(\text{CN})_5$	68
	$(\text{CN})_5\text{FeC}_8\text{H}_6\text{ON}_2$	
	$(\text{CN})_5\text{FeN}=\text{C}-\text{CH}$ $\text{HC} \quad \text{C}$ $\text{N} \quad \text{CH}_3$	
NH_2CNH_2	$(\text{NC})_5\text{FeX}$ X = nitrosothiocarbamic acid	

Ruthenium nitrosyl complexes are at once the pride and plague of the chemistry of this metal. The ruthenium(III) nitric oxide bond is exceptionally strong possibly because of the stability of the t_{2g}^6 electronic configuration that would be adopted by the metal ion if coordination were thought of in terms of equation 1 above. The nitrosyl will persist through treatment with boiling ammonium hydroxide, 8NHCl , and even, surprisingly, during oxidation-reduction reactions. Not only is the nitrosyl stable, but it is omnipresent. Exposure of ruthenium compounds to nitric acid, nitrates, nitrites, nitrous oxide, or nearly any nitrogen-oxygen compound will produce the nitrosyl.¹¹⁶ Often ruthenium metal is contaminated with chemisorbed nitric oxide. Once contaminated, the materials are exceedingly difficult to reclaim. The susceptibility of coordinated nitric oxide to nucleophilic attack suggests a possible route for purification of ruthenium compounds using mild reagents. The reversible reaction above is not particularly attractive, but reactions with nitrogen containing nucleophiles offer³³ hopeful pathways^{33, 34}:

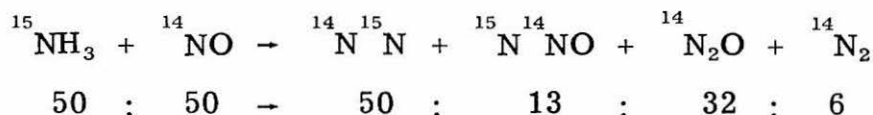




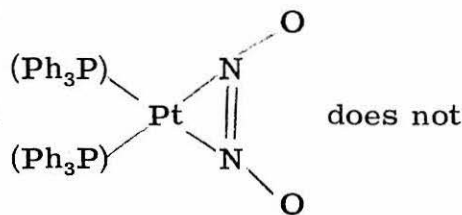
No studies of these reactions with isotopically labelled nitrogen have been reported, and the mechanism is not definitely established. Isotopic studies of analogous reactions with free nitric oxide do suggest a mechanism. Cooper, et al.³⁵ have shown that in the reaction between hydroxyl amine and nitric acid,



one nitrogen in each of the products comes from each of the reagents. In the reaction of $^{15}\text{NH}_3$ and ^{14}NO over platinum,³⁶ some mixing occurs:



An intermediate analogous to the compound



predominate.³⁷ A nucleophilic pathway is definitely insinuated.

The formation of N_2O and dinitrogen complexes from ruthenium nitrosyls seems generally possible. Since both these ligands can be aquated, unlike the nitrosyl,⁹⁸ a purification process is possible. The rates of aquation of $(NH_3)_5Ru(N_2O)^{2+}$ at $6.8^\circ C$ have been reported³⁸ as:



$$K_f = 9.5 \times 10^{-3} M^{-1}sec^{-1}, K_r = 1.35 \times 10^{-3} sec^{-1}$$

The equilibrium between pentaamine aquoruthenate(III) and the dinitrogen complex³⁸ is:

$$\frac{[Ru(NH_3)_5(OH_2)^{2+}][N_2]}{[(NH_3)_5RuN_2^{2+}]} = 9.1 \times 10^{-6}$$

By sweeping solutions of the N_2O or N_2 complex with inert carrier gases, these aquations can be driven to completion. A convenient purification of ruthenium nitrosyls is then at hand.

The reactions between nitrosyl complexes and nitrogen containing nucleophiles suggests a convenient pathway for the preparation of dinitrogen complexes should this reaction prove general for nitrosyls. Table 3 lists several known nitrosyl complexes which might yield known dinitrogen complexes or at least similar complexes when treated with hydrazine. References in this table refer to structural characterizations of the listed species.

Table 3

Transition Metal Nitrosyl Complexes Which May Yield Known Dinitrogen Complexes when Treated with Hydrazine

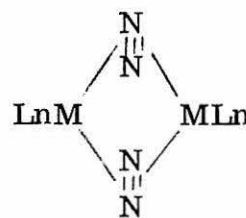
<u>Known Dinitrogen</u>	<u>Ref</u>	<u>Analogous Nitrosyl</u>	<u>Ref</u>
$[\text{Ru}(\text{NH}_3)_5\text{N}_2]\text{Cl}_2$	39	$[\text{Ru}(\text{NH}_3)_5\text{NO}]\text{Cl}_2$	1
$\text{CoH}(\text{PPh}_3)_3\text{N}_2$	40, 41	$\text{CoNO}(\text{PPh}_3)_2\text{Cl}_2$	52
$(\text{Cp}(\text{diphos})\text{Fe}_2\text{N}_2)$		$\text{Fe}(\text{NO})(\beta\text{-phthalocyanin})$	42
		$(\text{CpFe}(\text{NO})\text{CH}_3)_2$	43
		$\text{CpFe}(\text{NO})\text{CO}(\text{PPh}_3)$	44
$\text{Mo}(\text{N}_2)_2(\text{PR}_3)_4$	45	$\text{Mo}(\text{NO})_2(\text{PPh}_3)_2\text{I}_2$	46
$\text{ReX}(\text{N}_2)(\text{PR}_3)_4$	47	$\text{ReCl}_3(\text{NO})(\text{dipy})$	48
$\text{OsX}_2(\text{N}_2)(\text{AsR}_3)_3$	49	$\text{OsX}_2(\text{NO})(\text{AsPh}_3)_2$	50

Preparation of new dinitrogen complexes may also be possible. Experimentation in this would make use of the full diversity of metal-nitrosyl structural chemistry. Among the most interesting complexes would be those having bridging nitrosyls and/or metal-metal bonding. Examples of this type of nitrosyl are listed in Table 4.

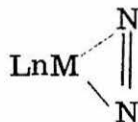
It is, of course, impossible to confidently predict the course of these reactions. The potential for undesirable side reactions is rampant. Should the reaction proceed successfully, one could anticipate dimeric products such as I or II or monomeric products such as III.



(I)

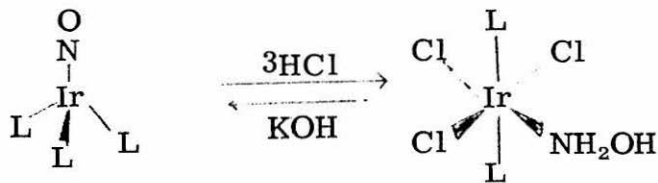


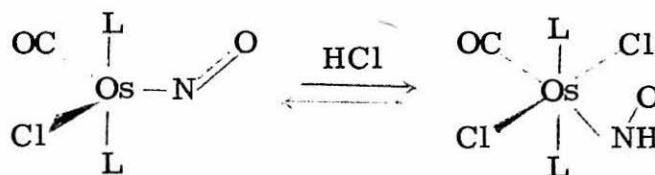
(II)



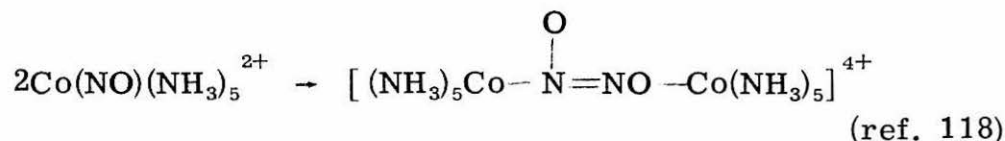
(III)

If the nitrogen of coordinated nitric oxide is electrophilic, the oxygen ought to be basic. Protonation reactions of coordinated nitric oxide have been reported^{9, 10}:





The latter of these examples is not an example of the class of coordinated nitrosonium ions that has been considered so far. It is a bent nitrosyl which is best thought of as coordinated NO^- .³ The reaction chemistry of coordinated nitric oxide would be expected to be dependent on the electronic structure adopted by the ligand. The bent nitrosyls tend to dimerize,^{3,55} as shown below,

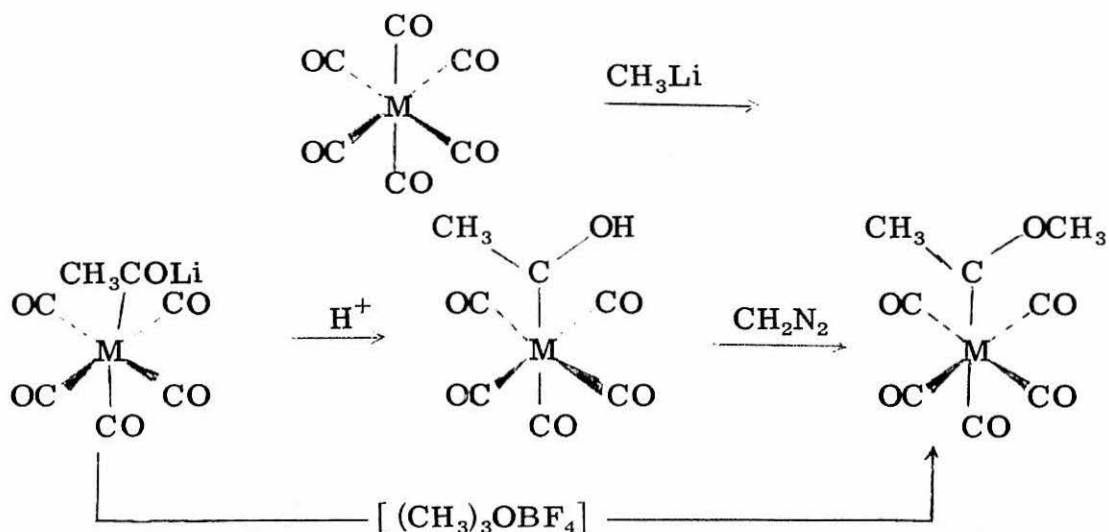


In any systematic investigation of the reactions of coordinated nitric oxide comparisons would be made between the reactivity of the linear, bent, and dimeric nitrosyl. Exceedingly interesting complexes for this type of comparison are $[\text{Os}(\text{NO})_2(\text{PPh}_3)_2\text{OH}]^{1+}$ ¹⁰² and $[\text{Ru}(\text{NO})_2(\text{PPh}_3)_2\text{Cl}_2]^{1+}$ ¹⁰³ which contain both linear and bent nitrosyl ligands.

B. Potential Reactions of Coordinated Nitric Oxide Analogous to Known Reactions of Coordinated Carbon Monoxide

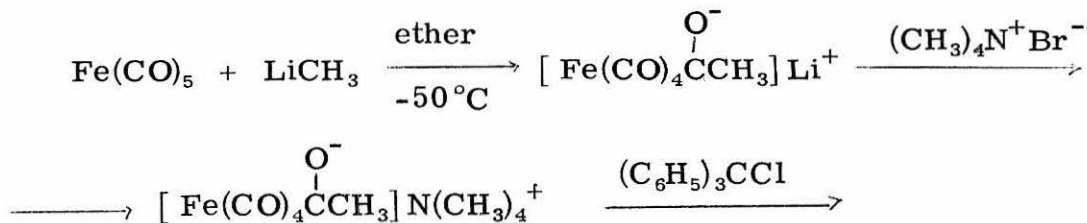
Though the charge of the nitrosonium ion cannot be ignored, the reactions of transition metal nitrosyls ought to parallel those of

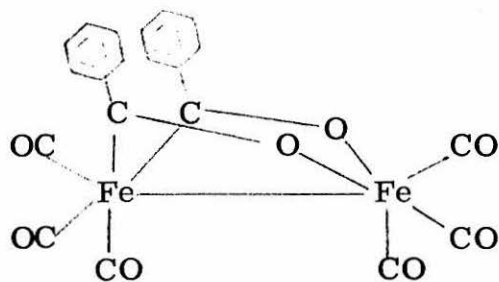
complexes of isoelectronic species such as CN^- and CO . Cyanide ion complexes are fairly inert, but carbonyl complexes have a rich chemistry. Fischer and Maasbal^{70, 71, 74} reported reactions between coordinated carbon monoxide and methyl lithium forming carbene complexes such as:



$\text{M} = \text{Cr}, \text{Mo}, \text{W}, \text{Mn}$

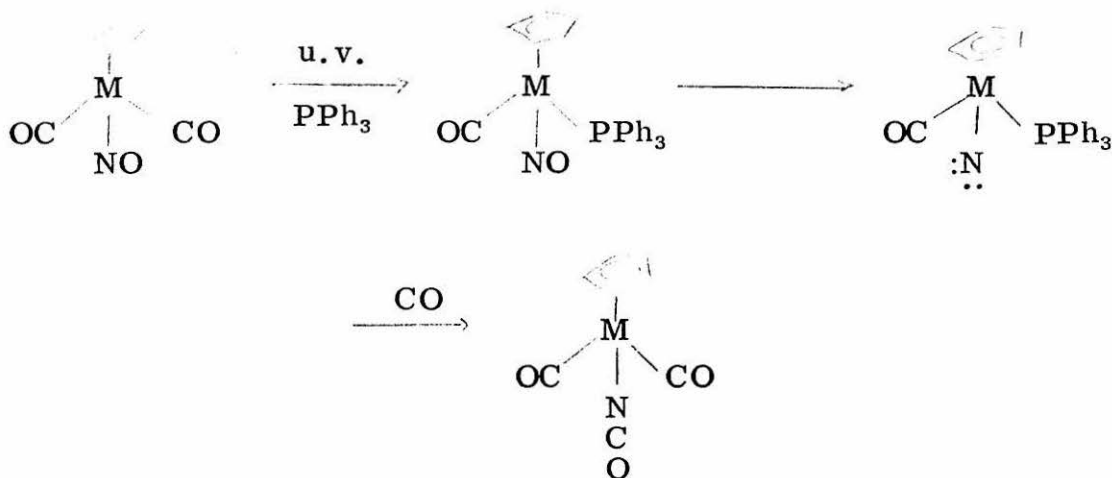
The reaction with ironpentacarbonyl followed a somewhat different course^{72, 73}:





The possibility of analogous reactions with nitrosyl complexes is obvious

MacPhail et al.⁵⁶ showed that nitrosyl complexes can be converted to highly reactive intermediates photochemically in reporting the reaction:



The rate of this reaction was $\text{Mo} > \text{W} \gg \text{Cr}$ which parallels the bond order between the metal and nitric oxide. Thermal reactions are less harsh and might be expected to produce a less reactive intermediate such as nitrene.¹¹⁹ Further, the reactivity of coordinated nitrosyl toward methylithium is suggested by the great reactivity of free NO with organic radicals.⁷⁵⁻⁷⁸ On the other hand, Fischer has shown⁷⁴ that

Table 4
Some Examples of Nitrosyl Complexes
Having Bridging NO

Complex	Ref.
	51
	51
	or
	51
	52, 2
	51, 53
$\text{Ru}_3(\text{NO})_2(\text{CO})_{10}$	117

when carbonyl nitrosyl complexes are treated with phenyl lithium only the carbonyl is attacked. This negative result may be due more to the choice of reagent rather than the inertness of the nitrosyl. Both methyl lithium and tertiary butyl lithium are more potent reagents. Treating carbonyl-free, nitrosyl complexes with these reagents may result in efficient attack on nitrogen.

Fischer's results do emphasize the importance of proper choice of nitrosyl complexes for these reactions. Most binary metal nitric oxide complexes are unstable^{1,3} and must be used with caution. Mixed carbonyl nitrosyl complexes cannot, of course, be used. Halide nitrosyl complexes are likely to yield methylated products by displacement of the halide. Further the complex must be soluble and stable in an inert solvent such as tetrahydrofuran or ether. Phosphene nitrosyls and organometallic nitrosyls are attractive. Table 5 lists some possible complexes. A variety of structures are listed since the course of reaction ought to be structure dependent and dependent on the electronic structure of the ligand. The compounds $CpM(NO)(PPh_3)$ ($M = Cr, Mo, W$) allow investigation of the effect of the metal nitrogen oxide bond order.

The course of the reaction with coordinated nitric oxide is again difficult to predict. One would hope that an intermediate similar to that in the carbonyl reaction would form. Such an intermediate might be called a nitron or methyl nitrosylate. It is most unlikely to behave

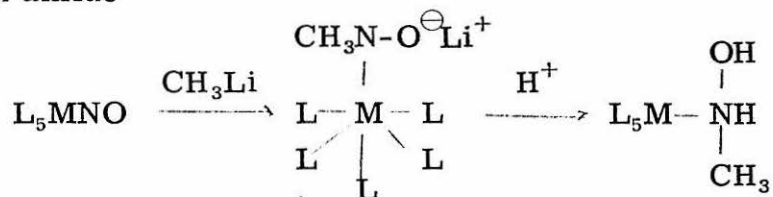
Table 5

(For specific structural information see references 1, 2, and 3.)

Nitrosyl Complex

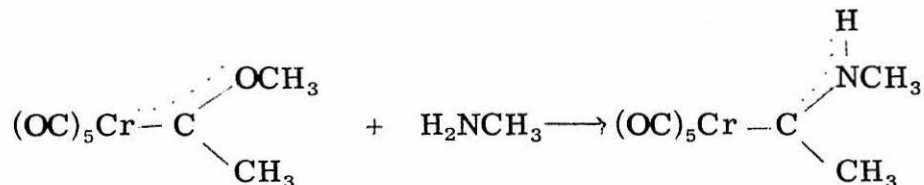
$\text{CpCr}(\text{NO})(\text{PPh}_3)_2$	a nice series for
$\text{CpMo}(\text{NO})(\text{PPh}_3)_2$	evaluation of the
$\text{CpW}(\text{NO})(\text{PPh}_3)_2$	effect of bond order
$\text{CpCr}(\text{NO})_2\text{R}$	$\text{R} = \text{CH}_3, \text{C}_2\text{H}_5, \text{C}_6\text{H}_5$
$\text{Cp}_3\text{Mo}(\text{NO})$	
$(\text{CpFe}(\text{NO})\text{Me})_2$	dimer, bridging NO
$(\text{CpCo}(\text{NO})_2)_2$	dimer with bridging and terminal NO
$\pi\text{C}_5\text{H}_5\text{Cr}(\text{NO})_2$	bent nitrosyl
$\pi\text{C}_5\text{H}_5\text{Ni}(\text{NO})$	linear nitrosyl
$\pi\text{C}_5\text{H}_5\text{Pb}(\text{NO})$	
$\text{Ni}(\text{NO})_2[(\text{R})_3\text{P}]_2$	$\text{R} = \text{C}_6\text{H}_5, \text{C}_3\text{H}_7$ sol. benzene, THF
$(\text{Co}(\text{NO})_2\text{NO}_2)_2$	also contains NO_2 group
binary metal nitrosyls	
of all types	

in ways analogous to the carbene intermediate. Nitrenes are highly reaction species.¹¹⁹ Rearrangement to oxazirane ($\text{CH}_2\text{---NH}$), formoximes, or further reactive to form oxime ethers is of special interest. Protonation of the intermediate may yield methyl hydroxylamine or an amide

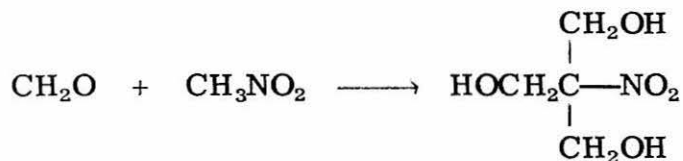


Rearrangement to coordinated $\text{CH}_2=\text{NH}$ which is unstable as a free species is possible.

Fischer and Klabuncle^{79, 80} found that carbene complexes were quite reactive to aminolysis

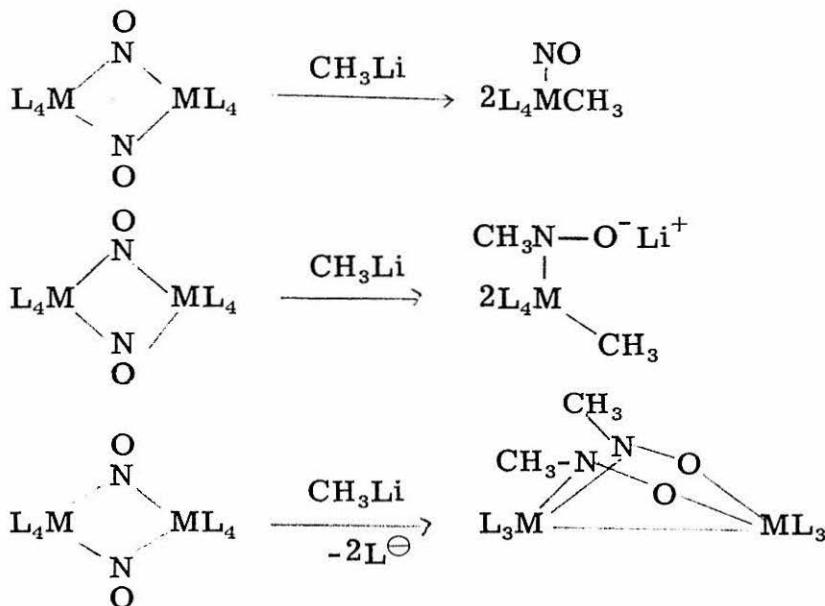


They conceived of $(\text{OC})_5\text{Cr}-\text{C}\begin{array}{l} \diagup \text{OCH}_3 \\ \diagdown \text{CH}_3 \end{array}$ as an ester of acetic acid with the ketonic oxygen replaced by the far more electronegative $(\text{OC})_5\text{Cr}^-$ group. Drawing upon this analogy, the product of the reaction with nitrosyl complexes is nitromethane with the ketonic oxygen replaced by the ML_5 group. Nitromethane is, of course, a very potent reagent. The methyl protons are quite acidic and susceptible to reaction:



This behavior will definitely be accentuated if the above analogy is correct. Intraligand reactions would definitely be possible.

Dimeric nitrosyl may react with methyl lithium to form methylated monomers, products analogous to those produced in the reaction of iron pentacarbonyl with methyl lithium (above), or both methylate and react as would monomers. One can be sure that the extent of metal-metal bonding will affect the course of reactions with dimers.

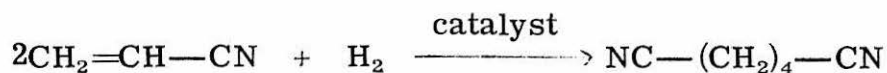


C. Catalytic Reactions of Coordinated Nitric Oxide

Two principal industrial reactions involving nitration are:

- (a) the formation of acrylonitrile ($\text{CH}_2=\text{CH}-\text{CN}$),
- (b) and the formation of adiponitrile ($\text{NC}(\text{CH}_2)_4\text{CN}$).

The two reactions are not unrelated since the hydrodimerization of acrylonitrile yields adiponitrile:



Many processes that facilitate this dimerization are known and a host of publications relate to it (for a review see ref. 86). However, yields do not now exceed 50%. Improvements have been suggested largely based on alterations of the starting material.⁸⁶ Transition metal nitrosyls may offer a more attractive solution.

Systematic design of catalytic reactions must be based extensively on analogy based on known catalytic systems and known chemistry. A systematic design will ordinarily be successful only in the case of homogeneous reactions. Often the best that can be done is to suggest a direction for an investigation to take. That is the intent of this proposition.

Table 6 outlines some of the important catalytic chemistry of transition metal nitrosyl complexes. A thoughtful reader will note how closely the data in this table parallel that assembled by Smidt et al. for their systematic development of the Wacker reaction.⁸⁵ These data are suggestive of a process for the formation of dinitriles. A flow

Table 6
Chemistry of Transition Metal Nitrosyls
Pertinent to Catalytic Discussions

- (1) Nitric oxide will convert methyl groups to nitriles over silver catalyst.¹⁰⁸
- (2) Mixtures of alkanes and nitric oxide will photolytically yield nitriles.^{92, 93}
- (3) Nitric oxide will convert alkenes to nitriles over a catalys of Bi_2O_3 , Nb_2O_5 , TiO_2 , P_2O_5 , or NiO .⁹⁵
- (4) NO reacts with propylene to form ethylnitrile.⁹⁶
- (5) NO reacts with ethylene to form $\text{C}_2\text{H}_4\text{NO}$.⁹⁶
- (6) Alkynes can be nitrated with nitric oxide.⁹⁴
- (7) Stable π -allyl complexes of iron nitrosyl carbonyls reported.^{87, 88}
- (8) Dienes can be converted to olefins over dicarbonyldinitrosyliron or dicarbonyldinitrosylcobalt.⁹⁷
- (9) πCpNiNO with Et_2AlCl will polymerize 1, 4-cis-polybutadiene in 82% yield.⁸⁹
- (10) πCpNiNO with Et_2AlCl will polymerize, dimerize, or copolymerize C_2 to C_{15} olefins in high yield.^{90, 91}
- (11) Reversible disproportionation of olefins over Mo or W nitrosyl complexes has been reported.¹⁰⁴

Figure 1

Catalytic Formation of Dinitriles

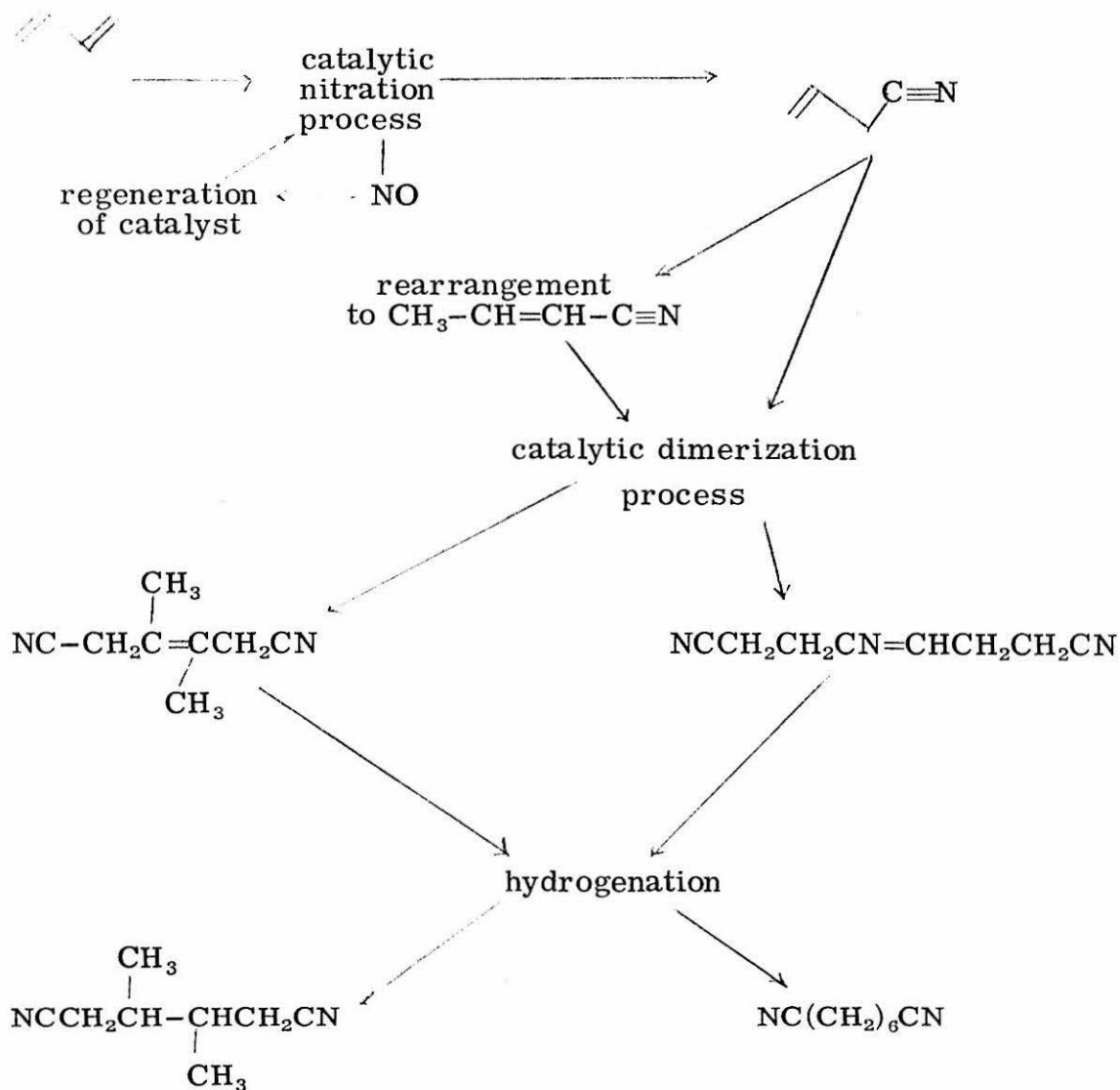
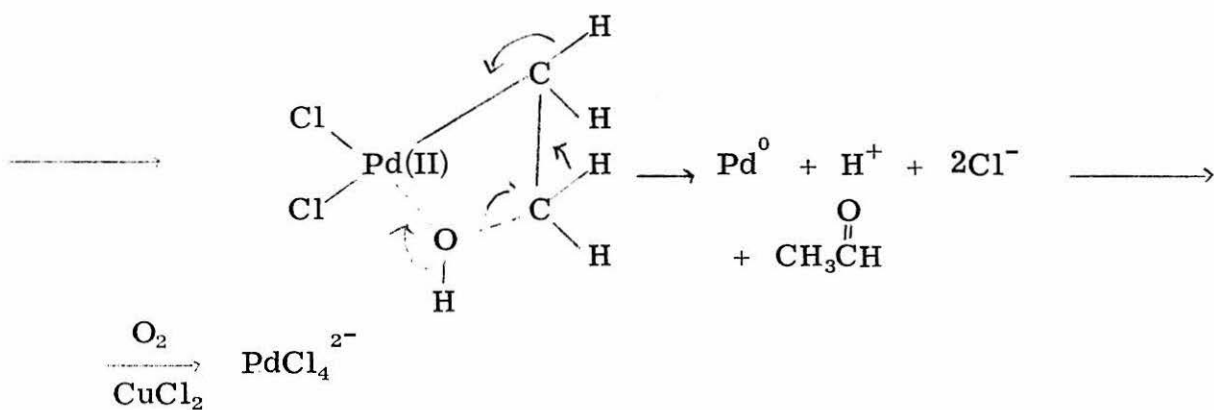
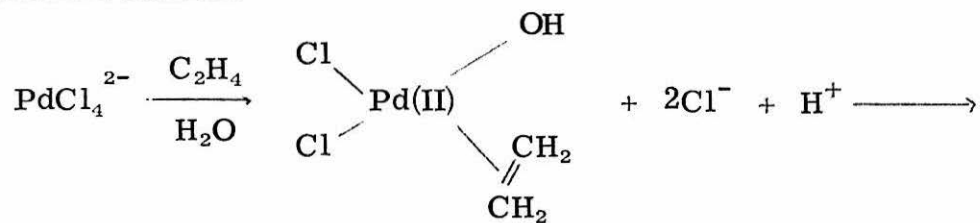
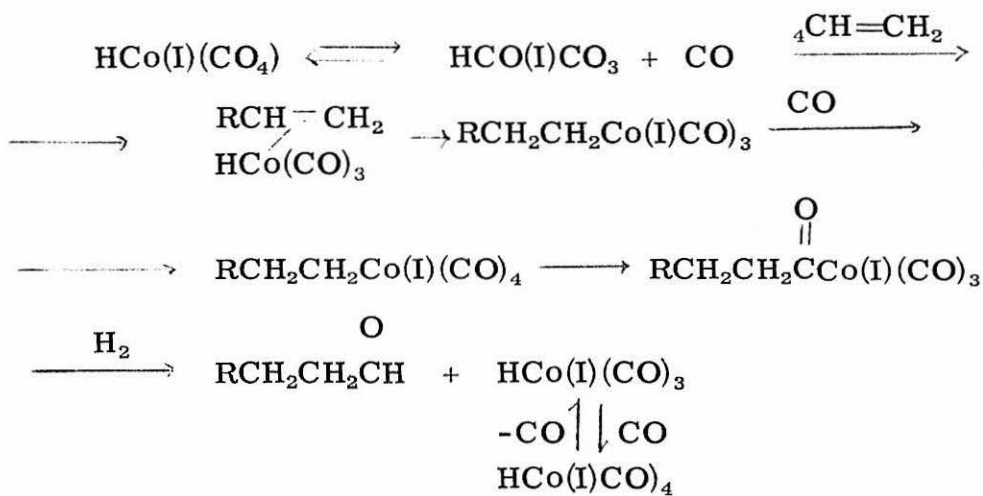


diagram of the potential process is illustrated in Figure 1. In the figure 1, 4-butadiene is converted to 1,6-dinitrilo-hexane, but one might speculate that a very analogous process might be formulated for the nitrilo-dimerization of allene. The data in Table 6 cannot be interpreted to conclusively support this, though.

The first step of the process is the formation of an olefinic nitrile. The data from points 3, 4, 5, and of Table 6 certainly show this is possible. These data apply to inhomogeneous reactions. The experience of the Wacker reaction suggests that these reactions might be extended to homogeneous systems. The NiO catalyst is especially encouraging in this regard (see below). One would expect the nitration of a diene to be more efficient than nitration of an olefin. The engineering aspects of any process could then be adjusted to restrict formation of the dinitrile ($\text{N}\equiv\text{C}(\text{CH}_2)\text{C}\equiv\text{N}$). Point 7 of Table 6 indicates that the choice of catalyst will be restricted by the stability of its dienyl complexes. Such stable complexes would, naturally, retard the reaction rate. Chemical intuition suggests that formation of weakly stable complexes of this type may be intimately involved in the nitration mechanism. Consequently, the catalyst must not be totally devoid of this type of coordinative ability. The catalyst is further restricted by point 9 which indicates that polymerization is a distinct possibility. Point 10, however, indicates that the conditions of reaction may be used to control this undesirable side reaction.

Figure 2

Wacker Process:"Oxo" Process

In the case of butadiene, the possibility of rearrangement of the olefinic nitrile to form a more conjugated double bond must be considered. Therefore in Figure 1 both possible products are carried through the remainder of the process. In the case of higher homologs of butadiene this would not be a consideration.

The second step of the process is the dimerization of the olefinic nitriles. Data from points 9 and 10 show that this may be by far the easiest part of the process. In fact by itself point 10 may be a more important reaction than now realized, since it will relieve the objections to the current acrylonitrile dimerization processes mentioned above. Point 11 at first appears to warn of a possible undesirable side reaction to the dimerization process. However, on reflection and the application of the principle of microscopic reversibility one sees that it is further evidence of the ease of the dimerization process. It also greatly expands the choice of catalysts.

Finally the olefin products are hydrogenated--a simple process deserving of no further comment.

A successful process would combine all three parts of this process in a single step. Here lies tremendous difficulty. The rate of hydrogenation of even moderately separated diolefins will exceed the rate for monoolefins. One must inhibit the rate of nitration of the olefin products while maintaining the olefin complex with the catalyst for hydrogenation. Many other potentially disastrous side reactions

can readily be seen by the reader. Thought experiments without a far greater body of hard data cannot provide a resolution of these difficulties.

The choice of the catalyst is impossible to make a priori. The data from Table 6 suggest that that nickel, iron, or cobalt nitrosyls might make efficient catalyst. However, each has its failings. The table intimates that second and third row transition metal nitrosyls merit closer scrutiny than they have so far received. Non-transition elements and silver have been successful heterogeneous catalysts. Unfortunately, nitrosyl complexes of these elements have been ignored in the past and it is not possible to evaluate their effectiveness in homogeneous systems. Hydrido nitrosyl complexes such as $\text{Ru}(\text{NO})\text{H}(\text{PPh}_3)_3$ ⁹⁹, $\text{Ir}(\text{NO})\text{H}(\text{PPh}_3)_3$ ¹⁰⁰ or $\text{Os}(\text{NO})\text{H}(\text{PPh}_2\text{Me})_3$ ¹⁰¹ may be potential catalysts which would also facilitate the hydrogenation reaction.

The process as described above involves the nitration of a di-olefin in direct analogy to the oxidation of an olefin by the Wacker reaction (Figure 2). Di-olefins are expensive to make. A more desirable reaction would be based on the formation of acrylonitrile by adding the nitrilo group to ethylene or acetylene, in direct analogy to the "oxo" process (Figure 2). Point 6 from Table 6 intimates that such a process is possible, but current data are not conclusive. Such a possibility would certainly be worth contemplation in any attempt to catalytically form dinitriles.

Table 7
Other Reactions of Nitric Oxide that
May Yield Catalytic Processes

- (1) NO reacts with cyclohexadienes to form benzene and N_2O . Rate determining step is proton extraction. ¹⁰⁵
- (2) NO adds to α methylstilbene. ¹⁰⁶
- (3) NO adds to C_2F_4 . ¹⁰⁷
- (4) NO catalyzes reaction between F_4N_2 and olefins. ¹⁰⁹
- (5) NO increases selectivity of halogenation of partially halogenated carbon. ¹¹²
- (6) NO accelerates chlorination of GeO_2 and SeO_2 . ¹¹³
- (7) NO catalyzes oxidation of naphthalenes over Se. ¹¹⁵
- (8) Extensive reactivity of nitric oxide to produce free radicals ¹²⁻³¹ suggest nitrosyls may form excellent polymerization initiators.

Some other reactions of nitrosyl complexes and nitric oxide which might spawn catalytic systems are listed in Table 7.

References

1. B. F. G. Johnson and J. A. McCleverty, Prog. Inorg. Chem., 7, 277 (1966).
2. W. P. Griffith, Adv. in Organometal. Chem., 7, 211 (1968); and references therein.
3. N. G. Connelly, Inorganica Chimica Acta Revs., 47 (1972).
4. P. T. Monoharan and H. B. Gray, J. Amer. Chem. Soc., 87, 3340 (1965).
5. J. H. Swinehart, Coord. Chem. Revs., 2, 385 (1967).
6. W. Hieber, H. Beutner, and J. Ellermann, Chem. Ber., 96, 1659 (1963).
7. W. Hieber and J. Ellerman, Chem. Ber., 96, 1643 (1963).
8. R. B. King, Inorg. Chem., 2, 1275 (1965).
9. C. A. Reed and W. R. Roper, Chem. Comm., 155 (1969).
10. K. R. Grundy, C. A. Reed, and W. R. Roper, ibid., 1501 (1970).
11. F. Bottomley and J. R. Crawford, ibid., 200 (1971).
12. S. N. Ganz and A. M. Vashkevich, Khim. Tekhnol., 9, 89 (1967); CA:70:61709c.
13. L. Ya Tereshchenko, M. B. Pozina, N. N. Bashlachevz, Zh. Prikl. Khim., 42, 2678 (1969); CA:72:74269c.
14. J. W. Hogue and J. B. Levy, J. Phys. Chem., 73, 2834 (1969).
15. J. Heicklen and V. Knight, J. Chem. Phys., 47, 4272 (1967).
16. H. Feilchenfeld, J. Kenat, and S. Manor, Trans. Faraday Soc., 65, 2350 (1969).

17. A. B. Ray, Inorganic Chem., 6, 110 (1967).
18. J. A. Coxon, Trans. Faraday Soc., 64, 2118 (1968).
19. J. C. Boden and B. A. Thrush, Proc. Roy. Soc. Ser. A, 305, 107 (1968).
20. B. M. Hughes and T. O. Tiernan, J. Chem. Phys., 51, 4373 (1969).
21. R. Shaw, F. R. Cruickshank, S. W. Benson, J. Phys. Chem., 71, 4538 (1967).
22. C. Tuzun and N. Yuksekisik, Comm. Fac. Sci. Ankara., 14, 34 (1967).
23. G. Doucet-Baudry and J. C. Biechler, Compt. Rend. C, 267, 1245 (1968).
24. A. V. Pankratov, L. A. Hkhanshchikova, O. N. Shalaeva, E. L. Gurinova and R. A. Bekker, Zh. Neorg. Khim., 13, 1787 (1968).
25. T. L. Nunes and R. E. Powell, Inorg. Chem., 9, 1916 (1970).
26. B. W. Tattershall and G. H. Cady, U. S. Govt. Res. Develop. Rept. 41, 59 (1966).
27. J. N. Cooper, J. E. Chilton, R. E. Powell, Inorg. Chem., 9, 2303 (1970).
28. A. V. Fokin and A. T. Uzun, Zh. Obshch. Khim., 31, 1798 (1966).
- 29.
30. J. L. Holmes and E. V. Sundaram, Trans. Faraday Soc., 62, 910 (1966).
31. O. Klaus, M. Shelef, and J. T. Kummer, J. Phys. Chem., 74, 2690 (1970).

32. T. J. Meyer, J. B. Godwin, and N. Winterton, Inorg. Chem., 10, 471 (1971).
33. F. B. Bottomley and J. R. Crawford, Chem. Comm., 200 (1971).
34. T. J. Meyer and F. J. Miller, J. Amer. Chem. Soc., 93, 1294 (1971).
35. J. N. Cooper, J. E. Chilton, and R. E. Powell, Inorg. Chem., 9, 2303 (1970).
36. K. Otto, M. Shelef, and J. T. Kummer, J. Phys. Chem., 74, 2690 (1970).
37. S. Cenini, R. Ugo, G. LaMonica, and S. D. Robinson, Inorganica Chim. Acta, 6, 182 (1972).
38. J. N. Armor and H. Taube, J. Amer. Chem. Soc., 91, 6874 (1969).
39. F. Bottomley and S. J. Nyburg, Acta Cryst., 24, 1289 (1968).
40. J. H. Enemark, et al., Chem. Comm., 96 (1968).
41. B. R. Davis, N. C. Payne, and J. A. Ibers, J. Amer. Chem. Soc., 81, 1240 (1969).
42. C. Ercolani, C. Neri, and G. Sartori, J. Chem. Soc. A, 2123 (1968).
43. H. Brunner and H. Wachsmann, J. Organometal. Chem., 15, 409 (1968).
44. G. Cardaci and S. M. Murgia, ibid., 25, 483 (1970).
45. T. A. George and S. D. Seibold, ibid., 30, 13 (1971).
46. B. F. G. Johnson, J. Chem. Soc. A, 475 (1967).
47. J. Chatt, et al., ibid., 842 (1970).

48. D. K. Hait, and P. Bandyopadhyay, J. Ind. Chem. Soc., 47, 1185 (1970).
49. J. Chatt, J. Chem. Soc. A, 702, 895 (1971).
50. A. Arnco, V. Valenti, and F. Cariati, J. Inorg. Nucl. Chem., 32, 1877 (1970).
51. R. B. King and M. B. Bisnette, Inorg. Chem., 3, 791 ((1964).
52. L. Y. Y. Chan and F. W. B. Einstein, Acta Cryst., 26B, 1899 (1970).
53. R. C. Elder, F. A. Cotton, and R. A. Schunn, J. Amer. Chem. Soc., 89, 3646 (1967).
54. D. A. C. McNeil, J. B. Raynor, and M. C. R. Symons, Proc. Chem. Soc., 364 (1964).
55. A. Schweizer, Ph.D. Thesis, California Institute of Technology, 1973; and references therein.
56. A. T. McPhail, G. R. Knox, C. G. Robertson, and G. A. Sim, J. Chem. Soc. A, 205 (1971).
57. L. Cambi, A. Cagnasso, T. Ricci, Gaaz. Chim. Ital., 61, 3 (1931); CA:25:2383.
58. N. O. Engfeldt, Z. Biochem., 159, 257 (1925); CA:20(1926)927.
59. I. M. Kolthoff and P. E. Toren, J. Amer. Chem. Soc., 75, 1197 (1953).
60. J. H. Swinehart and P. A. Rock, Inorg. Chem., 5, 573 (1966).
61. P. A. Rock and J. H. Swinehart, ibid., 5, 1078 (1966).
62. W. Moser, R. A. Chalmers, and A. G. Fogg, J. Inorg. Nucl. Chem., 27, 831 (1965).

63. A. G. Fogg, A. D. Jones, and M. Moser, ibid., 28, 2428 (1966).
64. A. G. Fogg, A. H. Norbury, and M. Moser, ibid., 28, 2753 (1966).
65. R. A. Chalmers, Anal. Chim. Acta, 36, 248 (1966).
66. K. W. Loach and T. A. Turney, J. Inorg. Nucl. Chem., 18, 179 (1961).
67. J. H. Swinehart and W. G. Schmidt, Inorg. Chem., 6, 232 (1967).
68. O. Baudisch, Science, 108, 443 (1948).
69. J. H. Swinehart, Coord. Chem. Revs., 2, 403 (1967); and references therein.
70. E. O. Fischer and A. Maasböl, Angew Chem., 76, 645 (1964).
71. E. O. Fischer and A. Maasböl, Angew Chem. Internat. Ed., 3, 580 (1964).
72. E. O. Fischer and V. Kiener, Chem. Ber., 102, 1148, (1969)
73. E. O. Fischer, V. Kiener, D. St. P. Bunbury, E. Frank, P. F. Lindley, and O. S. Mills, Chem. Comm., 1378 (1968).
74. E. O. Fischer, Pure and Appl. Chem., 24, 407 (1970)
75. V. A. Ginsburg, L. L. Mortynova, and M. N. Vasil'eva, Zh. Obschch. Kim., 37, 1083 (1967).
76. E. Kamaratos and W. Lampe, J. Phys. Chem., 74, 2267 (1970).
77. H. E. Van den Bergh, Trans. Faraday Soc., 67, 2017 (1971).
78. J. Heickler and N. Cohen, Adv. in Photochemistry, Vol. 5, eds., W. A. Noyes, G. S. Hammond, and J. N. P. Interscience, New York, 1968, p 157.

79. U. Klabunde and E. O. Fischer, J. Amer. Chem. Soc., 89, 7141 (1967).
80. U. Klabunde, Thesis, Northwestern University,
81. J. Masck, Inorg. Chim. Acta Revs., 3, 99 (1969).
82. I. M. Kolthoff and P. E. Toren, J. Amer. Chem. Soc., 75, 1197 (1953).
83. S. F. A. Kettle, J. Chem. Soc. A, 1013 (1966).
84. J. N. Armor and M. Buchbinder, Inorg. Chem., 12, 1086 (1973).
85. G. Szonyi, Advances in Chemistry Series, Vd. 70, R. F. Gould, ed., 1968, p 53.
86. M. B. Sherwin and P. H. Spitz, Chem. Eng. Prog., 68, 69 (1972).
87. H. D. Murdock, Z. Naturforsch, 20b, 179 (1965).
88. R. Bruce, F. M. Chaudhary, G. R. Knox, and P. L. Pauson, Z. Naturforsch, 20b, 73 (1966).
89. K. Tami and S. Yuguchi, Japanese patent.
90. N. Bergem, U. Blindheim. O. Onsager and H. Wang, French Patent, 1,519,181.
91. H. E. Dunn, U. S. Patent 3,558,738.
92. H. E. Gunning, U.S. Patent 3,371,024.
93. V. Ya. Shtern, Khim. Kinet. Tsepaye Reakts. Institute Khim. Fiz. Akad. Nauk. SSR, 286 (1966).
94. S. F. Reed, J. Org. Chem., 35, 3961 (1970).

95. J. M. Kruse, U. S. Patent 3,342,847.
96. N. N. Kikhailovskaya, A. F. Rozlovskii, K. S. Stepanora,
Dokl. Akad. Nauk. SSR, 184, 608 (1969).
97. J. P. Candlin and W. H. Janes, J. Chem. Soc. C, 1856 (1968);
British patent 1,085875.
98. F. Basolo and R. G. Pearson, "Mechanisms of Inorganic
Reactions," John Wiley and Sons, Inc., New York, 1967.
99. C. G. Pierpoint, A. Pucci, and R. Eisenberg, J. Amer. Chem.
Soc., 93, 3050 (1971).
100. D. M. P. Mingos and J. A. Ibers, Inorg. Chem., 10, 1479 (1971).
101. W. R. Robinson and M. E. Swanson, J. Organometal. Chem., 35,
315 (1972).
102. J. M. Waters and K. R. Whittle, Chem. Comm., 518 (1971).
103. C. J. Pierpoint, D. G. VanDerveer, W. Durland, and R.
Eisenberg, J. Amer. Chem. Soc., 92, 528 (1970).
104. E. A. Zuech, W. B. Hughes, D. H. Kubicek, and E. T. Kittleman,
J. Amer. Chem. Soc., 92, 528 (1970).
105. R. Shaw, F. R. Cruickshank, and S. W. Benson, J. Phys. Chem.,
71, 4538 (1967).
106. G. Doucet Baudry and J. C. Biechler, Compt. Rendes. C, 267,
1245 (1968).
107. A. V. Fokin and A. T. Uzun, Zh. Obshch Khim., 36, 1798 (1966).
108. E. Fischer, Ind. Chim. Belge, 32, 972 (1967).
109. A. V. Fokin, V. I. Zimin, Yu N. Studnev, and V. K. Korotov,

- Zh. Org. Khim, 6, 880 (1970).
110. B. W. Graham, K. R. Laing, and C. J. O'Connor, J. Chem. Soc D, 1272 (1970).
111. J. R. Bellinger, K. L. Lindfors, and D. X. West, J. Inorg. Nucl. Chem., 32, 3837 (1970).
112. C. Solvay, Belgium Patent 760,506.
113. V. I. Ivantova, L. I. Kutakova, and Izv Uyssh Ucheh, Zaved Tsvet Met., 14, 81 (1971).
114. C. G. Pierpoint and R. Eisenberg, J. Amer. Chem. Soc., 93, 4905 (1971); and references therein.
115. W. D. Vanterwerff and H. J. Peterson, U.S. Patent 3,637,830.
116. F. A. Cotton and G. Wilkinson, "Advanced Inorganic Chemistry," 2nd ed.,
117. J. Norton, J. P. Collman, G. Polcetti, and W. T. Robinson, Inorg. Chem., 11, 382 (1972).
118. P. Gan, J. Chem. Soc. A, 943 (1967).
119. J. Hamer and A. Macaluso, Chem. Revs., 64, 473 (1964);
L. I. Smith, Chem. Revs., 23, 193 (1938).